The University Of Sheffield.

Titanium Foams via Metal Injection Moulding in Combination with a Space Holder

By:

Mohammed Menhal Mohammed Shbeh

Registration No: 140226308

Supervisors:

Dr. Russell Goodall

Prof. Iain Todd

Dr. Aleksey Yerokhin

A thesis submitted in partial fulfilment of the requirements for the degree of
Doctor of Philosophy

The University of Sheffield

Faculty of Engineering

Department of Materials Science and Engineering

August 2018

Acknowledgements

I would like to express my deepest gratitude and appreciation to my supervisors Dr Russell Goodall and Dr Aleksey Yerokhin for their guidance and support throughout my PhD project. I could not have imagined having better supervisors for my PhD than them.

I would also like to thank my friends Raghdan Namus, Muntather Qasim, Muhaed Alali, Sameer Hamad, Radwan Aljuhashy, Ammar Al-Rubaye, Mohammed Noori, Anwer Al-Obaidi, Haider Al Shabbani and several others for making the PhD experience more enjoyable.

Special thanks go to Mosalagae Mosalagae and Mohammed Elbadawi and hope that our collaborations continue for many years to come.

I also like to acknowledge a studentship from the Iraqi Ministry of Higher Education and Scientific Research.

I would like to thank my family: my parents, brothers and sisters for motivating and supporting me financially to pursue my dream and overcome any challenges.

Last but not the least, my sincere and heartfelt thanks goes to Elif Oner, who has passionately supported me in my difficult time and helped me to overcome many problems throughout my PhD project.

Summary

In the last decade, there has been increasing interest in the production and characterisation of titanium foams due to the unique combination of properties that are offered by these advanced materials, such as extra light weight, high compressive strength, good energy absorption and high permeability, particularly for open celled foams. These foams have huge potential in a variety of applications, especially for biomedical applications as they offer the possibility to address the stress shielding problem by tailoring their mechanical properties to match that of the human bone. The latter phenomenon results from the non-uniform partitioning of load between the implant and the surrounding tissue or bone as a result of the large difference between the elastic moduli of the dense implant and the bone.

Ti foams are mostly produced by powder metallurgical foaming techniques, due to the high melting temperature of Ti and its extreme susceptibility to contamination during melting. One major challenge in producing Ti foams is the inability to easily shape these foams after production to the desired shape without resulting in the closure and smearing of the pores and hence, altering the pore morphology, while creating residual stresses and breaking some of the cells and deteriorating the mechanical properties. This problem could be addressed by developing a foaming technique that makes it feasible to produce foams with the final shapes desired for the component.

One promising technique with great potential for solving this problem, which also has the ability to mass produce net shaped open celled Ti foams, is Metal Injection Moulding in combination with a Space Holder (MIM+SH). This technique combines MIM technology, which is commonly used for producing net shaped complex parts in large quantities, with the space holder technique, thus ensuring flexible design with different pore morphologies.

The main aim of the project was to investigate the use of MIM+SH technique for the manufacture of Ti foams with different mesostructures with the potential for biomedical applications. The foams produced were characterized using Scanning Electron Microscopy (SEM), Micro-Computed Tomography (Micro-CT) and X-ray Fluorescence (XRF). The results showed that it is possible to produce net shaped Ti foams with different volume percentage of porosities and pore morphologies and with a structure that replicates the

structure of the natural bone in having a compact outer layer for increased strength and inner spongy layer for nutrient exchange. The volume percentage of porosity in the foams produced was in the range of 20-64%. In addition, it was found that the shape of the space holder does not have a significant impact on the percentage of final porosity in the samples. However, it has an influence on the mechanical properties of the foams produced, where foams made by spherical space holder was found to have a higher yield stress than those made with the cubic space holder.

Digital Image Correlation (DIC) test was also carried out in order to analyse the failure mechanism and figure out the distribution of strain across the samples. The analysis showed that much of the strain is concentrated at 45° in the samples and thus failure is likely to occur by plastic deformation leading to the growth of cracks in these regions driven by the shear forces.

After that two approaches were investigated to increase the bioactivity and to potentially address the bioinertness of Ti, which can be an obstacle towards inducing full integration between the bone and implant. The first approach involved introducing a bioactive material known as Hydroxyapatite (HA) into the structure of the foams, while in the second approach the foams were treated using Plasma Electrolytic Oxidation (PEO) to develop a ceramic coating.

It was found that adding HA to the Ti can induce brittleness in the structure and reduces the load bearing ability of the titanium foams by resulting in weak ceramic phases. The extent of this brittleness depends on the amount of HA added to the structure. While PEO treatment of the Ti foams produced develops thick surface layers that penetrate through the inner structure of the samples forming a network of surface and subsurface coatings. The results are of potential benefit in producing surface engineered porous samples for biomedical applications which do not only address the stress shielding problem, but also improve the chemical integration.

Table of Contents

List of Figures

List of Tables

List of Abbreviations and Symbols

DSC	Differential Scanning Calorimetry
EDS	Dispersive X-ray Spectroscopy
FTIR	Fourier Transform Infrared Spectroscopy
HA	Hydroxyapatite
KCl	Potassium Chloride
MIM+SH	Metal Injection Moulding in Combination with a Space Holder
Micro CT	Micro-Computed Tomography
n	Flow behaviour index
PEG	Polyethylene Glycol
PEO	Plasma Electrolytic Oxidation
PMMA	Poly Methyl Methacrylate
SA	Stearic Acid
SH	Space Holder
SEM	Scanning Electron Microscope
TGA	Thermogravimetric Analysis
XRF	X-Ray Fluorescence
C	Capacitance
K	Dissolution rate constant
t	time in seconds
S	Surface area
τ_y	Yield Shear Stress
η_p	Plastic Viscosity
Wt.%	Weight percentage
Vol.%	Volume percentage
$\dot{\gamma}$	Shear rate

Publications

Parts of the work described in this thesis has been published in the following articles:

Invited papers / special issue

1. Shbeh, Mohammed, Aleksey Yerokhin, and Russell Goodall. "Microporous Titanium through Metal Injection Moulding of Coarse Powder and Surface Modification by Plasma Oxidation." Applied Sciences 7.1 (2017): 105.
2. Shbeh, Mohammed Menhal, and Russell Goodall. "Open pore titanium foams via metal injection molding of metal powder with a space holder." Metal Powder Report 71.6 (2016): 450-455.

Research Papers

1. Shbeh, Mohammed, Aleksey Yerokhin, and Russell Goodall. "Cyclic Voltammetry Study of PEO Processing of Porous Ti and Resulting Coatings." Applied Surface Science (2018).
2. Shbeh, Mohammed Menhal, and Russell Goodall. "Open Celled Porous Titanium." Advanced Engineering Materials (2017) 1600664.
3. Shbeh, Mohammed Menhal, and Russell Goodall. "Design of water debinding and dissolution stages of metal injection moulded porous Ti foam production." Materials & Design 87 (2015): 295-302.
4. Shbeh, M.M. and Goodall, R., Single-and multi-layered porous titanium via metal injection moulding. Advance Materials Letters (2017), volume 8, issue 4, page 500-505,

Conference paper

1. Shbeh, Mohammed Menhal, and Russell Goodall. "Advanced Processing: Design and Optimisation of Powder Processed Metallic Foams for Different Applications." European Congress and Exhibition on Powder Metallurgy. European PM Conference Proceedings. The European Powder Metallurgy Association, 2015.

Awards

1- Engineering Researcher Symposium Best Presenter award, second prize, University of Sheffield (2017)
2- ABTA Doctoral Researcher Awards Honourable Mention for excellency in research (2017)
3- Postgraduate Researcher Experience Programme (£850) (2017)
4- Sheffield Metallurgical and Engineering Association Travel Award (£500) (2017)
5- Engineering Researcher Symposium Best Poster award, First prize University of Sheffield (2016)
6- Best poster award, first prize, Materials Science and Engineering Department, University of Sheffield (2016).
7- Best Scientific Image award, First Prize-Metals category, Materials Science and Engineering Department, University of Sheffield (2016)

Conferences

Invited Talks

1- Mohammed Shbeh and Russell Goodall ‘‘Biologically Active Titanium Foams’’ IDC Machining Science 2017, AMRC, Rotherham
2- Mohammed Shbeh and Russell Goodall, ‘‘Titanium Foams for Dental Implants’’ New Scientist Live, London, UK, September, 2016.
3- Mohammed Shbeh and Russell Goodall ‘‘Metal Injection Moulding Titanium Foams’’ Advanced Engineering, Birmingham, UK, November 2015

Talks

1- Mohammed Shbeh and Russell Goodall ‘‘Porous Titanium for Biomedical Applications’’ Middle East Technical University, December 2017, Turkey
2- Mohammed Shbeh and Russell Goodall ‘‘Bio functionalized Titanium Foams for Biomedical Applications’’ MetFoam 2017, Nanjing, China.
3- Mohammed Shbeh and Russell Goodall ‘‘Surface Modified Titanium Foams for Biomedical Applications’’ Titanium Europe 2017, Amsterdam, The Netherlands.
4- Mohammed Shbeh and Russell Goodall ‘‘Single- and multi-layered porous titanium via metal injection moulding’’ European Advanced Materials Congress, Stockholm, Sweden, August, 2016
5- Mohammed Shbeh and Russell Goodall ‘‘Titanium Foams for Biomedical applications’’ Set for Britain, House of Commons, London, UK, December 2015
6- Mohammed Shbeh and Russell Goodall ‘‘Designing and Processing Ultra-Light Functionally Structured Metallic Foams’’ EUROMAT, Warsaw, Poland, August, 2015.
7- Mohammed Shbeh and Russell Goodall ‘‘Design and Optimisation of Powder Processed Metallic Foams for Different Applications’’ PM 2015, Reims, France, September, 2015.
8- Mohammed Shbeh and Russell Goodall ‘‘Mesostructured Titanium Foam by Metal Injection Moulding’’ Titanium Europe, Birmingham, UK, July, 2015.

1 Introduction and aims

1.1 Introduction

Titanium is the fourth most abundant metal and the ninth most abundant element in the Earth's crust [1]. It is characterized by its light weight, high strength, high melting temperature and excellent corrosion resistance. It has a density of about 60% of that of steel and a lower thermal expansion coefficient, but it has a higher melting temperature of approximately 1668±10°C [2]. These superior properties have made Ti indispensable in several applications, such as in aero-engines, and the main focus of research for several decades. However, this focus has been shifted in the last decade towards Ti foams and their production due to the uniqueness of these foams in combining some of the most sought after properties of Ti (such as high melting temperature, biocompatibility, light weight and excellent corrosion resistance) with the distinctive properties of foams such as low density and high permeability to fluids, thus, producing ultra-light and stiff foams with excellent mechanical properties and good corrosion resistance. These foams can potentially be utilized in a variety of areas such as structural, biomedical and aerospace applications.

Owing to the high melting temperature of Ti and its high susceptibility to contamination during melting, Ti foams are mainly processed through powder metallurgical routes. Several researchers have tried producing Ti foams with controlled pore sizes and morphologies using different powder metallurgical foaming techniques such as slip casting [3], gel casting [4] and impregnation of a polymer foam [5]. However, hitherto most of the Ti foams produced do not have a desired shape or complex geometries. Furthermore, subsequent grinding and machining are usually required to shape these foams into the final shapes. These grinding and machining processes can result in significant contamination of the foams produced and closure of the pores, thus significantly deteriorating their performance in different applications [6]. In addition, some of these techniques are relatively slow and do not offer the possibility of producing Ti foams in large quantities and hence limiting these routes' viability on a commercial scale.

One promising foaming technique that could have the potential in addressing these issues is Metal Injection Moulding in combination with a Space Holder (MIM+SH). MIM is a well-known manufacturing technique for the production of net shaped complex metal parts in

large volumes [7], while a space holder is a material that is temporarily added during the processing stages to create pores in the metallic structure and is removed at an advanced stage in the manufacturing process. Examples of space holder materials include KCl, NaCl and PMMA [8-11]. Combining MIM with a space holder such as KCl could have a huge potential in producing net shape Ti foams in large quantities.

1.2 Aims of the project

The main aim of the project is to examine the use of Metal Injection Moulding in combination with a Space Holder (MIM+SH) for potential use in mass producing near net shape, open-celled Ti foams with different volume percentages of porosity and pore shapes via the development of special feedstock. A second aim of the project is to explore the possibility of controlling the mesostructure and mechanical properties of the foams produced through the optimisation of the processing and foaming parameters in order to achieve functionally graded mesoporous Ti for different applications. A third aim of the project is to assess the suitability of the developed feedstock in processing commercial biomedical parts with complex shapes. Another aim of the project is to investigate the possibility of improving the bioactivity of the foams produced by the addition of hydroxyapatite to the Ti during mixing and by surface modification via Plasma Electrolytic Oxidation.

1.3 Project outline

The first chapter states the motivation for the project and the main objectives of this research. Chapter two summarizes the previous work on Ti foams and reviews the core findings of these studies. Chapter three is focused on the methodology of the experiments. Chapter four is concerned with the development of feedstock without space holder and comparing its performance to that of commercial feedstock. Chapter five deals with the incorporation of space holder into the feedstock with preliminary trials for injecting porous parts. Chapter six describes the effect of space holder on porosity and mechanical properties. Chapter seven is about improving the bioactivity of Ti foams by adding hydroxyapatite. Chapter eight is concerned with modifying the structure of the Ti foams via plasma electrolytic oxidation. Chapter nine reviews the conclusions that have been drawn from the results.

1.4 Terminology used in thesis

The terminology used to describe metal parts with different percentages of porosities is quite varied, interchangeable and under huge debate. Examples of terms used for describing metal parts with different percentages of porosities include metal foams, metal sponges and cellular metals. The first three terms are used interchangeably in the literature and only cellular metals have a clear and precise definition and distinctive characteristics to be called cellular, which cannot be mistaken, where they have regular distinct cells with approximately similar size. One common classification system that is widely cited in the literature distinguishes between different porous parts according to the state of the matter used in processing them is shown in **Figure 1** as reported by Banhart [12].

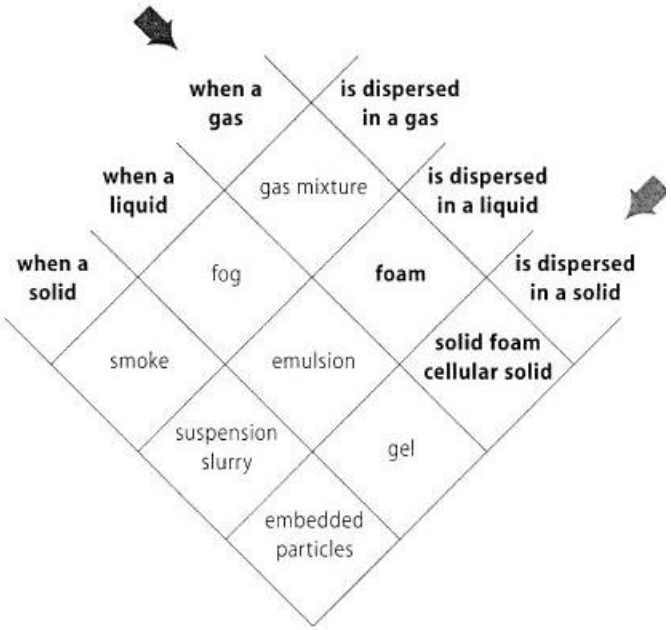

Figure 1. Possible designations for dispersing one phase into a second phase [13]

According to this classification the term foam is in its original sense reserved for describing porous parts which originate from a liquid foam by melting a metal into a liquid state and dispersing fine gas bubbles within it. Banhart also states that porous parts produced by powders or in solid state should preferably called sponges [13]. However, these recommendations are somewhat misleading particularly in the case of Ti, where Ti sponges (intentionally-made porous parts) can be mistaken for those Ti sponges produced during the first stage of processing and producing Ti powder from its ores, as well as the reactions involved in the production process, and hence the term has been mainly avoided in the

literature when it comes to describing porous Ti parts. Instead, researchers mainly use two expressions to describe foams produced by powder technology techniques, namely Ti foams [14-25] and porous Ti [3, 4, 9-11, 26-31] regardless of the porosity content. Thus, the term Ti foam will be used throughout the thesis.

2 Literature Review

2.1 Foams

Foams are advanced materials that consist of a network of interconnected or randomly spaced macropores separated by dense or microporous cell walls. These macropores can be either open or closed, or mix of those two, depending on the manufacturing process. Open pores are permeable pores that bridge the internal structure of the foam to the environment, whereas closed pores are often impermeable pores with their surfaces covered with a thin layer of the foam material. Open pore foams are typically not as strong and stiff as closed pore foams, but they possess a higher surface area to volume ratio which can be beneficial for a number of applications such as catalytic and heat dissipation applications [20]. Unlike common materials, where the microstructure is the sole player in dictating the properties, foams' properties can vary significantly according to both their mesostructure (how the porosity is arranged) and microstructure. Both of these structural levels play a role in altering the properties of foams. Thus, foams are often considered more complex and advanced materials compared to traditional ones [32]. This 'mesostructure' is the level of structure between the microstructure and macrostructure and is mainly concerned with the morphology, size and arrangement of the three dimensional macropores that present in the foams. **Figure 2** illustrates examples of different types of foams with different pore morphologies.

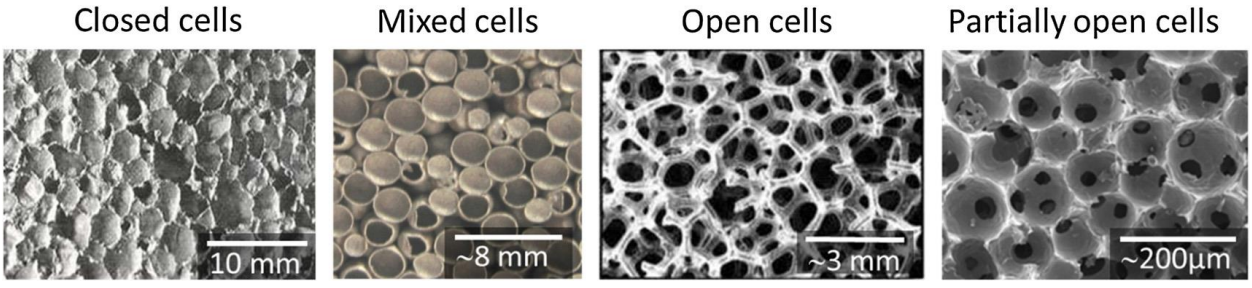

Figure 2. Different types of foams with different pore morphologies [33]

2.2 Manufacturing routes of Ti foams

It is well known that processing titanium in the liquid state can be very challenging due to its high melting temperature and its extreme affinity for atmospheric gases such as oxygen and nitrogen [34]. Therefore, Ti foams are almost always processed by powder metallurgical routes, generating and retaining a porous form from powder particles, and causing atomic-level bonding between the particles with a sintering treatment at a temperature below the melting point. Focusing on powder-based production methods used for titanium and its major alloys (i.e. CP-Ti and Ti-6Al-4V), it is still possible to delineate several different types of process, which are summarized in **Figure 3**, and discussed in the following sections. Apart from additive manufacturing techniques, where full or partial melting of particles occurs layer by layer via laser or electron beam [35], all of the processes mentioned in **Figure 3** require sintering in order to partially fuse the particles together and generate bonds. Hence, it is important to understand the process of sintering and its stages.

Sintering is the process of joining contacting powder particles together and reducing their surface area (which provides the driving force for the change) via heating them to a temperature typically two-thirds of the melting temperature of the powder material [36, 37]. During the first stage of the sintering process (shown in **Figure 4**), neck formation occurs in order to minimize the surface free energy of the system, which is the main driving force for the sintering process and reach more thermodynamically stable state through surface, volume and vapour diffusion, where the material evaporates or is transported from the convex surfaces of the powder particles and condenses on or moves to their concave surfaces [38]. Next, neck growth happens at the second stage of the sintering process and pores accumulate at the grain boundaries. The process continues until the pores become isolated [39]. The final stage of sintering is the elimination of the majority of the voids leaving behind small, isolated closed pores depending on the sintering time, temperature and grain coarsening [40].

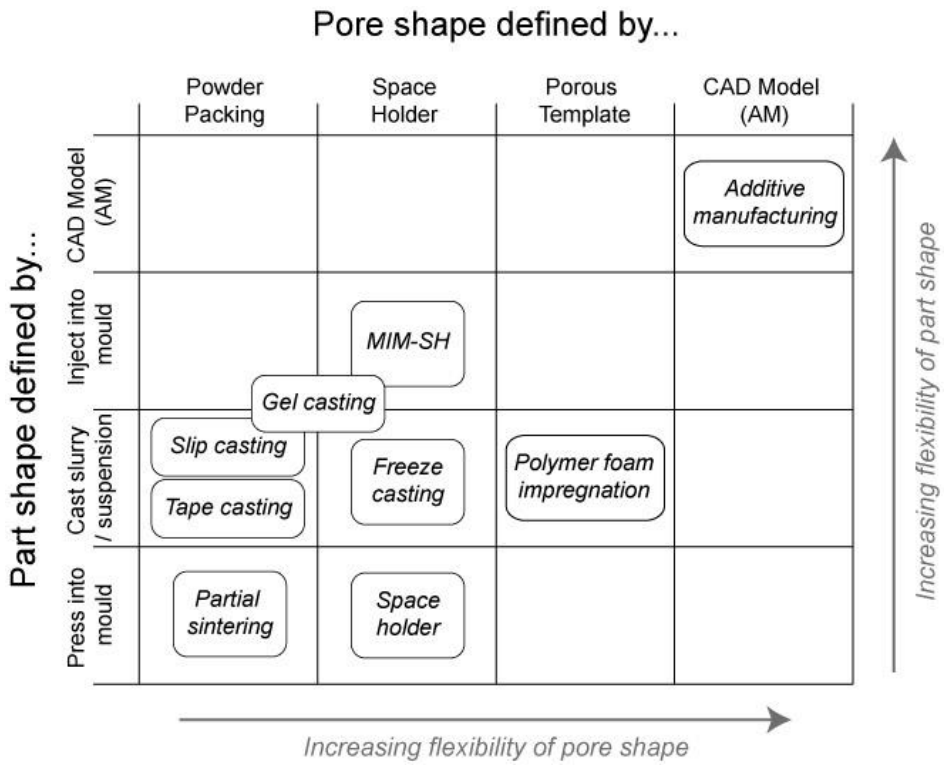

Figure 3. A schematic diagram classifying many of the processes reported for processing of open cell porous titanium. Because of their preponderance in the literature, only powder metallurgical methods are included. Reproduced from Shbeh, M. and Goodall, R. Adv Eng Mater. 19 (11) © 2017 WILEY-VCH Verlag GmbH & Co. KGaA, Weinheim

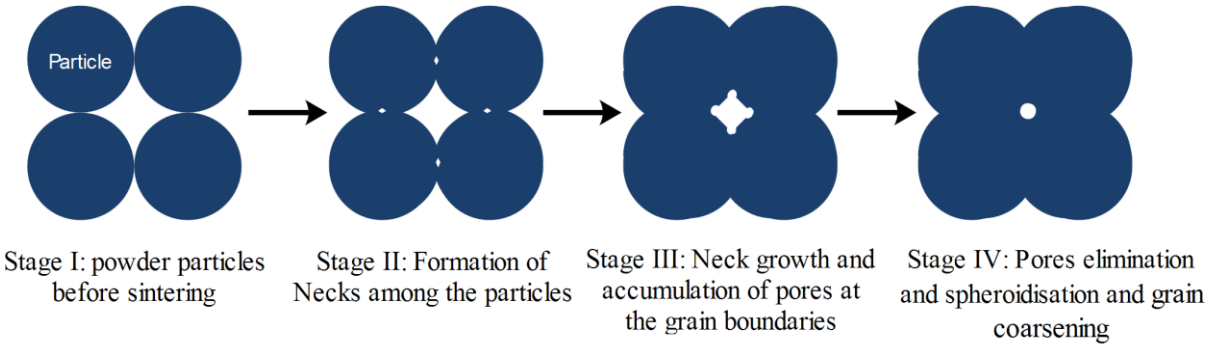

Figure 4. A schematic of the stages of the sintering process for solid powder particles.

2.2.1 Partial sintering

One of the simplest ways of producing porous Ti is to partially sinter the metal powder under vacuum (**Figure 5**). This will result in the initiation of small necks among the particles via diffusion and the retention of relatively small pores due to incomplete densification, provided the temperature and duration of the sintering step is appropriately controlled (sufficient to cause inter-particle bonding, but not enough to reach near full density). The process has been used for the manufacture of Ti with a total porosity of up to 60 %, showing an elastic modulus of 5-60 GPa [41]. The sintering characteristics, and hence porous structure, are affected by the size of the starting powder. Large particle sizes have greater inter-particle spaces, and will result in larger pores, along with increased porosity due to a reduced rate of sintering, with the opposite true for smaller particles [28]. Pore shape can be controlled to some extent via selection of powder particle shape and control of the sintering process, though these may also influence the pore size and density. Many foams which are processed by sintering as part of another method will contain some degree of microporosity even within the nominally dense metal parts, which can have a significant impact on overall porosity and on properties.

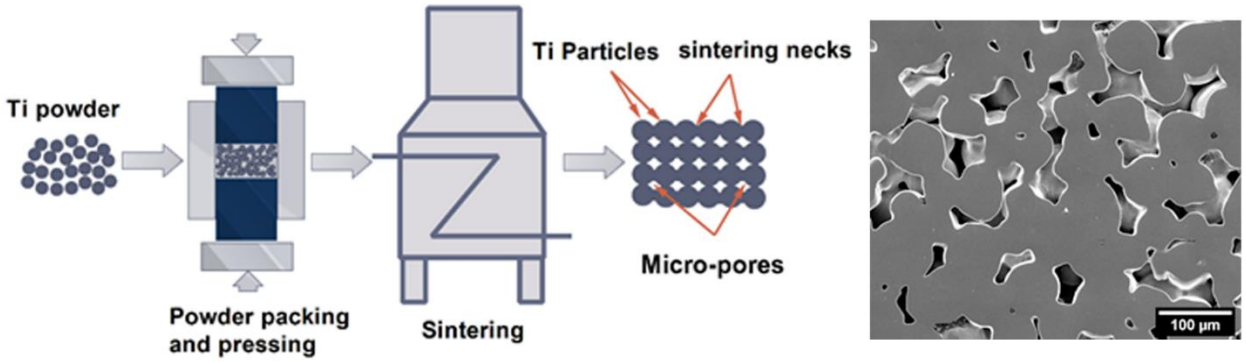

Figure 5. A schematic diagram of the partial sintering technique with a SEM image of a sample of microporous Ti produced by partial sintering of a coarse Ti powder reproduced from Shbeh, M. and Goodall, R. Adv Eng Mater. 19 (11) © 2017 WILEY-VCH Verlag GmbH & Co. KGaA, Weinheim.

2.2.2 Creation and sintering of hollow spheres

Sintering can also bind together other forms, including hollow spheres consisting of a relatively thin and dense outer shell with an inner void space. Hollow Ti spheres can be produced by several techniques (on a powder scale it can be created, normally

unintentionally, during the production of spherical Ti powders by gas atomisation [42]). One way of synthesizing hollow Ti spheres is by injecting a slurry of Ti hydride with a polymeric binder or disperser and solvent through a coaxial nozzle and bubbling it via a passing gas to form solidified, green hollow spheres by surface tension and hydrostatic forces [43]. These green spheres are then partially sintered to produce porous Ti parts with a relative porosity of more than 96%. Another way of producing hollow Ti spheres is by spray coating the slurry on to polymeric spheres to form Ti coated polymeric spheres [44]. Such spheres are either sintered to produce hollow Ti spheres, which are combined by partial sintering, or pre-compacted and then sintered to form a porous Ti part in one step [45].

2.2.3 Entrapment and expansion of gases

The main principle underlying this technique is the introduction and subsequent expansion of entrapped gas into Ti to form microporous part (**Figure 6**). It is made possible by the creep or superplastic behaviour of titanium, which means that, at appropriate temperatures, pressures achievable by gas are sufficient to cause significant shape change. The method involves Hot Isostatic Pressing (HIP) of Ti powder packed in a sealed steel container and backfilled with argon to form a partially densified Ti part with closed micron-sized pores filled with entrapped argon. The relatively small micropores are then enlarged by heating the part to a temperature high enough to cause creep in the metal surrounding the pores as a result of the pressure of the argon entrapped [46]. This early version of the process produced Ti with porosity up to 27% in the case of pure Ti, and 40% for Ti-6Al-4V [47, 48], and was also used to make a 35% porous Ti-6Al-4V sandwich structure [49], which remained closed. An example of Ti sandwich produced by this technique is shown in **Figure 7**. Because of the low levels of porosity and its closed nature, and the long duration of processing (which can be more than a day) this technique where creep occurs to increase pore size has not proved popular. However, where transformation superplasticity can be used for pore expansion, there is relatively shorter treatment time and accelerated pore growth reaching a higher volume percentage of porosity up to 52%, and including a significant fraction of open porosity [50]. Transformation superplasticity is carried out by thermal cycling of the partially consolidated Ti part at a temperature range around the α/β allotropic temperature of Ti, which is about 882.5 °C [51, 52]. The morphology of the final pores ranges from regular separated

small spherical pores to irregular coalesced pores with sizes in the range of 200–800 µm depending on the treatment time [53].

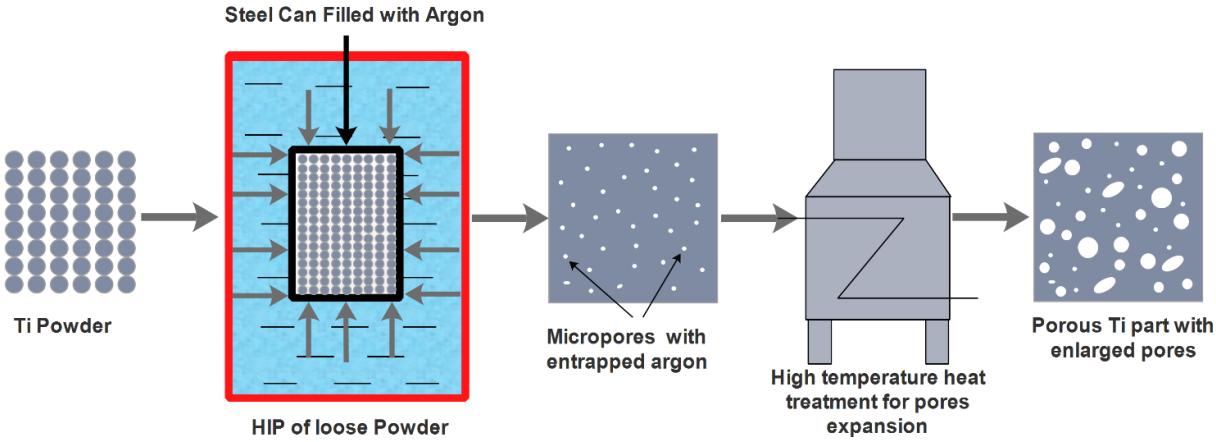

Figure 6. A schematic diagram of the entrapment and expansion of argon process for the production of porous Ti parts reproduced from Shbeh, M. and Goodall, R. Adv Eng Mater. 19 (11) © 2017 WILEY-VCH Verlag GmbH & Co. KGaA, Weinheim.

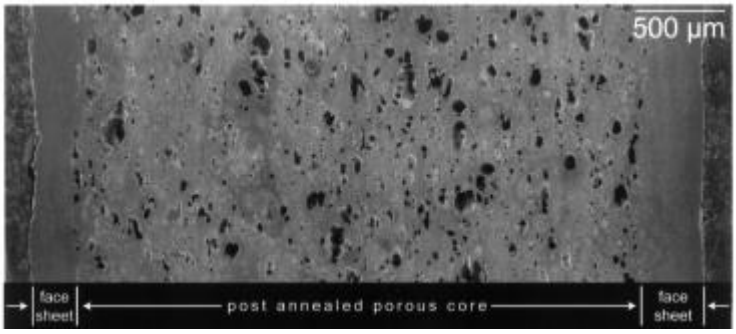

Figure 7. Low density Ti sandwich structure made by creep expansion of entrapped argon [29].

2.2.4 Slurry-based methods

2.2.4.1 Slip casting

Slip casting is a method commonly used in the ceramic industry, but more recently applied to porous Ti [3, 54]. A suspension or slip is first prepared by mixing Ti powder with a solvent and dispersant such as water and cyclohexane. A stabiliser and polymeric binder are usually added to the mixture to increase the stability of the solid part in the suspension and provide sufficient strength for later handling. This suspension is then poured into a porous gypsum

or plaster mould which absorbs the water from the suspension by capillary action, resulting in a green body with a very limited strength [55]. This cast body is then removed from the mould and dried for a period ranging from 8 to more than 24 hours before sintering. This method was successfully used for the production of Ti foams with a total porosity of up to 65 % [54], slightly higher than that achieved for partial sintering of powders, possibly as the mechanical compaction of the powders pre-sintering is less. An example of a foam produced by the slip casting is shown in **Figure 8**. Like partial sintering, the control of the pore size is low, and inhomogeneous structures may result. One of the drawbacks of the technique from a processing point of view is the long drying stage, particularly when large parts are produced, leading to greater suitability for small scale production [55], however the capital cost is low with relatively simple tools [3] . Another potential issue is contamination of the foam during thermal removal of the stabiliser and binder (which are usually polymers).

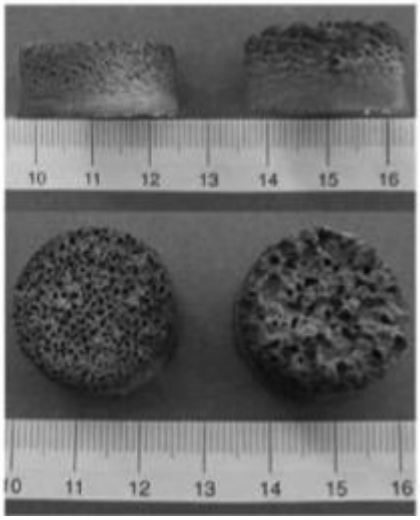

Figure 8. Side and top view of a Ti foam with gradient pore size and porosity produced by slip casting [54].

2.2.4.2 Tape casting

This process also uses a slurry of Ti powder with a solvent, binder and disperser. A small amount of TiH_2 may also be added to the mixture to facilitate the sintering process by releasing hydrogen into the sintering atmosphere as it breaks down at high temperature, reducing oxidation. The homogenised slurry is then poured into a chamber situated above a

moving carrier film or foil, **Figure 9**. The slurry passes through a small gap controlled by a doctor blade and is then left to dry at ambient temperature or in an oven to remove the solvent. After that the sheet produced is thermally debound to remove the organic binder and is then partially densified by sintering. This method has been used for producing porous Ti foil with a thickness of 370 µm and a total porosity of 36 %, with once again pore sizes limited to micropores (22 µm average pore size in this case) [56]. These porous sheets could have potential in several applications, such as in chemical reactors and fuel cells [56].

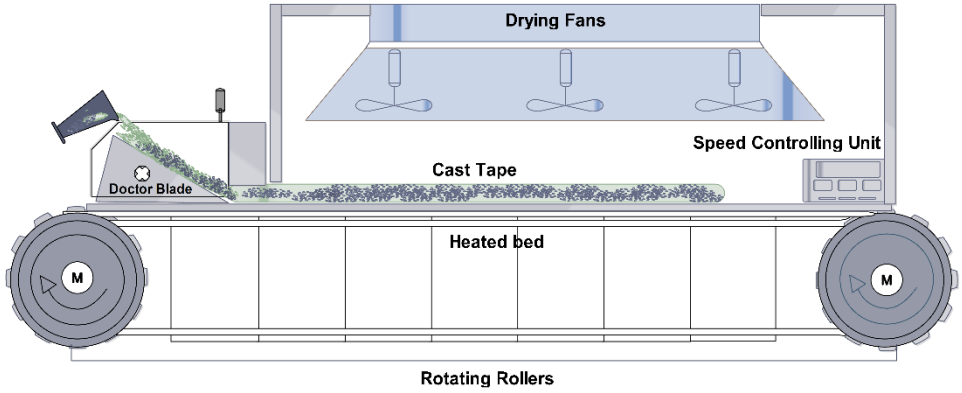

Figure 9. A schematic diagram of the tape casting process reproduced from Shbeh, M. and Goodall, R. Adv Eng Mater. 19 (11) © 2017 WILEY-VCH Verlag GmbH & Co. KGaA, Weinheim.

2.2.4.3 Gel casting

In this process, **Figure 10**, the slurry is prepared by mixing the Ti powder with a monomer and cross linker, to form a gel, and deionised water, to dilute the mixture. A small amount of a disperser is added to the slurry to prevent Ti segregation and settling. After that an initiator and catalyst are added to start the polymerization reaction, which forms a chemically crosslinked gel; this is agitated, before being cast into a mould and heated at a temperature of 60 ˚C for 2 hours [4]. Next, the gelled parts are demoulded and vacuum dried at ambient temperature for 24 hours before sintering under vacuum to produce a porous Ti part. As the internal structure of the gel plays a role in defining the porosity (although the degree of control thus achieved is not great), this process has the elements of a space holder method, where another phase defines the shape of the pores. A total porosity of 46 % has been achieved [4], which is relatively low in comparison with other methods and attempts to

increase this have been made [57] by first producing a gelled TiO_2 foam which was then reduced to metallic Ti by electrochemical reduction, reaching a total porosity of 88 %. However, the linear shrinkage observed on the reduction stage was substantial (27%), and a TiC phase is formed in the material which has a detrimental effect on the ductility. Another study explored the incorporation of organic space holder particles such as polypropylene and poly methyl methacrylate (PMMA) beads into the process and carried out gel casting of TiH_2 by mixing these with a triblock copolymer dissolved in a solvent [58]. The mixture forms a low viscosity liquid at high temperatures, but once cooled below a gelation temperature, it transforms into a thermoreversible, physically cross-linked elastic polymer network or gel. The triblock polymer and organic space holder are then removed by pyrolysis or thermal degradation. The TiH_2 is reduced and the part is sintered under vacuum. Titanium with a total porosity of 44 % was successfully produced by this procedure [58]. However, the carbon content for the foams produced was relatively high (0.66-0.73 wt. %) due to the high organic content in the mixture and the presence of their decomposition products during sintering.

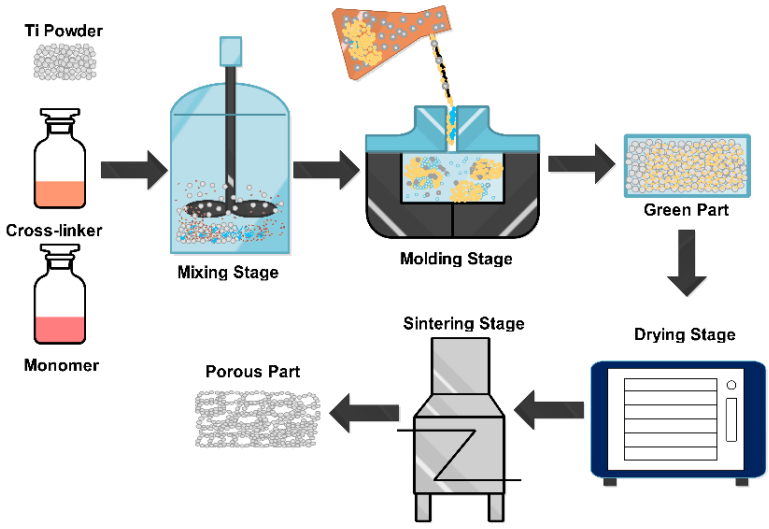

Figure 10. A schematic diagram of the gel casting process reproduced from Shbeh, M. and Goodall, R. Adv Eng Mater. 19 (11) © 2017 WILEY-VCH Verlag GmbH & Co. KGaA, Weinheim.

2.2.4.4 Freeze casting

The freeze casting process was first used for the manufacture of polymer scaffolds for biomedical applications (it is well known, as freeze gelation, in the polymer industry [59]) and has been used for the production of ceramic biomaterial scaffolds [60]. It was

implemented for the production of porous Ti in 2008 [61, 62]. Like other methods, the first step is the preparation of a slurry or suspension, with water the most commonly used solvent. This suspension is then uni-directionally solidified by freezing, **Figure 11**, leading to the formation of ice crystals among the metal powder particles. These growing ice crystals reject and push the Ti particles to the boundaries or spaces among the crystals, concentrating them in these regions and thus creating lamellar cell walls in between. The ice crystals are subsequently sublimated by freeze drying under vacuum, forming lamellar pores that replicate the shape of the crystals; the ice thus acts as a removable space holder phase. Finally, the porous cast is thermally debound and partially densified by sintering. Due to the directional solidification, the macropores are often elongated and aligned along the solidification direction, with a high aspect ratio. Indeed, the pores frequently form channels traversing one direction across a sample without interconnects in other directions, and therefore are potentially well suited for filter applications. An example of a Ti foam produced by freeze casting is shown in **Figure 12**. The critical role of water solidification means it is vital to control the cooling rate, which affects crystal formation, and the particle size of the powder, which affects its mobility and densification behaviour (this is particularly significant as, compared to other materials processed by freeze casting Ti has a high density and tendency to low mobility that might lead to settling and segregation from the suspension [63]). Very fast cooling rates can result in the formation of dense material [64], while large particle sizes can result in particle entrapment by the crystals giving lower porosity (for example 38 % [61]) and smaller, non-elongated pores. Careful control of the cooling rate is achieved by controlled reduction of the heat applied by the heating element (see **Figure 11**) to cause the water to freeze unidirectionally through the polymer mould. Thus, ice crystals form at a rate that allows sufficient time for the Ti particles to be displaced and gathered at the boundaries of these ice crystals, resulting in lamellar pores remaining after sublimation. The cooling rate typically ranges from 0.1 °C min^{-1} to 10 °C min^{-1} [65]. In addition to water, the use of camphene as a solvent in freeze casting of porous Ti has also been investigated [31, 62, 66, 67]. Unlike the lamellar pores produced by freeze casting with water based solvents, camphene-based freeze casting can result in structures with dendritic porous channels [63]. A total porosity of up to 69 % has so far been achieved by this method [67].

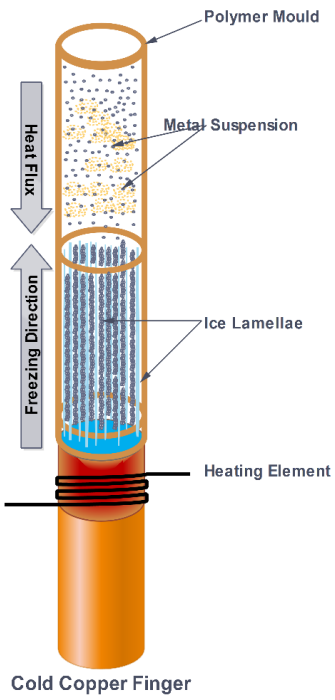

Figure 11.A schematic diagram of the freeze casting process from Shbeh, M. and Goodall, R. Adv Eng Mater. 19 (11) © 2017 WILEY-VCH Verlag GmbH & Co. KGaA, Weinheim

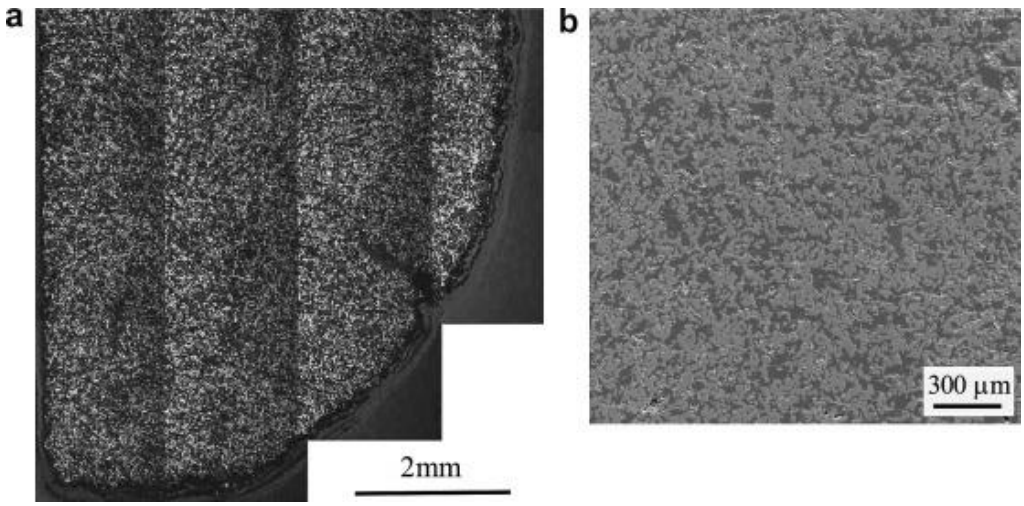

Figure 12. (a) Transverse section of a Ti foam produced by freeze casting (b) high magnification SEM image of the structure of the foam [61].

2.2.4.5 Impregnation of polymer foam

This process, **Figure 13**, also frequently involves a slurry, but rather than being shaped or cast into a mould, polyurethane foam is dipped into it, with the slurry impregnating the foam. Excess slurry is removed by squeezing or pressing it under a roller [68], and the foam is left to dry before thermal treatment to remove the binder, and also the polymer foam by pyrolysis. This method can yield Ti with high porosities (up to 84% [5, 69]) and good, well-controlled structures, leading to efficient mechanical properties (albeit with the ever-present risk of contamination due to binder removal). One challenge for using this technique is that the shape of the porous parts produced replicate the shape of the polymer foam used and thus very intricate parts require either post machining or specially made polymer foams that have a similar shape to the final product. Examples of Ti foams produced by this technique are shown in **Figure 14.**

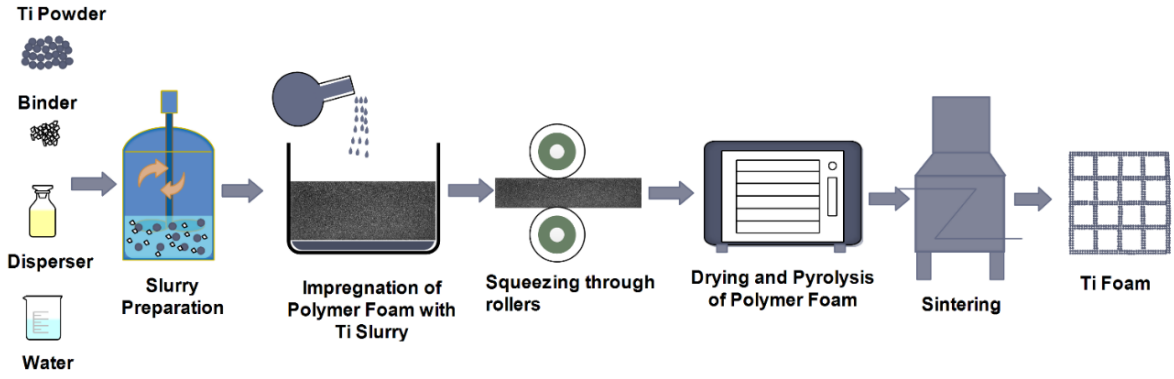

Figure 13. A schematic diagram of the impregnation of a polymer foam to produce porous Ti reproduced from Shbeh, M. and Goodall, R. Adv Eng Mater. 19 (11) © 2017 WILEY-VCH Verlag GmbH & Co. KGaA, Weinheim.

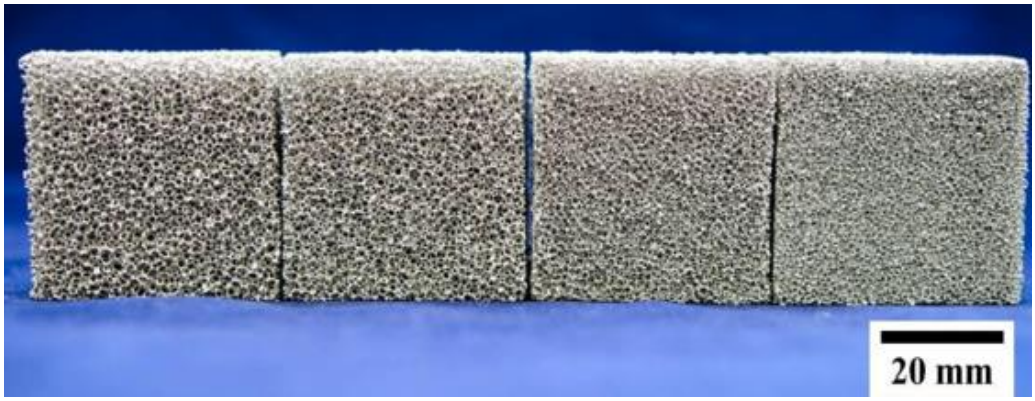

Figure 14. Titanium foams produced via the impregnation of a polymer foam technique using a polyurethane foam with 25, 30, 35 and 40 pores per inch from left to right respectively [70].

2.2.5 Space holder

The degree of control over pore size and shape, and to a lesser extent, porosity is limited with the methods discussed above where the pores develop during the process. In order to increase control, and achieve the highest porosities, a simple and widely-used strategy is to incorporate particles of a phase within the material which does not react or change significantly during the process, and can be removed at some stage, leaving behind open (and interconnected) pores. Such a material is known as a *Space Holder* (or sometimes *porogen*). The space holder needs to be low cost, easily removed and readily available with the desired shapes and sizes. Furthermore, it must withstand any applied pressure during processing without deforming. In addition, it must not react with the Ti to avoid undesirable phases that can have detrimental impact on the mechanical properties of the foam. Most of the space holders are temporary and usually removed by either water dissolution or thermal treatment. However, some space holders can be permanent such as cenospheres which are usually made of alumina silicates and commonly produced as a by-product in coal combustion thermal plants [71]. Moreover, foams produced by such permanent pore formers are often called syntactic foams. **Table 1** summarizes the investigated space holder materials in the literature and their method of removal.

Table 1. Space holder materials used for the production of porous Ti.

Material	Method	Removal	Comments	Ref.
Carbamide (Urea)	Space holder + Cold Isostatic Pressing	Thermal Removal [72] 200 °C for 2 hrs [22] 300 °C for 2 hrs. [27] 200 °C for 3 hrs+350 °C for 3 hrs	Low melting point (133°C). Very good water solubility. Possibility of deforming. Breaking at pressure > 200 MPa [73]	[22, 27, 72]
Ammonium Bicarbonate	Cold Isostatic pressing	Thermal Removal [74] 120 °C for 3 hrs [75] 95 °C for 12 hrs	Very low melting point (41.9 °C). Unsuitable for MIM and HIP	[74, 75]
Sodium Chloride	Space holder	Water Dissolution [76] 4 hrs at 50-60 °C. [9] 60 °C for 5 hrs	High melting temperature (801°C). Good water solubility & low cost	[8, 9, 11, 25, 76]
	MIM+Space holder	[9] 60 °C for more than 72 hrs [11] 50 °C for 40 hrs (92% removed)		
	Warm compaction	[8] 24 hrs (96% removed)		
	Hot Pressing	[25] 2-3 hrs		
Potassium Chloride	Space holder	Water Dissolution 60 °C for 5 hrs	Good water solubility & low cost. Available in different shapes and sizes	[9, 10]
	MIM+Space holder	[9] 60 °C for more than 72 hrs		
	Warm compaction	[10] 60 °C for 24 hrs		
Starch	Space holder	Thermal Removal 450 °C for 2 hrs	Low cost, high contamination	[77]
Saccharose crystals	Space holder	Water dissolution with magnetic stirrer at 20-80 °C for 2-6 hrs	Very good solubility in water & low cost.Very hard to use in MIM [78]	[17]
Poly(methyl methacrylate)	Space holder	Thermal Removal [79] 200-450 °C for 2 hrs.	Can be used as a binder and as a space holder	[11, 79]
	MIM+Space holder	Solvent Dissolution [11] Acetone 40 hrs (90-100% removed)		
Polyoxymethylene	Space holder	Catalytic decomposition at 110 °C	Melting point 175 °C.	[80]
Polypropylene carbonate	Space holder	Thermal Removal 220 °C for 1 h	High carbon contamination	[81]
Acrowax	Space holder	Thermal Removal 200 °C for 3 hrs.		[82]
Hydrogen Carbonate	Space holder	Thermal Removal 200 °C for 5 hrs.		[83]
Magnesium	Space holder	Evaporation by heating	Relatively expensive. Presence of MgO [84]	[24]
Steel spheres, wires and mesh	Space holder	Electrochemical Dissolution 10-20 hrs	Expensive. Hard to remove completely	[85]

It can be seen from **Table 1** that NaCl is one of the most investigated pore formers, which can be attributed to its low cost and ease with which it can be used. It is mostly cubic in shape and has a good dissolving rate in water. However, Tuncer et al [9] reported that KCl offers several advantages over NaCl. Firstly, it can be easily injected and rejected (i.e. removed from the mould) with reduced wall friction in comparison with NaCl. This is beneficial as it can reduce the chance of segregation among the space holder particles and Ti particles and create foams with homogenous properties [9]. Secondly, using KCl can result in lower wear rate for the screw and nozzle due to low wall friction [9]. However, it should be noted that the KCl used in their study was approximately spherical while the NaCl was cubic in shape, thus one might argue that their findings can be attributed to shape rather than the material as spherical particles have better flowability and less friction than cubic ones. This requires further investigation. One additional advantage is that KCl has a higher solubility in water in comparison with NaCl and consequently faster removal rate and less dissolution time than NaCl. The solubility of NaCl and KCl in water was thoroughly investigated by several researchers. One case study published in 2005 investigated the solubility of these two salts in water at different temperatures [86]. **Figure 15** summarizes the finding of this study.

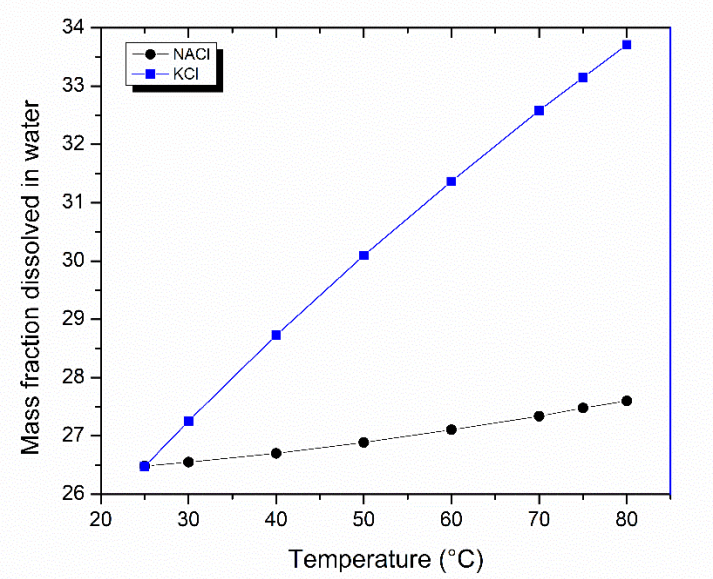

Figure 15. The change in NaCl and KCl dissolution in water with temperature.

It can be noted from **Figure 15** that both salts dissolve to an approximately similar amount in water under ambient conditions, but this trend changes noticeably as the temperature rises,

where KCl start to dissolve at a faster rate in comparison with NaCl. Interestingly, Tuncer et al reported that the removal rate of both the NaCl and KCl from the compacted samples were nearly equal in the first 15 minutes and then started changing in favour of KCl. This might suggest that the temperature was gradually increasing until it reached the experiment dissolution temperature (60 °C). Morelli et al [11] studied the feasibility of using NaCl and poly methyl methacrylate (PMMA) as space fillers for the production of Ti foams via injection moulding. They stated that PMMA results in foams with better shape retention than NaCl. In addition, foams processed with PMMA had higher total porosities for the same percentage of the space holder and lower compressive strength. Furthermore, foams produced by PMMA had lower carbon and oxygen contents compared to foams produced by NaCl, in spite of the fact that there are reports to suggest that PMMA can significantly increase the level of impurities in Ti alloy foams compared to other space holders [78, 87]. Another study argued that using carbamide as a space holder can result in Ti alloy foam with higher porosity compared to foam produced by NaCl for the same percentage of space holder and within the same size [88]. It is important to point out that in both of these studies cubic NaCl was used while the PMMA and carbamide had spherical and rectangular shapes respectively. Hence, it would seem reasonable to argue that the shape of the space holder can have an effect on the percentage of the resulting porosity. However, such claims need to be further investigated by experimental work since different space holder materials were used.

The aim is that the space holder imparts and defines the pore size and shape, yet there are several processes at work during or after space holder removal in many processing methods, and this relationship may not be exact. **Table 2** summarises the relationships between quoted space holder size ranges and those of pores. While commonly the same or very similar, smaller distributions of pores have been reported [89, 90]. The assessment could be complicated by space holder deformation during compaction, which has been noted to occur and result in pores with elliptical shape [91].

Table 2. The relationship between space holder size and pore size reported for porous titanium

Space holder	Size of space holder (μm)	Size of final pores (μm)	Process	Pressure MPa	Sintering temp. (°C)	Time (h)	Ref.
Sodium Chloride	50-500	50-500	SH	30-50	Hot pressing 780	2	[25]
Sodium Chloride	< 290	50-300	MIM+SH	100	1150	2	[26]
Sodium Chloride	300-500	50-500	MIM+SH	-	1000-1200	4	[11]
PMMA	D_{50}=600	50-500	MIM+SH	-			[11]
Table sugar	800-1000	800-1000	SH	500	1250	1	[17]
Ammonium Hydrogen Carbonate	200-500	200-500	SH	100	1200	2	[83]
Carbamide	800-2400	100-2500	SH	166	1400	1	[92]
Ammonium hydrogen carbonate	100-900	Smaller	SH	166	1400	1	[92]
Ammonium hydrogen carbonate	500-800	300-800	SH	-	1200	10	[90]
Polypropylene carbonate	100-600	50-500	SH	100-400	1000	2.5-10	[93]
Starch	100-400	100-300	SH	100	1200	3	[77]
Polyoxymethylene	D_{mean} = 500	80-400	SH	50-100	1300	2	[80]
Acrowax	300-500	300-500	SH	100	1100	2	[82]
Magnesium	425-600	Avg. 525	SH	500	1200	1	[24]
High carbon steel wire	250-500	250-500	SH	350	1050	12	[85]

2.2.5.1 Pressing with space holder

To create actual porous metal, the space holder needs to be combined with the powder and shaped. Simple pressing (hot or cold) of a blend of metal powder and space holder is one of the most widely reported methods. After this stage the space holder will be removed and the metal sintered to allow further integration of the powder. A schematic of the method is shown in **Figure 16**.

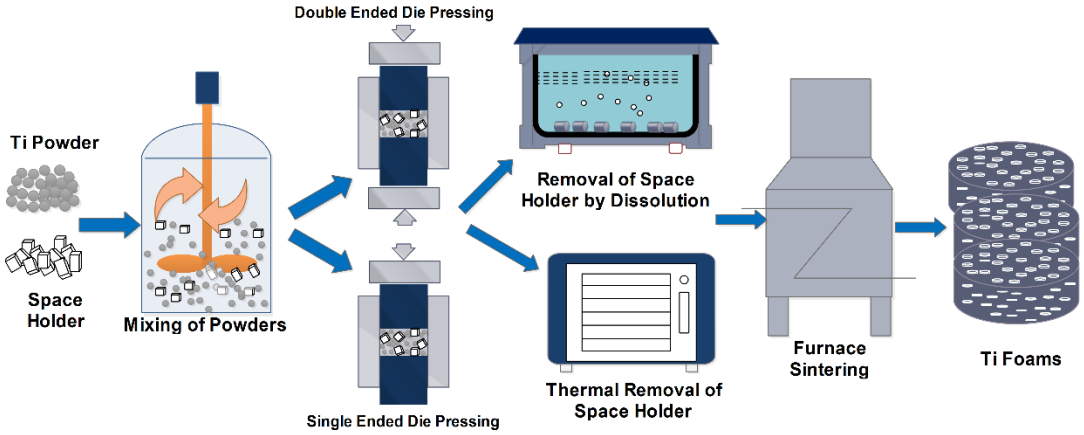

Figure 16. A schematic diagram of the space holder technique reproduced from Shbeh, M. and Goodall, R. Adv Eng Mater. 19 (11) © 2017 WILEY-VCH Verlag GmbH & Co. KGaA, Weinheim.

Several techniques (all taken from the powder metallurgy of conventional materials) have been used for the compaction of the Ti powder-space holder mixtures such as single and double ended cold axial pressing [17, 24, 77, 80, 89, 92, 94], Uniaxial Hot pressing (HP) [25] and warm compaction [9, 10, 95], producing titanium with a total porosity of up to 80 % [75, 92]. As well as the typically limited range of part geometries that can be created, a drawback of applying these techniques is that the pressures involved are high, and this can cause the space holder particles to deform and break during compaction, altering the final shape of the pores. For example, it has been reported that NaCl space holders are broken at a pressure higher than 350 MPa [76], and it has been noted that the space holder particles are deformed and flattened in the direction of the applied pressure during HP, leading to flattened pores with deformed shapes [25].

Where single ended uniaxial pressing is used, the pressure profile is non-uniform throughout the compacted specimen (higher at the top and in the centre [27]) thus leading to non-uniform

mechanical properties; correlations have been found with the expected pressure distribution and the fracture lines in tested samples [27]. As metal powder and space holder sizes and densities are frequently different, segregation can occur, which results in inhomogeneous distribution of the space holder particles in the Ti powder and a reduction in pore interconnectivity; to overcome this a polymeric binder may be included in the mixture [27, 80, 96]. Normally, the compacted blend of these powders is sintered in a furnace under vacuum or flow of an inert gas. However, there have been attempts to use faster and more advanced sintering techniques such as pressureless Spark Plasma Sintering (SPS) [97] as well as conventional SPS under uniaxial pressure [98]. An example of a Ti foam produced by the space holder technique is shown in **Figure 17**. It can be noted that pores are connected through a small micropore at the bottom part of the macropores, where the space holder particles were contacting each other during compaction.

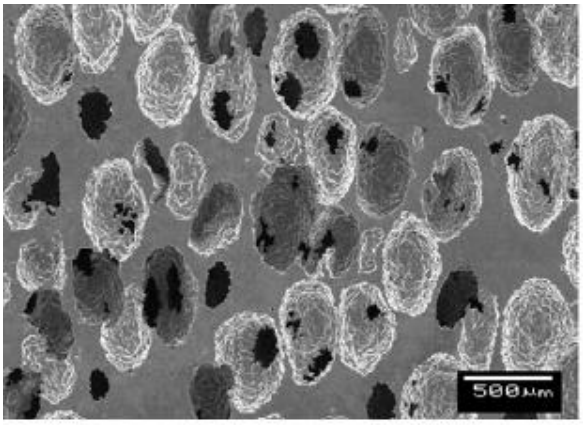

Figure 17. SEM image of a Ti foam with 60% porosity produced by the space holder technique using magnesium space holder [99] .

2.2.5.2 Metal Injection Moulding (MIM) with a space holder

Injection moulding is a net shape manufacturing process originally designed for mass production of plastic parts, which has been adopted for use with metals. Combining this with the use of space holders could have huge potential in mass producing porous Ti with near net complex shapes, overcoming some of the limitations of the space holder methods on their own [9], especially when the potential for pore structures to be closed by debris or altered by

deformation during machining is considered [6]. There are four key stages to the process, **Figure 18**; first a feedstock is prepared by mixing Ti powder with a polymeric binder and space holder, which is then granulated by extruding and cutting into small pellets; secondly the feedstock is injected at a relatively low temperature and pressure into a die cavity which imparts the desired shape; thirdly the space holder and binder are removed by different techniques (thermally or with a solvent) depending on their nature; finally, the porous green part is partially densified by sintering.

There are limited reports on the use of such a technique for the production of pure Ti foams in comparison with other methods such as the space holder method. This is due to several factors. One is that this method requires a large amount of feedstock to fill the barrel of an industrial injection molder as the equipment is designed for mass production, thus carrying out different experiments can be substantially expensive. Several trials have been carried out by a number of researchers to overcome this issue by simulating the MIM process using a process called warm compaction [8-10]. This simple simulation process involves heating and pressing the feedstock at a temperature and pressure equivalent to the temperature and pressure used in MIM. However, these trials were not successful. Tuncer et al [9] tried to simulate MIM by warm compacting Ti feedstock with a solid content of 80% using a multi-component binder. After successfully warm compacting it, they attempted to inject the feedstock through a MIM machine. However, the nozzle was immediately clogged. They believed that the failure was due to powder segregation during injecting. Simulating the MIM process by pressing a powder mixture with the aid of heat is not an optimum choice since it does not simulate the main principle behind MIM, namely a hot feedstock flowing through a nozzle into a die.

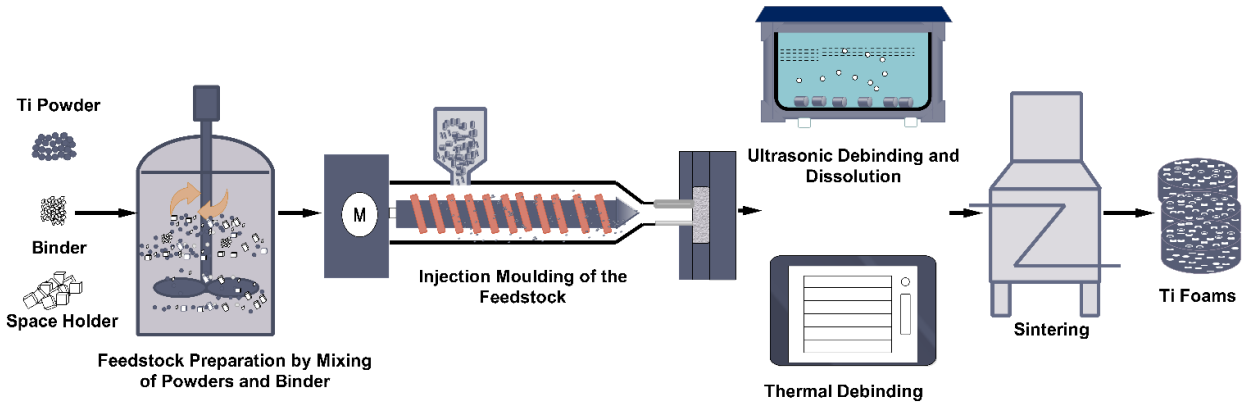

Figure 18. A schematic diagram of the MIM-SH technique reproduced from Shbeh, M. and Goodall, R. Adv Eng Mater. 19 (11) © 2017 WILEY-VCH Verlag GmbH & Co. KGaA, Weinheim.

2.2.6 Influential factors affecting foam characteristics

There are several crucial factors that need to be taken into consideration while producing Ti foams by powder metallurgy techniques. These important factors can hugely impact the final properties of the foams and their meso-structure. These factors will be discussed in the following sections.

2.2.6.1 Characteristics of the starting powder

Particle size and shape of the Ti powder can have a great influence on the final properties of the foams produced as they play an important role in determining the packing density of the powder. It is important to use a powder with high packing density since the pressure used in injection moulding is relatively low in comparison with other methods such as press and sinter. Using a powder with low packing density can result in substantial linear shrinkage (up to 20-25%) and warping [100]. Furthermore, low packing density powder can result in more micro-pores compared to high packing density powder. Since powder particles normally constitute the cell walls of the pores in porous foams, it is therefore very important to choose a powder that results in low number of micro-pores, as these micro-pores can substantially deteriorate the mechanical properties of foams [101].

In general, the smaller the particle sizes of the powder, the shorter the time required for densification, whereas using large particles requires longer densification time. Powders used

in MIM technology are typically very fine and their mean particle sizes usually ranges from 1 μm for hard metals up to 45 μm for stainless steel [102]. Using a powder with a uniform particle size is not an optimum choice since micro-spaces among the particles are not usually filled. Thus, it is preferred to use a powder with a broad particle size range in order to fill those empty spaces among the particles by finer particles and consequently minimising the possibility of micro-pore formation.

Particle shape also has a great impact on the properties of the foams produced. The shape of the powder is normally dependent on the production method. Common particle shapes of Ti powders are spherical and angular or irregular. Spherical Ti powders are usually produced by gas atomisation and they are relatively expensive compared to other types of powders. In comparison, angular Ti powders are typically produced by hydride-dehydride process and they are relatively cheaper. One study examining the effect of the shape of the starting powder on the mechanical properties of the produced parts was published in 2007 [103]. In this study, two different types of Ti powders, namely spherical and angular were used. One interesting finding in this study is that angular powders result in higher percentage of micro-porosity and poorer mechanical properties in comparison with spherical powders. However, detailed explanation for this behaviour has not been given. One might argue that the lower packing density of irregular powder is responsible for such a behaviour.

Another study explored the effect of the particle shape on the properties of parts produced by titanium injection moulding [104]. One major finding in this study is that parts prepared by irregular powders have lower mechanical properties and more closed porosity than samples prepared using spherical powders. This was attributed to the low packing density of the irregular powder in comparison with the spherical ones. Furthermore, the same study demonstrates that parts prepared by irregular powders had a better biocompatibility compared to the spherical ones. This might be due to them having more porosity which can promote cell growth.

It was also argued that spherical particles have the highest packing density compared to other shapes of particles where the highest packing density of spherical powders in random size distributions was estimated to be 63.7 vol. % compared to the irregular particles which was about 63 % [105]. The differences between these percentages are relatively small, however,

such a small difference can affect the properties of foams, as the properties are strongly reliant on the strength of the individual cell walls. The presence of micropores due to a reduced packing density among the powder particles can weaken these cell walls, thus reducing foams' strength. It was reported that a decrease in the porosity of about 17% can shift the compressive curve of Ti foam up by a factor of 10 [106]. Accordingly, spherical powders can help alleviating the micro-porosity issue and obtaining better mechanical properties. Thus, using spherical powders in the production of foams by MIM can result in lower micro-porosity in the cells walls of the foam and consequently enhanced mechanical properties.

2.2.6.2 Binder

Binders are mostly polymeric materials and waxes that provide mechanical stability and improve the uniformity of the powder-space holder mixtures. Furthermore, they are essential components in the production of foams via injection moulding in combination with space holder as they act as wetting and binding agents for both powders, thus providing enough flowability for the mixture to be injected under heat and shear. However, their use is not only confined to injection moulding as they can also be used in other foaming techniques such as gel casting, slip casting, tape casting and space holder method [4, 27, 54, 56, 80]. Binders can serve many useful purposes. Firstly, they can improve the uniformity of the powder-space holder mixtures and prevent space holder-powder segregation due to differences in densities and particle sizes. Secondly, they provide mechanical stability for later handling, particularly after space holder removal. Thirdly, they can act as a load transmitting and dissipating component or phase between the space holder and the metallic powder during injection or compaction, thus, ensuring more uniform distribution of pressure throughout the whole compact. Injection moulding binders are usually composed of three main components. The first component is the low viscosity part. This part is often responsible for facilitating the injection process of the powder mixtures and usually consists of a low melting point polymer or wax with low viscosity such as Polyethylene glycol (PEG) or Paraffin wax. The second component is the high viscosity part. This part is usually denser and more viscous than the first part and typically consists of a polymer with a high melting point, such as PMMA or Polyethylene (PE). This part is usually called the backbone and is normally responsible for providing increased viscosity during injection and mechanical stability for

later handling, especially after the removal of the space holder and the first part of binder. The third part is a lubricant and surfactant. Stearic acid (SA) is mostly used as the third part. **Table 3** illustrates typical binders used in the literature for the production of foams via injection moulding.

The first part of the binder is usually removed by solvent leaching, whereas the second and third parts are mainly removed by thermal debinding. However, there are reports to suggest that SA can be dissolved in water to a certain extent and its solubility increases as the water temperature rises [107]. One major difference between PEG and paraffin wax is that the former can be removed by water dissolution without any hazards [108-110] while the latter is usually removed by the use of relatively hazardous and un-environmentally friendly organic solvents such as chloroform [111] and hexane [8, 9, 112]. The first part of the binder mostly comprises more than half of the binder content and plays a major role in dictating the rheological properties of the binder and its suitability for MIM. The third part is normally less than 6 % and can play an important role in reducing the abrasion of the powder-binder mixtures against the die walls and minimising the segregation of the mixture during injection [113].

The binder-powder mixtures are often called feedstock in the MIM industry. This feedstock usually needs to meet certain requirements in order to guarantee the success of the injection process. One requirement is that the viscosity of the feedstock should be less than 1000 Pa·s (or in another report in the range between 10 to 1000 Pa·s) at the injection temperature [114, 115]. It is also preferable for the feedstock to exhibit some shear thinning or pseudoplastic behaviour during injection where the viscosity decreases with increasing shear rate. This is particularly crucial and beneficial for producing parts with complex shapes [116, 117]. It is believed that this drop in viscosity occurs due to reduced friction among the powder and binder components at high shear rates [116]. However, some argue that this phenomena takes place due to the re-orientation of particles and breakage of agglomerates [118].

Table 3. Common binder systems used for the fabrication of Ti foams.

1st part	2nd part	3rd part	Reference
PEG+ Paraffin Wax	High density PE	SA	[26]
Paraffin Wax	High density PE	SA	[8]
PEG	PMMA	SA	[108]
Paraffin Wax	PE	/	[112]
Paraffin Wax	PE	SA	[111]
PEG+ Paraffin Wax	Low density PE	SA	[11]
Paraffin Wax	Low density PE	SA	[11]
Paraffin Wax	High density PE	SA	[9]

2.2.6.3 Thermal debinding and sintering

Thermal debinding is the process of removing the second and third parts of the binder as well as residue from the first part by thermal treatment at a temperature equal or just below to the decomposition temperature of the binder components, while sintering is usually the final step in the process of producing foams and it involves heating the green foam to a temperature high enough to initiate and form bonds by atomic diffusion among the neighbouring particles. Debinding and sintering can both immensely affect the mechanical properties of the produced foams, as well as the final pore sizes. Hence, careful control of both of these steps is imperative. These two processes can be either done in one furnace and under the same atmosphere or separately with different conditions. There are four prominent parameters that need to be controlled during the debinding and sintering processes, namely temperature, heating rate, holding time and atmosphere.

One investigation explored the effect of the debinding rate on the injected parts under argon atmosphere was reported by Thian et al [119]. An important finding in their study is that using high heating rate during the debinding process can result in the formation of external and internal cracks and consequently deteriorating the mechanical properties of the injected parts. It was also observed that increasing the flow rate of the argon gas from 50 to 250

cm^3/min can cause a drop in the carbon content of the produced parts by 34.5 %. This drop was attributed to faster removal rate of the binder vapours at high gas flow rate, thus preventing them from condensing into carbon [119]. Another study focused on the influence of the debinding atmosphere on MIM parts was published in 2006 [120]. In this study, injected Ti alloy parts were debinded under argon and vacuum atmospheres and a comparison was made between those two. It was noted that argon debinded parts had a lower carbon contamination than vacuum ones, whereas vacuum debinded parts showed lower oxygen levels than those debinded under argon atmosphere. Thian et al [119] argue that multiple stage debinding at temperatures below the decomposition temperatures of the binder components can result in better shape retention and complete removal of the binder. The same researchers have also tried in another study to find out the contribution factor and the extent of influence of each of those parameters during sintering on the mechanical properties of MIM parts through the use of the Taguchi method [121]. They found that the sintering temperature is the most important factor affecting the mechanical properties followed by the heating and cooling rate whereas the holding time was insignificant. However, an alternative view was put forward by Nor et al [122] who stated that the dwell time was the third most important factor after the sintering temperature and heating rate, while the cooling rate was the last factor in terms of contribution. Whilst it is a fact that cooling rate is an important factor during sintering, yet dwell time is more influential on the final properties of porous materials as the sintering time can have a significant impact on reducing the porosity and pore size [123]. Thus, it seems reasonable to go in favour of the Nor et al argument.

Although these studies give a strong indication of the contribution of the sintering parameters on the mechanical properties, they have not considered the impact of the sintering atmosphere. An interesting study investigating the importance of the sintering atmosphere was reported by Gerling et al [124]. In this study injection moulded titanium aluminide parts were sintered under three different atmospheres, namely vacuum, argon 300 mbar and 900 mbar. It was found that vacuum sintering can result in inhomogeneous microstructure and considerable loss in Al, while argon sintering at a pressure of 900 mbar results in lower oxygen, carbon and nitrogen contamination than sintering at 300 mbar.

It is commonly known that as the sintering temperature and time increase, the mechanical properties improve while the porosity decreases. This is due to the elimination of a greater proportion of micropores as a result of increased densification rate and complete growth of necks among the powder particle. Hence, some researchers recommended carrying out sintering without densification in order to achieve the highest volume percentage of porosity [125]. However, this is usually accompanied by poor mechanical properties, due to smaller bonding areas among the powder particles and the presence of micro-pores. Furthermore, it is extremely difficult to avoid the formation of these micro-pores while maintaining the sizes and shapes of the macro-pores. This can be supported by the results of several reports [24, 84, 88, 89]. Despite claims that these micro-pores can be beneficial in some applications such as in biomedical scaffolds, they are stress concentration sites where cracks are likely to initiate, thus deteriorating the mechanical properties. One study supports the advantageous impact of these micro-pores in biomedical applications was reported in 2002 [83]. This study claims that these micro-pores can help facilitating the transportation of body fluids and nutrients. While Kotan and Bor [101] reported that these pores reduce the load bearing cross-sectional area and result in significantly lower mechanical properties. Heating and cooling rate can also play an important role in the sintering process. Thian et al [119] argue that higher heating rate results in higher porosity and lower mechanical properties in comparison with lower heating rate while high cooling rate can lead to the formation of cracks. This increase in porosity and decrease in properties were attributed to insufficient time for the necking stage to occur. However, even if these findings hold true, they cannot be generalised as different sintering temperatures were used for different heating rates in that study.

2.3 Properties of Ti foams

The use of Ti foams in different areas such as in structural and biomedical applications is strongly reliant on their properties. Therefore, it is extremely important to measure the properties of foams as they can give an idea of the usefulness of these foams for different applications and also help comparing Ti foams produced by different foaming techniques in terms of performance. In addition to typical influential factors that can affect the properties of dense parts produced by powder metallurgy such as the morphology of the starting powder, sintering temperature and time, several additional parameters can hugely influence the

properties of foams such as the volume fraction of pores as well as their sizes and shapes. Thus, predicting the properties of foams is a challenging task and hitherto there is no clear and general consensus on a model that perfectly predicts these properties for different foams produced by different foaming techniques. In this section, prominent models for predicting the dependence of mechanical properties on porosity will be discussed.

2.3.1 Models for predicting the properties of open celled foams based on porosity

Several models have been proposed by different researchers to try to predict the dependency of properties of foams on porosity. The majority of these models are based on idealised structures with uniform shapes and sizes of pores which are far from the real foams. Thus, up to this moment there is no general agreement on a model that perfectly predicts the mechanical properties of foams based on porosity indeed, with the complex structure of most foams, this may not be possible. It is extremely important to understand the nature of this relationship and try to estimate it as accurately as possible so that correct structure can be selected. Predicting and simulating this relation accurately is strongly connected to how well the modelled structure resembles the real structure of foams. Most of the derived models are usually applied to simplified representations of the real structure due to the complexity and difficulty in replicating the real structure of foams. In addition, as reported by some researchers, different properties of foams are affected by porosity in different ways. For example, Rice reported that heat capacity, dielectric constant and refractive index are reliant on the composition, whereas most of the physical and mechanical properties rely upon the volume percentage of porosity as well as one or more aspect of the pores such as pore shape and size [126]. Some of the most widely reported models are:

1. Micromechanics-Based Models
2. Minimum Solid Area Models
3. Gibson-Ashby Models

2.3.1.1 Micromechanics-based models

In most of these models porous materials are treated as a special case of two phase materials where one of the phases is assumed to consist of spherical pores that are randomly distributed in a matrix of a second phase (solid material). These theoretical models usually involve two

key steps: establishing the stress and strain distributions for a two phase material and then modifying these distributions taking into account the interaction between pores [127]. Most of these models were derived using continuum mechanics for the purpose of calculating the effective elastic modulus, Poisson's ratio and shear modulus for porous materials with mainly spherical pores. Though, some were derived for two phase materials with ellipsoidal pores or inclusions [128]. One of the most widely reported models was derived by Ramakrishnan and Arunachalam [129]. In this model, porous materials were considered composite materials consisting of a group of hollow spheres packed together in a way that constitute a solid material. **Figure 19** shows the basis of this model.

Each hollow sphere is assumed to be composed of two phases, namely an outer layer of solid material concentrically surrounding a spherical pore. These composite spheres have different diameters and the same void fraction. In addition, each of these spheres has a uniform wall thickness. The pressure is assumed to be transmitted equally to each of these hollow spheres and the volume strains of the hollow sphere and the whole material are the same.

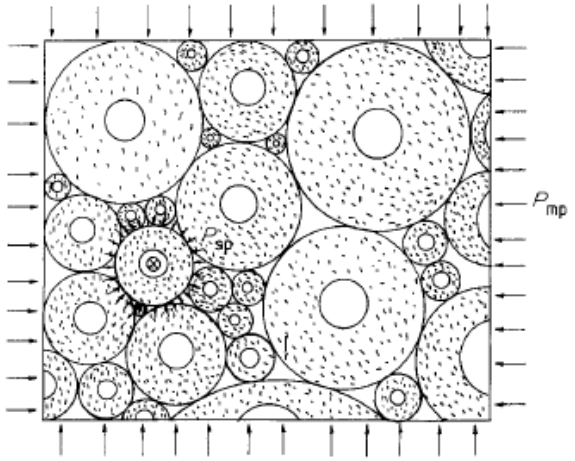

Figure 19. Hollow spheres assembled forming a porous part [129]

According to this model, the effective moduli and Poisson's ratio of porous solids can be estimated using the following equations [129]:

$$M^* = M(1-\theta)^2/\,(1+b_m\theta) \qquad (1)$$

$$\mu^* = (1/4)(4\mu + 3\theta - 7\mu\theta)/(1+2\theta-3\mu\theta) \qquad (2)$$

where M^* is the effective modulus, M is the modulus of the dense material, θ is the porosity, b_m is a constant dependent on the measured modulus and is a function of the Poisson's ratio of the solid material. μ^* is the effective Poisson's ratio, whereas μ is the Poisson ratio of the solid material.

There are lots of drawbacks for using such models for describing and estimating the mechanical properties of porous materials based on porosity. Firstly, such models consider only one shape of pores at a time and mostly were derived for spherical pores for the simplicity of the calculation. This is far from real foams, where usually different shapes of pores are present or shape alteration can occur due to shrinkage during sintering. Secondly, these models assume that these hollow spheres stay spherical after sintering without interaction and this is impossible as necks and bonds among those spheres have to be formed to give the structure mechanical stability in order to be a solid material. Thirdly, pores are assumed to be surrounded by a uniform solid layer of material and this is not usually the case with real foams where non-uniform microporous cell walls are usually surrounding the macropores. Thus, these models have a limited applicability, but it might be highly applicable to foams that are made by partial sintering of hollow powders, though they do not take into account the effect of micropores that are formed among the hollow particles during sintering. These micropores can have a great impact on the results since these calculations are based on stress and strain distributions.

2.3.1.2 Minimum solid area models

In these models porous materials are assumed to be ideally represented by a dense regular stacking of identical cells. These cells are composed of either pores that are located in the centre of the cells and surrounded by solid struts (**Figure 20.A**) or spherical particles located in the centre and surrounded by porosity (**Figure 20.B**).

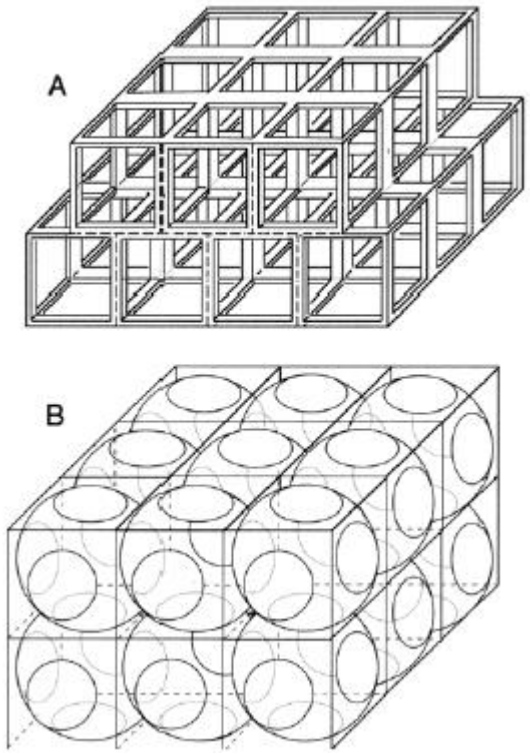

Figure 20. Idealised stacking of: (A) regular foam cells ; (B) uniform solid spherical particles contained within cubical cells [126].

According to these models, the properties of a porous material is dependent on the properties of the Minimum Solid Areas (MSA) which are the bonding areas among the spherical particles and the minimum strut cross-sectional areas among the pores. The minimal solid areas normal to the stress (or conductive flux) are believed to dominate the transmission of stress (relating to strength and fracture toughness or energy) and conduction of fluxes in the porous material [130]. The results of MSA models are not given as equations, but are usually reported as graphs of the minimum solid area fraction against volume fraction of porosity, which may then interpreted as a proportional change in the properties. There are several issues associated with the use of such models for describing the dependency of properties of solid materials on porosity, such as difficulty in estimating the MSA. It is extremely difficult to calculate the actual minimum solid areas for a porous material due to the change in volume during sintering. Therefore, the results of such models are usually reported as plots of the MSA values for each type of porosity normalised by the cross-sectional area of porosity

against the volume fraction of porosity [131]. Examples of MSA plots are shown in **Figure 21**

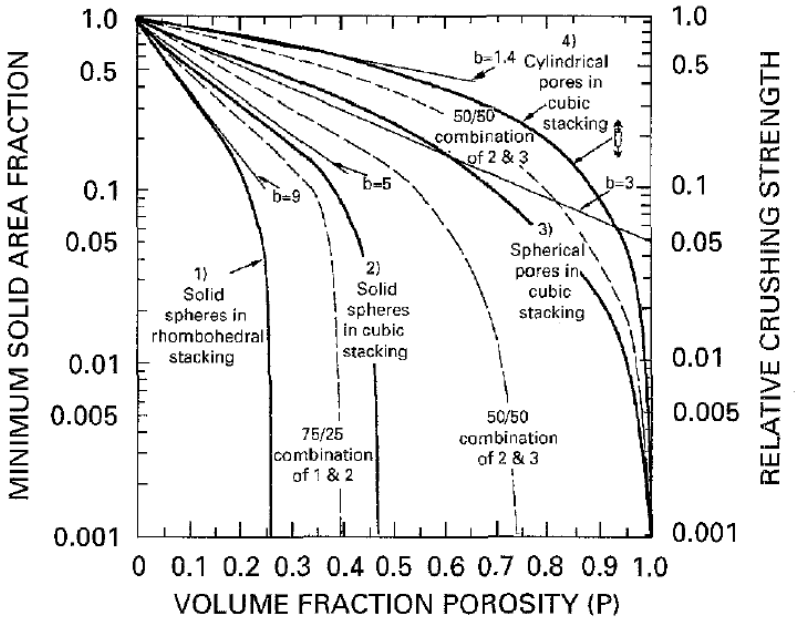

Figure 21. MSA plot for different idealised stackings [126]

Another limitation is that these models assume that the properties of porous materials rely on MSA without taking into account the effect of stress concentrations or the presence of micro-cracks that can result due to the manufacturing process which can affect the mechanical properties. Furthermore, these models are based on idealised models where particles and pores have similar sizes and shapes and this is not the case for real foams where different particle shapes and sizes are used. In addition, foams produced by powder metallurgical routes such as the space holder or MIM-SH technique usually have a mixed structure between the two models in **Figure 20** where the cell walls are microporous surrounding macropores. So, the struts in model A should be similar to model B unless complete densification is realised. This can make the use of such models very complicated since the result of such models is a plot for each type of pores and it will require the consideration of different types of pores with different sizes.

2.3.1.3 Gibson-Ashby model

In this model, foams are assumed to consist of a group of cubic unit cells that are joined together at their midpoints. These cubic cells are uniform in size and have a side length of ℓ and edge thickness (cell wall thickness) of *t*. In addition, the cell walls or struts of these cells are solid and the cell faces are open (in the simplest version of the equations). A schematic graph of the Gibson-Ashby model structure is shown in **Figure 22**. During uniaxial loading, these cell struts are assumed to deform elastically by bending initially, and then starting to buckle as soon as the load reaches a critical value. The estimation of the elastic properties is based on simplifying the case into a beam that is loaded at its midpoint in a way that the load is uniformly transmitted into the struts of the cells [132].

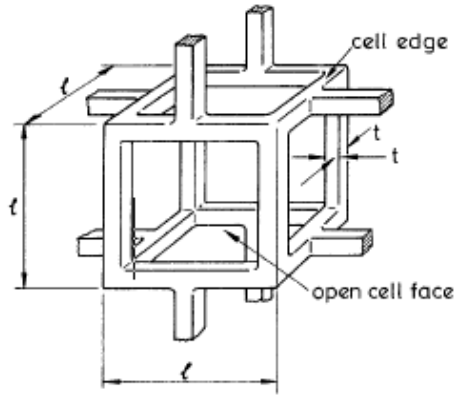

Figure 22. Gibson-Ashby Model for open cell foams [132]

According to this model, the elastic and shear moduli of an open celled foam can be estimated using the following equations:

$$E^* = E_s C_1 \left(\frac{\rho^*}{\rho_s}\right)^2 \qquad (3)$$

$$G^* = E_s C_2 \left(\frac{\rho^*}{\rho_s}\right)^2 \qquad (4)$$

where E^* and G^* are the foam elastic and shear moduli respectively, E_s is the modulus of the dense material. ρ^* is the foam density, whereas ρ_s is the density of the strut's material. C_1 and C_2 are constant values estimated by curve fitting and they are dependent on the shape of the cells. For equiaxed shape C_1 is equal to approximately one, whereas C_2 is approximately

(3/8) [132]. However, C_1 value is below 1 for foams with porous struts as the micropores which result from the incomplete sintering of powders leads to weaker struts and can dramatically reduce the properties.

Among the three aforementioned models, the Gibson and Ashby model is the most accepted and widely reported in the literature. Nevertheless, there are several studies which cast doubt on the applicability of the model to Ti foams produced, which was attributed to several reasons. One study by Esen and Bor reported that Gibson-Ashby model is only valid for foams with volume percentage of porosity about 70% or higher and found that the mechanical properties of their foams change with relative density according to a power law [24]. Another study in the literature reported similar findings [27], while a third reported a linear relationship between strength and relative density for foams with a volume percentage of porosity in the range 36-63% [133]. Thus, this leads to the conclusion that these models can only be used to give rough estimation of the properties as there are many variables (such as pore size, shape, non-uniformities in the structure of the foams produced, percentage of micropores in the struts or cell walls and production technique) that make the process of precisely predicting the properties of foams produced by powder metallurgical routes quite challenging.

2.3.2 Mechanical properties of foams

2.3.2.1 Uniaxial

By far the most frequently applied test for the mechanical response of porous materials is compression. As a result, there is a significant amount of data available for the uniaxial response of various porous titanium samples made by different foaming techniques with different percentages of porosities. A typical stress-strain curve of a Ti foam under uniaxial compression loading is shown in **Figure 23.**

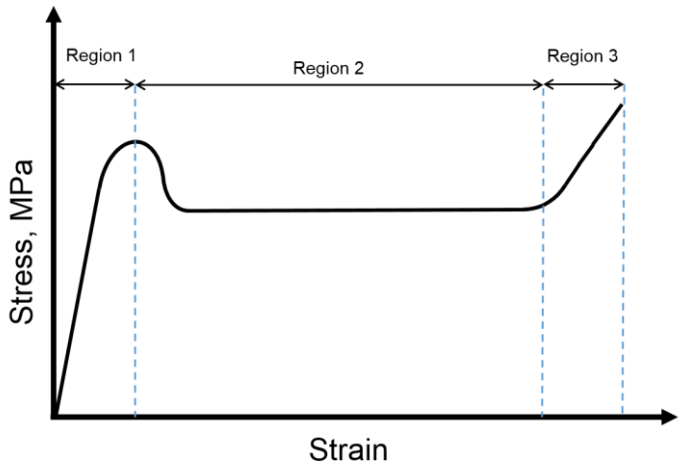

Figure 23. Stress-strain curve of a Ti foam under compression.

The curve is normally considered to consist of three distinctive regions, namely the linear elastic deformation region followed by a yielding and plateau region and ending with a densification region. In the first region, the foam is believed to be deforming elastically by cell wall bending up to a certain stress, above which the foam starts to deform plastically by cell wall buckling [24]. This buckling is thought to start initially in weak cells that are perpendicular to the applied load. This increases the local stress applied on the rest of the cell walls in the same layer until a whole layer of cell walls buckle. Then the adjacent layer of cell walls that are parallel to the loading axis keeps the foam stable under the applied stress and starts to deform elastically in a similar manner to the previous layer [134]. Thus, the stress remains constant until a certain number of cell walls collapse. This process continues until the material's behaviour shifts from porous material into a bulk material due to cell flattening, leading to a dramatic increase in stress [101].

Each layer consists of a number of cell walls separating a group of pores (depending on the space holder volume fraction). These cell walls are typically composed of metallic particles bonded together by either small necks or grown ones depending on the sintering temperature. It is also important to point out that these cell walls can also be porous due to the presence of micropores that are formed due to incomplete densification during sintering. Thus, foams in this case are multi-layered materials that consist of a network of interconnected or randomly spaced macropores separated by microporous cell walls. Hitherto, almost all of the studies in

the literature reported the presence of such micropores in powder metallurgical Ti foams [17, 22, 24, 25, 27]. The presence of these micro-pores can detrimentally affect the mechanical properties of foams since most of the applied load is transmitted and concentrated on these 'load bearing cell walls'. Therefore, it is extremely important to point out that the mechanical properties of foams are not only dependent on the characteristics of the starting powder, space holder size and volume fraction, but are also strongly connected with the sintering temperature and time as both can prominently dictate how well these cell walls are densified to withstand the applied loads.

The uniaxial properties, namely Young's modulus and yield strength for the most commonly reported processing methods and materials in the literature are summarised in **Figure 24** and **Figure 25**.

Figure 24 shows how the value of E changes with the relative density of a series of randomly-structured porous samples made from non-alloyed titanium. The majority of reported data are for foams processed by the space holder method (albeit using a variety of space holders), MIM-SH, freeze casting and gel casting, and a small number of points for the impregnation of polymer foams. A number of lines showing the predictions for simple models for the elastic behaviour of a foam (the Rule of Mixtures upper limit and the Gibson Ashby model for 4 different values of the constant C, from 1-0.1) are given. For the plot, variations in processing conditions and pore sizes have been ignored in classifying the data into different series. This may be one of the reasons behind the large variability seen within each method, along with minor variations in testing and analysis procedures. Looking at the data, it is seen that, while there is significant overlap, in the reported data the space holder methods have achieved some of the highest stiffness values (approaching even the upper bound specified by the Rule of Mixtures) at a given density, while MIM-SH is frequently among the lowest. Having a higher percentage of binder in the mixture would reduce the points of contact among the Ti particles in the case of MIM-SH and hence material has to travel larger distances to form bonds via boundary diffusion than in the case of space holder technique. The spread however implies these are more due to variations within the techniques, and not fundamental characteristics. As an additional point, the flexibility of the methods is demonstrated by the large range of relative densities which have been made and tested.

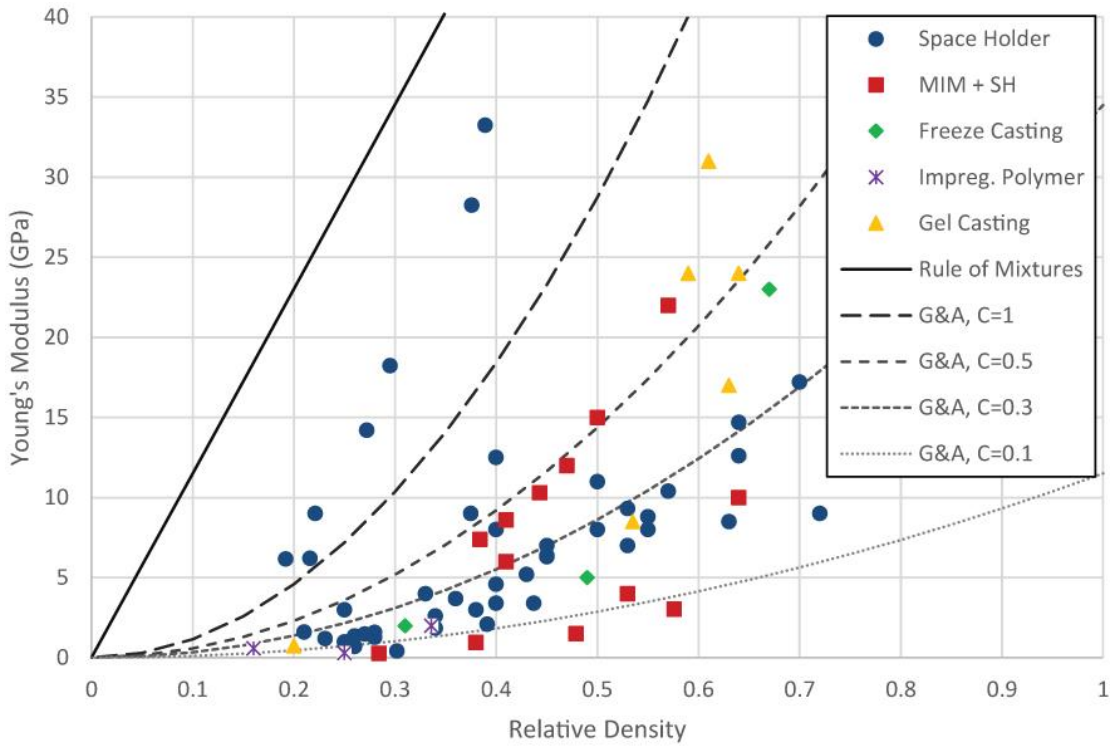

Figure 24. Reported values for the Young's modulus of non-alloyed porous titanium with random structures, plotted against the relative density. Data are grouped into the broad class of methods, ignoring variations in how the technique is applied and pore size. Also shown are the prediction lines from the Rule of Mixtures and the Gibson-Ashby approach with different values of the constant, C. Data are from [4, 9, 11, 25-27, 58, 62, 67, 69, 74, 75, 77, 80, 82, 135-143].

The plastic behaviour of a porous material can be characterized in several ways, leading to a smaller quantity of data which can be analysed together; sometimes the plateau strength is reported, and in other instances it may be the yield (or offset yield) stress. Due to the importance of the point of initiation of plastic flow for different applications and the relatively poor definition of the plateau stress in porous materials that do not show the classical form of the curve with a perfectly flat region, the yield strength is used (taking the offset yield strength as being an acceptable measure where this is reported), and these are collated and plotted in **Figure 25** for porous titanium produced by different foaming techniques.

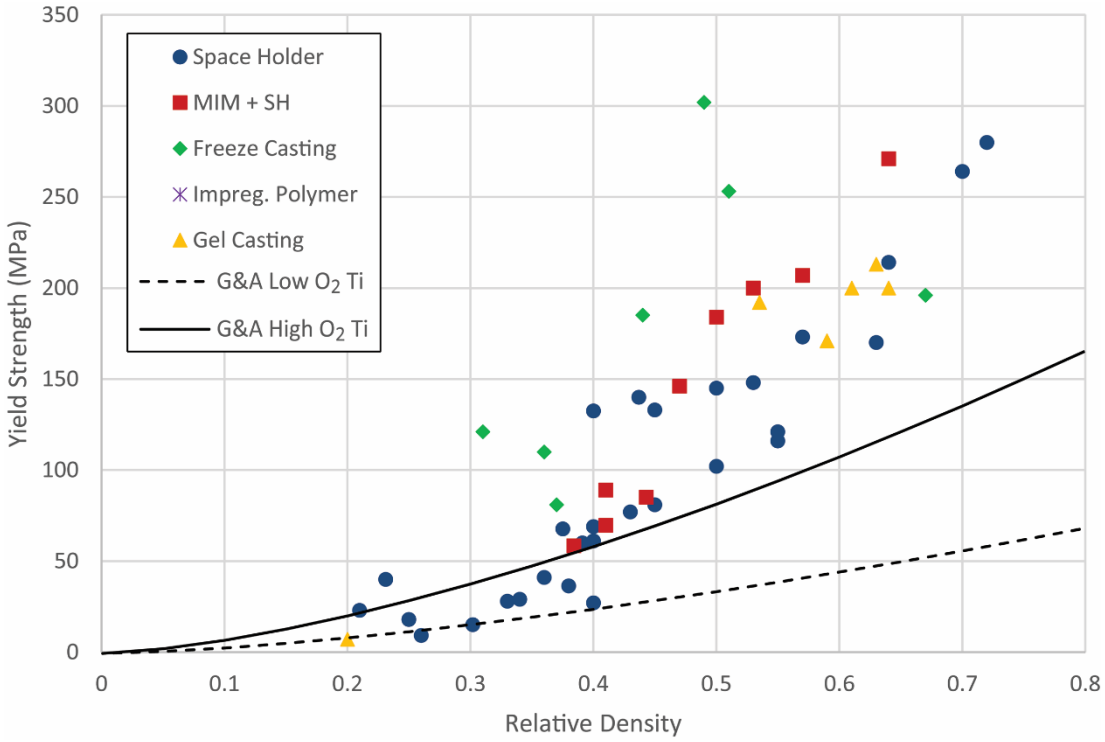

Figure 25. Reported values for the yield strength of non-alloyed porous titanium with random structures, plotted against the relative density. Data are grouped into the broad class of methods, ignoring variations in how the technique is applied and pore size. Data are from references given in **Figure 24**. Also shown are the predictions of the Gibson-Ashby model [132] for the strength of porous materials with C=0.4 for Grade 1 Ti (low O_2, yield strength taken as 240 MPa) and Grade 4 Ti (high O_2, yield strength taken as 580 MPa).

The strength data in **Figure 25** show more consistency than the Young's modulus, without significant differences based on manufacturing method. This observation is perhaps surprising, as it would be expected that microstructural variation, significant degrees of which would be expected, would affect plastic behaviour more strongly. However, as yield is likely to be affected by defects present (such as misformed pores or missing struts), this may reflect the fact that in such porous materials the structure on the scale of the porosity is determining the transition from purely elastic to elastic and plastic deformation.

2.3.2.2 Fracture

Fracture behaviour and toughness of porous metals is experimentally more challenging to address, although evidence exists that the behaviour on fracture is more dependent on the

deformation mechanisms possible within the dense material [144]. There are few studies investigating the fracture toughness of porous Ti in the literature. One example reports the fracture toughness measured in pre-cracked specimens for titanium with 60 and 70% porosity [145]. The K_{IC} values were 7.0 and 4.0 MPa√m respectively, significantly lower than dense Ti (75 MPa√m), reduced by a greater proportion than the reduction in material present, in general agreement with proposed scaling laws for the fracture toughness of porous metals [146].

2.3.2.3 Creep

More advanced properties, such as creep, have been experimentally studied for some porous metals including aluminium [147, 148], and nickel based foams [149, 150] as well as the development of predictive frameworks and analytical models [151, 152], but experimental exploration for porous titanium has not been reported, reflecting the recent focus on biomedical rather than high temperature applications.

2.3.2.4 Fatigue

As porous titanium is likely to be used in applications with some structural role, assessing the behaviour under cyclic loading is extremely important. However, the fatigue life of porous materials (particularly those produced by powder methods) is much more difficult to assess than ordinary dense material, due to the presence of macro and micropores, and high surface roughness, including on the internal surfaces. One study investigated the fatigue behaviour of Ti foams was reported by Kashef et al, where they tested a notched Ti foams with a total porosity of 60% (made by the space holder technique), and compared it with another foam having similar percentage of porosity, but coated with a thin layer of solid Ti by localized melting of the surface [153]. Samples were cyclically loaded with a maximum load of 200 N and frequency of 40 Hz. A dominant crack was observed to form in a pre-cracked cell wall and grow continuously along the weakest path until fracture. It was also noted that the uncoated porous Ti displayed a higher Paris exponent (m=17.1±0.3) than the coated sample (m=14.2±0.2), attributed to the closure and bridging of the cracks [153]. Fatigue has also been investigated in porous Ti samples made by the space holder technique

[154] with porosities ranging from 51-65% under compression–compression fatigue with a frequency of 5 Hz and a constant stress ratio of 0.1 up to failure or a million cycles. It was reported that the fatigue limit could be normalized with the yield strength for a particular density, being 0.75 of the normalized maximum stress applied.

While not taking samples through to failure, the effect of fatigue-induced damage was tested by applying cyclic compression across stress ranges up to 50-60 MPa (below the compressive yield strength) at a frequency of 6 Hz and a minimum to maximum load ratio of R=0.1 in simulated body fluid, to Ti with 62.5% porosity, made by the space holder technique. A reduction in the compressive strength by two thirds was seen [75].

2.4 Applications

Ti foams offer several advantages over other foams such as extra light weight combined with good compressive strength, high operating temperatures and excellent corrosion resistance combined with good biocompatibility [34]. This extraordinary combination of properties differentiates them from other foams and makes them excellent candidates for a number of applications. Some of these applications will be mentioned in the following section.

2.4.1 Biomedical applications

Due to the small part dimensions typically required, and the relatively small volume of production, of the potential applications open celled porous titanium is often suggested for use in biomedical implants into hard tissue, for example as reviewed for dental implants in [155]. The advantages for such applications come from the inherent inertness in the body of titanium, and its good fatigue resistance under corrosive conditions, combined with the availability of pores for cells to grow into and provide better fixation and the ability of a porous structure to be designed with a particular Young's modulus, below that of the dense metal (for example by adjusting the level of porosity). This latter behaviour is thought to provide a potential route to avoid the stress shielding problem, where a stiff implant supports mechanical load, leading to unloaded bone around the fixation being resorbed by the body. Foams with gradient or graded porosity can also be made so that they replicate the structure of the bone itself by having some more porous regions for stiffness reduction and ingrowth, and some denser regions for improved strength. This might be of a great benefit in some

biomedical implants such as intramedullary rods or hip stems [156]. Techniques such as the space holder technique [157] and metal injection moulding in combination with a space holder were used to produce foams with gradient porosity. Porous titanium has also been investigated for drug release applications and promising results have been reported [158]. Examples of the use of porous Ti in biomedical applications are shown in **Figure 26**. The first and second examples shown in **Figure 26** are for commercial porous dental implant with up to 80 % porosity produced by Zimmer Biomet and U2^{TM} Matrix porous stem produced by United Orthopaedic Corporation (the upper part of the stem is made of coarse Ti particles sintered together forming a network of interconnected micropores). The third example shown is for porous Ti intramedullary rod made via additive manufacturing using electron beam melting.

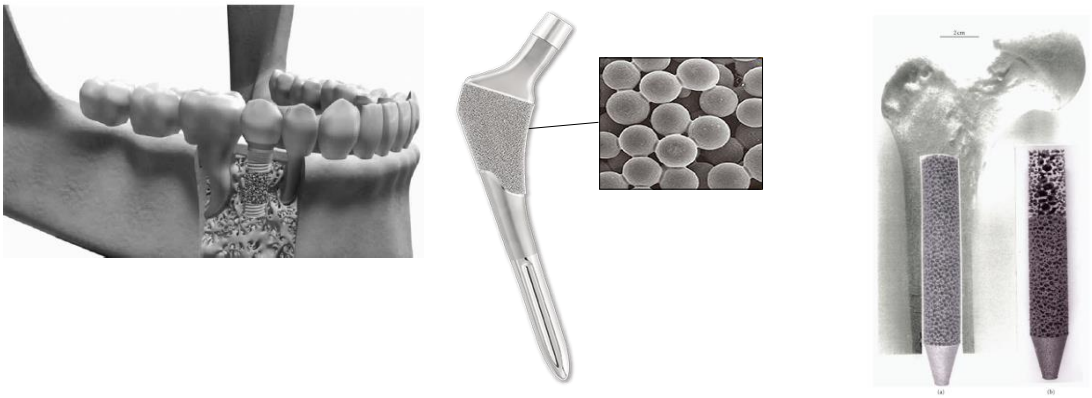

(a) (b) (c)

Figure 26. (a) Porous Ti dental implant produced by Zimmer Dental with up to 80% porosity [159]. (b) U2^{TM} Matrix porous stem produced by United Orthopaedic Corporation [160]. (c) porous Ti intramedullary rod insert for human proximal femur [156].

2.4.2 Functional applications

2.4.2.1 Electrodes

Having an extremely high specific surface area makes porous Ti a potential candidate for several functional applications, including as a material for electrodes in batteries. For example, the 3C Crista Chemical Company reports the use of Ti foams in next generation lightweight car batteries (shown in **Figure 27**), claiming that the higher active surface area of these foams leads to the energy/volume ratio being greater than lead-acid batteries, and

also that batteries using titanium foams can support many more charging cycles. The manufacturing technology is based on electroplating of Ti on to the surface of a carbon or polymer foam by pulse plating technique after activating its surface with an activator solution [161].

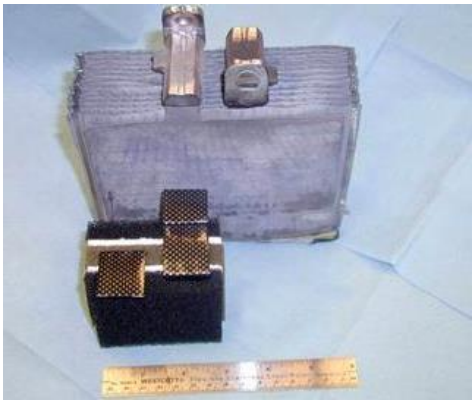

Figure 27. Traditional 2-volt cell with a foam cell below [162].

2.4.2.2 Filters

The chemical and temperature resistance make porous titanium suitable for certain applications in filtration, and some Ti filters, produced through sintered powder, are already commercially available. LOFMET^{TM} Filter Cartridges from Eaton Technologies GmbH (Nettersheim, www.eaton.de/filtration) and TPM™ Series Filter Cartridges from Graver Technologies (Glasgow, www.gravertech.com), are both sold for filtering in the size range 0.5-100 and 35μm respectively under extreme operating conditions with a maximum operating temperature of 371°C and aggressive fluids and gases.

2.4.3 Aerospace applications

The extra light weight, high operating temperatures, high permeability and excellent corrosion resistance made Ti foams a perfect candidate for aerospace applications [34]. One potential application is the use of porous Ti as a skin material for slot suction of the turbulent boundary layer in order to achieve smooth laminar flow across the aircraft wings and reduce friction and drag [163].

Figure 28. F-16XL jet with a porous Ti glove [164]

Part of the left wing of the F-16XL jet shown in **Figure 28** was made of a porous Ti and was successfully tested by NASA for achieving laminar flow at supersonic speeds [164]. This can help reducing the weight of the plane and fuel consumption. In addition, Ti foams can be used as a core material in the production of structural sandwich panels for aerospace applications, where they are fixed between two thin and stiff metal sheets, or they can be manufactured directly in one step through the use of the gas entrapment and expansion technique mentioned in **section 2.2.3**. In this latter case, a Ti container is used and the partially-densified part (including the canister) is hot rolled before creep expanding the pores via thermal treatment at high temperatures [29].

2.5 Summary

The common techniques for producing Ti foams have been reviewed in this chapter. However, MIM-SH appears to set itself apart from others in offering the possibility of potentially mass-producing net shaped Ti foams with different intricate shapes and percentages of porosity without the need for any subsequent machining. Thus, MIM-SH is a very attractive technique, particularly for producing biomedical implants. Nevertheless, there is still much work to be done in order to be able to use this technique in creating Ti foams with different pore sizes and shapes, high percentage of porosity, good mechanical properties as well as gradient porous structure, as may be desired for such applications. Therefore, the aim of this work is to adopt MIM-SH technique and develop it to produce Ti foams with the potential for biomedical applications.

3 Methodology

3.1 Preparation of Ti foams via Metal Injection Moulding

As we mentioned previously in **section 2.2.5.2**, Ti foams are produced by metal injection moulding in combination with space holder in four key stages. The first stage involves mixing of the powders and binders to form feedstock. The feedstock is the powder-binder mixture after mixing and homogenisation. In the second stage, the feedstock is fed into the injection moulder in the form of pellets to mould parts with the desired shape. In the third and fourth stages, the parts are water debound and sintered to form Ti foams. Flow chart of the process of producing foams by metal injection moulding with the four key stages highlighted is shown in **Figure 29**

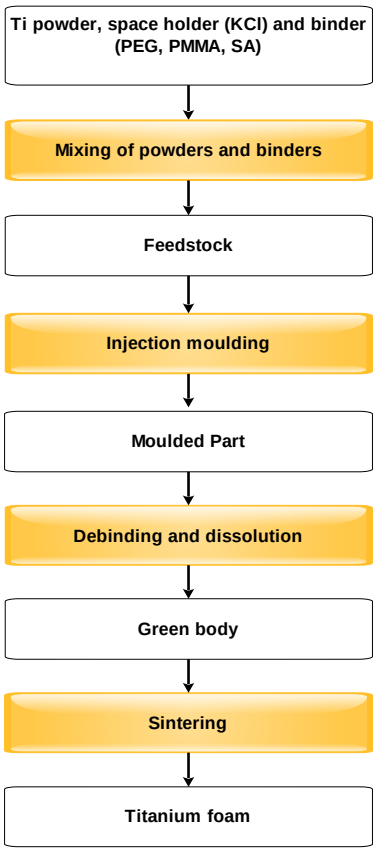

Figure 29. Flow chart of the process of producing foams by metal injection moulding in combination with space holder.

3.1.1 Starting materials

Relatively coarse, commercially pure Ti powder grade 2 (Arcam AB, Sweden) with spherical particles was used as a raw material in this study. The particle size distribution of the Ti powder was analysed via a Malvern Mastersizer 3000 using the wet dispersion method and the results are shown in **Table 4**. Generally, powders with particle size below 45 µm are used in injection moulding in order to result in minimal porosity within the samples and a density near the theoretical density for improved mechanical properties [165]. However, the smaller the particle size, the higher the surface area and the more the Ti part is prone to contamination and oxygen pick up during processing, debinding and sintering. In addition, the use of fine powders can result in more shrinkage, as the smaller the particles used, the greater the rate of sintering or the rate at which bonding between the particles, neck formation and growth (as well as densification) occurs [166]. Hence, it was decided to use relatively coarse Ti powder in order to reduce shrinkage and the extent of contamination, as well as lower the cost. This will not only be more economical, but can also result in more intentionally-induced micropores. These micropores are advantageous, particularly for biomedical applications, where they promote bone ingrowth and cell attachment [72, 167]. In addition, the use of coarse powders can shorten the time required for solvent debinding and facilitate the process of thermal debinding, where the larger the powder particles, the smaller the contact areas among the particles or the larger the channels between them making it easier for the solvent to penetrate the part and dissolve the binder and provide larger porous channels for the gases to escape [168].

The space holder used in the formation of pores was potassium chloride (KCl). This was chosen over NaCl (a more common choice) due to having a higher solubility in water, and availability in different shapes. Two KCl powders were used, namely cubic and spherical potassium chloride (Sigma-Aldrich, Steinheim, Germany) and their particle size distributions were analysed using a Malvern Mastersizer 3000 with the dry analysis method, with results shown in **Table 4**. The space holders were sieved through 710 µm, 500 µm and 250 µm sieves. The morphologies of the Ti powder and KCl space holders are shown in **Figure 30.** The cubic KCl particles had a Hopper-like shape in some cases, as shown in **Figure 30 (b)**. This shape usually results from a crystal growth mechanism where atoms add preferentially

at the edges, leading to a faster growth at the edges compared to the centre. Ti particles, produced by gas atomisation, were approximately spherical in shape.

A three-component polymeric binder was used in the preparation of feedstocks. The first part of the binder (the low viscosity part) was Polyethylene Glycol (PEG) (Sigma-Aldrich, Steinheim, Germany), and it was chosen due to its ready availability, as well its good solubility in the water. The second part of the binder (the high viscosity part) was Poly Methyl Methacrylate (PMMA, Sigma-Aldrich, Germany) and it was chosen due to its high strength in comparison with other common polymers used in MIM, such as low and high density polyethylene, so that green samples can be easily handled after removal of PEG without sample collapse [169]. Stearic Acid (SA) with purity of ≥ 97% (Fluka, Sigma-Aldrich) was the third part and was added for two main purposes, namely as a lubricant to reduce the friction between the powder and the inner walls of the mixing and moulding equipment, as well as a surfactant to improve the dispersion of the Ti powder in the polymeric binder [113, 170]. The density of the powders and binder constituents were measured using a helium pycnometer (AccuPyc II 1340, Micromeritics, USA) with a filling pressure of 10 psi over 10 cycles and the results are presented in **Table 4**.

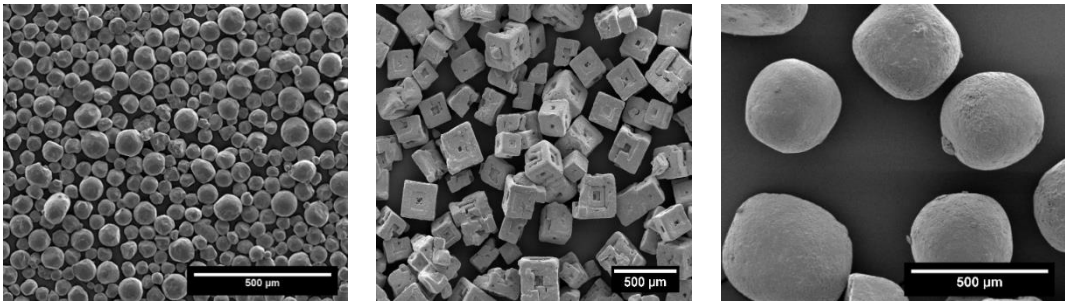

(a) (b) (c)

Figure 30. The morphology of the raw materials: (a) Ti powder, (b) cubic KCl, (c) spherical KCl

Table 4. Characteristics of the starting materials

Name	Dx (10)	Dx (50)	Dx (90)	Density, g/cm^3
Ti Powder	52	72.5	102	4.54
Cubic KCl Powder	229	329	461	1.99
Spherical KCl Powder	188	307	476	1.99
PEG 1500	-	-	-	1.13
PMMA	-	-	-	1.21
Stearic Acid	-	-	-	1.01

3.1.2 Feedstock preparation

The feedstock was initially prepared by mixing the Ti powder with PMMA and stearic acid using a centrifugal Speedmixer 800 FZ (Hauschild; supplied by Synergy Devices Ltd, UK). Next, four cylindrically-shaped dispersion media made of zirconia was added to the mixture to homogenise and uniformly distribute the binder ingredients. After that the space holder (KCl) was added and the mixing process continued according to the mixing programme shown in **Table 5**.

Table 5. Mixing programme of feedstock

Mixing Speed (rpm)	1300	1600	1800	1400	1600	1800
Time, (minutes)	4	4	2	2	2	2

The mixing programme was chosen so that the heat generated from friction as the constituents mix was sufficient to melt the PMMA. It consists of 2 sets of increasing speeds, intended to build up the heat each time. PEG was added in the last three stages of the mixing programme in order to guarantee that the PMMA is melted and homogenised in the mixture before adding the PEG, as the latter has a lower melting temperature. It should be noted that the temperature of the mix cannot be directly measured in the equipment, so visual observation of molten state was used to determine when the temperature was sufficient. The

total period of mixing, 16 minutes, is much shorter than that reported in the literature (e.g. over 1h for the same binder components for MIM of stainless steel powder, with a blade mixer at a speed of 30 rpm and a temperature of 70°C [171]) due to the effectiveness of the high speed centrifugal mixer, including the dispersion media, in mixing and homogenising the powders and polymers. However, the mixing programme was modified later on so that the KCl is added after the addition of PEG to the mixture and taking out the dispersion media in order to avoid any breakage for the space holder particles. The mixture was then pelleted by extruding it twice through a vertical plunger-type injection moulder at 150°C and cutting it into small pellets, the length of which ranges between 0.5-1 cm. The pellets were then allowed to cool for 5-20 minutes before carrying out any subsequent processing.

3.1.3 Sample preparation procedure

A vertical plunger-type injection moulder (J.B. Engineering, Chippenham, UK) was used to injection mould green cylindrical parts of the prepared feedstocks at a temperature of 150 °C and pressure of 45 MPa. A schematic of the machine is shown in **Figure 31**.

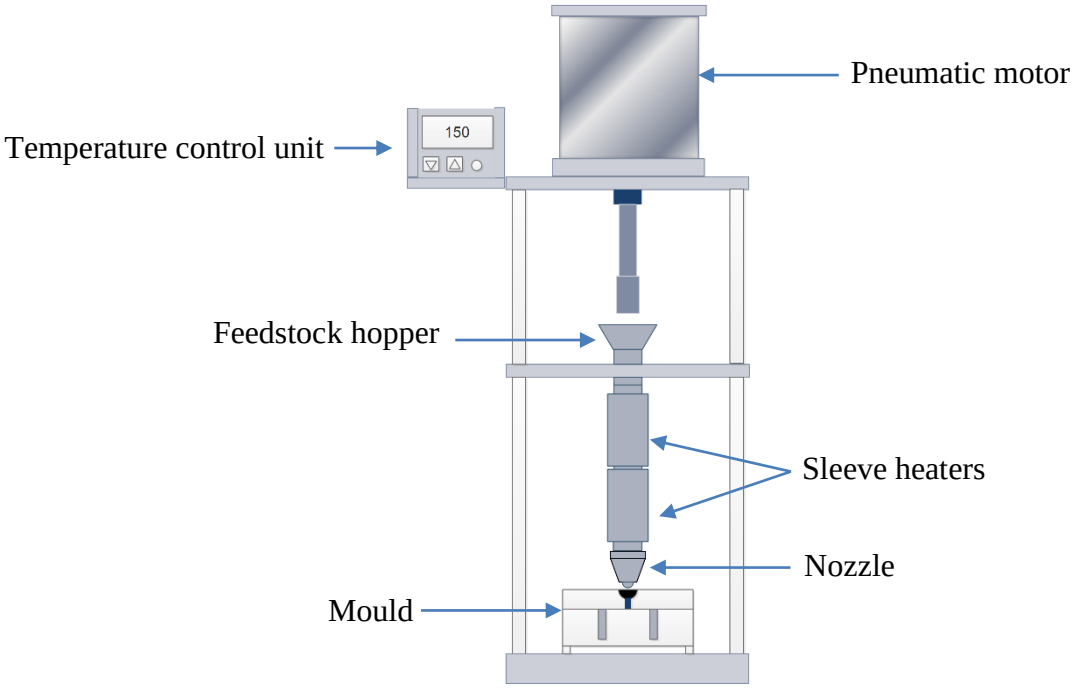

Figure 31. A schematic of the vertical plunger type injection moulder

The machine is composed of a pneumatic motor that pushes a piston or plunger down into the cylindrical barrel of the machine at a pressure of 45 MPa. A hopper is fitted on the top of the cylindrical barrel in order to hold a larger amount of feedstock and to facilitate the process of filling the barrel with feedstock. The lower part of the cylindrical barrel is heated through two sleeve heaters and a thermocouple is embedded inside the nozzle in order to record the temperature of the feedstock. The machine was switched on for 10 minutes before feeding the feedstock to heat the barrel to the required temperature of extrusion and injection. Initially, the feedstock is fed as irregular chunks obtained from the mixing process and extruded twice into very long pellets which are then cut into small pieces and allowed to cool before feeding them into the barrel again. The pellets are left inside the barrel for at least 15 minutes before moulding parts in order to reach thermal equilibrium and achieve a homogenous temperature in the feedstock. Then, the pneumatic motor is brought down into the barrel injecting the molten feedstock through the nozzle into the moulding gate of the die. Next, the feedstock runs through the gate into the cylindrical cavities of the mould, the height of which can be adjusted via screws at the mould base. The moulded specimens here were 10 mm in diameter with a varied height. In some cases (injecting commercial feedstock), the mould was heated inside an electric furnace in order to facilitate the process of filling the parts up to a temperature of 60 ºC.

3.1.4 Water debinding and dissolution of the space holder

One advantage of using partially water soluble binder is that a fraction of the binder and the space holder can be removed in one process unlike other binders where organic solvent debinding and water dissolution are required and have to be carried out separately. The water soluble part of the binder and space holder were removed by water dissolution using different techniques. The first technique was performed by real time monitoring of weight loss of both the binder and space holder using a Mettler Toledo density balance with resolution of 0.1 mg. The sample was put in the weighing basket of the density balance under water and weight loss was recorded with time. The temperature was recorded using a thermometer supplied with the density balance. The following equations were used to calculate the percentage of space holder and binder removed with time:

$$P_{KCl+PEG} = \frac{W_i - W_t}{W_i - W_f} \times 100\ \% \quad (5)$$

$$W_f = (w_{Ti} + w_{PMMA} + w_{SA}) \times W_i \quad (6)$$

where:

$P_{KCl+PEG}$: The percentage of binder and space holder removed

W_i: The initial weight of the sample (in water in the case of the first experiment and in air in the case of other experiments) (g)

W_t: The weight of the sample at time t (g)

W_f: The expected weight of the sample after complete dissolution of the water soluble space holder and binder components (g)

w_{Ti}: The weight fraction of Ti

w_{PMMA}: Weight fraction of PMMA

w_{SA}: Weight fraction of stearic acid

Although stearic acid can be dissolved in water to a certain extent, and its solubility increases as the water temperature rises [107], it was assumed to be insoluble in the first experiment as the temperature was relatively low (20 °C). The second technique was performed using an ultra-sonic bath at room temperature. The sample was weighed in air using Mettler Toledo balance with resolution of 0.1 mg and then put on the metal gauze of the ultrasonic bath and vibrated ultra-sonically. The weight loss was monitored with time by taking the sample out of the bath every 15 minutes and drying it using heated compressed air for 15 minutes before weighing the sample three times at different intervals in order to make sure that a consistent reading was taken. The third technique was done using heated ultrasonic bath supplied with a thermostat and built-in thermometer in order to have precise control over temperature. The temperature was set to 50 °C (set according to the DSC analysis of the PEG) and the sample was ultrasonically vibrated. Every 15 minutes, the sample was taken out of the bath and dried, using similar drying procedure to the second experiment, followed by weight loss measurement. The fourth dissolution technique was performed using a hot plate stirrer with

magnetic bar to mix the water vigorously (shown in **Figure 32.(b)**). The sample was put on a metal basket and hung using a metal stand. The basket was placed inside a 1000 ml water beaker. The beaker was put on a hot plate stirrer. The rotation speed of the magnetic bar was set to 900 rpm while the temperature was set so that the water temperature inside the beaker was equal to 50 °C. The temperature was monitored using a digital thermometer with a K-type thermocouple (Digitron TM22, England). The drying procedure and weight loss measurement were performed in a similar manner to the previous experiments. In calculations for these experiments, equation 3 was used without inputting a value for the weight fraction of stearic acid (w_{SA}) as at 50°C stearic acid dissolves much more easily in water than at 20°C [107], and is considered therefore not to contribute to the final weight.

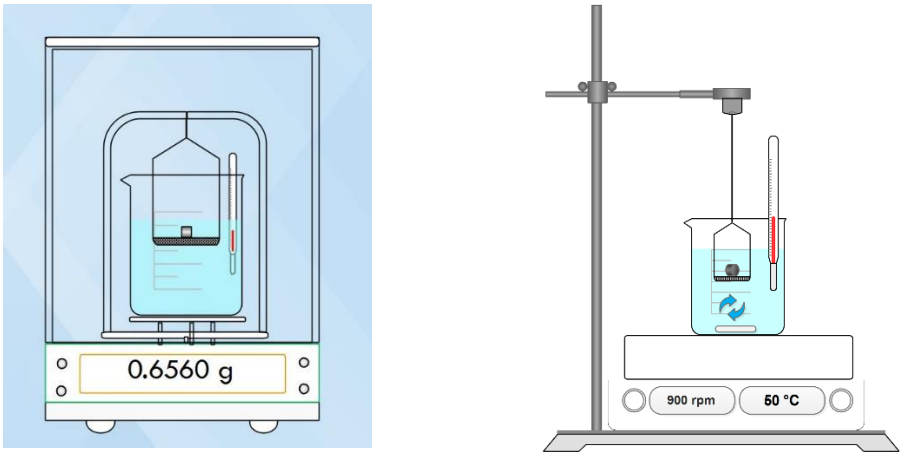

(a) (b)

Figure 32. (a) Debinding in a density balance, (b) debinding with water stirring

3.1.5 The effect of temperature on dissolution of space holder and binder

Specimens were placed in the metal basket of a heated bath at different temperatures. The temperatures were decided according to the melting temperature of PEG which was obtained through DSC analysis (found to be 50.12 °C). The dissolution processes were carried out at three different temperatures below the melting temperature of the PEG and three temperatures above the melting temperature of PEG in order to understand the effect of

temperature on the dissolution of binder and space holder. The first set of temperatures were 25, 30 and 40 °C, whereas the second set of temperatures were 60, 70 and 80 °C. The debinding and dissolution processes were carried out for three hours at these sets of temperatures. The samples were taken out of the bath every hour in order to measure the weight loss. The samples were dried and weighed using a similar technique to that mentioned previously. The cube root of mass was calculated and plotted against time in order to find the dissolution rate constant (K) for each temperature using the Hixson–Crowell cube root law [172].

$$\sqrt[3]{m} = \sqrt[3]{m_i} - Kt \quad (7)$$

where:

m: The remaining mass of binder and space holder at time t

$m_{i:}$ The initial mass of binder and space holder

K: The dissolution rate constant, also counting the temperature-dependent component of the rate

t: time in seconds

After calculating the dissolution rate constant for each temperature, an Arrhenius plot was constructed by drawing the logarithm of *K* against the inverse temperature. Finally, the activation energy for the dissolution process was calculated by calculating the negative slope of Arrhenius plot and multiplying it by the gas constant (8.314 J/mol.K).

3.1.6 Thermal debinding and sintering of samples

The removal of the high viscosity part of the binder (PMMA) and sintering of samples were performed in one cycle under different sintering times. The green samples were placed in a high temperature alumina sintering trays filled with yttria stabilized zirconia spheres in order to avoid any reaction between the sintering trays and the samples. The first group of samples were sintered at 1400°C for 2 h using two furnaces, namely a tube furnace and a vacuum furnace (CENTORR, USA shown in **Figure 33**) in order to compare the extent of contamination that results in the parts. The cycle is performed under an inert atmosphere

(argon). The samples were firstly heated at a rate of 2.6 °C/min to 450 °C and held there for 1 hour in order to ensure the complete removal of PMMA according to the TGA results. After that the samples were heated at a rate of 2.3°C/min to 800 °C and dwelled there for 1 hour for pre-sintering to give some initial structural integrity (a common practice in powder production of foams [18, 173]) before heating them again at a rate of 3.7 °C/min to 1400°C and sintering them there for 2h. The parts were cooled at a rate of 11.6 °C/min to room temperature. The aforementioned cycle was used initially to sinter parts using vacuum and tube furnace. However, the sintering cycle was changed later on due to the very long time required for the sintering cycle and due to the huge consumption of inert gas as well as available equipment time. A second group of samples were sintered at 1250 °C for 2h and cooled at a rate of 15 °C/min. A third group of samples were sintered at 1320 °C for 2h in order to compare samples made by the developed feedstock without space holder with samples made by commercial feedstock in terms of performance and porosity.

Figure 33. CENTORR vacuum sintering furnace

3.2 Characteristics of the Feedstock and produced Ti foams

3.2.1 Rheological characteristics of the feedstock

Viscosity is one of the important parameters in assessing the suitability of feedstocks for injection moulding. The viscosity needs to be below 1000 Pa.s in a shear rate range of 10^2-10^5 s^{-1} [118]. The viscosities of the prepared feedstocks were analysed using a twin bore

barrel capillary rheometer (Rosand RH2000, Malvern, UK) with a capillary die that has a diameter of 2 mm and a height of 16 mm. The temperature of the test was set up and the rheometer was left in order to reach the testing temperature before feeding the feedstock pellets into the barrel of the rheometer and after feeding them, the feedstock was left for 15 minutes in order to attain thermal equilibrium [95, 174]. Rabinowitsch correction was applied to the results in order to get absolute viscosity readings by correcting the shear rate value and obtaining the true shear rate as the flow of the feedstock is pseudoplastic (non-Newtonian) [175]. The flow behaviour index was calculated using the following power law equation [176]:

$$\eta = K\dot{\gamma}^{n-1} \quad (8)$$

where η is the viscosity, K is a constant, $\dot{\gamma}$ is the shear rate and n is the flow behaviour index (shear sensitivity). For non-Newtonian fluids with shear thinning behavior, the shear sensitivity value is below 1, while for Newtonian fluids it is equal to 1. Another critical variable in assessing the capability of the feedstock to take the shape of the mould cavity is the yield shear stress. Yield shear stress is the minimum stress required to cause the feedstock to flow, below which no flow occurs. The yield stresses for feedstocks were calculated via the Bingham model using the following equation [177]:

$$\tau = \tau_y + \eta_p\dot{\gamma} \quad (9)$$

where τ_y is the yield shear stress, η_p is the plastic viscosity.

There are limited studies in the literature on the viscosity of feedstocks prepared using a mixture of metal powder, binder and space holder, and the feedstock system is much more complex than in the case of having one powder, due to the differences in terms of density, particle size and shape between the metal powder and space holder, each of which has a different effect on the viscosity. Hence, it is important to assess the impact of these parameters for both powders on the viscosity. In addition, choosing the right grade of binder to be mixed with the powders is also crucial in preparing a homogenised feedstock with moderate viscosity and good shear thinning behaviour without resulting in any moulding defects.

3.2.2 Differential scanning calorimetry and thermogravimetric analyses of the binder

Differential Scanning Calorimetry (DSC) is a technique used for characterising the melting behaviour and thermal properties of the materials by measuring the amount of energy flowing into or out of it [178]. The material needs to be characterised is placed inside an aluminium pan covered with lid and placed on the first side of the heating chamber, while an empty reference pan is placed on the other side of the heating chamber. The differential scanning calorimeter measures the difference in heat flow between the reference pan and material during heating and cooling and records it automatically. This value corresponds to the amount of thermal energy absorbed or released from the sample. The DSC analysis was performed in order to find out the melting behaviour of the binder and its constituents and according to the results the injection temperature was set. The analysis was carried out using a DSC Pyris 6, Perkin Elmer, USA. The weight of the samples used for analysis was about 4±0.3 mg and the samples were scanned at a rate of 10 °C/min in the temperature range 25-200 °C.

Thermogravimetric (TGA) analysis is used in monitoring the changes in the weight of the sample as the material is subjected to a controlled temperature programme using a thermobalance [179]. The programme can be either isothermal or non-isothermal. TGA analysis was done in order to assess the decomposition behaviour of the binder and according to which the debinding temperature was set during the sintering cycle. The thermogravimetric analysis was carried out under argon atmosphere and the binder was heated up to 726 °C using a Pyris 1 TGA instrument, Perkin Elmer, USA.

3.2.3 Fourier Transform Infrared Spectroscopy (FTIR)

FTIR is a very widely-used characterisation technique for polymers and polymer blends, which involves passing IR radiation through the polymers and measuring the energy absorbed at different wavelengths. The incident energy causes atomic vibrations in different parts of the molecules of the sample at different energy levels causing characteristic absorption [180].

FTIR analysis was carried out in order to specify and identify the polymeric constituents of the commercial feedstock by putting a sample through a Perkin Elmer FTIR with monolithic diamond ATR and analysing it in the wavelength range from 4000 to 400 cm^{-1} with a sampling number of 16 times.

3.2.4 Estimating the volume percentage of porosity in the samples

The volume percentage of porosity in the foams produced was determined by subtracting the true volume of the foams (the solid part only), which was obtained using a helium pycnometer, from the bulk volume that was calculated using the dimensions of the sample via a Vernier caliper with a resolution of 0.01 mm. The true volume measurement was carried out using AccuPyc II 1340 helium pycnometer by Micromeritics, USA under filling and purging pressure of 10 psi over 10 cycles. The helium pycnometer works by measuring the amount of helium gas displaced by the sample (shown in **Figure 34**), where the sample is placed in a sealed chamber with known volume (chamber 1) and a helium gas is then pumped into the chamber filling the pores within the sample. The pressure is monitored during the filling process and the helium gas is then purged into another empty chamber (chamber 2) where the volume is estimated.

$$Porosity\ (\%) = Bulk\ volume - True\ Volume \tag{10}$$

$$Bulk\ volume = \pi * \left(\frac{d}{2}\right)^2 * h \tag{11}$$

where *d* is the diameter of the sample, *h* is the height of the sample. The diameter and height of the samples were measured four times and average values were used in calculating the percentage of porosity.

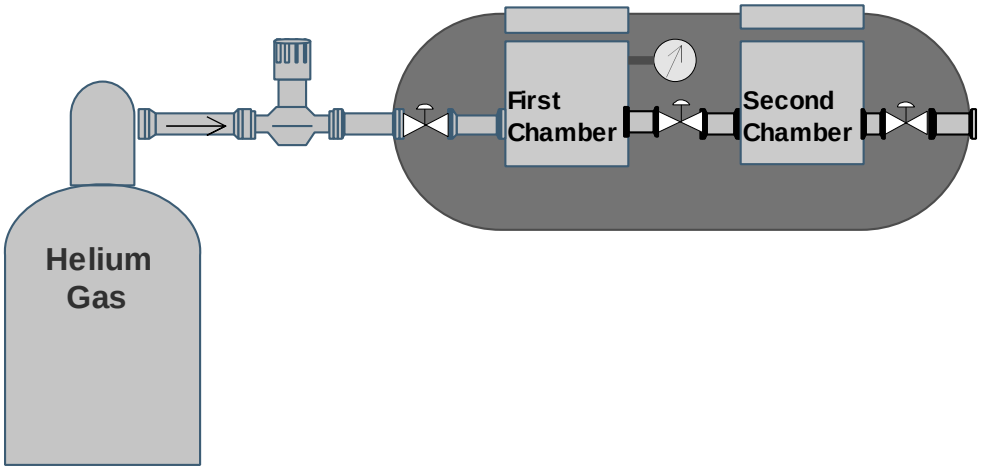

Figure 34. A schematic representation of the working principle of helium pycnometer.

3.2.5 Characterisation of the produced foam via Micro-computed tomography

Micro-Computed Tomography (Micro-CT) is a non-destructive imaging technique that utilizes an X-ray source to produce high resolution three dimensional models of the imaged parts comprised of multiple two dimensional trans-axial projections or slices [181]. The X-ray beam is collimated and filtered before traveling through the sample and gets recorded via a charge coupled device camera coated with a phosphor-layer that helps converting the X-rays into visible light [182]. For complete rendering of the 3D structure, the sample is rotated at the end of each projection by a certain degree and the process continues until full rotation of the sample has been achieved and a complete set of projections are obtained.

Micro-CT analysis was carried in order to estimate the percentage of open porosity as well as analyse the structure of the produced foams and find out the pore size distribution in the sample. The analysis was carried out using a SkyScan1172 Bruker, USA Micro-CT system with a voxel size of 6 μm using 1mm Al filter. The voltage was 100 kV and images were recorded using a camera with resolution of 2000×1000 pixel. The sample was partially embedded in a polystyrene block with a hole in the middle and the block was fixed via a silicon gun on to a chuck which placed inside the rotating platform of the Micro-CT. The sample was rotated 360° at a rate of 0.7° per min. The images obtained were reconstructed

and analysed using CTAn 2.2.3 software by Bruker, USA. Each obtained image contained 256 grey values and every voxel in it possessed a grey value between 0 and 255. A segmentation process was then performed in order to assign each voxel a colour either white or black depending on a pre-set threshold value. Any voxel with a grey value greater than the threshold value is considered white, and vice versa. The main principle behind the porosity analysis in CTAn software is that it considers any group of white pixels a solid object, while any group of black pixels surrounded completely by white pixels is considered a pore. Numbers of such pixels can be counted and a porosity measure calculated. For ease of data analysis, a 4 mm section of the foam was analysed in 3D using three values of threshold value, namely 60, 70 and 80 in order to investigate the effect of threshold value on porosity.

3.2.6 Micro-preparation and pore size analysis

Samples were cold mounted using two component epoxy resin Epofix™ with CitoVac vacuum impregnation unit by Struers, Denmark. The samples were left under vacuum for at least 30 minutes before extraction to remove the air bubbles and allow enough time for the resin to impregnate the pores so that good bonding is obtained between the sample and resin. The epoxy is then left to harden.

Samples were then ground until they were a plane using Struers MD-Mezzo 120 disc followed by MD-Largo with a diamond suspension of 9 µm before finishing with Struers chemo-textile cloth using a solution of colloidal silica plus 30% hydrogen peroxide in order to reveal the microstructure. Highly porous samples were ground and polished using successive silicon carbide papers starting with P600 and ending with P1200 as it was noted that their mesostructure cannot withstand diamond-based polishing and grinding pads as they deform drastically and pore closure takes place, turning the foam into a relatively dense sample. One example of a foam with approximately 55.9 % ground for 4 minutes using silicon carbide paper with grit size P600 and another one ground using MD-Mezzo 120 diamond disc are shown in **Figure 35**.

The average pore diameter for the samples sintered as well as their degree of roundness was determined using image analysis software (ImageJ, a public domain Java image processing program, www.imagej.nih.gov) by binarizing the images and measuring pore diameters using

minimum and maximum Feret diameters and then averaging them. For Ti foams which have interconnected pores with no boundaries or cell walls among the pores, spherical particles with size equal to the average particle size of the Ti particles in the image were drawn in order to separate the two pores before estimating their pore size. For better explanation, an SEM image of a Ti foam with a porosity of 63.8 % is shown in **Figure 36 (a)** and can be taken as an example. The pores in the sample are interconnected with no cell walls in between and thus particles were drawn in the image in order to separate the pores; the processed image after drawing of particles is illustrated in **Figure 36 (b)**. After that, each individual pore is selected through the use of wand tracing tool of ImageJ which traces the boundaries of objects with uniform colour (black in the case of pores) and added manually to ROI manager after assigning them with designated numbers (**Figure 36 (c)**) using the cell counter function in ImageJ in order not to count the same pore twice and then Feret diameters are subsequently measured and averaged for all of the pores using the measure function.

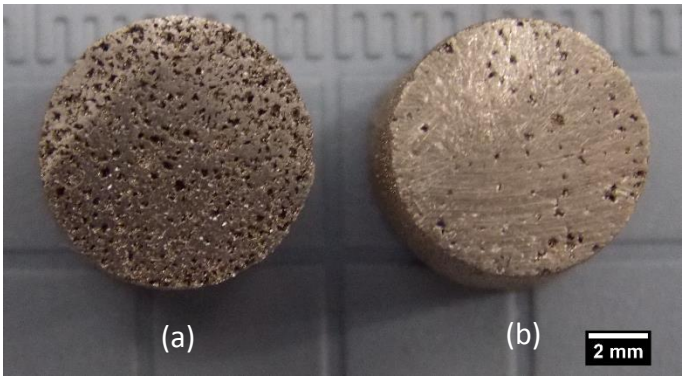

Figure 35. Ti foam ground for 4 minutes using (a) SiC paper with grit size of 600, (b) diamond based grinding disc.

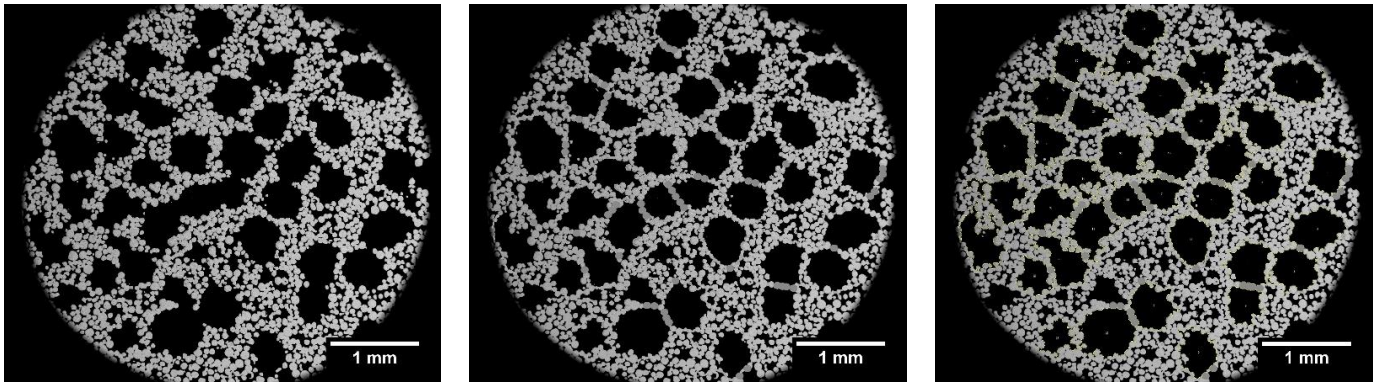

(a) (b) (c)

Figure 36. SEM image of a Ti foam: (a) before processing, (b) after closing the pores with drawn particles, (c) after designating numbers for the pores and measuring them.

3.2.7 Optical microscopy analysis

Optical microscope was used to visualize the mesostructure and microstructure of the samples with low porosity. The analysis was carried out using Nikon Eclipse LV150 microscope under polarized light equipped with a digital camera (shown in **Figure 37**).

Figure 37. Nikon Eclipse LV150 microscope

3.2.8 X-ray diffraction

X-Ray Diffraction (XRD) is a very powerful non-destructive analytical technique used for characterising the structure and phase composition of crystalline materials [183]. The technique is based on passing collimated monochromatic X-rays into the sample (**Figure 38**) which get diffracted by a set of parallel crystal planes and interfere constructively when the path difference between the reflected rays from successive planes is equal to an integer value of the wavelength (λ), satisfying Bragg's Law (shown in equation 12) [184].

$$n\lambda = 2d \sin\theta \qquad (12)$$

where d is the spacing between the parallel planes, θ is the incident angle, λ is the wavelength of the ray and n is an integer.

These diffracted X-rays are collected via special X-ray detector, counted and compared with a standard database for identification.

XRD analysis was carried out in order to analyse the phase composition of the powders used, as well as the samples produced, using a D2 PHASER, Bruker, USA, equipped with CuKα source (λ = 0.154 nm) operated at 30 mA and 40 kV. The samples were scanned in the range 15-80° with a step size of 0.02 and a counting time of 3 s. The obtained XRD spectra were analysed using the ICDD PDF-4+ 2016 database.

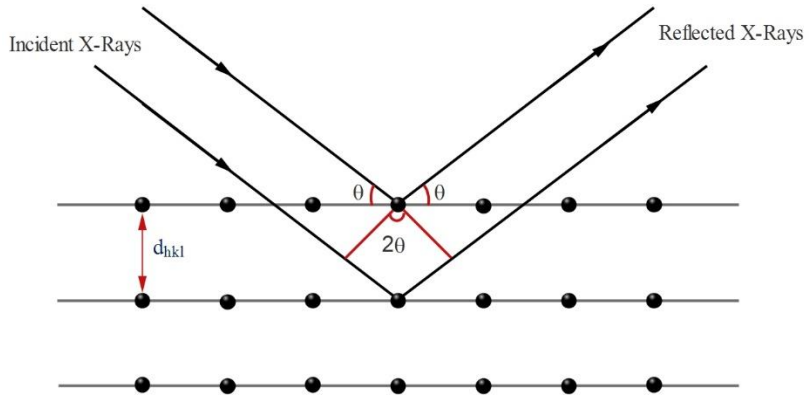

Figure 38. A schematic representation of Bragg's law

3.2.9 Scanning Electron Microscopy

Scanning Electron Microscopy (SEM) was used to characterise the mesostructure of the foams and to analyse the type of failure in the samples after mechanical testing. The analysis was carried out using Inspect F (FEI, Hillsboro, OR, USA) with a voltage of 20 kV and spot size of 3 after coating the surface of the samples with a thin layer of conductive carbon in order to avoid charging or electron build up in the mounting resin. The SEM is equipped with Energy Dispersive Spectroscopy Systems (EDS, Oxford Instruments, UK). The distribution of elements in the specimens were mapped using EDS element coloured mapping with a frame count of 20 and pixel dwell time of 20 µs. For quantitative analysis, peak calibration was performed using a cobalt standard.

3.2.10 X-Ray Fluorescence (XRF)

XRF is a non-destructive analytical technique for determining and quantifying the chemical composition of the samples and it involves passing a collimated and concentrated X-ray beam through the sample causing electron expulsion from the lower energy orbitals in the atoms and creation of holes or vacancies which destabilises the atoms [185]. The atoms then de-excite back by filling the created vacancy with electrons from a higher energy orbital (shown in **Figure 39**) and the process is accompanied by the emission of fluorescence radiations with energy equal to the energy difference between the levels of the transition and characteristic to a particular material [186, 187]. The intensity of these fluorescent rays are then measured using X-ray spectrometer and compared with the materials database to find out the chemical elements in the sample and their concentration.

X-ray Fluorescence spectrometer (XRF) was used in order to analyse the chemical composition of the surface of the samples. The system used was Zetium XRF spectrometer from PANalytical, Netherlands. The samples were placed in a special steel cup that has aperture with a diameter of 6 mm and analysed under vacuum three times before averaging them. The XRF spectra were analysed and the total element concentrations were obtained using SuperQ software, supplied with the instruments.

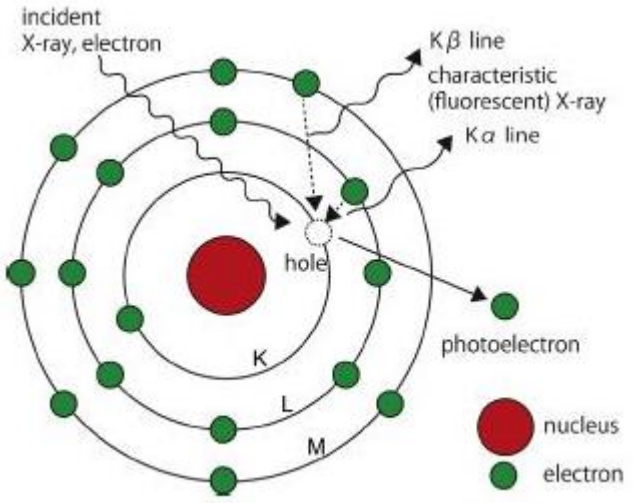

Figure 39. A schematic of the generation process of fluorescence X-rays during atom irradiation [188].

3.2.11 Chemical analyses

Chemical analysis for the samples was carried out in order to measure the extent of contamination during thermal debinding and sintering as this can noticeably affect the mechanical properties of the foams produced, particularly oxygen and nitrogen. Chlorine content was also assessed as a means to check the removal of the KCl. The analysis was performed using LECO melt extraction system by AMG Analytical, UK. The test involves heating the sample in ceramic crucibles and analysing the gases released as well as the sample by thermal conductivity spectroscopy and IR Spectroscopy. The error of the analysis is less than 1%.

3.2.12 Compression testing of samples and failure analysis

Samples with a height of around 12.4 ± 0.7 mm were tested under compression loading at a strain rate of 0.001 s^{-1} and a maximum load of 40 kN according to ISO 13314 using a Zwick Z50 testing machine (Zwick Roell, Ulm, Germany). A compliance test was performed before testing the samples in order to account for any deformation in the machine (non-sample displacement in the testing fixture [189]). The yield strength for the samples was estimated using the 0.2% offset method.

Failure analysis and distribution of strains in some porous samples were carried out using Digital Image Correlation (DIC). DIC is a non-contact optical technique for measuring deformation on the surfaces of materials by tracking the movements of physical points or speckles during deformation relative to their original positions in a reference image using high speed cameras [190, 191]. The accuracy and success of such technique in estimating deformation is reliant on several parameters including the size of the points tracked and their density on the surface of the sample as well as the calibration process and subset and step size used during processing. The speckles or points to be tracked are typically black dots spray-painted on the surface of the sample before painting it with a matte white paint. This helps making the process of detecting the black speckles easier due to the high degree of contrast between these two colours. The high speed cameras are fixed on a stand or tripod which placed within an appropriate distance and points towards the sample with a stereo angle typically ranging from 15-25°depending on the length of the lenses used [192]. Before carrying out the test and acquiring the images during deformation, a calibration process is performed during which a set of intrinsic and extrinsic parameters are defined, such as focal length, sensor centre and dimensional displacements between the cameras, etc.[193].

The DIC test for the porous samples was carried out in order to analyse the failure mechanism and try to visualise the extent of deformation that occurs in the samples during compression. The samples were firstly painted with white paint from DecoArt, Stanford, USA and then black speckled uniformly using a dual-action, siphon feed airbrush. Great difficulty was encountered during the white painting stage due to the porous nature of the samples and their high surface area, and the best results were achieved through the use of a high viscosity paint (20% solvent and 80% paint), less viscous paints either flowed off or were sucked into the pores of the sample. Samples with higher amount of porosity were more challenging to paint as the paint did not have enough time to settle on the surface due to increased permeability, as shown in **Figure 40**, where less porous samples get fully impregnated with the white paint, unlike high porosity samples.

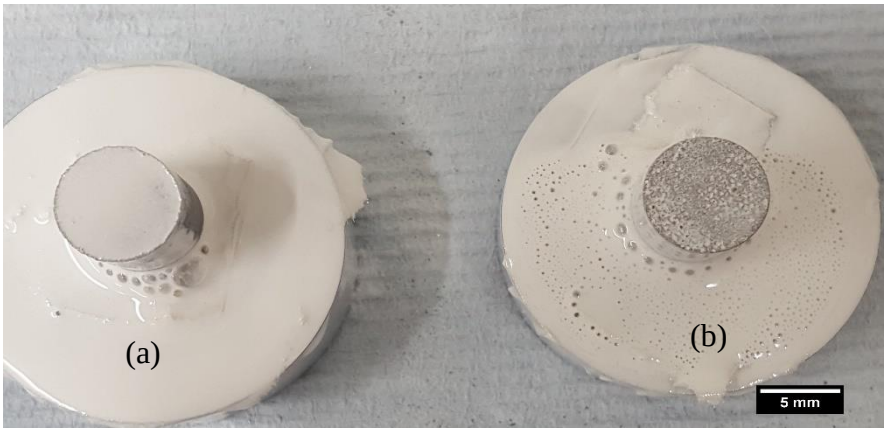

Figure 40. White painting of (a) porous sample with 20% porosity, (b) porous sample with 62% porosity.

Specially-developed platens had to be used due to the small size of the samples and their poor visibility in the cameras when normal platens are used. The platens used were composed of two hardened steel screws with their heads ground and polished up to 2000 paper. The small platens were screwed into the universal testing machine and samples were placed on them as demonstrated in **Figure 41**.

The software used for image analysis was LA Vision with a subset size of 17 and step size of 5. The subset size specifies the part of the image which is used to monitor the displacement between the taken images, while step size limits the spacing between points that are analysed during correlation [192].

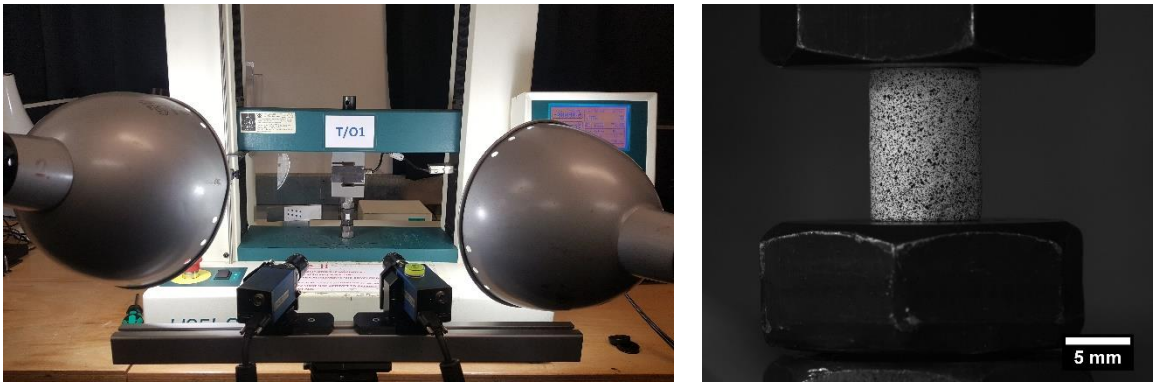

(a) (b)

Figure 41. (a) DIC test set up, (b) porous sample in between two hardened steel screws.

3.3 Preparation of multi-layered radially graded Ti foams and biomedical staples

The preparation of multi-layered, radially-graded porous Ti was attempted by injecting two different feedstocks into the same mould at different intervals. The first feedstock was prepared using the coarse Ti powder with a solid content of 58%vol and 0% KCl, while the second feedstock had 58% solid content of which 60% KCl. It should be noted that the solid content refers to the volume percentage of the Ti powder and the space holder added and mixed with the binders to form a feedstock. The KCl used was cubic with a mean particle size of 348 μm. The process was designed so that the samples have three porous layers, two microporous layers with one macroporous layer positioned at the centre of the samples. Another attempt was carried out by injecting one microporous layer with one macroporous layer. The main source of pores for the microporous layers are the micropores that result from partial bonding and incomplete neck formation among the Ti particles during sintering. Shear testing for the triple porous layers was performed using two specially developed holders that enable holding the samples from the microporous layers, thus ensuring much of the shearing load is localised at the macroporous layer. The shear testing assembly is shown in **Figure 42**.

In order investigate the suitability of the process for complex parts, an attempt was made to produce porous surgical staples by injecting a feedstock with 35%vol KCl into a barbed staple mould and the injected parts were then debound and sintered. The KCl used for the medical staples was cubic with a mean particle size of 348 μm. For comparison, some medical staples were injection moulded using a feedstock with similar solid loading, but without space holder. Another attempt was made to deposit a porous layer onto the surface of a femoral stem for a hip implant in order to investigate the suitability of the developed technique to process a potential biomedical part.

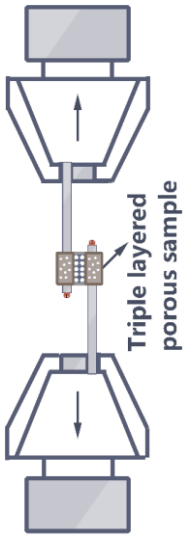

Figure 42. Shear testing assembly for porous Ti with gradient porosity.

3.4 Ti foams as a potential material for biomedical applications

The three most popular materials used for biomedical implants these days are Ti-6Al-4V, Co-Cr-Mo and 316 stainless steel. However, each of these alloys contains some elements which are reportedly cytotoxic. For example, Shettlemore et al studied the toxicity of these three alloys and found that the most toxic was Co-Cr-Mo followed by 316 stainless steel, while Ti-6Al-4V is minimally toxic, which was attributed to the high toxicity of Cr, Ni and Co elements in the former alloys [194]. Another study however reported that Ti-6Al-4V is synergistically toxic due to the occurrence of synergistic interaction between the titanium, aluminum, and vanadium [195]. Thus, in this study commercially pure Ti was chosen. The excellent corrosion resistance, good biocompatibility and low cytotoxicity of pure titanium makes it a good candidate for biomedical hard tissue implants. However, there are two main issues associated with the use of such a biomaterial that are yet to be addressed. The first one is the stress shielding problem that arises from the differences between the elastic moduli of the natural bone and Ti, which leads to bone resorption around the implant and is one of the main causes of failure in implants. The second problem is the bioinertness of Ti which results in poor bone cell adhesion to the implant compared to bioactive materials such as

hydroxyapatite or bio-glasses [196]. Such bioactive materials form spontaneously a layer of bonelike apatite to promote chemical integration to the bone tissue [196, 197]. One way of addressing the first problem is by incorporating intentionally-induced pores into the material structure to produce porous Ti with adjustable elastic modulus so that its properties match the desired mechanical properties of different implants for different parts of the body. The presence of pores in the structure can additionally help promoting bone ingrowth and cell attachment thereby creating a better mechanical fixation to the surrounding tissue [198, 199].

The process of producing foams with different porosity and pore shapes to remedy the first issue associated with the use of Ti has already been addressed in the previous sections through the addition of different amount of space holders with different particle morphologies resulting in porous bioinspired structure that replicates the natural structure of the bone for better mechanical fixation and reduced stress shielding. However, the second problem still has not been addressed as the Ti foams produced will be mainly dependent on mechanical fixation to bond into the surrounding tissue without chemical integration. Hence, two ways of addressing the second issue were explored.

1- The addition of hydroxyapatite into the Ti foams.
2- The modification of the surface of foams via Plasma Electrolytic Oxidation

3.4.1 The addition of hydroxyapatite into the Ti foams

The addition of Hydroxyapatite (HA) was examined by adding HA powder to the mixture of the Ti and space holder powders during feedstock preparation stage. Two types of HA powders from two different suppliers were used. The first HA powder was micro-sized powder supplied by Plasma Biotal, UK, while the second HA powder was nano-sized powder supplied by Sigma-Aldrich, Germany. The volume percentage of HA added to the mixture was 7%vol. The space holder used was spherical in shape (D_{50}=366 µm) and constituted 52%vol. of the solid content. In the case of the nano-sized HA, powder was initially added to the Ti powder with four cylindrically-shaped dispersion media and mixed without a binder in order to break the agglomerates using a high speed centrifugal mixer Speedmixer 800 FZ Synergy Devices Ltd., UK for 4 minutes at a speed of 1900 rpm and then a multi system polymeric binder and KCl as a space holder were added to the mixture and mixed in a similar

manner to our previous experiments. The composite feedstock was then pelleted and extruded twice using a low pressure injection moulder in order to homogenize the feedstock before injecting cylindrical samples. After that, water debinding was performed before sintering the samples using a vacuum furnace Centorr, USA under flow of argon at a temperature of 1320°C for 2h.

3.4.2 The modification of the surface of foams via plasma electrolytic oxidation

There are several techniques to develop biologically active porous ceramic coatings on Ti surfaces such as Physical Vapour Deposition (PVD) [200], electrodeposition [201], anodization [202] as well as Plasma Electrolytic Oxidation (PEO) [203]. Among those, PEO is preferred due to the non-line-of-sight nature, low cost, high productivity, environmental friendliness, as well as short treatment times required to produce thick ceramic coatings with high adhesion strength, wear and corrosion resistances [203-206].

Plasma Electrolytic Oxidation (PEO) is an advanced anodization technique that involves the growth of anodic oxides on Ti electrode in an aqueous electrolyte at potentials high enough to cause electrical discharges on the Ti surface forming a relatively thick and porous ceramic coating. The process offers the possibility of adjusting the chemical composition of the coating by adding different salts to the electrolyte including phosphates, sulfates, silicates and aluminates [206-209]. In addition, the PEO treatment can be carried out in different current and potential modes, including AC, DC, pulsed and bipolar electrical regimes [210]. However, DC mode is the simplest and the most convenient to study fundamental aspects of the coating process [211].

The possibility of coating porous Ti samples with PEO was explored using three groups of porous Ti samples with different amount of porosity, namely 7%, 20%, and 62% with average pore size of 17 μm, 57 μm and 348 μm respectively. The samples had diameter of 8.84±0.30 mm and height of 12.35±0.46 mm and were ultrasonically cleaned in acetone for 10 min and dried after tap threading holes in them. The threaded samples were then fastened onto a Ti bar with external insulation and connected to the positive output of a power supply, while the negative output of the power supply was connected into a water cooled steel tank (**Figure 43**). The electrolytic solution was prepared by gradually dissolving of 14 g L^{-1} reagent grade

disodium phosphate (Na_2HPO_4) in distilled water. Electrolyte stability was assessed based on the values of pH and conductivity before and after experiments, which were found to vary insignificantly, from 9.6 to 9.8 and from 10.4 to 8.1 mS cm^{-1}, respectively. The cyclic voltammetry studies were performed in DC mode by sweeping the potential up to a maximum value of 500 V at scan rates of 2.12 and 4.22 V s^{-1}. After that the samples were cleaned with acetone and distilled water in an ultrasonic bath for 4 minutes before drying them at about 85 °C for 5 min. For cross-sectional analysis, the samples were cut in half, cleaned and cold mounted and then ground using successive grades of SiC grinding papers followed by polishing up to 1 µm with a diamond suspension and Chemo-textile cloth. Then, the samples were sputter-coated with carbon to avoid charging during SEM characterisation. The PEO treated samples were then imaged and analysed using an Inspect F, Scanning Electron Microscope (SEM; FEI, USA) equipped with Energy Dispersive X-ray Spectroscopy (EDS) attachment. In addition, X-Ray Fluorescence (XRF) as well as X-Ray Diffraction (XRD) analyses were utilized in examining the elemental and phase composition of the sample surfaces. The thickness of the oxide layers developed on the surface was measured using Image J image analysis software.

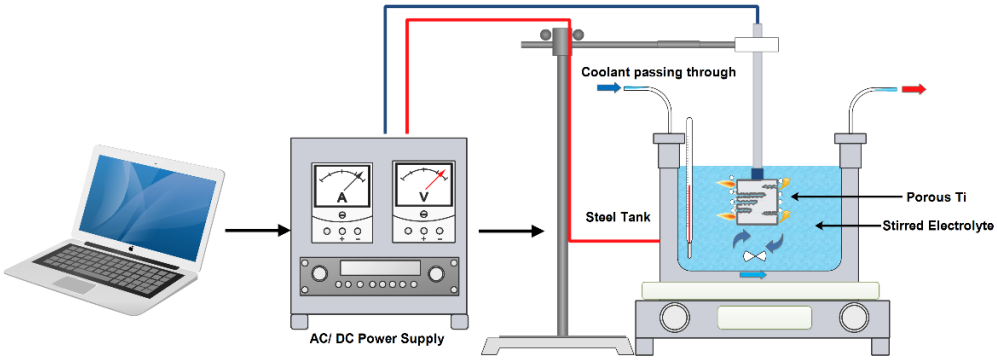

Figure 43. A schematic of the PEO process with an image of the PEO process during coating of porous Ti

3.5 Cell culture

To evaluate the suitability of the fabricated Ti-HA composite foam to support bone formation, in vitro biological characterisation was performed on two different types of titanium foam scaffolds with and without HA. MLO-A5 osteoblastic mouse cells were seeded

on the samples. Cells were cultured at 37°C and 5% CO_2 humid environment in culture medium containing Minimal Essential Medium-α (α-MEM, Lonza, Castleford, UK). It was supplemented with 10% Foetal Bovine Serum (FBS, Labtech,UK), 1% L-Glutamine solution (0.2 M), 1% Antibiotic solution containing penicillin (10,000 U/mL) and streptomycin (10 mg/mL), Ascorbic Acid-2-Phosphate (AA, 0.2 mM), and β-glycerophosphate (β-GP, 5 mM) (Sigma Aldrich,UK). Culture media was changed every 2-3 days during the cell culture period. Prior to cell seeding, samples were autoclaved for 30 minutes at 121°C, and then submerged in a culture medium with 30 minutes incubation. MLO-A5 at passage 48 were seeded with 3,000 cells in 25µl expansion media per scaffold a 24- well plate. To allow cell attachment scaffolds were incubated for 45 minutes. Then 2 ml of culture media was added to each sample and incubated overnight. Negative controls without cells were also used.

3.6 Metabolic activity

The metabolic activity of cells was assessed at 1, 4, 7, 14, 21 and 28 days after seeding using Resazurin reduction (RR) assay. 1 mM resazurin sodium salt (Sigma Aldrich,UK) in diH_2O was diluted (10 vol%) in a culture mediam. 2 ml of RR was added to each sample with 4 hours incubation. Aluminium foil was used to wrap the well plates during the incubation because of the sensitivity of RR to light. The blue non- fluorescent resazurin sodium salt was reduced by the metabolic activity of cells to form pink fluorescent resorufin after the incubation period. In a transparent 96-well plate 200 µL of the reduced solution was transferred and the absorbance read with a plate reader (Tecan infinite 200-pro) at λex : 540 nm and λem : 590 nm. samples were washed twice with PBS then replaced with fresh media.

3.7 Calcium staining

Alizarin Red S Stain Assay (ARS) is a qualitative method used to detect extracellular calcium deposition after 28 days of cell culture. 1% w/v of Alizarin Red S (Sigma Aldrich, UK) powder in deionized water (dH2O) was used to stain seeded scaffolds for 30 minutes under gentle orbital shaking at 100 rpm. Before staining, samples were fixed with 3.7% formaldehyde and washed three times. 5% v/v perchloric acid in distilled water was used to destain samples for 20 minutes with gentle orbital shaking. 150 µL of destaining solution

from each well was added to a clear 96 well plate in triplicate. The absorbance was measured in a plate reader at 405 nm.

3.8 Collagen staining

Collagen deposition within the scaffolds was assayed using Sirus Red Stain. After performing the calcium assay, all scaffolds were washed with dH2O three times to remove any of the ARS destain. To prepare the SRS, direct red 80 was dissolved in saturated picric acid (1% w/v) and filtered to 0.2 μm to remove undissolved particles. 2 ml of SRS working solution was added to each sample and left on orbital shaking at 100 rpm for at least 18 hours. After that, the SRS was removed and washed off with dH2O until no trace of the SRS was present in the washes. The scaffolds were de-stained with 2ml of 0.2M NaOH:methanol (1:1) on an orbital shaker for 20 minutes at 100rpm. In triplicate 150μl of solution from each well plate was added to a clear 96 well plate and absorption was measured at 405nm in a plate reader.

4 Comparison between the developed and commercial feedstocks

The first step towards successfully producing Ti foams by metal injection moulding is the development of a homogenised feedstock (without space holder) that can be easily injection moulded into the desired shapes with a minimum amount of energy and without the occurrence of powder-binder separation. This is crucial before moving into the next step of introducing a space holder material into the feedstock and developing Ti foams. It is also important to point out that the main current hurdles which negatively impact the competitiveness of the MIM process in processing Ti parts are the cost of the fine Ti powder, the high shrinkage in the produced parts and the high interstitial content. These aforementioned drawbacks could be potentially solved through the use of relatively coarse Ti powder as the cost is reduced, it results in more micropores that are potentially useful for biomedical applications and it has less surface area compared to the fine Ti powder and thus less prone to contamination. Therefore, relatively coarse Ti powder with a mean particle size of 75 µm was chosen in our initial experiments. However, before using such a powder with a mean particle size more than three times higher than that preferred for MIM powders [212], it needs to be compared in terms of performance against a benchmark or a commercial feedstock in order to assess its suitability for the production of Ti foams. The commercial feedstock which was chosen for comparison purposes was PolyMIM Grade 2 supplied by PolyMIM® Germany, which is produced using Ti powder grade 2. The feedstock developed by the current study had a 58 vol % solid content and was prepared using the relatively coarse Ti powder with a multi component polymeric binder composed of 70 vol % PEG1500, 25 vol % PMMA and 5 vol % stearic acid. It should be noted that PEG is commercially available in different molecular weights and detailed discussion of it and its impact on the injection process is reported in **section 5.1.** The two feedstocks were compared in terms of melting behaviour, viscosity as well as the percentage of porosity in the sintered samples.

4.1 DSC comparison

DSC analysis was carried out in order to identify the peak melting temperatures of both commercial and prepared feedstocks and analyse their melting behaviour. The outcome of such analysis can be beneficial in facilitating the process of choosing the optimum extrusion and injection temperatures for the feedstocks prepared. Several samples of each feedstock were heated up to a maximum temperature of 200 °C at a rate of 10 °C/min. The results of the DSC analyses for both of the commercial and developed feedstocks are plotted in **Figure 44**.

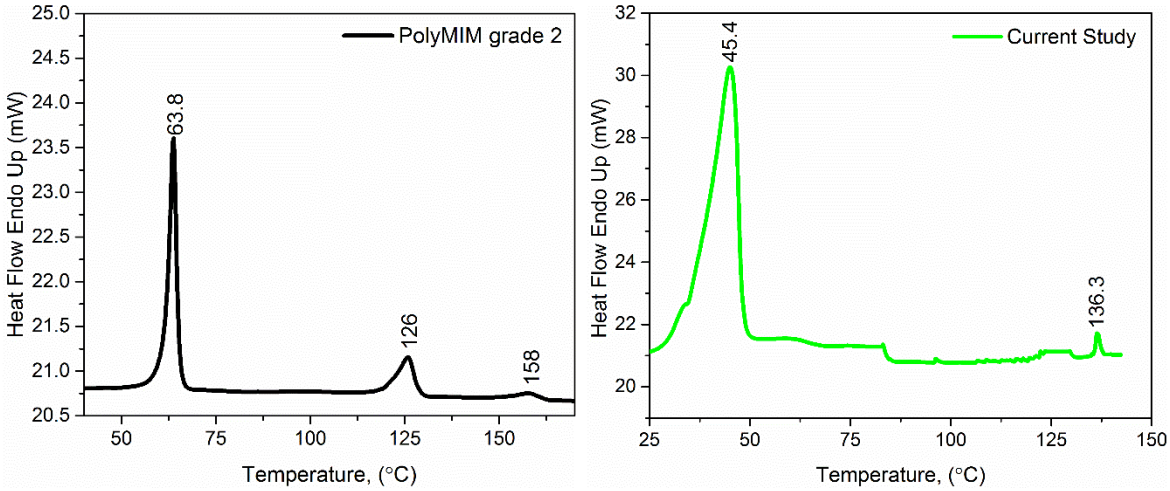

(a) (b)

Figure 44. DSC thermograms for the (a) commercial feedstock and (b) current study feedstock.

It was found that the first part of the binder for the commercial feedstock had a higher peak melting temperature of about 64 °C compared to that used in the current study (PEG 1500), which was approximately 45 °C, whereas the second part of the binder for commercial feedstock had a lower peak melting temperature than that of the current feedstock (about 126 °C), which was about 136 °C. A small third peak was also noted at about 158 °C in the commercial feedstock, which might indicate that there is a third polymeric component. Auzène et al [213] investigated the use of different commercial feedstocks including 316L stainless steel PolyMIM and reported that the feedstock had a similar infrared spectrum to polypropylene, though they did not give their findings in detail. One might argue that the second part of the binder for commercial feedstock is actually high density polyethylene, as

the peak melting temperature lies in the peak melting temperature range for high density polyethylene, which is about 125.8–138 °C. In addition, the small third peak could correspond to the peak melting temperature of the isotactic polypropylene which ranges from 160 to 166 °C [214]. In order to investigate this further, an FTIR test (Fourier Transform Infrared Spectroscopy) was carried out in the wavelength range from 4000 to 400 cm^{-1} with a sampling number of 16 times. The result of the test is shown in **Figure 45**.

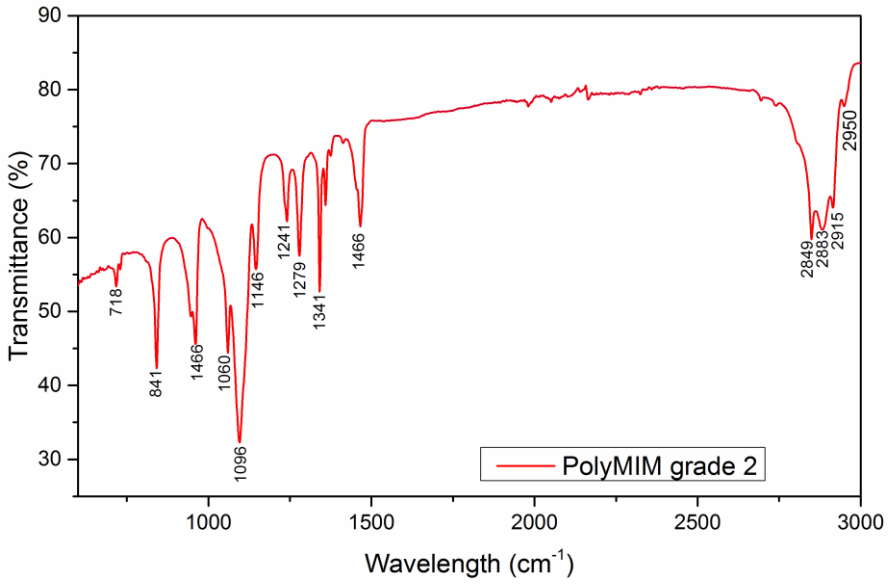

Figure 45. FTIR spectrum of the commercial feedstock.

The obtained data were compared with the results in the literature, and it was found that several peaks coincide with the high density polyethylene peaks reported by Kumar and Singh, as shown in **Table 6** [215] from work on the recovery of hydrocarbons from high density polyethylene waste. Other peaks could not be explained due to the complexity of the binder system used, which makes the analysis process more challenging.

Table 6. FTIR assignments of the commercial feedstock

Wavenumber (cm^{-1})	**Type of Vibration**
2950/2915	C-H Stretching
2883	CH_3 and CH_2 Stretching
2849	C-H Stretching
718	CH_2 Rocking (Methylene rocking)
1466	C–H scissoring (Methylene scissoring) [180]

4.2 Rheological analysis results

The viscosity of the feedstocks was measured in order to assess their sensitivity to temperature and shear rate as well as to measure the yield shear stress for both. It should be noted that the commercial feedstock could not be tested at a temperature below 170 °C, as the capillary die of the rheometer became clogged below this temperature. This is expected, as it is recommended in the specification sheet of the PolyMIM feedstock to inject the feedstock at a minimum temperature of 178 °C, even though the peak melting temperature of the highest part of the binder of the commercial feedstock was found to be 158 °C according to the DSC results. This might be due to the high percentage of solid loading in the commercial feedstock, which seems to affect the flow of the feedstock with temperature under shear in the capillary die. Hence, the viscosity of commercial feedstock was tested at three different temperatures, namely 170, 185 and 195 °C. The feedstock prepared in this study with the relatively coarse Ti powder was tested at 120, 135 and 150 °C due to both the lower peak melting temperature of the highest viscosity part of the binder, and its reduced amount compared to the second part of the binder PEG. Rheograms of both commercial and current feedstocks are shown in **Figure 46.**

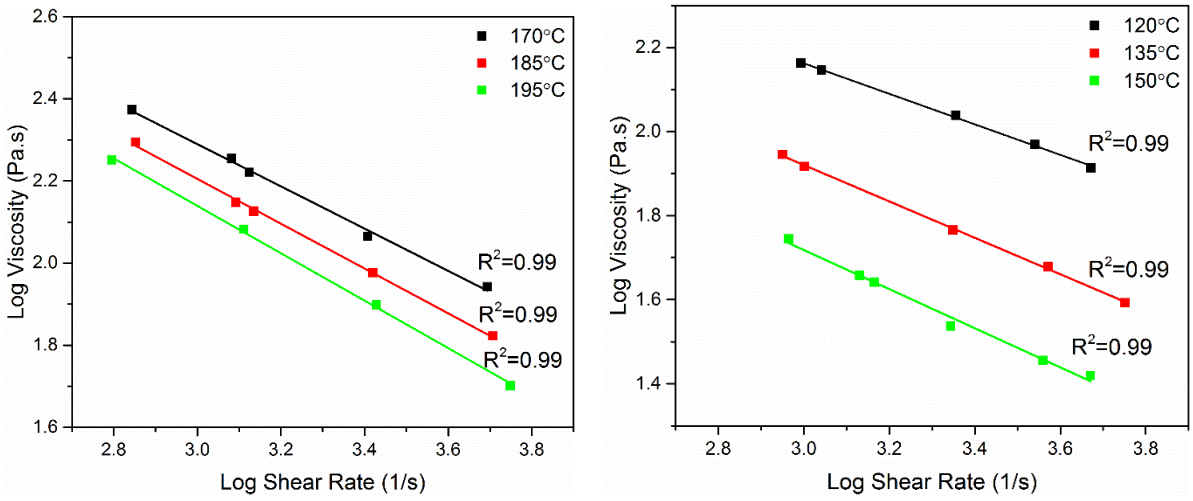

(a) (b)

Figure 46. Results of the viscosity measurements for (a) commercial feedstock PolyMIM Grade 2; (b) current study feedstock made by relatively coarse Ti powder with a solid loading of 58% and binder content of 42% of which 70 vol % PEG, 25 vol % PMMA and 5 vol % stearic acid.

It can be seen from **Figure 46** that the viscosity of the commercial feedstock is much higher than that of the feedstock used in the current study even accounting for the higher test temperature, which means that higher injection and tool temperatures are needed in order to successfully inject the samples into the desired shapes. Both of the feedstocks showed some shear thinning behavior, which is desired in the MIM industry, especially for intricate parts. The yield shear stresses as well as the flow behavior indices for both feedstocks are summarized in **Table 7**. Although the commercial feedstock was tested at much higher temperatures (as required by its higher viscosity), it was found that it has a much higher yield stress than the current feedstock and, also a lower flow behavior index.

Table 7. Flow behavior index and yield stresses for commercial and current feedstocks

Feedstock	Temperature (°C)	Yield stress (kPa)	*n*
Commercial	170	135	0.49
	185	118	0.45
	195	107	0.42
Current Study	120	79	0.63
	135	42	0.56
	150	35	0.53

4.3 Preparation and characterisation of green and sintered samples

A vertical plunger-type injection moulder was used to injection mould small cylindrical parts of both feedstocks at a pressure of 45 MPa. The commercial feedstock was injection moulded at a temperature of 185 °C into small cylindrical parts with a diameter of 10 mm and a height of approximately 13.50 mm. The mould was heated to 60 °C in order to facilitate the process of filling the cavity of the mould. It should be noted that great difficulty was encountered during moulding at a lower mould temperature, where the feedstock either freezes before reaching the mould cavity or partially fills it before freezing, resulting in an incomplete part. In contrast, the feedstock prepared by this study was injection moulded using the vertical plunger-type injection moulder at a temperature of 150 °C into cylindrical samples without the need to heat the mould. Some green samples of both feedstocks were broken and their surfaces were characterized using Scanning Electron Microscopy (SEM). The surface of as-broken samples of injected but not debound samples from both feedstocks are shown in **Figure 47**.

It can be observed that the Ti powder used in the commercial feedstock is spherical and therefore there is a high probability that it is a gas atomized powder with, as a result, a good packing density. The particle size for the Ti powder used was determined by estimating the size of spheres with equivalent dimensions to those of Ti particles, which were observed in six SEM images for the commercial feedstock [16]. The analysis was carried out using image analysis software (Image J, a public domain Java image processing program, www.imagej.nih.gov) and the Ti particle size was found to range from 12-45 μm, with average particle size of about 23 μm. This is not far from the recommended size of the Ti powder for MIM, which is about 20 μm. It was also noted that the Ti particles were coated with a layer of what is believed to be polyethylene, referring to the large amount of the second part of the binder in the commercial feedstock. In comparison, the relatively coarse Ti particles used in the current study were surrounded by the binder, consisting of PEG with some PMMA.

Several moulded parts were then water debound at a temperature of 50 °C in a water tank filled with distilled water for 35 h. Next, the parts were taken out of the tank and dried for 2 h at 100 °C in order to remove the moisture. After that, the samples were sintered at 1320 °C for 2 h under the flow of argon. Images of the sintered parts from both feedstocks are shown in **Figure 48.** Note that these binders without space holder produce nominally dense samples, not foams.

It was noted that samples made with the commercial feedstock using the vertical plunger type injection moulder had some cracks on the surface of the samples. These cracks might be due to the insufficient injection and backing pressure of the injection moulder used to mould the commercial feedstock, as it had a much higher yield shear stress than the feedstock developed here, and thus requires being processed and moulded at much higher temperature and pressure. Hence, another batch of samples was made to investigate this further using an Arburg 320 all-rounder at a pressure of 1400 bar and a temperature of 195°C with a dosage volume of 10 cm^3. The samples prepared were cylindrical in shape. After water debinding of the samples, they were sintered under the same conditions as the previous experiments. It was observed by visual examination of the samples that there were also small cracks, but less

apparent than the ones seen on samples made using the low pressure injection moulder. Some of the sintered samples are shown in **Figure 49.**

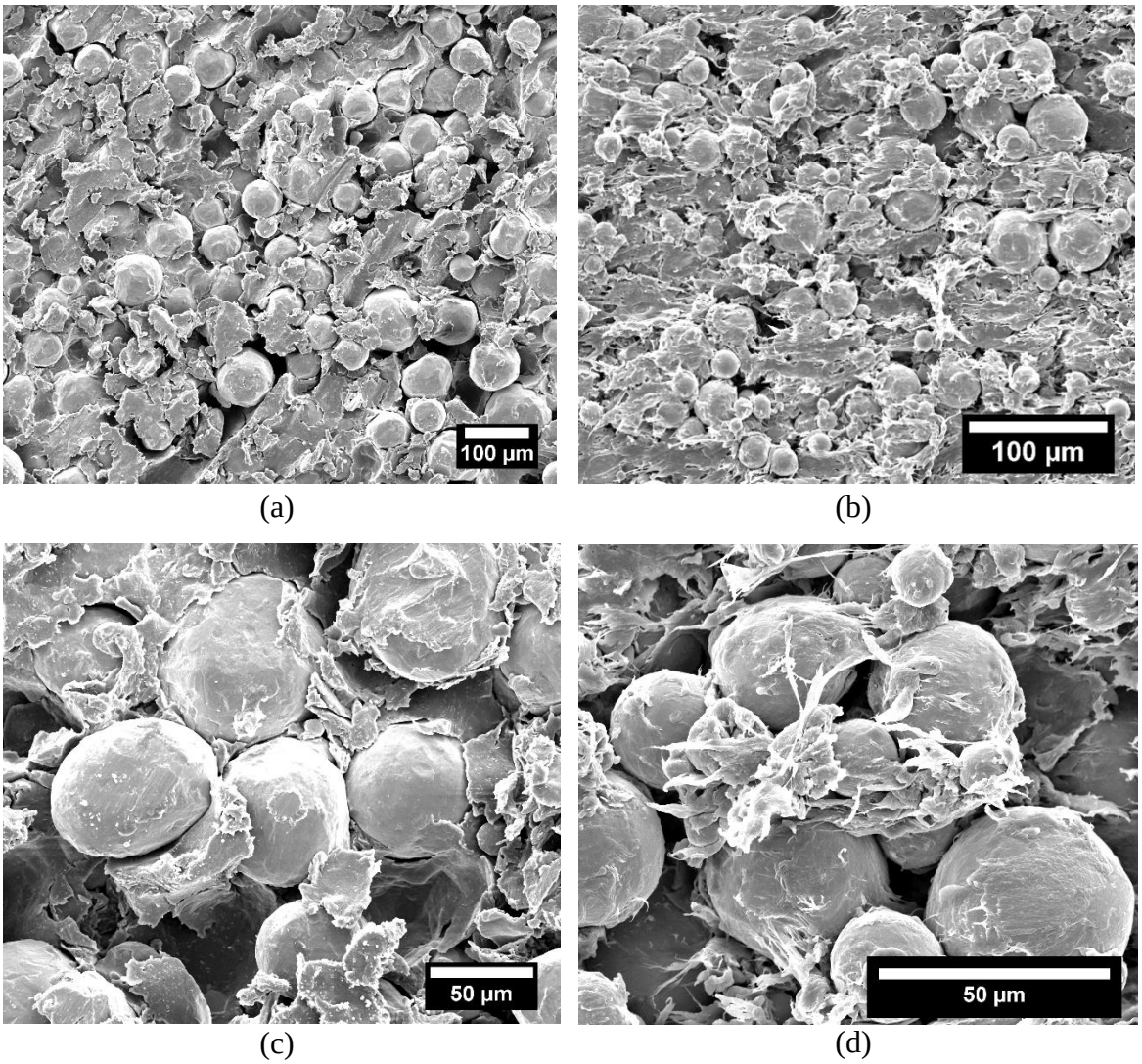

(a) (b)

(c) (d)

Figure 47. SEM images of the surface of as-broken samples of feedstocks from: (a) current study made by relatively coarse Ti powder with a solid loading of 58% and binder content of 42% of which 70 vol % was PEG, 25 vol % was PMMA and was 5 vol % stearic acid at low magnification; (b) commercial feedstock at low magnification; (c) current study at high magnification; (d) commercial at high magnification.

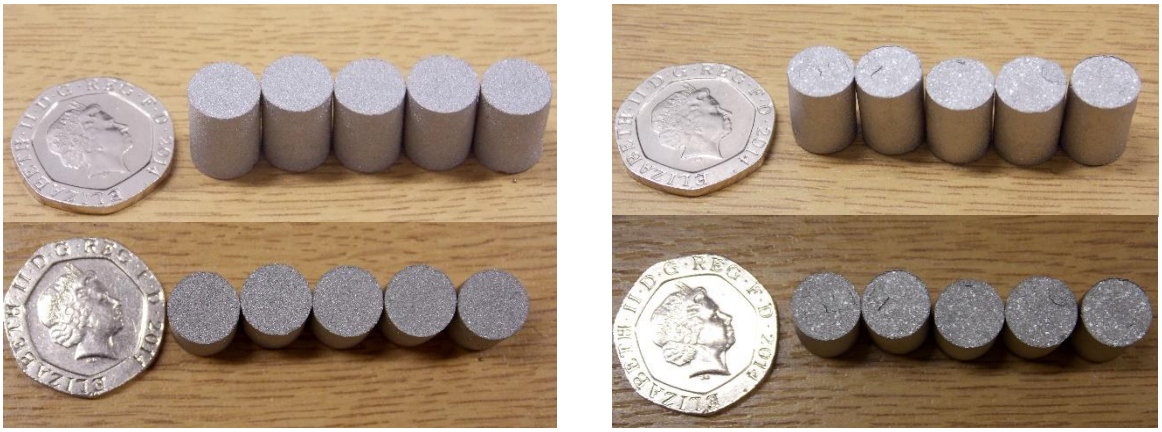

(a) (b)

Figure 48. (a) side and top views of the sintered samples made by coarse powder using current study feedstock; (b) side and top views of the sintered samples made by commercial feedstock PolyMIM grade 2.

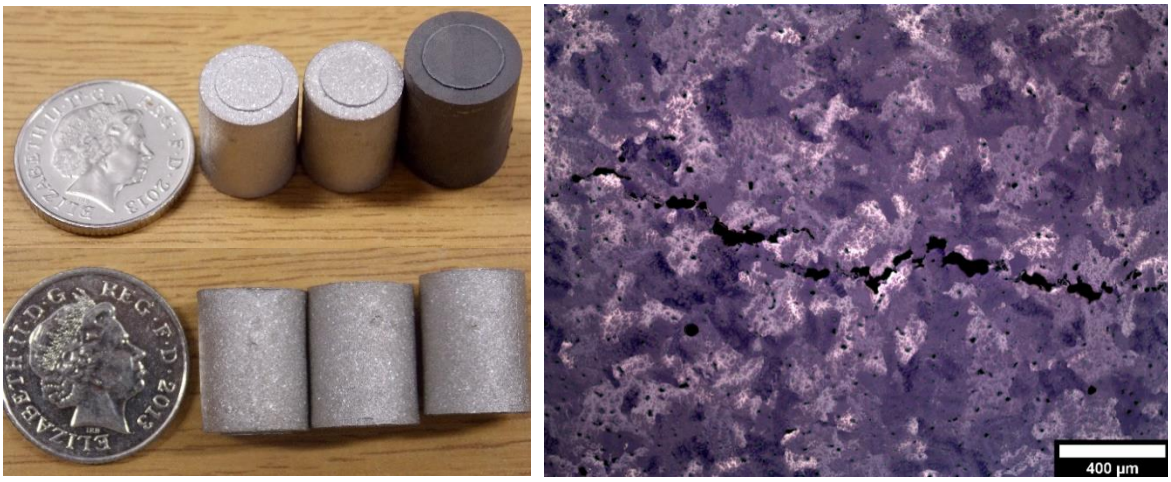

(a) (b)

Figure 49. (a) Side and top view of sintered and green samples of commercial feedstock produced by Arburg 320 all-rounder at a pressure of 1400 bar and a temperature of 195°C with a dosage volume of 10 cm^3 ; (b) lateral view of a crack observed in the structure of the sample.

It was also noted that the majority of the samples had small crater-like defects at the surface and some blistering. These craters are believed to be formed due to the thermal decomposition and diffusion of the high viscosity part of the binder from the inside of the sample through the surface during the initial stages of the sintering cycle, leaving a small

volcano-like blister with a crater-like features. The final densities of the samples were measured using a helium pycnometer with a filling pressure of 10 psi (0.07 MPa) over 10 cycles and the volume shrinkages after debinding and sintering of the samples were monitored by measuring the dimensions of the samples using a Vernier Caliper with a resolution of 0.01 mm (by the average of at least 4 readings). The relative densities and volume shrinkages of the samples after sintering are shown in **Figure 50**.

It can be seen that samples made using current study feedstock with the coarse Ti powder had a lower relative density than those made from commercial feedstock PolyMIM with the fine powder, and consequently also had a higher porosity. This can be attributed to the size of the titanium powder used in this study compared to the commercial feedstock, where finer particles sinter at a much higher rate, resulting in greater growth of the necks and spheroidization of pores compared to coarser particles. However, the volume shrinkage after sintering for the samples made by commercial feedstock was found to be much greater than that of the samples made by the current study, where samples processed with the coarse powder shrank 20.7% in volume, while samples made of commercial feedstock shrank 32%–33% in volume. Owing to the fact that the sintering process is mainly driven by the surface free energy of the powder, the higher the surface area of the powder, the greater the rate of sintering, resulting in more volume shrinkage in the samples [216].

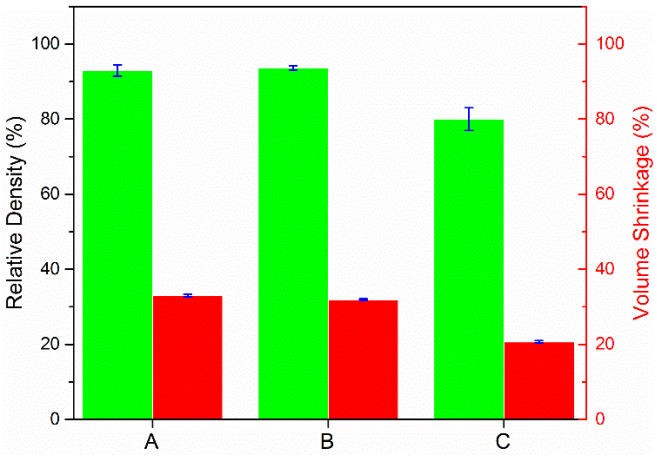

Figure 50. Relative densities and volume shrinkages after sintering for: (A) samples processed using commercial feedstock PolyMIM with the fine powder by plunger injection moulding; (B) samples processed using commercial feedstock PolyMIM with the fine powder by Arburg 320; (C) samples processed using current study feedstock with the coarse powder by plunger injection moulding.

Although the solid content for the commercial feedstock (which can have an impact on the volume shrinkage) is not known, generally the solid content for such fine powders in commercial feedstocks ranges from 60%–65%. It can also be noticed that the standard deviation for the volume shrinkage after sintering for the samples made by the commercial feedstock using the Arburg injection moulder was the lowest (about 0.18 compared to the samples made by the current study feedstock using the vertical plunger-type injection moulder of about 0.31). In comparison, the standard deviation for samples made by commercial feedstock using the vertical plunger-type injection moulder was 0.35. These differences in shrinkage and standard deviation between samples made by the vertical plunger-type injection moulder and the ones produced by the Arburg 320 could be a consequence of the high backing and injection pressure used in the Arburg compared to the vertical plunger-type injection moulder; the pressure used in the Arburg was more than triple that used in the vertical plunger-type injection moulder.

Samples were analysed for contamination by using a LECO melt extraction system by AMG Analytical, Rotherham. The extent of interstitial elements contamination in the sintered samples is summarized in **Table 8**.

Table 8. Chemical analysis results of sintered samples.

Contaminant	Sintered Sample from Commercial Feedstock (wt %)	Sintered Sample in the Current Study (wt %)	Ti Powder (wt %)	Error in each analysis
C	0.044	0.079	0.006	±0.050
O	0.273	0.277	0.093	±0.1
N	0.033	0.023	0.010	±0.050

It can be observed that the carbon concentration in the parts produced by the commercial feedstock is much lower (around half) than that of the current study, which might be due the reaction of Ti with the carbonaceous gases that result from the decomposition of the second part of the binder (PMMA) during sintering, leading to a higher carbon content. Zeng et al. [217] studied the burning behaviour of PMMA under argon and found that PMMA decomposes at about 300 °C into a monomer and other products, such as CH_3OH, CH_4, CO_2, CO and H_2O. This monomer is then decomposed at higher temperatures to produce more gaseous molecules, such as CH_4, CO_2 and CO. While this may aid removal, these gaseous

products may react to some extent with Ti, resulting in more carbon residue in the samples. The difference in oxygen concentration in the parts produced by both feedstocks is negligible, whereas the nitrogen concentration in the parts produced by the current study is somewhat lower (about 2/5) than that in the parts produced by the commercial feedstock. One might argue that this difference in nitrogen content is not that significant; nevertheless, nitrogen has the highest influence on the strength compared to other interstitial contaminants, such as oxygen, where increased nitrogen content leads to a significant increase in the strength and a slight drop in impact toughness [218].

4.4 Microstructural and mechanical analysis results

Optical microscopy images of the polished cross-sections of the prepared samples of both feedstocks are shown in **Figure 51**. It was found that samples made by the coarse Ti powder had much larger micropores with less sphericity. These micropores are formed due to incomplete sintering and bonding amongst the adjacent Ti particles. In comparison, samples processed by commercial feedstock had much finer micropores and more spherical sizes that tend to increase towards the outer edges of the specimens. As pores corresponds to residual free space that originates from interstitial sites in the original packed powder, a correlation between powder and pore size is reasonable.

The average pore diameter for the commercial feedstock was about 17 μm with a sphericity of about 0.63, whereas the average pore diameter for the current feedstock was about 57 μm with a sphericity of about 0.49. Hence, it is expected that samples processed by commercial feedstock have better mechanical properties than those processed with the coarse Ti powder. Nevertheless, the relatively large micropores in the samples processed by the coarse Ti powder are in size at least well suited for biomedical applications, where pore sizes greater than 50 μm are required for rapid osteoconduction [219].

The results of mechanical tests for the samples are presented in **Figure 52 (a)** and summarised in **Table 9**. The compression test results indicate that samples processed by the commercial feedstock have a significantly higher yield strength compared to those processed by the coarse Ti powder, where the average yield strengths ($\sigma_{0.2}$) for the samples were about 473 and 191 MPa, respectively. However, when tested under stress-limited conditions the

energy absorbed by the samples processed by the coarse Ti powder was notably higher than that absorbed by the samples made with the commercial feedstock. This is one of the unique characteristics of porous materials, and reflects the lower stress deformation and good ductility of the samples processed by the coarse powder, which had an average volume percentage of porosity around 20%. Yet, the stress-strain curve for these porous samples did not show any plateau stress, such as that classically expected during testing of porous materials. Nevertheless, there are many examples, particularly in metal foams which show work hardening, where this is not seen, e.g. [220]. The samples after testing did not show nor develop any cracks and showed some signs of barrelling, which is typically observed during compression testing due to sample-platen friction, as seen in **Figure 52 (b)**.

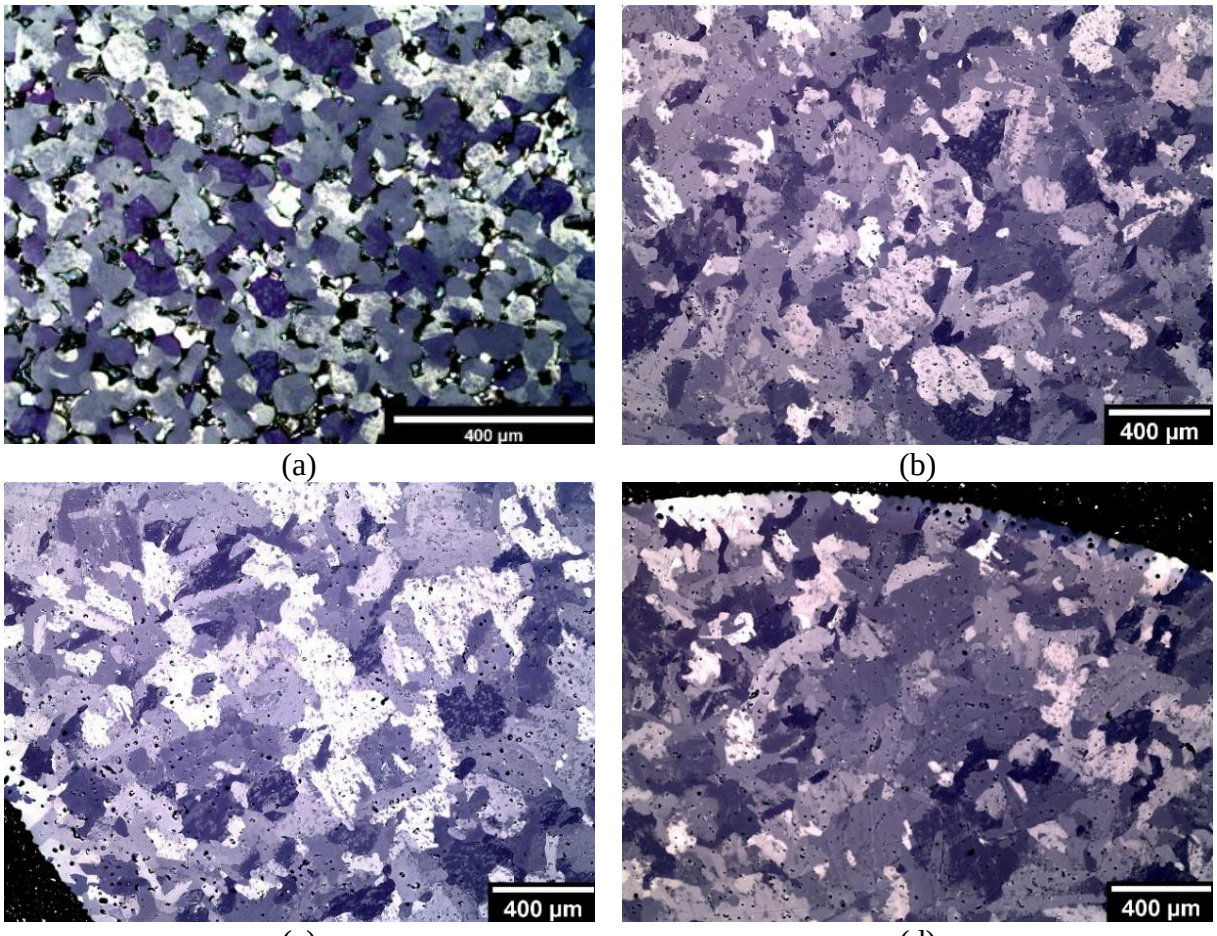

(a) (b)

(c) (d)

Figure 51. Optical micrographs of the polished samples for: (a) sample sintered using the current study feedstock; (b–d) centre and edges of a sample sintered using commercial feedstock.

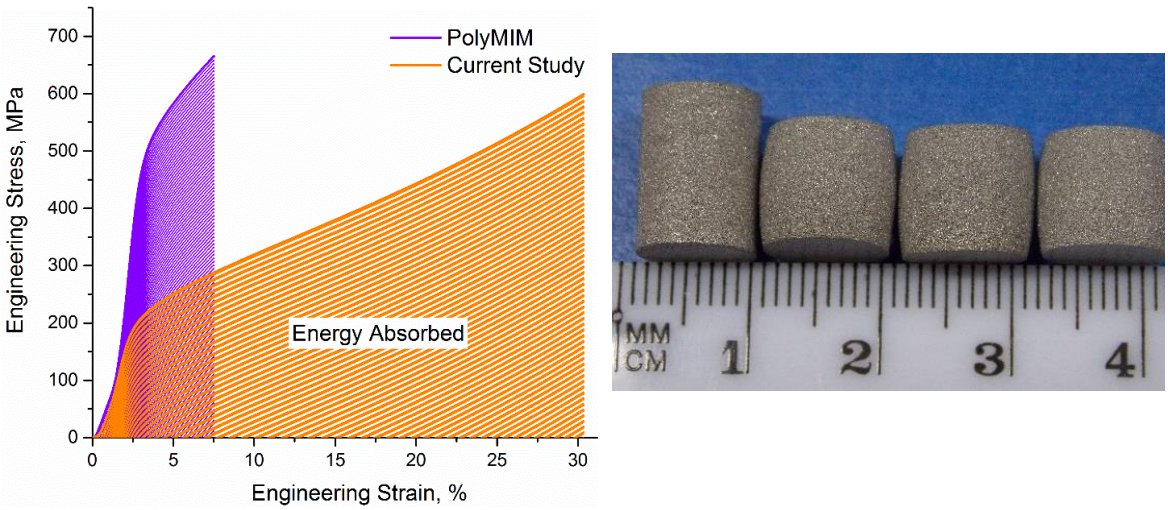

(a) (b)

Figure 52. Typical examples of results of the mechanical tests showing: (a) stress-strain curves of the sintered samples; (b) samples processed by the coarse powder after compression.

Table 9. Characteristics of the samples produced by the commercial and current study feedstocks.

Variable	Samples processed by current study feedstock	Samples processed by commercial feedstock
Porosity (%)	20±3.0	7±1.5
Yield strength (σ0.2) (MPa)	191±6.2	473±7.1
Average pore size (μm)	57±17.5	17± 3.8

4.5 Discussion

DSC curves (**Figure 44**) showed that the current study feedstock requires a lower temperature to be successfully injection moulded than commercial feedstock, where the peak melting temperature of the high viscosity part of the current study binder (PMMA) was 14% lower than that for commercial feedstock. It should be noted that the SA peak could not be detected in the DSC diagram for the current study binder, which could be ascribed to the small amount of SA in the mixture, as has been observed in the literature [8]. In addition, the results of the DSC analysis suggested that the commercial binder consists of more than two parts and does not only contain polypropylene as previously reported, but also high density polyethylene. This was supported by the results of the FTIR analysis, **Figure 45**. Based on the DSC results,

the current study feedstock was injection moulded at a temperature 10% higher than the peak melting temperature of the high viscosity part of the binder, to ensure complete melting. In contrast, the commercial feedstock was injection moulded at a temperature of 185 °C (chosen based on the specification of 178–186 °C), which is about 17% higher than the melting point of the high viscosity part of its binder.

Viscosity analysis results (**Figure 46**) demonstrated that both feedstocks exhibit some shear thinning behaviour, which is desirable in MIM. This can arise where shear rate decreases viscosity due to the unfolding, stretching and alignment of the tangled polymer chains and the breakage of the particle agglomerates [221]. The sensitivity with which the shear viscosity changes with shear rate is usually assessed by the flow behaviour index (n). The lower the n value, the higher the shear sensitivity and the more the feedstock shows pseudoplasticity or shear thinning [222]. Thus, **Table 7** shows that the commercial feedstock exhibits the most pseudoplasticity. However, a low value of n may also be associated with some moulding defects, including jetting, and leads to the slip flow phenomenon [223]. It was also found that the commercial feedstock has a much higher shear viscosity and yield stress, despite being tested at much higher temperatures. The high shear viscosity, yield stress and shear sensitivity could be attributed to several factors, including the high viscosity of the polymers used in the commercial binder and the high solid content for such commercial feedstocks [223] (usually in the range of 60%–65%), as well as the small Ti particle size used [224].

Sintered samples of the commercial feedstock injection moulded using the vertical plunger-type injection moulder showed relatively large macro-cracks, as shown in **Figure 48 (b)**. These cracks were up to 2 mm in length and might be formed due to the insufficient injection and backing pressure of the vertical plunger-type injection moulder. Sintered samples processed by the same feedstock using the Arburg 320 all-rounder with a pressure more than three-times higher and a temperature of 195 °C exhibited smaller cracks, **Figure 49**. In comparison, sintered samples of the current study feedstock processed using the vertical injection moulder did not show any cracks.

The average relative density of the samples sintered using the current study feedstock was found to be 14% lower than that of the samples processed using commercial feedstock with a volume percentage of porosity of about 20%, while the average volume shrinkage for the

samples after sintering was 35% lower than that for samples processed by the commercial feedstock. The differences in shrinkage and density between the samples produced by commercial and current study feedstock could be attributed to the relatively large Ti particle size used in the current study feedstock compared to that of the commercial feedstock, as the use of a smaller particle size results in sintering (and therefore, shrinkage) proceeding more rapidly [225], due to the greater amount of surface energy present [226]. This may also explain the fact that pores in the samples made using the commercial feedstock were much more spherical and more regular in shape (**Figure 51**).

The average linear shrinkage of the parts processed by the commercial feedstock (12.51%) lies in the typical range of linear shrinkage for MIM parts in the literature (14%–18%) [227], whereas for samples produced by the current study feedstock, it was significantly lower (7.3%). Hence, the use of a coarse particle size can be advantageous in increasing the competitiveness of MIM among other manufacturing processes in terms of cost, as well as dimensional tolerances and shrinkage.

In terms of pore size, the average pore diameter for samples processed by the current study feedstock was found to be three-times higher than that of the commercial feedstock, and the pores were less regular.

It should be noted that samples made here using the commercial feedstock had a slightly lower density (higher porosity) and larger pore size compared to that reported for sintered MIM parts using other commercial feedstocks, e.g., for Catamold® Ti BASF (Ludwigshafen, Germany), porosity is about 4% with a pore size of less than 10 μm [228]. These differences might be attributed to the sintering time and temperature (samples were sintered in the previous study at 1300 °C for more than three hours), as well as the Ti particle size (reported to be 2–35 μm in the BASF feedstock [228]), finer than that estimated here for PolyMIM feedstock (12–45 μm). It should however be noted that, as the solid content for both commercial feedstocks is not known, an exact comparison is not possible.

Chemical analysis of the interstitial elements (**Table 8**) showed that samples made by the commercial feedstock had a carbon content approximately half of that detected in samples made by the current study feedstock, even though the finer Ti powder would be more prone to contamination. This could be attributed to the use of PMMA in the current study binder, which decomposes during thermal debinding, releasing large amounts of carbonaceous gases,

which may subsequently react with Ti. Nevertheless, the amount of carbon in samples made using the current study feedstock is lower than that reported for BASF feedstock (0.09%–0.11% [228]).

The results of the mechanical tests (**Figure 52**) showed that samples made by the current study feedstock had a yield stress ($\sigma_{0.2}$), 60% lower than that for samples made using commercial feedstock, but a much higher ability to absorb strain. The higher porosity and larger micropores of the samples made by the current study feedstock will lead to reduced strength, though the porosity also increases the energy absorption capacity in plastic deformation [229].

5 Incorporation of space holder to form Ti foams

After assessing the performance of the feedstock made with the relatively coarse Ti powder, it is crucial now to investigate the effect of adding another material to the feedstock, namely the space holder material (KCl) as well as to understand the impact of various processing parameters on the viscosity of the feedstock in the presence of this space holder material (such as Ti particle size, PEG molecular weight and the percentage of solid loading, among others). These parameters could have a significant effect on the performance of the feedstock and thus on the success of the process of producing Ti foams. Hitherto, there is a very limited number of studies in the literature which investigate the effect of these parameters on the MIM process in the presence of a space holder material with a size several times larger than the size of the Ti particles. Therefore, this chapter will modify the MIM process to account for the space holder material in terms of binder, debinding and sintering and establish a standard procedure for producing Ti foams.

5.1 The effect of PEG molecular weight on the viscosity in the presence of space holder

It was mentioned earlier on in **chapter 4** that PEG is commercially available with different molecular weights that can reach up to 20,000 g/mol. PEG is a non-toxic, water soluble polymer with an open helical structure and has a chemical formula of HO-[CH_2-CH_2-O]$_n$-H) [230]. Choosing a PEG with a suitable molecular weight is of crucial importance, as the viscosity of PEG and its rate of solubility in water are dependent on the molecular weight. Thus, in order to investigate the effect of molecular weight of PEG on the viscosity and porosity of the feedstock, as well as the ease with which parts can be moulded, three feedstocks were prepared using PEG with three different molecular weights, namely 1500, 4000 and 8000 g/mol. The feedstocks prepared had solid content of 50% vol of which 50 %vol was Ti and 50%vol was cubic KCl. The mean particle size of the KCl particles used was 338 µm. Feedstock preparation and mixing was carried out using the procedure outlined in **section 3.1.2**. It was noted during mixing that the colour of the binder changed according to the PEG used, being highly viscous and milky with high whiteness in the case of PG8000,

but with the degree of whiteness decreasing with reducing molecular weight of PEG. The three feedstocks prepared were designated as F50Cu50L250PEG1500, F50Cu50L250PG4000 and F50Cu50L250PEG8000. The formulation of these identifying names is shown below:

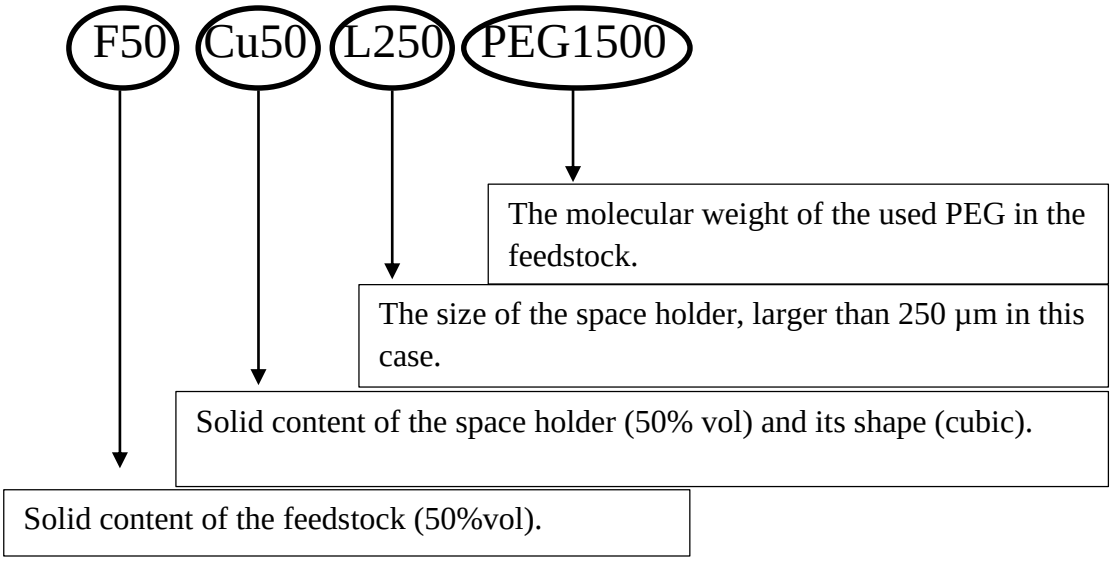

These feedstocks were then extruded through a low pressure injection moulder at different temperatures. The temperature of extrusion of each of these feedstocks was set according to visual inspection. Feedstocks made with PEG 4000 and PEG 8000 were extruded at 120°C due to their high viscosity, whereas feedstock made with PEG1500 was extruded at 110 °C as it was too liquid to be extruded at 120°C. The extruded feedstocks were then cut or pelleted into small pellets about 0.5-1 cm in length. The viscosity of the feedstocks was measured at four different temperatures, namely, 120, 130, 140 and 150 °C at least three times to make sure that consistent data were obtained. The feedstock pellets were then fed into the barrel of the capillary rheometer and left for 15 minutes in order to reach thermal equilibrium throughout the feedstock. The shear rate was set from 900 to 4000 s^{-1}. The results of the viscosity analysis for the feedstocks prepared are shown in **Figure 53.**

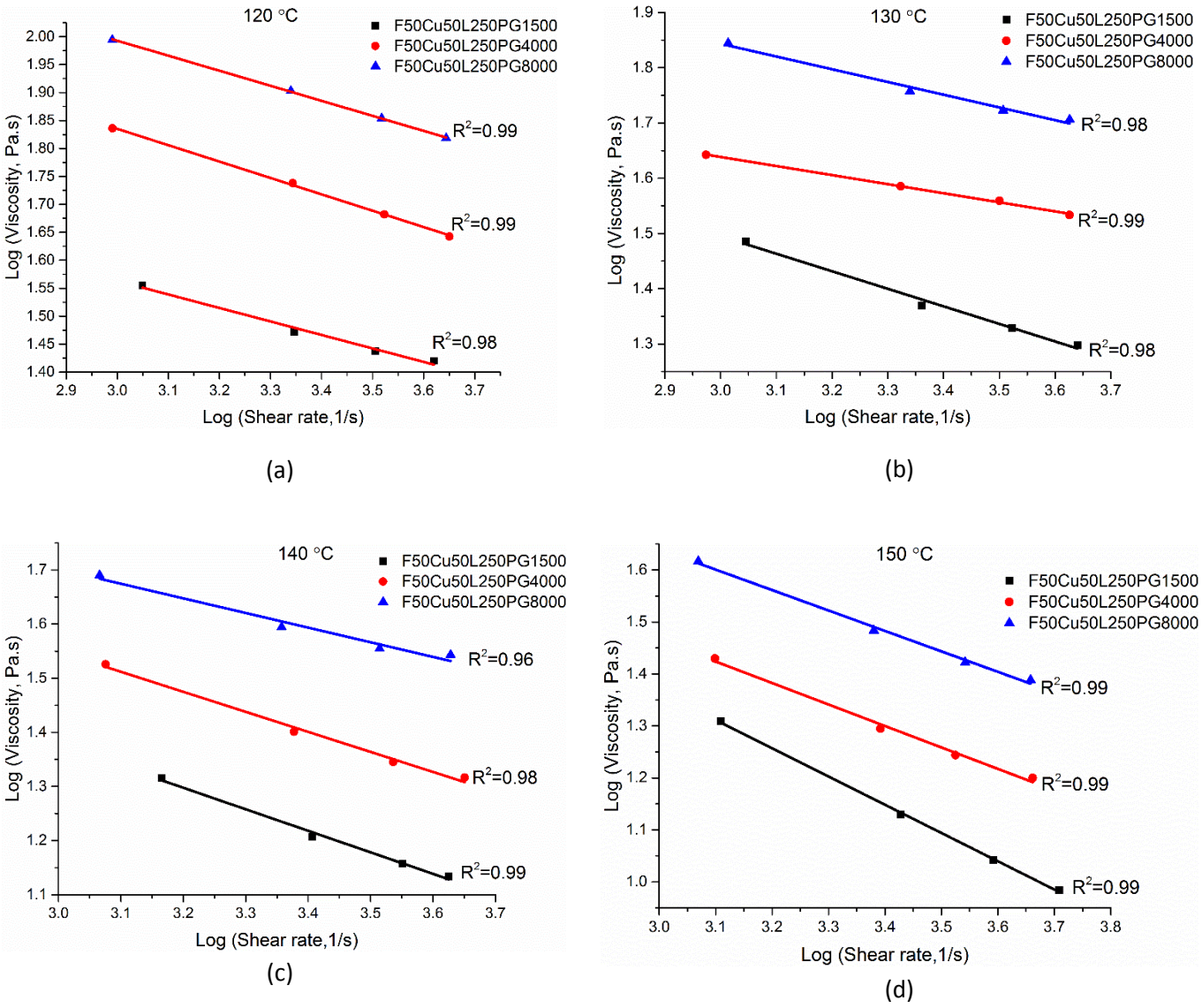

Figure 53. Viscosity rheograms of the feedstocks prepared using PEG with different molecular weights at a temperature of: (a) 120 °C, (b) 130 °C, (c) 140 °C, (c) 150 °C.

The results show that the higher the molecular weight of PEG, the higher the viscosity, which can be attributed to an increased degree of entanglement in the longer polymer chains of the higher molecular weight polymers compared to the lower molecular weight (shorter) ones, resulting in higher resistance to flow, and hence higher viscosity at a given temperature. It was also generally found that the viscosity of all feedstocks decreases with increasing temperature and shear rate as shown in **Figure 53**. In terms of the yield shear stress, feedstock made with PEG8000 had the highest yield shear stress compared to other

feedstocks, where its yield shear stress was about 46 kPa at 120 °C, dropping to around 27 kPa at 150 °C, compared to the yield shear stresses of the feedstocks made by PEG 4000 and PEG 1500 which were approximately 35 and 19 kPa respectively at 120 °C and dropped to about 19 and 13 kPa at 150 °C. In addition, It was also noted that feedstocks processed with PEG1500 came out of the capillary die and spread non-uniformly on the moving tray such that the shape of the strands of the feedstock was lost, (as shown in **Figure 54)**. Feedstocks made with PEG 4000 and 8000 came out of the capillary die and kept their strand shape, as they solidified faster than the feedstock made with PEG1500. Feedstocks made with PEG 1500 stayed soft after 1 minute of cooling at room temperature, whereas feedstocks made with PEG 4000 and 8000 became solid within approximately 20 and 10 seconds respectively. Furthermore, the sensitivity (*n*) with which the shear viscosity changes with shear rate was found to be highest for the feedstock made with PEG 1500 at the test temperature of 120 °C, where it was about 0.78, compared to 0.71 and 0.73 for feedstocks made with PEG 4000 and PEG 8000 respectively. However, this trend changes with increasing test temperature from 120 to 150 °C, where the shear sensitivity value becomes lowest for feedstock made with PEG 1500, dropping to 0.46, whereas the shear sensitivity values for feedstocks made by PEG 4000 and PEG 8000 were about 0.59 and 0.61. It should be noted that the lower the *n* value, the higher the shear sensitivity and the more the feedstock shows pseudoplasticity or shear thinning. This is desirable, particularly for complex MIM parts as it aids mould filling and shape retention [222]. Thus, it can be concluded that feedstock made with PEG 1500 has a higher flowability and can easily fill the cavity of the mould at a lower yield stress. However, higher dwell time is expected to be needed to cool the feedstock down as it solidifies slower than feedstocks made with higher molecular weights.

PEG molecular weight does not only have an influence on the viscosity, but can also have an impact on the percentage of porosity in feedstock. The entrapment of air during the process of mixing and extrusion of the feedstock can result in the incorporation of some pores in the feedstock obtained. These pores can have an influence on the density of the injected parts as well as on their mechanical properties. Therefore, estimating the amount of porosity in the feedstock is crucial in monitoring the quality of the feedstocks as well as assessing their suitability for the production of high quality products. The amount of this porosity does not depend only on the mixing and extrusion procedures, but also on the characteristics of binder

used, such as the viscosity and speed of solidification during cooling as well as the shape of the starting powder. The viscosity of the binder is strongly reliant on the molecular weight of the polymer used which in turn dictates the length of the polymer chains and their propensity to entangle. Thus, using polymers with different molecular weights can result in different percentages of porosity in the feedstock. The percentage of porosity in the feedstock was estimated by comparing the theoretical density of the feedstock calculated using the 'rule of mixtures' (**equation 13**) and the measured one using a helium pycnometer and finding the difference between them.

$$\rho_{Th.} = (\rho_{Ti} * V_{Ti}) + (\rho_{KCl} * V_{KCl}) + (\rho_{PEG} * V_{PEG}) + (\rho_{PMMA} * V_{PMMA}) + (\rho_{SA} * V_{SA}) \quad (13)$$

where $\rho_{Th.}$ is theoretical density and *V* is volume fraction.

It was found that feedstock prepared using PEG 4000 had the lowest amount of porosity compared to other feedstocks, where the amount of porosity was found to be equal to 1.6 %, compared to feedstock prepared with PEG 1500 which was 1.9%, while the highest amount of porosity was associated with the use of PEG 8000, reaching 2.8%. This might be attributed to the high viscosity of PEG 8000 and its rapid solidification which does not give sufficient time for the air bubbles to escape during cooling. PEG 4000 can therefore result in the lowest amount of porosity during processing. However, it is harder to water debind it compared to PEG 1500 as the penetration of the water molecules into its longer molecular chains and the transportation of these solvated molecules into the surface is much more difficult, resulting in higher possibility of cracking and swelling and longer debinding times [230]. In addition, trials of injecting samples using a feedstock with a solid content of 58% made with PEG 4000 at 150 °C have shown that either the injected samples had a high defect content due to the insufficient pressure of the vertical plunger injection moulder, or the nozzle was clogged as shown in **Figure 54 (b)**. Using a high density PEG can affect the process of filling of the cavity of the mould as high molecular weight PEGs have a higher viscosity and require processing at higher temperatures than PEG 1500. They also have higher yielding stress, which means high pressure is required during injection in order for the feedstock to flow and fill the cavity without any defects. The presence of relatively coarse KCl particles in the mixture can also contribute to aggravating the problem by increasing the friction between the

mould and the molten viscous feedstock leading to incomplete filling of the mould cavity, particularly if the injection pressure was insufficient. Therefore, PEG 1500 was chosen as the main component of the binder due to reduced debinding time and the ability to process feedstocks at lower temperatures and with reduced injection pressure.

(a) (b)

Figure 54. (a) Extruded feedstock at 150 °C made by PEG1500 (upper) and PEG 4000 (lower), (b) samples before and after sintering of a feedstock made with PEG 4000 58% solid content of which 60% KCl injection moulded at 150°C and 45 MPa.

5.2 Effect of solid loading on the viscosity of the feedstocks

Solid loading or solid content is the volume percentage of solid powder in the feedstock and it is a very important factor that has a significant influence on the process of producing porous parts by MIM. It dictates the percentage of space holder that can be added with the Ti powder in the feedstock, as well as the ease with which green parts can be moulded. In processing of MIM parts using a single powder, solid loading has a major role in dictating the sensitivity of the feedstock to the change in temperature, distortion in the produced parts as well as the final density and tolerance control [231]. High solid loading feedstocks can result in less shrinkage and distortion in the produced parts, but lead to a higher temperature sensitivity

and more difficulty in moulding parts without defects depending on the size, shape and density of the powder to be processed [232].

Adding a space holder to the feedstock mixture, such as potassium chloride with a density about half that of the metal powder, could potentially have a beneficial impact in decreasing the viscosity of the system by replacing some of the metal powder in the feedstock with a lighter material [233]. Nevertheless, the size of the space holder could be problematic in increasing the possibility of nozzle clogging, as its size is more than triple that of the metal powder, and the diameter of the die of the rheometer is 2 mm. Therefore, it is important to assess the impact of the solid loading including the space holder on the viscosity of the feedstocks in order to be successfully able to produce porous parts by MIM-SH. In order to do so, three feedstocks with different solid content or loadings were prepared using different volume percentages of cubic KCl and spherical Ti powder with mean particle sizes of 338 and 75 µm respectively. Viscosity measurement was carried out at four different sets of temperatures 120, 130, 140 and 150 °C. Each test at each temperature was performed multiple times in order to make sure that the values are consistent. The feedstocks were designated as F50CU50L250PG1500, F58CU50L250PG1500 and F61CU60L250PG1500.

Figure 55 shows the viscosity rheograms for the three feedstocks with different solid contents. It is worth noting that the feedstock with the solid content of 61vol% could not be tested at a temperature below 130 °C, where the capillary die of the rheometer become immediately clogged. It can be seen from the plotted graphs that the higher the solid content, the higher the viscosity. It was also noted that the shear sensitivity value for the feedstock with the highest solid content (61%) was much more influenced by the testing temperature than other feedstocks, where the value dropped from 0.59 at 130 °C to about 0.22 at 150 °C. Such a low value of shear sensitivity can be associated with certain moulding defects, including jetting, and leads to the slip flow phenomenon [223]. Feedstock with 58% solid content was considered to be the best as it had a good solid content, higher than that for the feedstock with 50 vol%, and its shear sensitivity value did not change significantly with temperature, dropping from 0.83 at 120 °C to about 0.49 at 150 °C, and hence this solid content was chosen for further experiments in making foams.

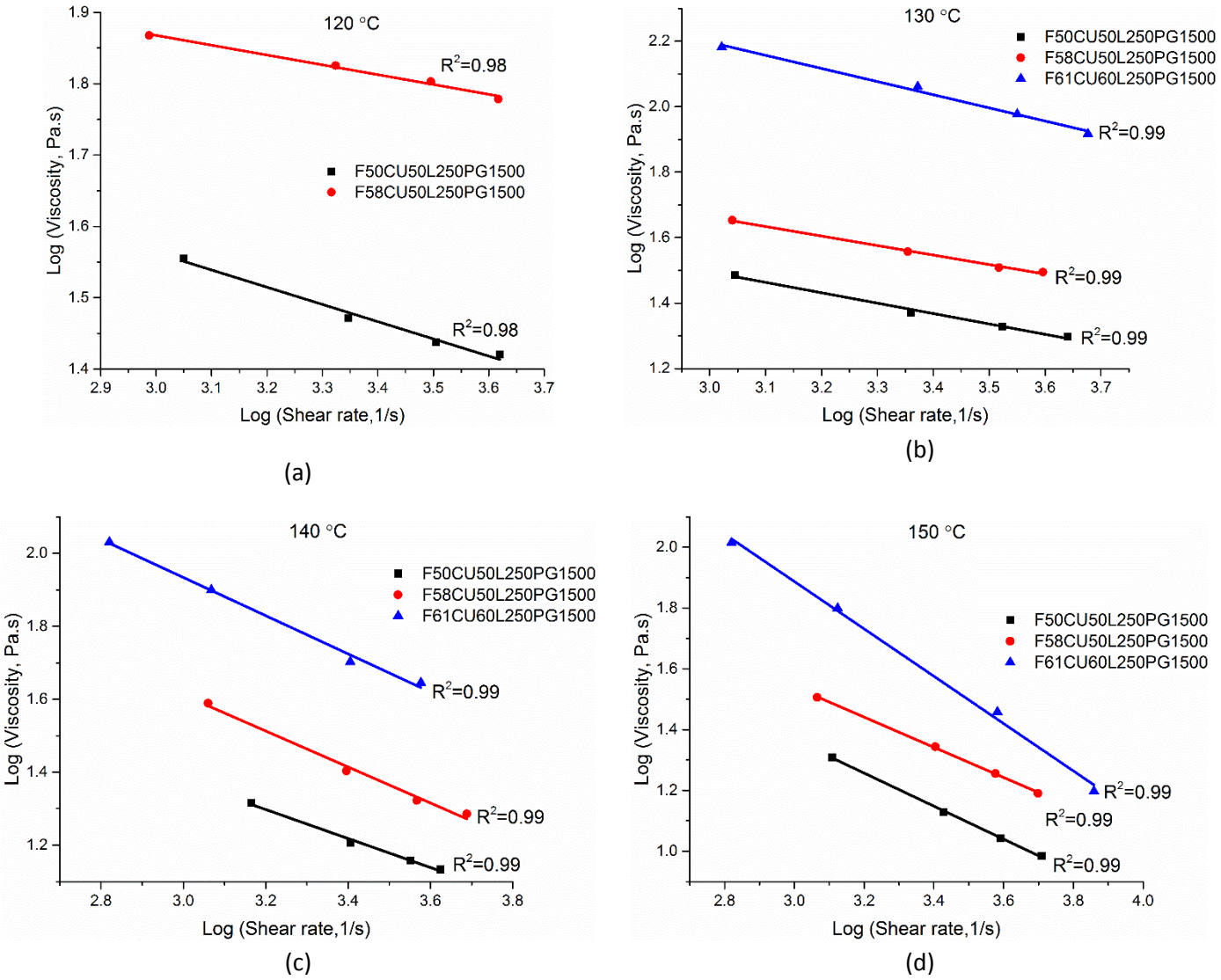

Figure 55. Viscosity rheograms of three feedstocks with different solid contents at: (a) 120 °C, (b) 130 °C, (c) 140°C, (d) 150°C.

5.3 The effect of the shape of the space holder particles on viscosity

It is important to be able to produce foams with different pore morphologies (e.g. cubic, spherical, etc.) to meet different demands for different foam applications. This diversity in pore morphologies can be achieved by using space holders with different particle shapes. Thus, investigating the influence of the space holder particle shape on the viscosity of the feedstocks is important in assessing the suitability of these feedstocks for the production of foams with different pore morphologies by MIM-SH. Two shapes of space holder particles were used, namely cubic and spherical KCl, and their particle size distribution was mentioned

previously in **Table 4 in section 3.1.1.** A third feedstock was prepared using a mixture of fine cubic (D_{10}= 147 µm, D_{50}= 222 µm, D_{90}=325 µm) and spherical KCl powder (D_{10}= 88.3 µm, D_{50}= 201 µm, D_{90}=340 µm). The feedstocks were prepared using the procedure previously described in **3.1.2** with a solid content of 58% of which 60% was KCl and 40% was Ti. The feedstocks were assigned the symbols of F58SPPG1500, F58CUPG1500 and F58CU+SPPG1500 for those prepared by spherical KCl, cubic KCl and a mixture of cubic and spherical KCl respectively. The rheological analyses of the feedstocks were performed at a series of four temperatures, namely 120, 130, 140 and 150 °C.

The viscosity rheograms of the feedstocks made with different KCl morphologies are shown in **Figure 56**. It was observed that feedstocks made with cubic KCl particles had a much higher viscosity than those made using spherical KCl particles and a slightly higher viscosity than that of feedstock made with a mixture of finer cubic and spherical KCl particles. Spherical KCl particles flow much better than cubic particles (moving past each other more easily) with reduced die wall friction, resulting in lower viscosity and reduced resistivity to flow. Tuncer et al [9] favoured KCl over NaCl as a space holder and reported that KCl powder can be compacted at lower pressure to almost full theoretical density and can give lower wear of screw and valve components compared to NaCl. However, one might argue that the shape of the space holder is a significant contributor to their findings, rather than just the material, as the KCl particles used in their study were approximately spherical, while the NaCl particles were cubic. It has also been reported in the literature that feedstocks made by spherical powders have lower viscosity than those with irregular powders and can have a higher maximum solid content in single-system Ti feedstocks [234]. In binary feedstock systems, the same effect has been observed on the viscosity in the case of adding secondary spherical powders compared to cubic or irregular powders. Thus, more spherical KCl can be added to the feedstock to produce foams with larger percentage of porosity compared to the cubic case. It can also be noted that feedstock prepared with a mixture of cubic and spherical KCl powders had a viscosity value between the spherical and cubic, albeit the particle size was finer. At lower shear rates, the viscosity of the feedstock with the cubic KCl and that with the mixture of finer cubic and spherical particles were close to each other. However, this trend changes noticeably as the shear rate increases where spherical particles flow easily, yet their movement is still restricted by the presence of cubic KCl particles which keep the

viscosity relatively high compared to viscosity of the feedstock made with spherical KCl alone. It is worth mentioning that the shear sensitivity value for the feedstock made with spherical KCl was the lowest among the tested feedstocks at the test temperature of 120 °C, where the value was equal to 0.78, whereas the shear sensitivity values for feedstocks made with cubic and a mixture of spherical and cubic were about 0.83 and 0.81 respectively. This value drops significantly with temperature to 0.35 at 150°C in the case of feedstock made with spherical KCl, while it drops to 0.49 and 0.39 for feedstocks made with cubic particles and the mixture of spherical and cubic particles. This means that feedstocks with spherical space holder particles show higher pseudoplasticity or shear thinning behaviour, which increases with increasing test temperature.

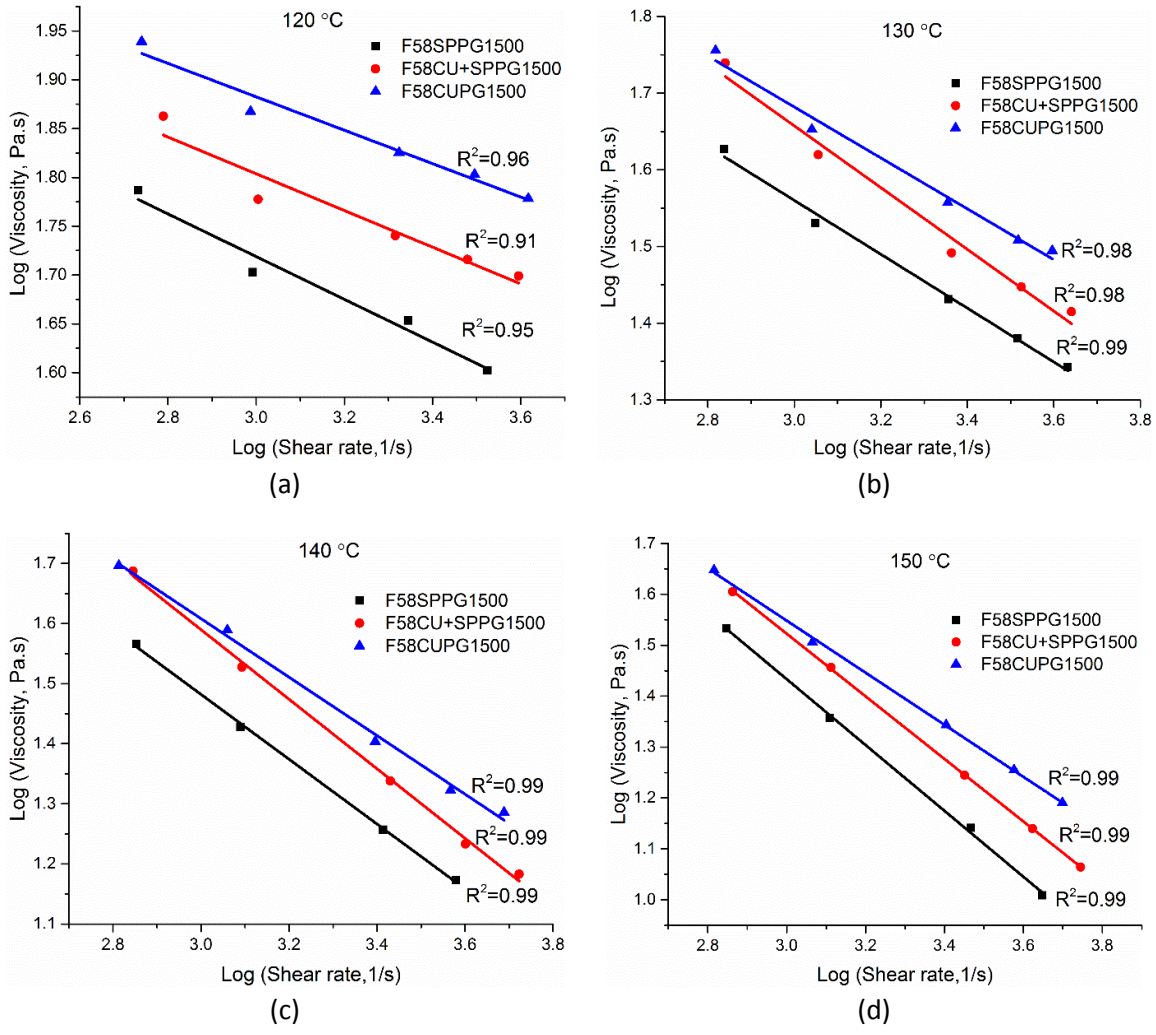

Figure 56. Viscosity rheograms of three feedstocks with different KCl morphologies at: (a) 120 °C, (b) 130 °C, (c) 140°C, (d) 150°C.

5.4 The effect of Ti particle size on viscosity

It is reported that feedstocks made with fine powders have significantly higher viscosity and lower shear sensitivity compared to feedstocks made with coarse powders in single system feedstocks (without space holder) [235]. However, adding space holder with very large particle size and lower density to fine metal powders can result in a reduction in the viscosity and a greater chance for the powders to segregate due to the differences between the sizes of the powder and space holder. Thus, it is important to examine the effect of Ti particle size on the viscosity of the feedstock with the addition of the space holder and its sensitivity to shear rate.

The effect of Ti particle size was investigated by comparing the viscosity of the feedstock prepared by a mixture of the coarse Ti powder and cubic space holder with that made using a mixture of fine Ti-6Al-4V (AP&C, Canada) and cubic space holder. It should be noted that Ti-6Al-4V has a lower density than Ti (the density measured by the helium pycnometer for the fine Ti-6Al-4V was about 4.51 g/cm^3), and is expected to result in foams with improved mechanical strength due to the presence of the beta phase, which yield more strength in the samples than those contain only alpha phase [2]. Nevertheless, it was used due to its availability in the case of this test. The particle size distribution for the fine Ti-6Al-4V is shown in **Table 10**. The two prepared feedstocks were designated as Ti64F50CU50L250PG1500 and F50Cu50L250PG1500. The viscosity of the feedstocks was tested at two different temperatures, namely 120 and 150 °C.

Table 10. Particle size distribution for the fine Ti-6Al-4V powder

Powder	Dx (10)	Dx (50)	Dx (90)
Ti-6Al-4V	15.5 μm	31.3 μm	52.4 μm

The results of the viscosity analysis for feedstocks made with different Ti particle size are illustrated in **Figure 57.**

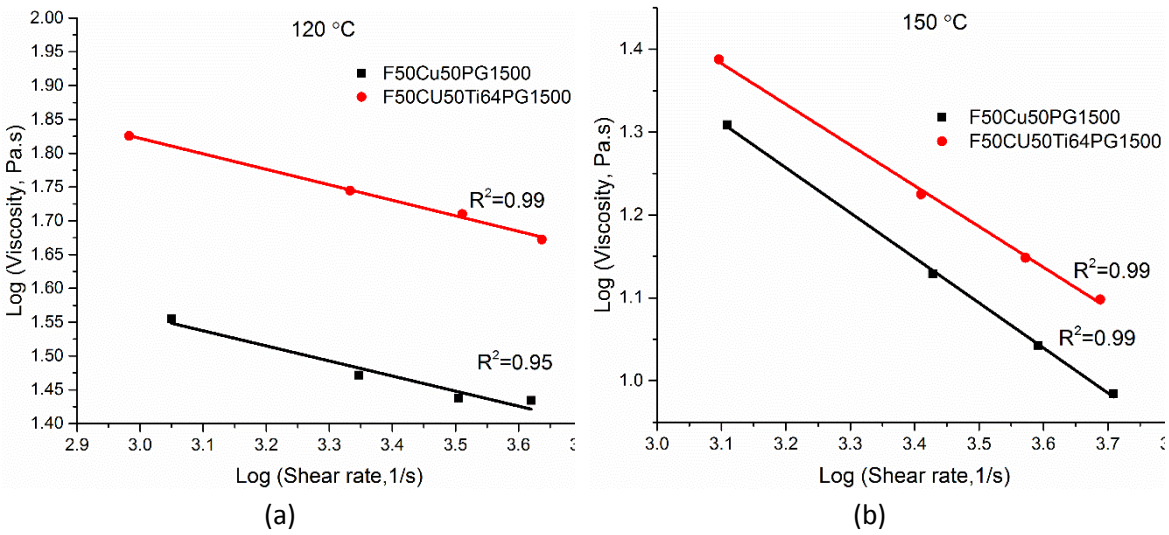

Figure 57. Viscosity rheograms of two feedstocks made with different Ti particle size at: (a) 120 °C, (b) 150°C.

It can be observed that the viscosity of the feedstock prepared using sub-45 µm Ti-6Al-4V particles at 120 °C was much higher than that of the feedstock prepared using the relatively coarse Ti powder with a mean particle size of 75 µm. However, this difference in viscosity decreases with increasing the temperature to 150°C. This might be due to a higher chance for the breakage of agglomerations of the sub-45µm Ti-6Al-4V particles at higher temperatures, where the polymeric binder has enough fluidity to give more freedom for the particles to move compared to at lower temperatures. During shearing and compression of the feedstock against the capillary die, the particles tend to agglomerate forming flocs. The sizes of these flocs depend on the particle size, shape and the percentage of solid content [236]. The smaller the particle size of the powder, the higher the tendency to agglomerate [237, 238]. These flocs gather near the capillary die of the rheometer or the nozzle of the injection moulder and lead to an increase in the viscosity of the feedstock initially. In order for the feedstock to flow through the capillary die or the nozzle of the injection moulder, the shear rate applied has to be higher than the yield stress of the highly filled polymer system and sufficient to partially or completely break down these flocs. Once the shear rate meets the required value, the powder particles pass through the capillary die and line up in a chain-like manner. Increasing the shear rate further would result in polymer chain dis-entanglement leading to a reduced viscosity at higher shear rates. Furthermore, this decrease in viscosity continues until a certain stage where the shear rate would be high enough to break these flocs completely into primary

particles and dis-entangle the polymer chains. Beyond this the viscosity will stay constant with further increase in the shear rate.

5.5 Thixotropy of feedstocks

Some viscous materials exhibit time-dependent shear thinning, a phenomenon called thixotropy. It is often related to the breakdown of the structure under shear with time leading to a reduced viscosity reading. This breakdown in the internal structure can be time-reversible where the structure of the material rebuilds once the shear stress is removed and the material is allowed to rest [177]. Feedstocks need to be checked for this phenomenon in order to make sure that there is no segregation between the polymeric binder and powders which might result from the breakage of the structure under shear. This can be carried out by subjecting them to ascending shear rate up to a maximum value and then decreasing it at the same rate to the starting value. Thixotropic materials often display a wide hysteresis loop, whereas normal materials do not show any hysteresis. Two feedstock samples were prepared using cubic KCl particles with mean particle size of 229 µm and tested for their structural stability by shearing them up to a maximum value of about 2200 s^{-1} and then reducing it to the starting value at the same shear rate. These tests were carried out at two different temperatures, namely 140 and 150 °C. The thixotropy test results for the feedstock are shown in **Figure 58.**

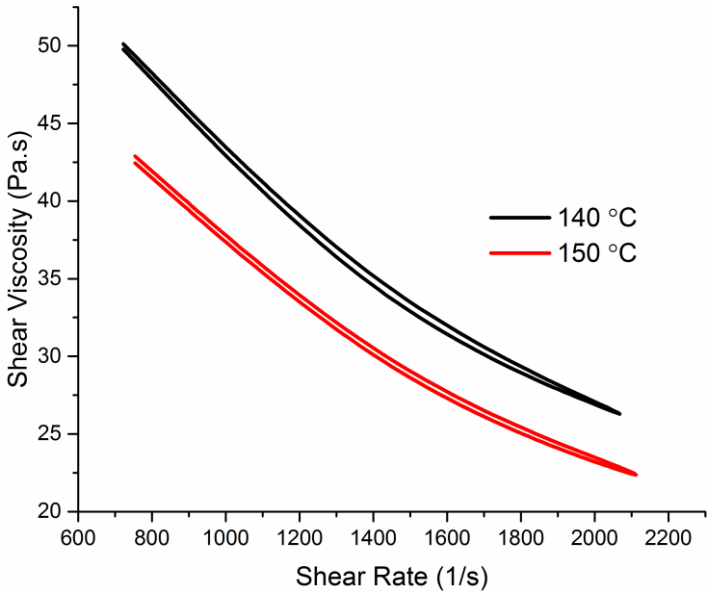

Figure 58. The hysteresis behaviour of feedstock.

It can be noted that there is no obvious hysteresis loop at the injection temperatures, which is an indication of the feedstock having good structural stability and consistency, sufficient to inject the feedstock into different part shapes [239].

5.6 Initial trials for producing Ti foams

After understanding the effect of different processing parameters on the viscosity of the prepared feedstocks in the presence of the space holder material, it is now necessary to produce Ti foams using feedstock with a relatively low percentage of solid loading. This helps establish a standard procedure for producing these foams to be followed in further experiments, and provides a basis to increase the percentage of space holder content systematically in order to avoid any wastage of materials by unsuccessful trials. Thus, a feedstock with a solid loading of about 55% was chosen as a starting step and prepared using the procedure mentioned in **section 3.1.2**. The percentage of space holder added was 50% of the solid content, while the rest was Ti powder with a mean particle size of 75 μm. The space holder used was cubic KCl with average particle size of about 348 μm. The percentage of the binder was equal to 45% of which 65% PEG, 30% PMMA and 5% stearic acid. The binder was analysed using DSC and TGA before carrying out any sample production.

5.6.1 DSC and TGA analyses of the binder

DSC analysis was performed in order to find out the melting behaviour of the binder and its constituents and the results help in dictating the injection and extrusion temperatures for the feedstock in order to make sure that all the binder components are melted. The DSC analyses were carried out at a scan rate of 10 °C/min in the temperature range 25-200 °C. The onset and offset melting temperatures were obtained by extrapolating the baseline and finding the points which intersect with the tangents of the peak. TGA analyses were also performed in order to assess the decomposition behaviour of the binder components and according to which the thermal debinding temperature was set during the sintering cycle. The TGA test was carried out under argon atmosphere and the samples were heated up to 726 °C at a rate of 5°C/min.

The results of the DSC analyses of the binder and its constituents are shown in **Figure 59**. As can be seen from **Figure 59** the peak melting point of PEG was shifted to the left in the

presence of PMMA and stearic acid (i.e. lowered from 50.12 °C for pure PEG 1500 to 48 °C for PEG in binder), while the onset temperature of melting was increased from 42°C in the case of pure PEG to 43 °C for PEG in the binder. Conversely, the offset melting temperature for PEG reduced from 53 °C for the pure state to 51 °C for PEG in the binder. In addition, the peak melting temperature of the PMMA was shifted to the right (i.e. increased from 126 °C for pure PMMA to 139 °C in the presence of PEG). This is an indication of interaction among the binder polymers where the crystalline PEG interacts with the amorphous PMMA resulting in a blend of some amorphous regions with crystalline regions composed of PEG entirely. Jian and Guoqin [240] studied the behaviour of interaction between PEG and PMMA and found that PEG and PMMA can form semi-interpenetrating polymer-networks that are composed of mixtures of crystalline and amorphous regions when the PEG content is greater than 35 wt %. Thus, in order to make sure that all the binder components are melted, a temperature of 150 °C was chosen for further investigations and sample preparation. Furthermore, a temperature of 50 °C was chosen for the dissolution and debinding processes to guarantee PEG melting.

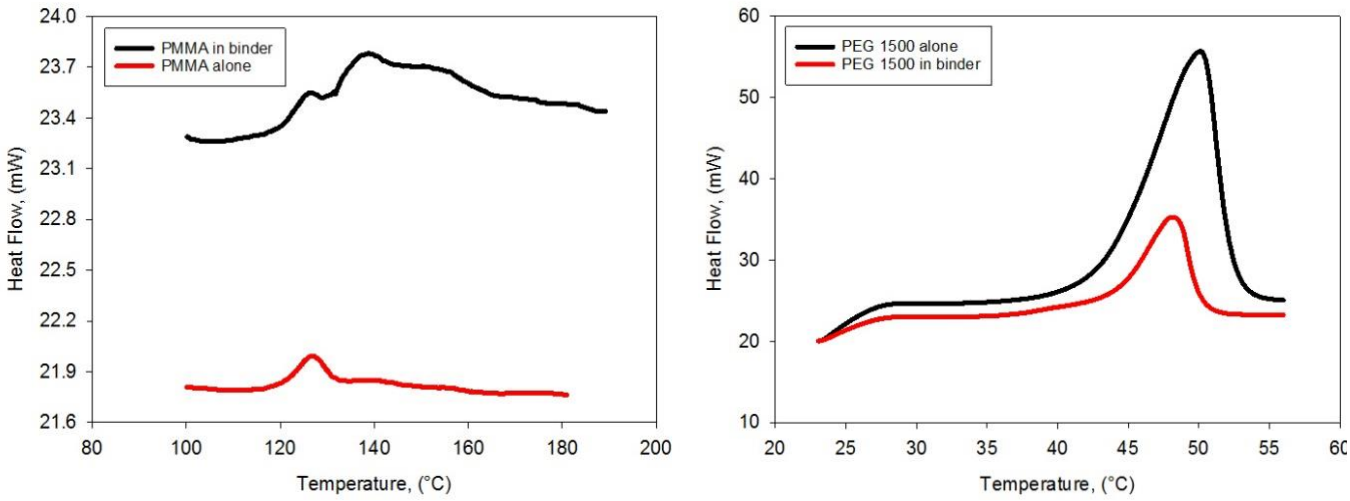

Figure 59. DSC results (heating) of PMMA and PEG.

The results of TGA analyses of the binder (PEG, PMMA and SA) and pure PMMA are shown in **Figure 60**.

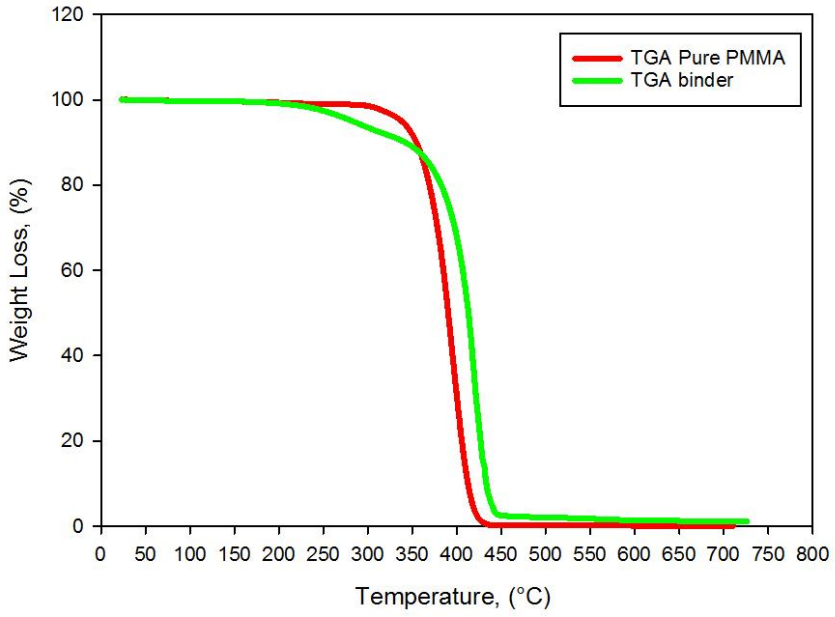

Figure 60. TGA results of the binder and pure PMMA

It can be noted from **Figure 60** that pure PMMA was completely decomposed at approximately 430 °C, whereas almost all of the binder was decomposed at a temperature of 450°C. This means that the thermal debinding stage should be carried out at a temperature equal to or above 450 °C in order to guarantee the removal of components remaining after water debinding and dissolution of the space holder. The binder shows a higher decomposition temperature than pure PMMA because of chemical interaction among the binder components. Thus, it is expected that PEG removal from the mixed binder will be more difficult than its debinding in the pure form. In addition to this, several factors will affect the removal of PEG from the samples, including the percentage of PMMA in the binder, the particle size and shape of the injected powder as well as the molecular weight of the PEG used [230].

5.6.2 Sample preparation

Small cylindrical parts were injection moulded at a temperature of 150 °C using the sample preparation procedure outlined in **section 3.1.3**. The specimens were 10 mm in diameter and 6 mm in height. One green sample was broken and its surface was gold coated by sputtering for 3 minutes in order to investigate the surface of the sample using SEM. **Figure 61**

illustrates the morphology of the broken sample which was imaged using SEM at 6 kV. It was noted that the KCl particles remain cubic in shape and are not coated with the binder to the same extent as the Ti powder. This can be helpful for rapid removal of the space holder from the sample by water dissolution, where water penetrates into the specimen faster and breaks up the ionic lattice of the KCl resulting in solvated ions.

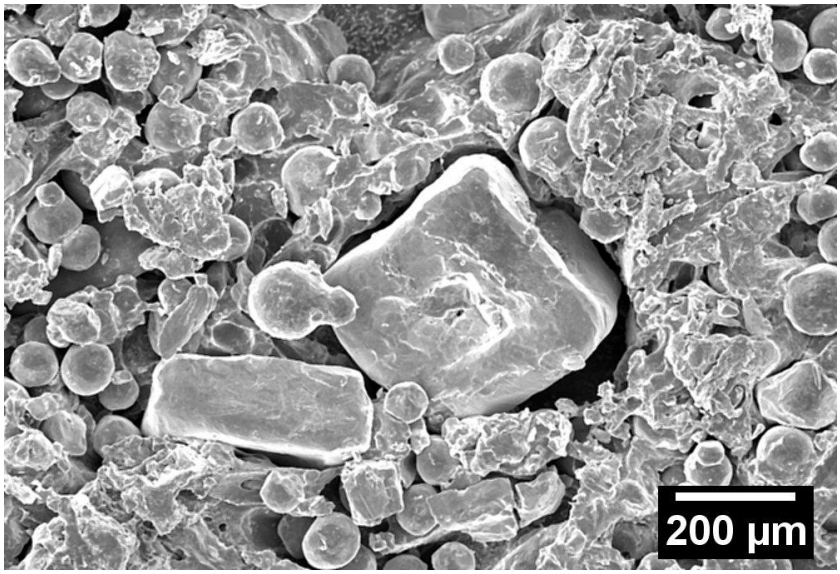

Figure 61. Secondary electron SEM image of the surface of as-broken green sample with a solid loading of 55% reproduced from Shbeh, M. and Goodall, R. Mater Design. 2015; 87:295-302.

5.7 Debinding and dissolution results

One of the greatest challenges in producing Ti foams by MIM in combination with space holder is the removal of the main component of the binder and space holder during the debinding stage, where the process is very time consuming and can take up to 72 h [9]. Hitherto, most of the reports on the production of Ti foams via MIM-space holder method used paraffin wax as a major binder constituent and organic solvent debinding for binder removal [111, 241]. However, this will not only result in the use of environmentally unfriendly organic solvents for the removal of paraffin wax such as chloroform, but will also require another separate dissolution stage for removal of the space holder. In comparison, the major part of the binder used here is a water soluble polymer (PEG) and this offer the

advantage of removing both PEG and the space holder (KCl) in one stage. The debinding and dissolution stage was performed following the procedure outlined in **section 3.1.4** under four different conditions. In the first condition the water debinding and dissolution stage was carried out at 20 °C and weight loss in the samples was monitored with time using a density balance, while in the second condition the process was performed using an ultrasonic bath at room temperature. In the third condition the removal of the space holder and PEG was carried out using heated ultrasonic bath at a temperature of 50 °C. In the final condition the process was performed using a hot plate stirrer with a magnetic bar at a temperature of 50 °C. The results of the different water debinding and dissolution techniques used are shown in **Figure 62**. It can be noted that the ultrasonic water debinding and dissolution at a temperature of 50 °C was the quickest method in comparison with other water debinding and dissolution techniques, where the PEG and space holder were completely removed (assessed by weight loss and DSC measurement) after 4 hours. The hot plate stirring method came second with double the removal time of the heated ultrasonic bath method. The third and last methods were ultrasonic dissolution at ambient temperature and dissolution at 20 °C. It can also be seen from **Figure 62** that the linear parts of the curves of the heated ultrasonic dissolution and hot plate stirring were much larger compared to the other two methods. This is due to the fact that temperature has a great impact on the removal rate of both space holder and PEG, the latter especially as the melting temperature of PEG (50°C as assessed by the DSC experiments, **section 5.6.1**) was reached in the experiments. Hence studying the temperature effect would be a matter of great importance in the removal rate of PEG and space holder. Furthermore, it can also be observed that the removal rates were approximately equal for the heated ultrasonic and hot plate stirring dissolution in the initial stages of water debinding and dissolution, but this trend changes with time in favour of the heated ultrasonic bath. This is due to the high efficiency of the ultrasonic vibrations in removing the dissolved space holder and PEG faster from the inside of the sample and consequently lifting the limitation of the rate being controlled by diffusion of the dissolved space holder and PEG to the outer surface. This has been considered previously as the bottleneck in slowing the removal process of the space holder and PEG from the sample [242-244].

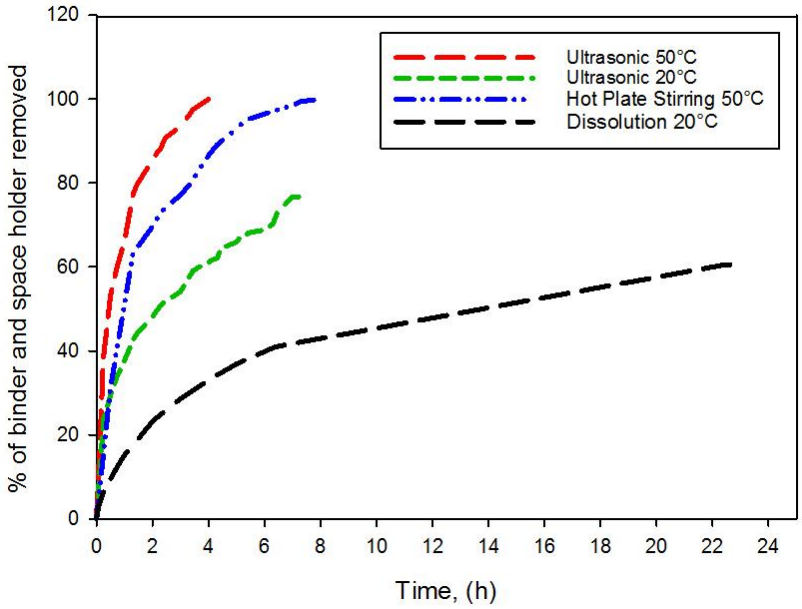

Figure 62. Results of different debinding and dissolution methods.

It can also be noticed that the real time monitoring of water debinding and dissolution using a density balance gives a smooth curve over time. However, the complete removal of space holder and PEG (based on the known weight added) was not realised. This can be attributed to the low temperature of the experiment (20°C) compared to the peak melting temperature of PEG (50°C). SEM images of the 20°C water debinded specimen are shown in **Figure 63**.

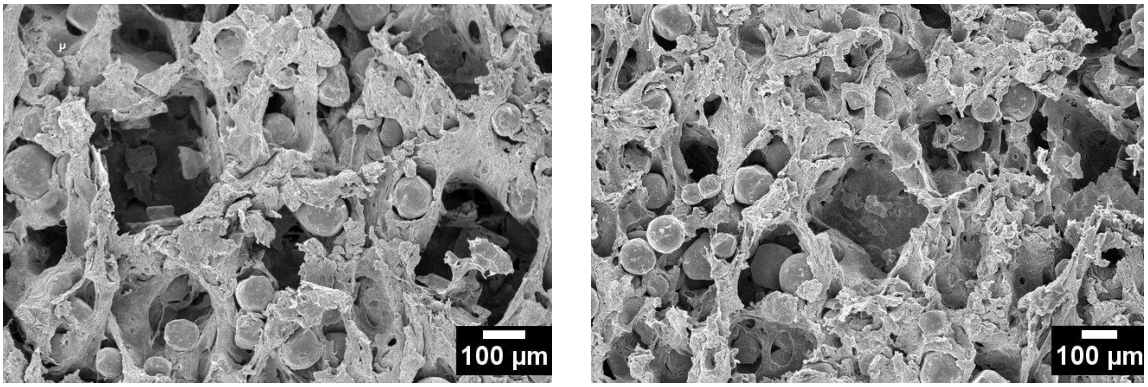

Figure 63. Secondary electron SEM images of the sample after 23 hours of dissolution reproduced from Shbeh, M. and Goodall, R. Mater Design. 2015; 87:295-302

As can be seen from the SEM images, the KCl space holder was dissolved in water and the shape of pores replicated the shape of the space holder, while the PEG and PMMA networks are still apparent after 23 h of dissolution at 20°C. These networks could be eliminated by increasing the temperature of the dissolution up to or above the melting temperature of PEG.

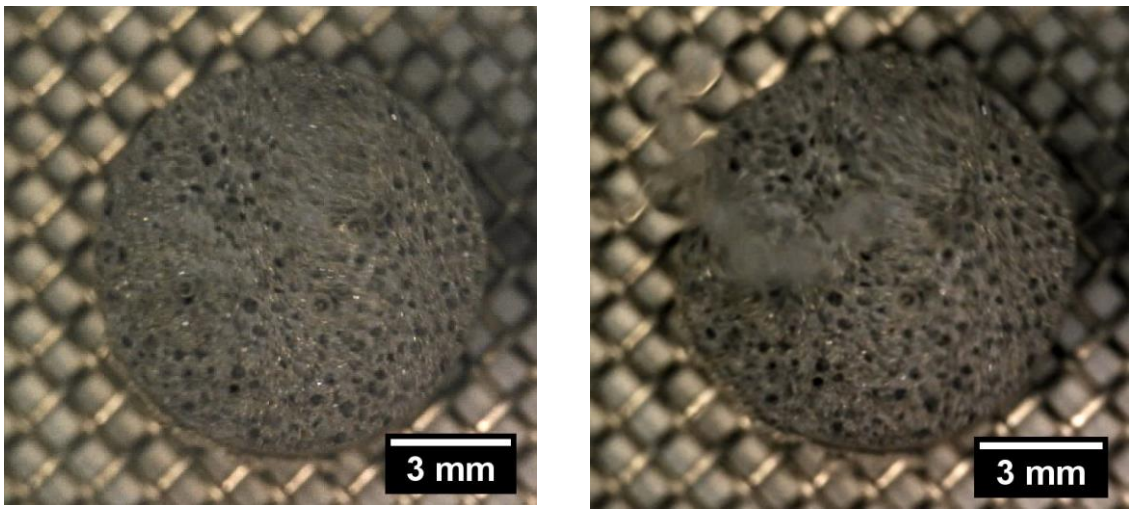

(a) (b)

Figure 64. Image of (a) sample made of a feedstock with a solid loading of 55% of which 50% KCl during debinding without ultrasonic shaking, (b) sample during debinding with ultrasonic shaking

Based on the results, ultrasonic water debinding was chosen to remove both the space holder and the water soluble part of the binder (PEG). However, in order to investigate the effect of ultrasonic vibrations on the samples, another trial of debinding was carried out in an ultrasonic bath and the changes in the sample were monitored using Dino Lite digital microscope which was placed above the ultrasonic bath. It was found that once the sample put in the ultrasonic bath and switched on, KCl and PEG start dissolving from the surface and the solvated molecules depart from the sample leaving porous channels behind. These porous channels act as an exit gate, aiding the process of removing the solvated molecules from deep inside the specimen. It was also noted that a large number of bubbles leave the samples and these bubbles were noted to form both with and without ultrasonic shaking, though their intensity increases with ultrasonic shaking (**Figure 64**). These bubbles were noted to float up to the surface of the water, forming a cloud of bubbles in the case without ultrasonic vibrations, while they break up and new bubbles form if ultrasonic shaking is used.

It is believed that these bubbles are formed due to the presence of trapped air inside the sample which is liberated as the binder dissolves. Once the water diffuses into the inside of the sample, this trapped air tries to escape with the solvated molecules up to the surface of the sample. It was also observed that these bubbles break up in small micro explosions in the general mode of shaking, while they break up and form intermittently in the case of the degassing mode of vibrations. In the sweeping mode, the whole samples move laterally backward and forward in addition to the formation of these bubbles.

5.8 The effect of temperature on dissolution of space holder and binder

Investigating the effect of temperature on the debinding and dissolution stage can help identifying the optimum water temperature for the removal of the PEG and space holder. **Figure 65** indicates the results of debinding and dissolution at different temperatures

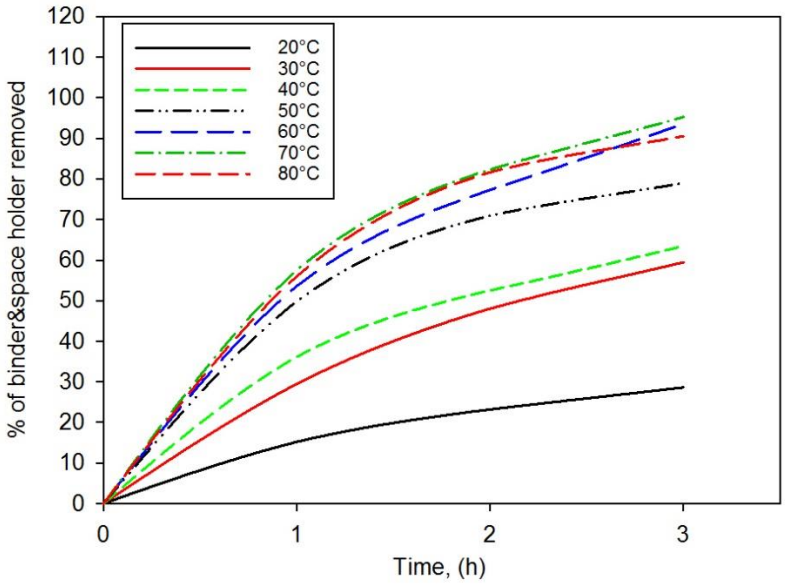

Figure 65. Dissolution curves at different temperatures

In general, as the temperature of the dissolution increases, the rate of removal of the space holder and PEG rises. This is due to faster removal of PEG and KCl at higher temperatures, where there is greater thermal energy for diffusion and activation-dependent processes, especially when the temperature reaches the peak melting point of PEG (50°C). However, this trend changes as the dissolution temperature reaches 80°C, where the removal rate

becomes slower than that at 70°C, particularly after longer dissolution times. This is suspected to be due to the fact that under these conditions the sample was significantly swollen, narrowing the internal channels and making it much harder for the space holder to be removed. Observations of the samples after dissolution found that the sample surface area at 80°C had swelled by around 20 %. This might be due to water uptake by the binder on a microscale; such swelling could also close the channels through the structure, reducing the dissolution rate. Thus, it is not recommended to carry out water dissolution at a temperature higher than 70°C. In addition, the data for the 80°C experiment were not used in constructing the Arrhenius plot which follows, as another mechanism is thought to have been activated by this stage. The weight percentage of space holder and binder removed after three hours of dissolution at 70°C is equal to 95 %, whereas only 28 % was removed after 3 hours of dissolution at 20°C. An example of cube root mass plot obtained under equation 3 for the 30°C experiment is shown in **Figure 66.(a)**. All the tests at different temperatures showed a similar degree of fit. The correlation values for the plotted root mass curves ranged from 0.95 to 0.99. The Arrhenius plot obtained is illustrated in **Figure 66.(b)**.

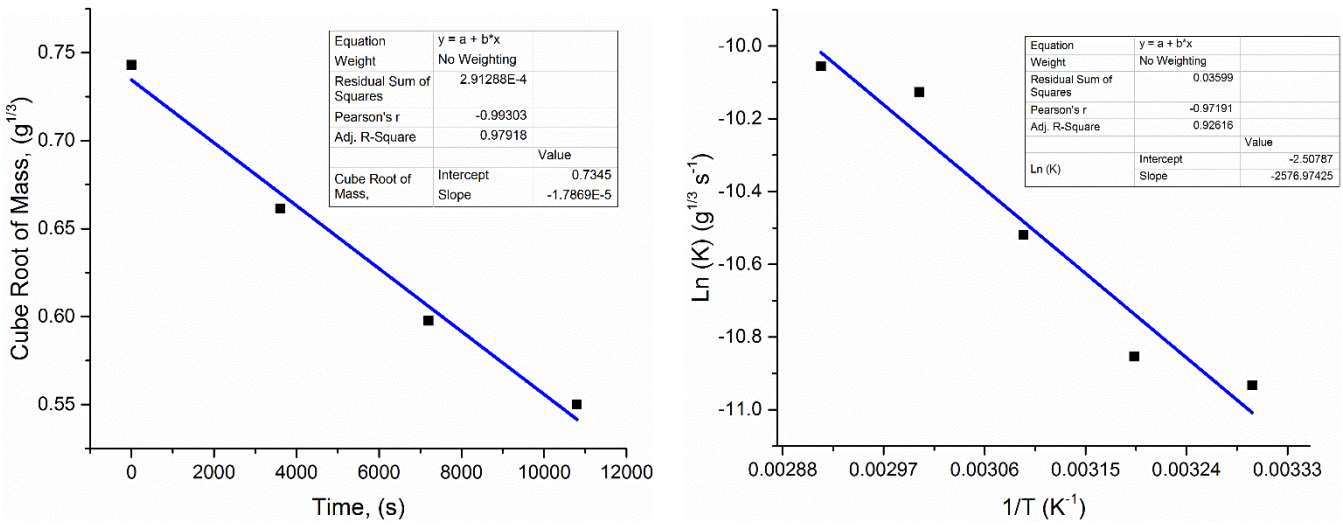

(a) (b)

Figure 66. (a) plot of cube root mass against time for the 30°C experiment, (b) Arrhenius plot for water debound MIM-SH foams at different temperatures.

The fact that these plots show a straight line indicates that the Hixson–Crowell law applies in the first stages of the dissolution and that the process at this stage is not controlled by slow rate diffusion. Thus diffusion does not play a significant role in the first stages of dissolution.

However, its importance in determining dissolution time would be expected to increase at later stages in the dissolution process or where samples have larger size (with additional dependency on sample shape, debinding technique and percentage of space holder). It is also interesting to note that there is not a dramatic departure from the linear fit as the temperature passes the measured peak melting point of the PEG, 50 °C.

The activation energy for the dissolution process was estimated by calculating the negative slope of Arrhenius plot and multiplying it by the gas constant (8.314 J/mol.K). The activation energy for the dissolution process was found to be equal to 21.4 kJ/mol. This value is comparable to the value reported in the literature for dissolution of PEG from injection moulded dense Ti parts, namely 21.5 kJ/mol, and approximately equivalent to the attraction energy between the water molecules (23.3 kJ/mol) [243, 245]. Thus, PEG plays an influential role in the dissolution process and is the main barrier for accelerating it. By contrast, the KCl does not act as the rate controlling phase. The dissolution process takes place by interaction of water molecules with PEG and KCl. KCl dissolves faster than PEG leading to the creation of macropores that replicate the shape of KCl particles. These macropores promote rapid water penetration through the sample. Depending on the dissolution temperature, the hydration process of PEG molecules begins and proceeds at a particular rate. These hydrated PEG molecules move out of the sample leaving amorphous networks of PMMA behind and creating micropores. These amorphous PMMA networks are therefore responsible for providing mechanical stability for the parts after dissolution, but before sintering (the green state).

5.9 Process design of the debinding stage

As noted earlier, the debinding stage makes up the dominant fraction of the time required for the processing of titanium foams by MIM in most currently reported methods. To achieve a feasible processing time industrially, this should be minimised. As expected, and shown above, increasing the temperature is one way to do this, yet this also comes with an associated financial cost. The balance between the two may vary with different applications, and so a selection diagram has been created, based on the data found here (**Figure 67**). As the moment of complete dissolution is difficult to determine precisely, this chart is constructed taking the time to 60% dissolution as a representation of the dissolution speed. It shows that, while

many different sets of conditions could be optimum, depending on the relative importance of keeping temperature or time low, the ultrasonic method would always be preferred, and the optimum conditions for an equal weighting of low time and temperature would be estimated to be ultrasonic conditions at 50°C. Hence, these conditions will be used for debinding samples in all further experiments.

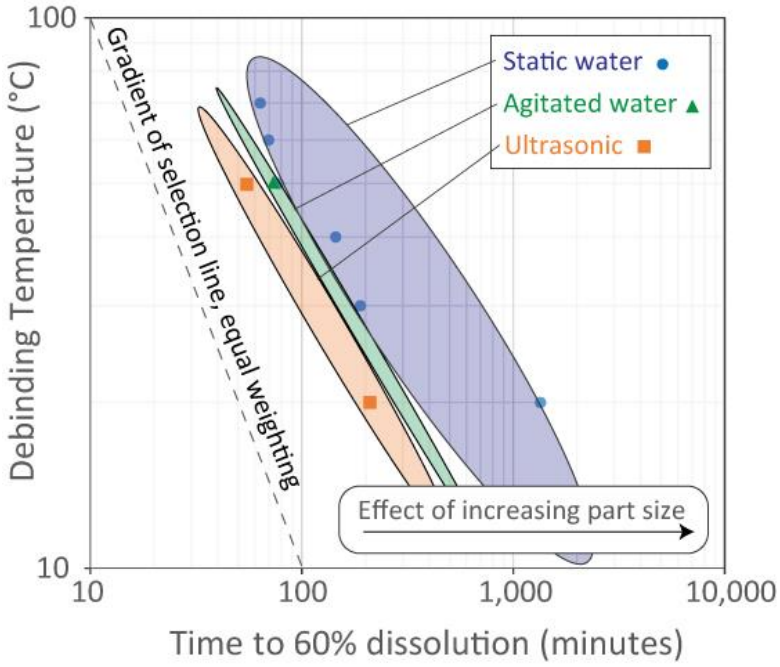

Figure 67. A selection diagram for the different debinding processes explored, showing the trade-off between dissolution temperature and time reproduced from Shbeh, M. and Goodall, R. Mater Design. 2015; 87:295-302. The data points from this study are plotted, along with indicative envelopes of the ranges they occupy. A selection line following Ashby's method is included for the gradient when minimisation of each parameter is of equal importance [246].

5.10 Sintering results for the samples made in the initial trials

To validate that the materials processed were suitable for the production of titanium foams, several debinded samples were sintered using the outlined procedure in **section 3.1.6** after drying them at about 85 °C for 5 min in order to remove any moisture. The sintering process was carried out at 1400 °C for 2 h. The samples were first heated to 450 °C and held there for 1 h in order to ensure the complete removal of PMMA according to the TGA results. There was then a dwell at 800 °C for pre-sintering to give some initial structural integrity

before sintering the samples [18, 247]. Some sintered samples are shown in **Figure 68 (a**), while an SEM image of as-sintered foam surface is shown in **Figure 68 (b**).

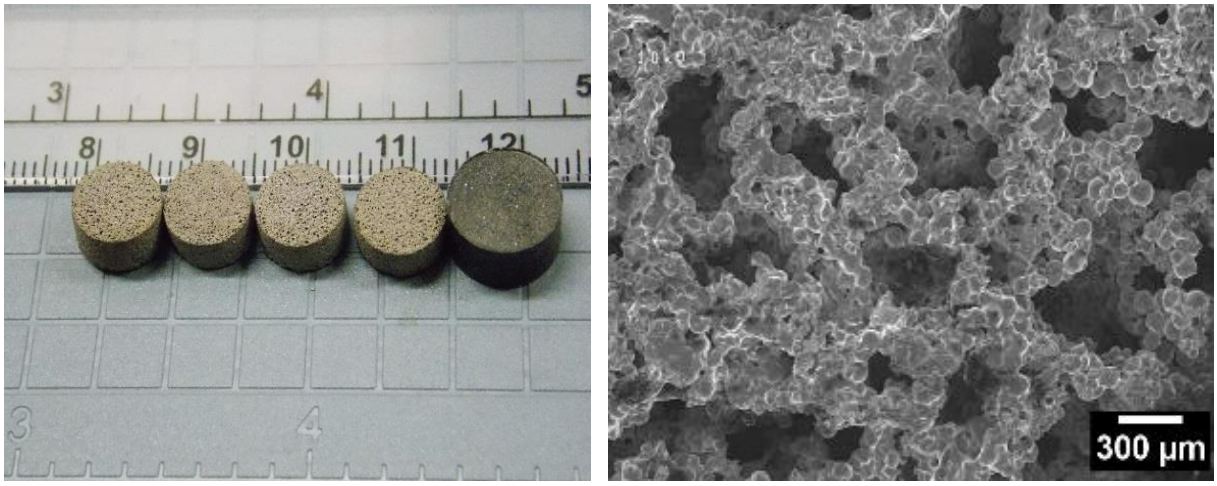

(a) (b)

Figure 68. (a) Un-sintered and sintered samples produced by a feedstock with a 55% solid loading of which 50% was KCl sintered at 1400 °C for 2 using tube furnace, (b). As sintered sample surface reproduced from Shbeh, M. and Goodall, R. Mater Design. 2015; 87:295-302.

As can be seen the shape of the pores has been altered during the sintering process from a cubic shape to approximately elongated irregular pores. The average pore diameter was estimated using the procedure outlined in **3.2.6** and found to be 333 µm with a roundness of 0.38. The change in the shape of the pores is believed to be due to shrinkage during sintering under a relatively high sintering temperature (1400°C) in comparison with what is typically used in the literature (1100-1200°C) [9, 11]. The diameter of the samples shrank by 16.5% to become around 8.6 mm after sintering, while the height of the samples shrank by 12% to be equal to 5.3 mm. It also can be noted that the inner cell walls of the foams are microporous. These micropores will act as microporous bridges connecting the macropores, and should thus lead to higher porosity and permeability. Although some argue that these micropores can be beneficial (e.g.in transporting body fluids and nutrients in biomedical applications [83]), the presence of such micropores can negatively impact the mechanical properties of foams by reducing the load bearing cross sectional area of the cell walls [101]. The true density (i.e. not counting open pores accessible by the helium in the pycnometer area) was

found to be equal to 4.5 g/cm^3 which is equivalent to the density of Ti and an indication that all pores present are open pores, whereas the foam density was equal to 2.005 g/cm^3 meaning that the volume percentage of porosity is equal to 55%. This percentage is much higher than the volume percentage of the space holder, which was about 27.5% vol. This could be attributed to several factors. One of which is the amount of microporosity that results from the partial sintering of the Ti particles. Another is the large percentage of binder used, which decomposes during sintering leaving pores behind that add on to the percentage of porosity. In addition, the presence of initial porosity in the samples before sintering can also play an important role in increasing the porosity in the samples. The presence of the micropores can be ascribed to several parameters such as the relatively large particle size of the starting powder and the low solid loading as well as the nature of binder system used (PMMA, PEG and SA), which is reported to lead to micropores [248]. Increasing the space holder percentage has been observed to lead to decreased cell wall thickness and reduced chances for the formation of micropores among the powder particles [84, 249].

Table 11. Interstitial analysis of the foams produced

Foam	Vol% Space holder	Vol% binder	Sintering Temperature, ℃	% porosity	C wt.%	O wt.%	N wt.%	Cl wt.%
Ti foam, Vacuum Furnace	36	40	1400 for 2h	56	0.091	0.786	0.026	<0.01
Ti foam, Tube Furnace	27.5	45	1400 for 2h	55	0.672	0.730	0.042	<0.01
Ti foam[11]	25	50	1200 for 4h	36	0.17	0.66	0.020	-

One critical issue in producing Ti parts by MIM is carbon and oxygen contamination during processing (mainly during debinding and sintering stages). It has been shown that the binder system used can give low content of these interstitial elements [109]. Carbon, oxygen and nitrogen content in an example of a MIM foam sintered at 1400 for 2 h in both a vacuum and a tube furnace with flow of argon were assessed using a LECO melt extraction system by

AMG Superalloys, Rotherham. Chlorine content was also assessed as a means to check the removal of the KCl. The results are shown in **Table 11**, and are compared with a Ti foam produced by MIM in the literature using NaCl as a space holder and a binder composed of PEG, low density polyethylene, paraffin wax and SA [11].

The low chlorine content indicates that KCl removal has been largely successful. In addition, the results indicate that the type and cleanliness of the furnace used play a significant role in dictating the extent of contamination during debinding and sintering as the carbon content for foams produced in a vacuum furnace was much less than that for foams produced in a tube furnace under flowing argon. The level of oxygen found is also quite high for titanium foams generally, which would be expected to impact the mechanical properties, a result that is comparable to material from the literature. This problem can be addressed by improving the vacuum of the sintering environment and reducing the sintering temperature [120, 250]. It is worth noting that the amount of interstitial elements is significantly higher in the Ti foams produced using the vacuum furnace compared to the relatively dense samples produced without space holder (the data of which are reported in **section 4.3**). The carbon and nitrogen contents increased by 13%, while the oxygen content rose by 64.8%. This significant increment in contamination in the samples processed with space holder could be ascribed to two main factors. The first one is the percentage of binder in the feedstocks prepared, where the percentage of binder for the relatively dense samples processed without space holder was 42% of which 25% PMMA, whereas the percentage of binder for samples processed with space holder was about 45%. Thus higher binder content means more PMMA to be thermally debound during sintering and consequently result in more contamination in the samples. The second reason is the differences in the sintering programme, as samples without space holder sintered at a lower temperature (1320 °C) and without a dwell at 800 °C for 1 h. Sintering the Ti foams at a higher temperature and having a dwell time at 800 °C for 1 h might have increased the exposure of Ti to these contaminants during the sintering cycle leading to increased level of contamination. Kato studied the extent of contamination in Ti parts produced by MIM using a gas atomised Ti powder [251]. He reported that the oxygen content in the Ti parts is influenced by the sintering temperature, and found that the oxygen content was increased by 39.3% when the sintering temperature was raised from 975 °C to 1075 °C for 2h. Thus it was decided to follow the sintering programme and the solid

content used for parts without space holder for further foam processing in order to avoid any excessive contamination and reduce the oxygen content. After establishing a standard procedure for preparing feedstocks with space holder and identifying appropriate debinding and sintering programme, the next step or chapter is devoted to investigate the effect of increasing the space holder volume percentage on the porosity and mechanical properties of both green and sintered foams.

6 Effect of space holder on porosity and mechanical properties

6.1 The effect of the space holder on the initial porosity and green strength

The presence of any initial porosity in the feedstock as well as in the samples before sintering (green samples) can hugely impact the green mechanical strength of the samples as well as their final mechanical properties. The amount of this porosity depends on several factors such as the volume percentage of binder added to the mixture, particle size and shape of the Ti powder as well as the temperature of extrusion and injection for both of the feedstock and samples respectively. Good volume percentage of binder and low viscosity are required to achieve low initial porosity by efficiently wetting the Ti particles and bonding them together. However, increased amount of binder can result in an increase in the volume shrinkage of samples. Therefore, a balance between those two must be reached for reduced initial porosity and acceptable volume shrinkage.

Adding another material to the feedstock during mixing in addition to the Ti (such as the space holder) can make it more difficult for the binder to wet all of the particles without leaving voids, consequently resulting in an increased amount of initial porosity, depending on the mixing procedure. Thus, it is important to investigate the effect of adding space holder to the samples on the initial porosity and green strength in order to assess the ability of these samples to withstand mechanical handling before debinding, as well as making sure that this initial porosity is maintained at an acceptable level. Therefore, five feedstocks were made, one without space holder addition and four with four different volume percentages of space holder (KCl), namely 17, 35, 52 and 60% vol. The percentage of solid loading in the feedstocks prepared was 58%. The mixing procedure was carried out according to our previous experiments. All feedstocks were extruded at the same temperature (150°C) twice and then pelleted into small pellets before injecting cylindrical samples with a 10 mm in diameter and 13 mm in height at an injection temperature of 150°C and pressure of 45 MPa. The initial porosity of the samples was determined using a helium pycnometer, while the

compressive green strength of the samples was assessed using Zwick Z050 system at a strain rate of 0.001 s^{-1}. Compliance testing was carried out and data were subtracted from the results. The results of the pycnometer measurements as well as the compression tests for the samples are shown in **Figure 69**.

It can be seen from **Figure 69** that the initial porosity in the samples generally increases slightly with the addition of space holder and there are no significant differences in the amount of porosity among samples with different volume percentages of space holder, whereas the results of the mechanical tests showed that the green compressive strength of the samples decreases with increasing amount of KCl powder in the samples, with the highest strength for samples having no space holder. The decrease in the strength with increasing the space holder percentage could be attributed to the large particle size of the KCl and its small surface area compared to the Ti powder, resulting in weaker bonding to the polymeric binder. The strength of such composites made of polymer with fillers like Ti and KCl is strongly dependent on the efficiency of the stress transfer between the polymer matrix and the mixture of Ti and KCl fillers, and this efficiency is reliant on how well these fillers are bonded to the polymer. If the large KCl particles do not bond well to the polymer matrix, then inefficient load transfer occurs due to the inability of the large KCl particles to carry and transmit any load. Thus the strength decreases with increasing KCl content. It is also generally reported that the strength of particle reinforced polymer composites increases with reducing the particle size of the fillers and increasing their amount up to a certain limit beyond which the strength decreases [252]. Hence, exchanging the smaller Ti particles with more weakly-bonded, larger KCl particles would result in a deterioration in the strength of the composite. It was also noted that failure occurs in the samples by forming one or two cracks at 45° and these cracks grow gradually to the other end of the sample as shown in **Figure 70**. In addition, it was also observed that KCl particles are ejected from the sample as the samples are compressed and settled on the platens of the compression testing machine, which can be taken as an evidence for the weak bonding between the KCl particles and the binder compared to the Ti particles, which stayed bonded to the binder.

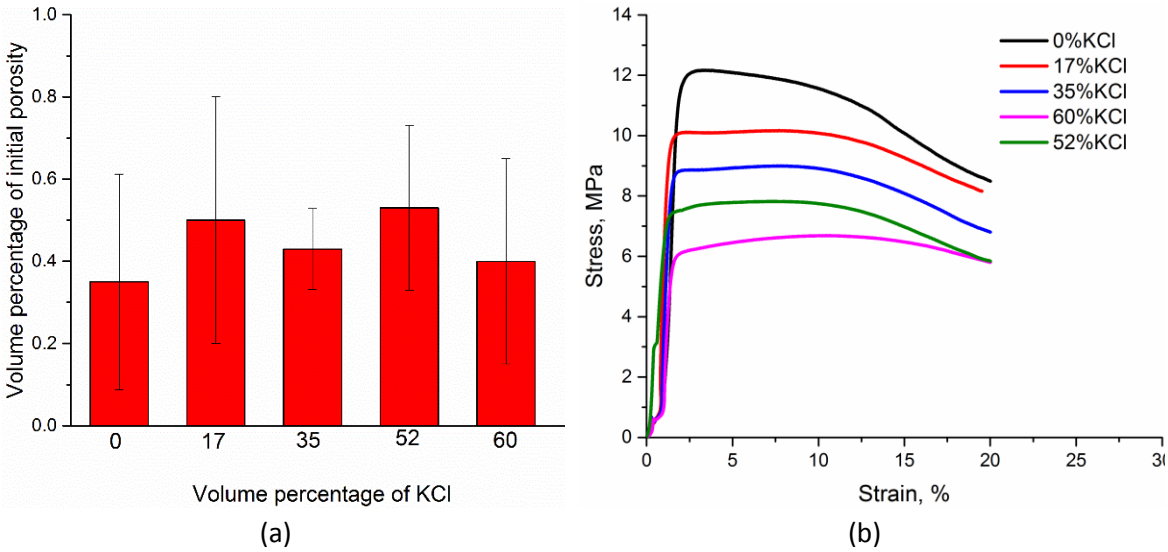

Figure 69. (a) The amount of initial porosity in the green samples with the space holder added, (b) The green strength of the samples with the space holder.

Figure 70. Green samples with 0, 17 and 35 vol % space holder after compression testing at a strain rate of 0.001 s^{-1}.

6.2 The relationship between the space holder percentage and the amount of final porosity and strength

The volume percentage of final porosity in the samples depends hugely on the amount of space holder added to the mixture as well as the sintering parameters. Sintering samples at high temperatures for longer times can lead to better bonding between the Ti particles and the formation of complete necks, but at the same time it can reduce pore volume, increase volume shrinkage as well as resulting in closure of the pores. Thus, care must be taken during sintering of porous materials. In order to investigate the effect of the space holder volume

percentage on the final amount of porosity, four groups of samples with different volume percentages of KCl were synthesized, water debinded and sintered at 1320°C for 2h. The solid loading in the feedstock used was 58%vol. The percentage of space holder in the feedstock ranged from 17-60 vol%. The space holder used was spherical KCl and its particle size distribution is shown in **Table 12**. An additional group of samples was made without adding space holder as a control. Samples were tested under compression at a strain rate of 0.001 s^{-1}. The volume percentages of porosities for samples as well as their compression behaviour are depicted in **Figure 71.(a)** and **(b)**.

Table 12. Particle size distribution of the space holder used

D_{10}	241 μm
D_{50}	366 μm
D_{90}	544 μm

It can be seen from **Figure 71 (a)** that the relationship between the space holder amount added to the mixture and the final amount of porosity in the foams is not linear and follows a more complex one-phase exponential decay function in increasing form, where the percentage of porosity in the samples seems to increase very rapidly at first, and then the increase slows down to become asymptotic to an upper limit. This might be ascribed to increased volume shrinkage in the samples with increasing amount of space holder. Increasing the space holder percentage will result in more connections between the KCl particles in the green samples and increased distance between the Ti particles surrounding the space holder. Thus these Ti particles have to travel further during sintering to initiate atomic bonds between each other and form cell walls, and these movements will consequently result in more volume shrinkage in the samples. This hypothesis could be supported by the amount of shrinkage measured in the sintered samples with the amount of space holder added which is shown in **Figure 71 (c)**. It has been found that the amount of volume shrinkage in the samples increases exponentially with increasing the amount of space holder added. This could also be supported by the finding of Laptev et al that with increased amount of space holder added, the samples lose their stability and collapse under the action of gravity [139]. In addition, it was also noticed that the compressive strength of the foams

was dramatically reduced with increasing the amount of porosity (**Figure 71 (b)**). Furthermore, the stress-strain curves for foams made with high volume percentage of porosity, particularly those made with 52 and 60% vol. space holder, showed clearly a very long plateau region before densification compared to those with low volume percentage of porosity, where this plateau region is shorter and not well-defined, and the densification region is more prominent. Similar observations were reported in the literature for foams made by the space holder technique by Esen and Bor [24], where they stated that the plateau region starts to disappear with reduced porosity and the stress after yielding increases sharply. Foams with a large amount of porosity may have more uniform porous structure with more uniform deformation to densification while those with a lower amount of porosity reach densification earlier.

In terms of the relationship between the relative density and the yield strength of the foams produced, the range of the data obtained seems to fit both linear and power law regressions as shown in **Figure 71 (d)** provided that the law's exponent for the latter regression is equal to 2.17±0.25. It should be noted that the value is slightly higher than that predicted by Ashby for open cell cellular materials, where the value reported is 1.5 according to the following equation [253]:

$$\frac{\sigma_f}{\sigma_s} = C\left(\frac{\rho_f}{\rho_s}\right)^{3/2} \qquad (14)$$

where σ_f is the yield strength of the foam, σ_s is the yield strength of dense or solid Ti and was assumed to be 450 MPa for pure Ti [254], C is a proportionality constant (which is, however, well-known to take slightly different values), ρ_f and ρ_s are the densities of the foam and solid Ti respectively. One study reported an exponent value of 3.57 and proportionality constant of 2.13 for foams with porosities ranging from 45-69.8% produced by the space holder technique and ascribed the difference to parameters that are related to the mesostructure of the foams produced such as cell morphology, shape and curvature of the cell walls [24]. It also reported that Gibson-Ashby model is only applicable for foams with volume percentage of porosity about 70% or higher. Although the value obtained here is closer than that reported in their study to the predicted value, the porosity is below 70% and this might have resulted in the small discrepancies in the exponent value. It is also worth

noting that the data obtained here can also be fitted using linear regression, in agreement with the results reported by Wang et al [133]. Hence, it is difficult to draw a firm conclusion and be certain of the overall trend of relative yield strength with relative density due to the limited range of porosity studied here which might lead to a potential error in predicting the general trend.

The results of the DIC analysis for compression of cylindrical samples of foams made by 17 and 52% KCl are shown in **Figure 72**. This shows sections of the curved surface analysed to produce strain maps (ε_1 shown), with the colour indicating the measured local strain. Thus the red end of the spectrum indicates the regions where longitudinal strain is concentrated. It was found that much of the strain is concentrated at 45° in the samples in a similar manner to the failure of the green state and thus failure is likely to occur by plastic deformation leading to the growth of cracks in these regions driven by the shear forces. Compared to foam made by 52% KCl, foam made with 17% KCl was much less deformed, which is expected due to reduced volume of porosity and improved mechanical strength.

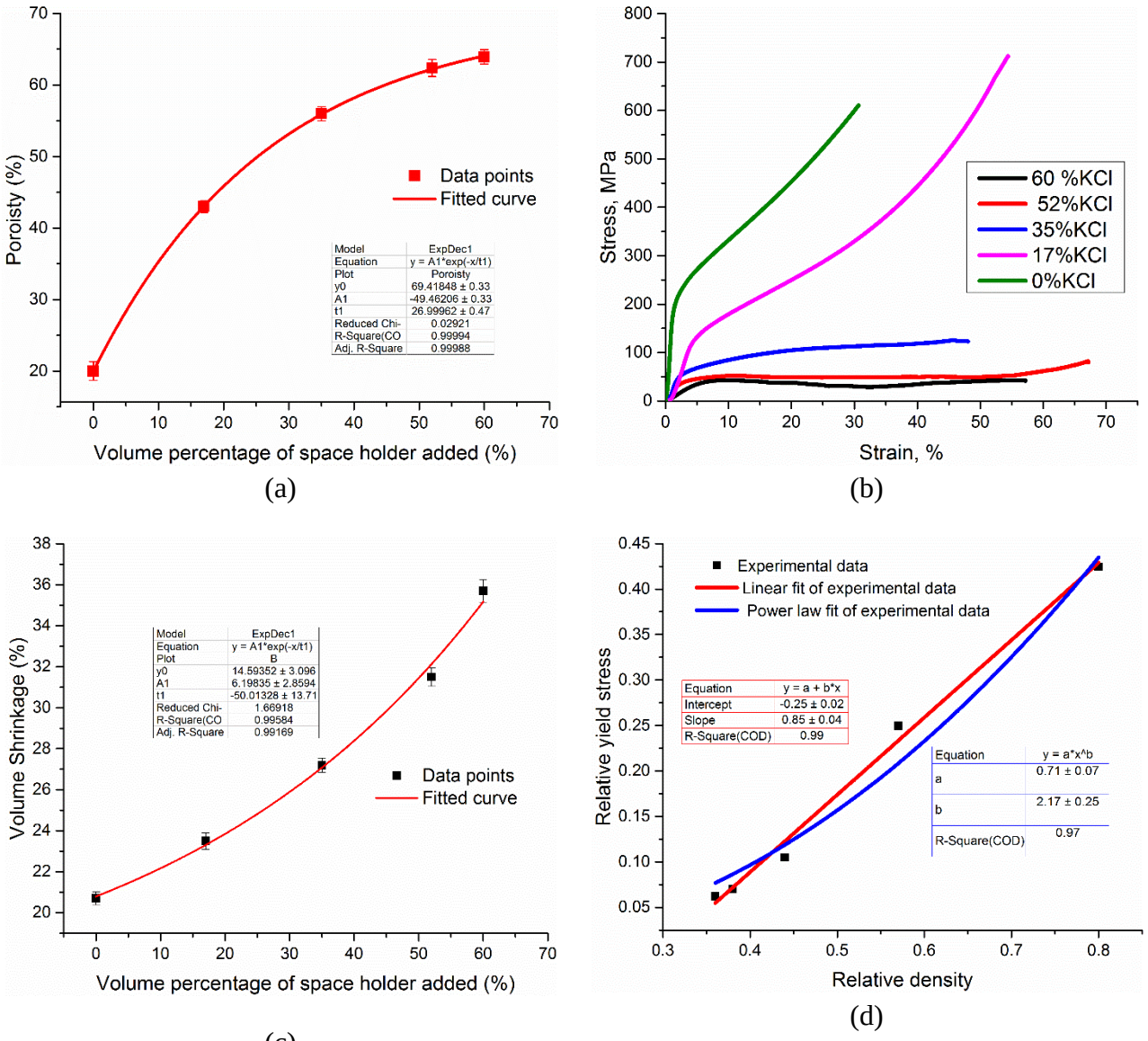

Figure 71. (a) the relationship between the amount of space holder added and the final percentage of porosity in the sintered samples, (b) mechanical strength of samples with different amount of porosity under compression, (c) The relationship between the amount of space holder added and the volume shrinkage of samples after sintering, (d) The change in the relative yield stress with the change in the relative density with two fitted curves, namely linear and power law.

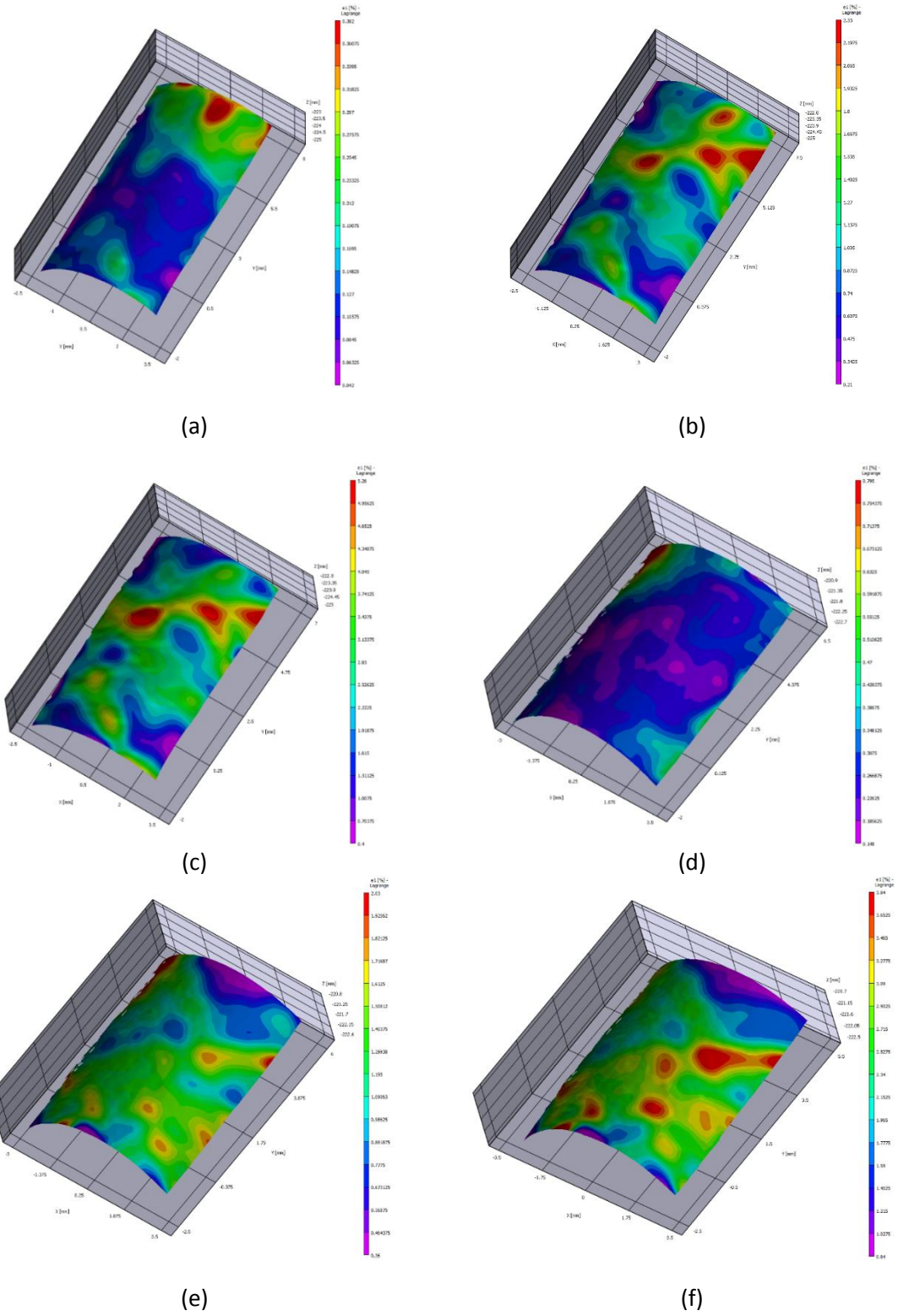

Figure 72. The results of the DIC showing: (a) Ti foam made by 52% KCl after 5% deformation, (b) Ti foam made by 52% KCl after 17% deformation, (c) Ti foam made by 52% KCl after 15% deformation, (d) Ti foam made by 17% KCl after 5% deformation, (e) Ti foam made by 17%KCl after 10% deformation, (f) Ti foam made by 17% KCl after 15% deformation.

6.3 Effect of filling pressure of pycnometer on the percentage of porosity

The helium filling pressure of the pycnometer can have an effect on the amount of porosity calculated. Generally, the higher the filling pressure the more the helium is able to penetrate smaller micropores and consequently, the more the results are accurate. Nevertheless, this comes at a price, where the time of testing could be dramatically increased from about 20 minutes per sample to 70 minutes depending on the filling pressure and the number of cycles for purging. In order to investigate this, three pycnometer measurements were carried out on a foam made by adding 52 % of space holder using three different filling pressure values 10, 15 and 19 psi (corresponding to 689, 1034 and 1310 in mbar). The results of these measurements are shown in **Figure 73**

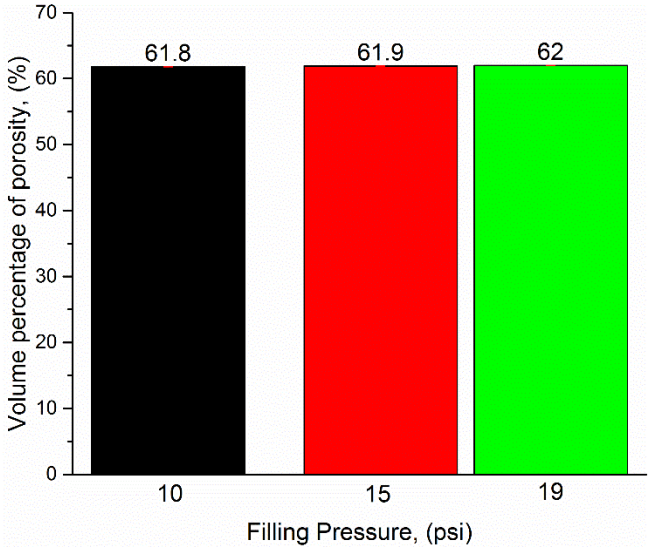

Figure 73. Effect of helium filling pressure on the final amount of measured porosity.

It can be noted that increasing the filling pressure results in only a slightly higher estimation of porosity and this can be attributed to the presence of very small micropores that are not easily penetrated using low filling pressure. Nevertheless, these pores do not significantly contribute to the total percentage of porosity. Thus, a filling pressure of 10 psi was chosen for all further measurements of porosity.

6.4 The effect of the shape and size of the space holder

The influence of the space holder particle's shape and size on the initial and final amount of porosity in the feedstock and samples were investigated by preparing four different

feedstocks with different particle shapes and sizes of space holder, namely cubic KCl particles with mean particle size of 336 µm (CU336), cubic KCl with mean particle size of 381 µm (CU381), spherical KCl with a mean particle size of 380 µm (SP380) and spherical KCl with mean particle size of 607 µm (SP607). The particle size distributions for the KCl powders used are shown in **Figure 74.**

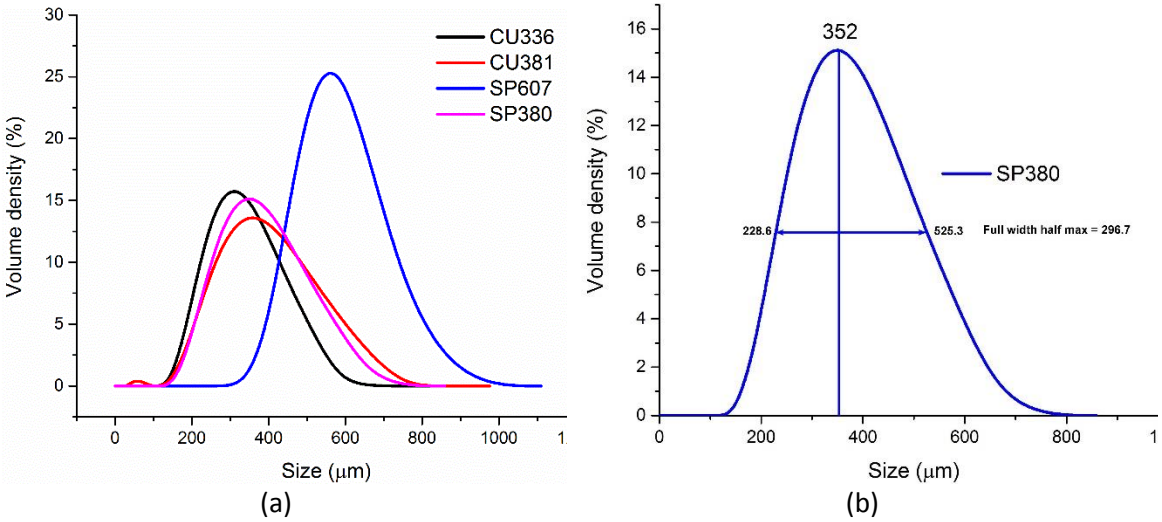

Figure 74. (a) The particle size distribution of KCl used, where CU336 is a cubic KCl with mean particle size of 336 µm, CU381 is a cubic KCl with mean particle size of 381µm, SP607 is a spherical KCl with mean particle size of 607 µm and SP380 is a spherical KCl with mean particle size of 380 µm, (b) An example for calculating the full width at half maximum for space holder SP380

In order to compare the particle size distribution width for the space holders used, the full width at half maximum was determined for each space holder by drawing a horizontal line at 50% of the maximum and finding the difference between the two values that intersects the drawn line (see **Figure 74 (b)**) [255]. It was found that SP380 and SP607 space holders had the highest full width at half maximum, as the values were 294.6 and 271.1 µm respectively compared to those for CU381 and CU336 space holders, which were 253.4 and 188.3 µm respectively. Hence, spherical SP380 had the widest particle size distributions compared to other space holders. The percentage of the solid content in the feedstocks prepared was 58% of which 60% was KCl. The feedstocks were prepared and extruded using the same procedure mentioned previously and injection moulded at a temperature of 150°C. Several samples of each of those feedstocks before and after injection of samples have been taken and tested using a helium pycnometer at a pressure of 10 psi. The results were compared with the

theoretical density and the percentage of porosity was calculated using the following equation:

$$\text{Porosity (\%)} = \frac{\text{Expected Density} - \text{Measured Density}}{\text{Measured Density}} \quad (15)$$

The percentage of initial porosity in the feedstock was found to be highest in the feedstock made with CU336, where it was equal to 1% and this value reduced to 0.6 % after moulding of the samples. In comparison, other feedstocks had negligible amount of porosity ranging between 0.4 for feedstock made with CU381 to about 0.3 and 0.1 for feedstocks made with SP380 and SP607 respectively. Thus it seems reasonable to say that the space holder particle size has also to some extent an effect on the percentage of initial porosity in addition to the shape and size of the metal powder as well as the type of binder. This difference in the percentage of porosity can be attributed to the surface area of the particles. As the size of the KCl particle increases, the surface area to volume ratio decreases, thus keeping the volume percentage of porosity low by requiring less amount of binder to wet the KCl particles. Finer KCl particles on the other hand have higher surface area to volume ratio and require more binder to wet the particles. Although this porosity was noticeably reduced during the injection stage, there is still a small difference in the percentage of initial porosity between the prepared feedstocks.

Several samples were sintered from each feedstock at 1320 °C for 2h after water debinding at 50 °C to check the percentage of final porosity in the foams produced. The results are shown in **Figure 75**. It can be seen from **Figure 75** that foams produced by CU381 space holder had the highest porosity compared to other foams with a total average volume of porosity about 64.4% and a standard deviation of 0.4. This might be due to having a better packing density resulting in improved pore connections, by smaller KCl particles sitting among larger ones. Despite the fact that it had the widest particle size distribution, samples processed with space holder SP380 had slightly less porosity than those processed using CU381 space holder and approximately equal to those made by CU336 and SP607. Thus, our findings seem to suggest that the shape of the space holder does not have a significant impact on the percentage of final porosity in our system, unlike what has been reported in the literature for other systems [11, 256].

SEM images of each group of the sintered samples which are made by different sizes and shapes of space holders are illustrated in **Figure 76.** All of the samples showed interconnected macropores with microporous cell walls surrounding them and the shape of the pores replicates the shape of the space holders used. The average pore diameter in the Ti foams produced and their degree of roundness were analysed on multiple images using image J software, and are summarised in **Table 13**. Generally, the average pore diameter for samples was noted to be somewhat lower than the average particle size of the space holder used. This could be ascribed to pore shrinkage during sintering as the space holder is removed during water debinding leaving a network of open pores without any mechanical support during sintering. Furthermore, the roundness and the uniformity of the shape of the pores in the foams produced with spherical space holder were much higher than that for samples made with cubic space holder.

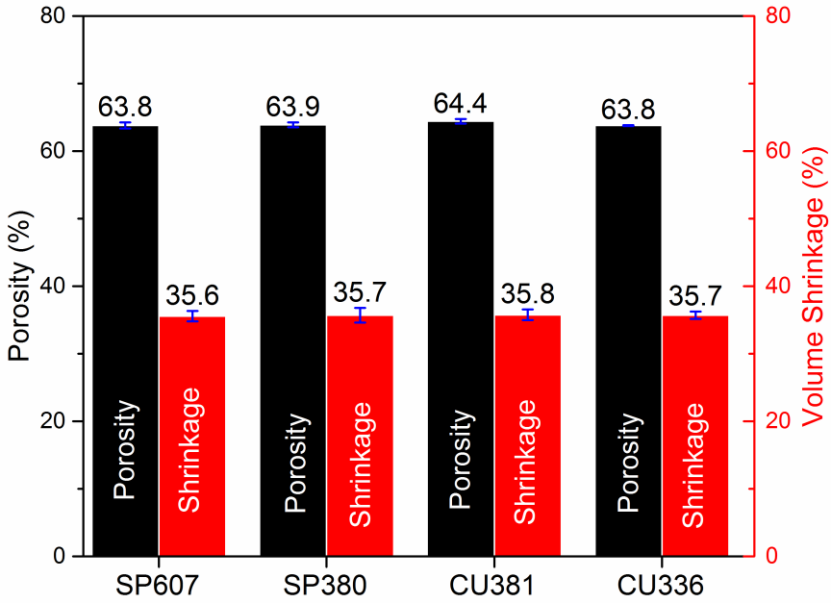

Figure 75. The relationship between the shape and size of space holder added and the final percentage of porosity and shrinkage in the sintered samples.

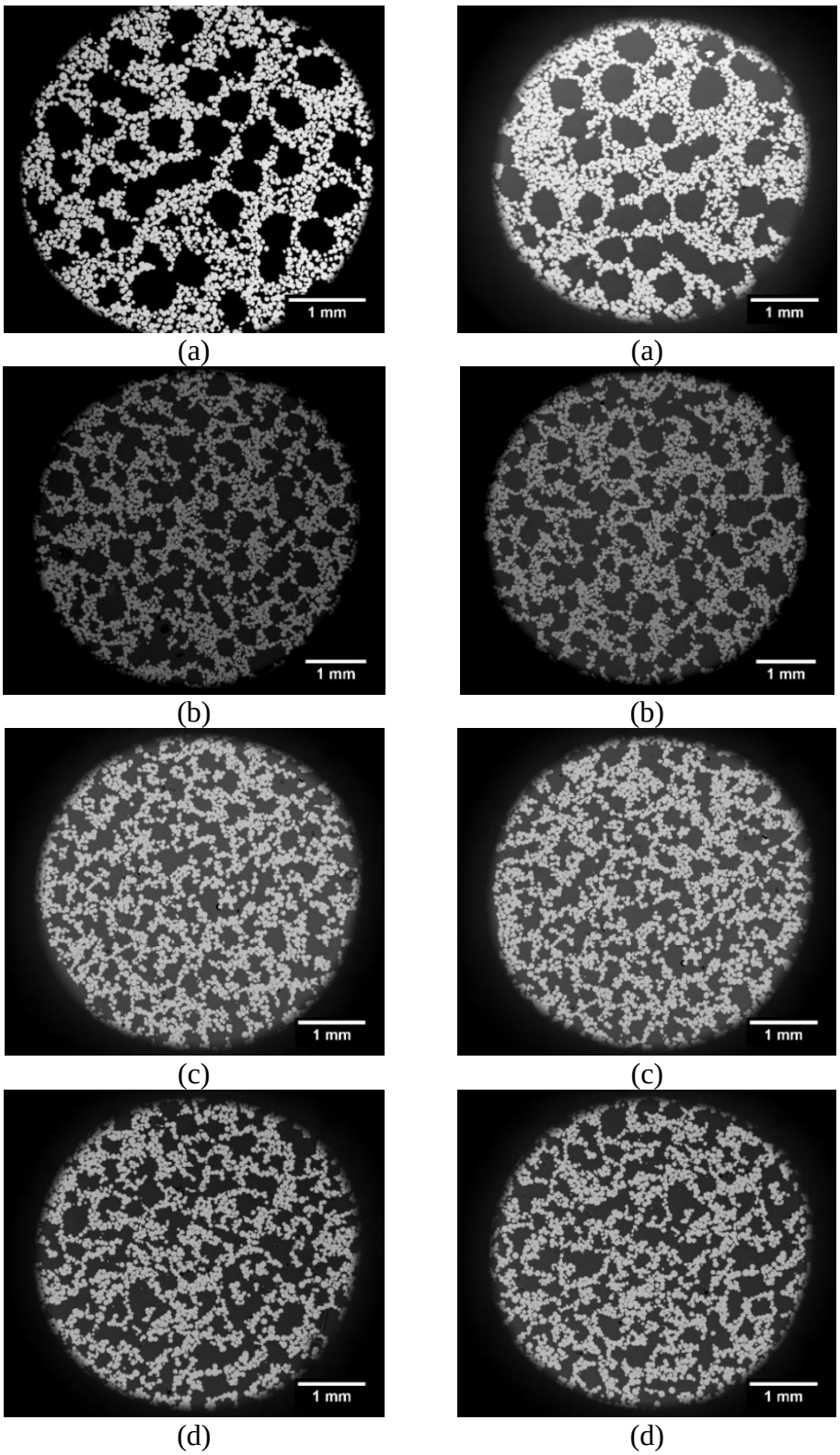

Figure 76. SEM images of: (a) Ti foam made using SP607 space holder, (b) Ti foam made by SP380 space holder, (c) Ti foam made by CU336, (d) Ti foam made by CU381.

The results of the compression testing of the Ti foams made by different shapes and sizes of space holders are shown in **Figure 77**. The results of the compression testing demonstrated that Ti foams made by spherical space holder have higher yield stresses than those made with the cubic space holder. This might be due to the shape of pores present in the samples, where cracks can initiate more easily in the samples with irregular and angular pores compared to regular spherical pores as they act as stress concentration sites with preformed crack tips or sharp corners, and thus samples yield at a lower stress value. Similar findings were reported in the literature for foams made with the space holder technique [257] as well as foams made by the entrapment and expansion of argon gas technique [258]. SEM images of the foams after failure are shown in **Figure 78**. It was noted that all of the samples showed signs of a striated failure structure with some marks that resemble beach marks in fatigue failure. Furthermore, EDS results showed that samples were mainly composed of Ti with some interstitial elements and no signs of other phases which are usually reported in foams due to the interaction of the space holder material with Ti. This could be taken as an indication of the success of the process of removing the space holder by the ultrasonic water debinding [96, 139, 256].

Table 13. Average pore diameter in the Ti foams produced

Feedstock used	**Average pore diameter (μm)**	**Standard Error**	**Roundness**	**Standard Error**
Cu336	320	12	0.66	0.04
Cu381	370	8	0.69	0.04
SP607	541	5	0.80	0.05
SP380	362	10	0.76	0.07

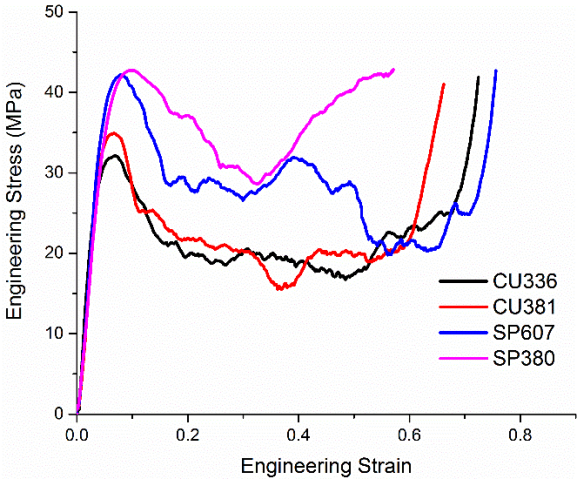

Figure 77. Mechanical strength of foams under compression testing at a strain rate of 0.001 s^{-1} made by cubic KCl with mean particle size of 336 µm (CU336), cubic KCl with mean particle size of 381µm (CU381), spherical KCl with mean particle size of 607 µm (SP607) and spherical KCl with mean particle size of 380 µm (SP380).

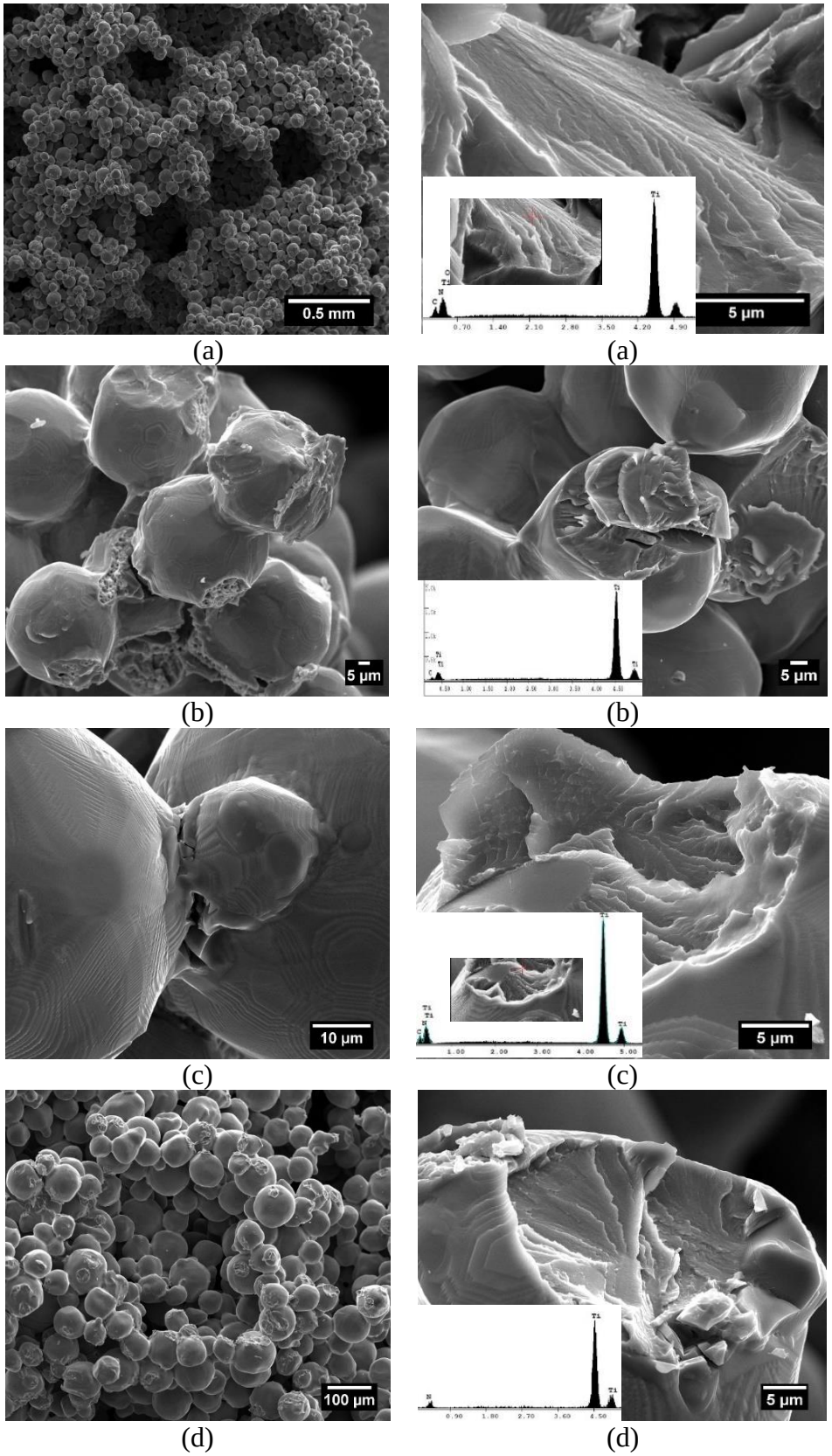

Figure 78. SEM images of Ti foams after compression testing made with: (a) SP607, (b) SP380, (c) CU336, (d) CU381.

6.5 Micro-CT analysis of the foam produced

Two samples of Ti foam produced with a porosity percentage of about 61.25%±0.29 were analysed using micro CT in order to assess the pore size distribution in the sample produced and compare the results of the pycnometer measurement of porosity with the results of the micro CT by analysing the sample in 3D using CTAn software. **Figure 79** shows the Ti foams analysed with a 3D volume rendered 4 mm diameter section of the foam produced.

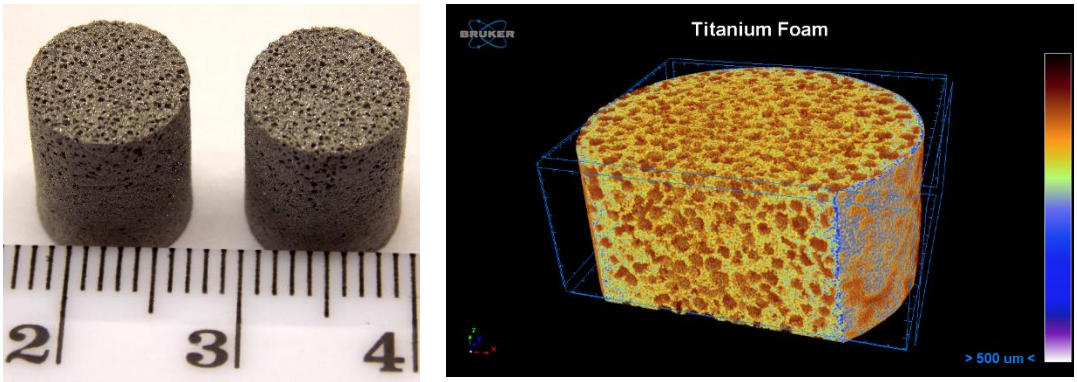

(a) (b)

Figure 79. (a) Ti foams with 61% porosity, (b) Volume rendered model of a 4mm section of the foam produced. The colour spectrum indicates density, with dark red being lowest density and blue the highest.

The results of the 3D analysis of the micro CT showed that the foam had a total percentage of porosity of about 61.5% of which 0.18% is closed porosity. This result is in good agreement with the pycnometer measurement, provided that a lower grey threshold value of 70 is applied during the analysis of the data of the micro CT (see **Figure 80**), as this value dictates the appearance of each voxel in the scanned data. Increasing the lower grey threshold value to 80 would increase the measured porosity to around 68.48%, whereas reducing the value to about 60 would results in a decrease in the measured porosity to about 54.47%. It was also found that the foams produced had a denser outer layer with a much lower amount of macropores compared to the centre of the sample. This is expected due to the fact that the KCl particles cannot get closer to the surface than when they were touching the mould. This observation can be clearly seen in the volume rendered CT section, where the colour bar is indicative of the density difference between different regions in the foam.

The blue colour refers to the highest density part of the foam, while the dark red colour refers the lowest. This distribution of density difference is potentially quite beneficial, particularly for biomedical applications, as this structure mimics the structure of the bone, where the outer layer provides strength and structural integrity, and the inner layer consists of micro and macro porous channels, that enable bone ingrowth, nutrient exchange, as well as cell migration and attachment [259].

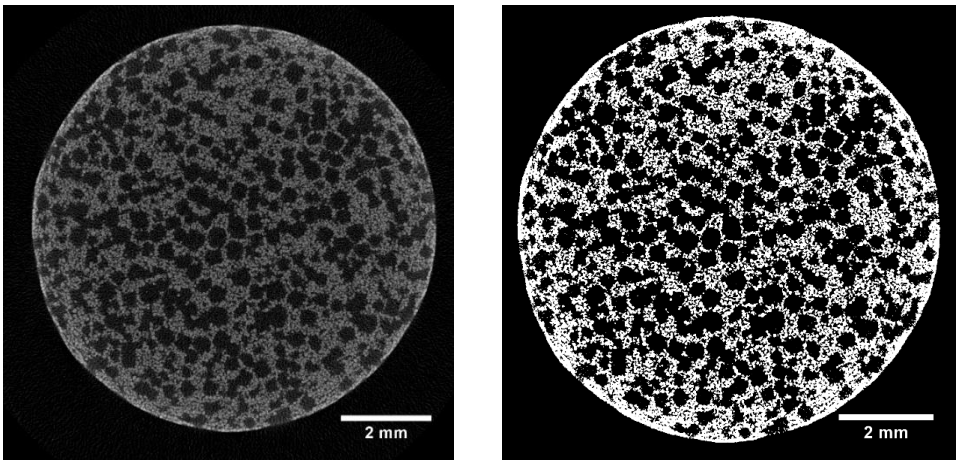

(a) (b)

Figure 80. (a) Transverse cross-section before binarization, (b) Transverse cross-section after binarization with a lower grey threshold value of 70.

Table 14 shows some important parameters for the analysed 4 mm section of the foam which were obtained via the micro CT analysis. As seen from the data, the surface area of all the solid objects within the volume is more than 22 times higher than the surface area of the volume scanned (i.e. the area of the cylinder-like section) showing the much greater internal surface area that these foams have as a result of their porosity with great potential for biomedical applications.

The results of the pore size analysis are shown in **Figure 81**. It can be clearly seen that there are two distinctive regions in the curve, one with much more narrow Gaussian distribution starting from 6 μm and extending up to 67μm, reflecting the size of the micropores that result from incomplete sintering of the Ti particles. The second region has a much wider Gaussian distribution with larger sizes of pores up to 481 μm, which reflects the broad range of the KCl particle size distribution that was used in this study. It is important to point out that there is a transitional region that connects the microporous region with the narrow Gaussian

distribution from the KCl induced macroporous region with the wide Gaussian distribution, and the pores in this third region range from 67-150 µm. Hence, the foams produced have a very wide pore size distribution with high interconnectivity and resemble the natural cancellous bone structure, where the pores in cancellous bone vary in sizes and can reach up to 470µm [80, 260]. Having this broad pore size distribution is also important in relation to biomedical applications for osteoconductivity as it has been reported that for the metal foam to be osteoconductive, it has to have pore sizes in the range of 100-500µm [261].

Table 14. Some characteristic parameters obtained via CT analysis

Parameter	**Value**
Total volume of a 4mm section (mm^3)	248
Object or solid volume (mm^3)	95.60
Surface area of the Total Volume (mm^2)	254
Surface area of solid object (mm^2)	5790
Surface area of closed pores (mm^2)	40.20

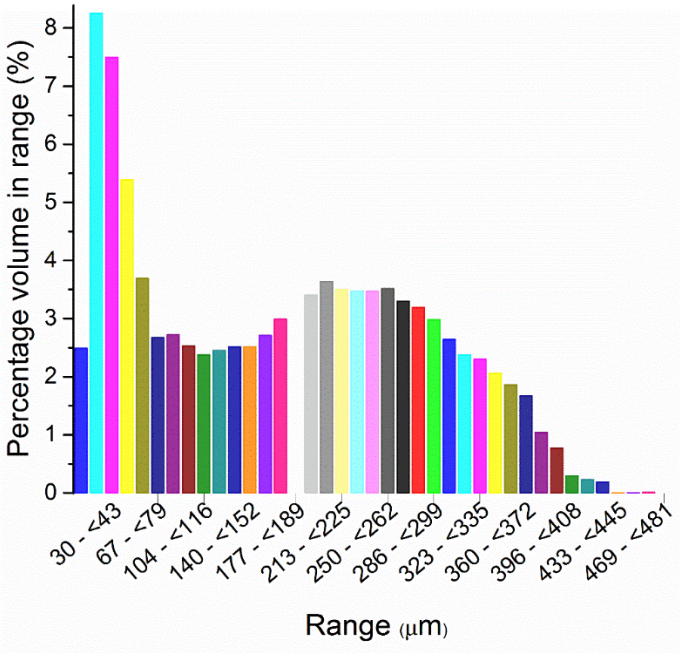

Figure 81. Pore size distribution in the Ti foam produced. Pore sizes ranged from 6 to 100 µm for micropores and from 100 to 480 µm for macropores. Although these ranges intersect, the distribution showed concentrations around these two separate size ranges, leading to the description in terms of the two pore types.

6.6 Processing of multi-layered porous samples and complex biomedical products

Most of the bones in the human body are composed of an outer compact shell characterised by relatively high density and low porosity, namely cortical bone surrounding a core of spongy and highly porous cancellous bone with lower density [262]. An example of such a bone is the femur (see **Figure 82**). However, in some cases such as the calvaria (skullcap), the structure of the bone is composed of a sandwich of relatively dense cortical layers on the outer surface with a layer of reinforcing cancellous and spongy structure [263]. Making foams that mimic the structure of such a bone with a hierarchically organised structure and gradient porosity by one manufacturing step would be extremely difficult without having the ability to join different porous layers with different pore sizes and volume percentage of porosity. Furthermore, processing of porous foams with gradient porosity is a little-explored area, yet is of great importance as components making use of porous titanium are likely to also require dense regions (e.g. for strength) and the bond between the two is critical. In order to achieve this, samples were injection moulded using sequential injection moulding with different feedstock compositions.

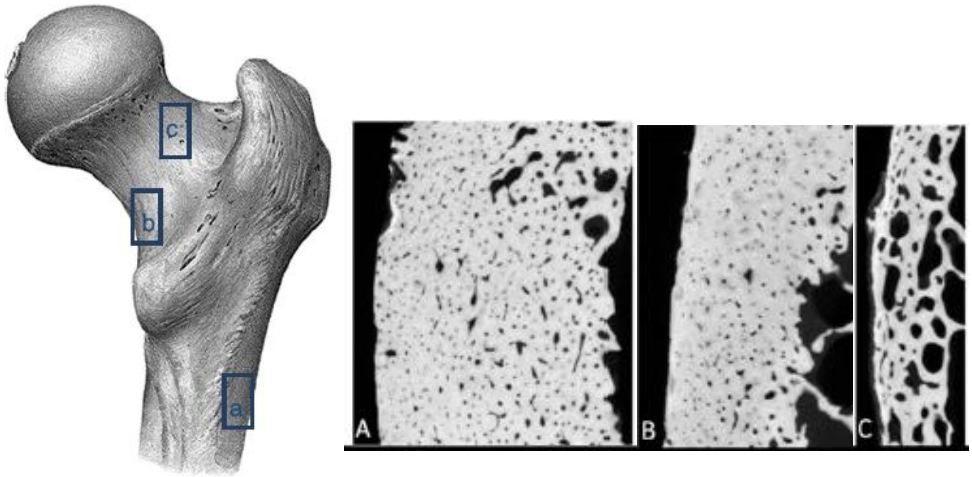

Figure 82. Female femur with Micro-CT cross-sectional images of the cortical bone showing: (a) diaphysis, (b) inferior neck, (c) superior neck [264].

The first feedstock was prepared using the coarse Ti powder with a solid content of 58% and 0% KCl, while the second feedstock had 58% solid content of which 60% KCl. The KCl used was cubic with a mean particle size of 348 μm. The first trial was designed to produce double

layer samples (relatively dense/porous) by injecting dense layer first (feedstock without space holder), then emptying the barrel of the vertical injection moulder and filling it with a feedstock with space holder, followed by injecting a porous layer (about 6 mm in thickness for each layer). The second and third trials were designed to make triple layer samples (porous/dense/porous and dense/porous/dense, approximately 4 mm each layer in thickness). All the multiple shot green samples appeared to be strong and exhibited good mechanical strength during handling. **Figure 83 (a)** illustrates some double and triple layered samples made through this procedure. While there was no difficulty in making these green samples, layer separation was found to occur during water debinding at the region of the bonding between the layers. This separation can be attributed to the higher volume shrinkage of the porous layers compared to dense ones during debinding, where both KCl particles and the soluble part of the binder (PEG) are removed. In addition, the dissolution of KCl particles at the interface of the layers could also aggravate this problem by reducing the bonding area between the layers and consequently, reducing the mechanical strength. This observation was noted in both triple and double shots samples. However, it was more apparent in the double and triple layered samples (porous/dense/porous) as seen in **Figure 83 (b)** and **(c)**. Furthermore, porous/dense/porous samples did not have sufficient mechanical strength to be handled for sintering and thus, further work on them was stopped.

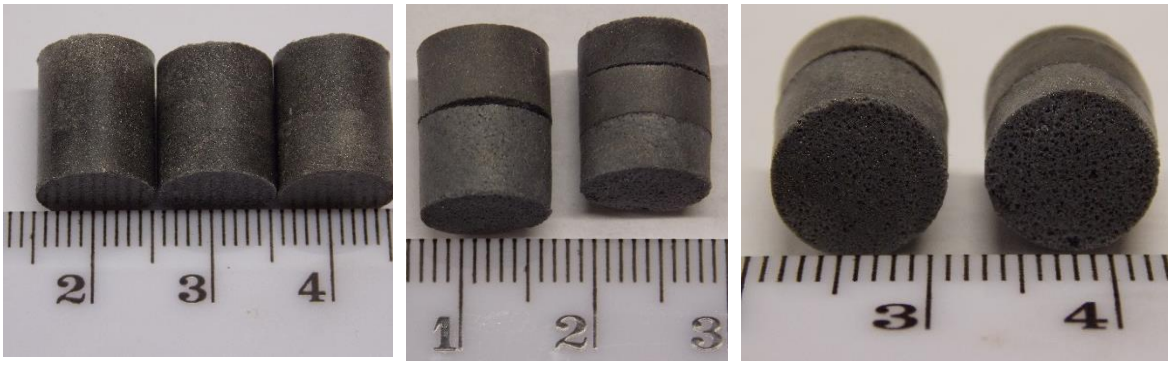

(a) (b) (c)

Figure 83. (a) Double and triple layered green samples made of two different feedstocks, one of which had a solid content of 58% and 0% KCl and the other one had a 58% solid content of which 60% KCl. (b) &(c) Side and top view of some double and triple layered samples after water debinding at 50 °C showing some layer separation.

The diameter shrinkage of each layer in the samples during debinding and after sintering was recorded using a Vernier caliper with a resolution of 0.01 mm (by the average of at least 4

readings) and numerated in **Table 15**. The average diameter shrinkage for the porous layers after debinding is more than four times that of the relatively dense layers, whereas the average diameter shrinkage after sintering is approximately three times higher than that for the dense layers. Some double and triple layered porous samples after sintering are depicted in **Figure 84**. The relatively dense layers which made using feedstock without space holder were microporous, while those made with space holder were macroporous. Hence, the former will be referred to microporous layer, while the latter will be referred as macroporous layer. It can also be observed from **Figure 84** that there is good bonding between the macroporous and the microporous layers as we move away from the outside edges towards the centre of the samples. However, layer separation was noted at some edges of the interface between the macro and micro porous layers. This layer separation was initiated during debinding as noted earlier and the depth of separation ranged from 300 µm up to 1 mm. The separation can be attributed to two main factors, namely, the differences in the volume shrinkage between the porous and dense part during debinding and the time interval of injection between each shot or layer due to equipment limitation. As each layer was injected with a time difference of about 10-15 minutes (required to empty the barrel of the feedstock with no space holder and load it with a feedstock that has 60% KCl). This resulted in poorer bonding at the green body stage than would be achieved if injection were sequential with no delay.

Table 15. Average diameter shrinkage of double and triple layered porous samples

ID	No.	Dense layer 1 diameter shrinkage %		Porous layer1 shrinkage %		Dense layer 2 Shrinkage %	
		Debinding	Sintering	Debinding	Sintering	Debinding	Sintering
Dense/porous	1	0.3±0.2	4.0±0.6	2.6±0.4	12.5±0.3		
	2	0.4±0.2	4.1±0.2	2.5±0.6	12.3±0.5		
	3	0.3±0.1	3.9±0.4	2.4±0.5	12.0±0.6		
	4	0.4±0.2	3.7±0.7	2.4±0.2	12.4±0.3		
Dense/porous/ dense	1	0.5±0.1	3.8±0.3	1.8±0.7	11.6±0.7	0.5±0.2	3.77±0.5
	2	0.5±0.2	3.7±0.8	2.1±0.4	11.9±0.6	0.5±0.3	4.27±0.4
	3	0.5±0.3	3.4±0.5	2.4±0.3	11.3±0.4	0.5±0.3	4.02±0.6
	4	0.3±0.2	3.4±0.6	2.1±0.2	11.7±0.7	0.5±0.2	4.07±0.2

This could be solved with the use of two component injection moulding or low pressure injection system with multiple barrels. It was also noticed that some KCl particles have

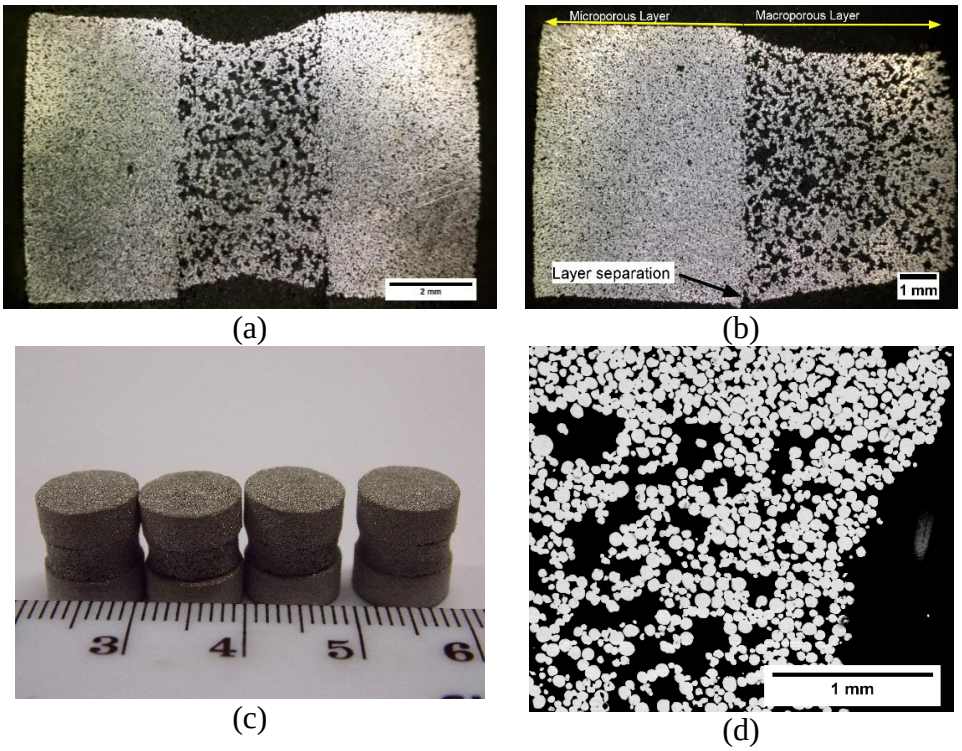

Figure 84. (a) Triple layered porous Ti composed of two microporous layers with a macroporous layer in-between, (b) Double layered porous Ti sample composed of one microporous layer joined to one macroporous layer, (c) Triple layered porous Ti foams, (d) Backscattered electron SEM image of the interfacial bonding between microporous and macroporous layers.

infiltrated the bottom of the microporous layers, which could be due to left over feedstock with KCl in the nozzle or barrel. In addition, the foam or the macroporous layer in the triple layered porous samples took a neck-like shape, where the microporous layers confined the movement of the particles at the interface during sintering leaving the centre of the foam to shrink freely. Although the production of the triple layered porous samples with gradient porosity was successful, the presence of the preformed cracks at the interface due to layer separation is expected to lead to failure at an early stage. This was confirmed by the shear test results for the triple layered porous samples as shown in **Figure 85**. All of the samples failed at the interface between the macro and micro porous layers as expected. Nevertheless, some parts of the macroporous layer were still intact and bonded to the microporous layers even after fracture, indicating the presence of good bonding in some areas among the microporous and macroporous layers (see **Figure 86**). It was also observed that necks were

mostly broken with few Ti particles with striated structure. This might suggest that crack propagation follows the weakest bonds or necks between the bonded Ti particles.

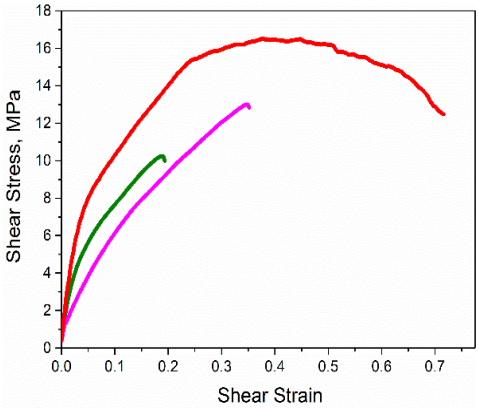

Figure 85. Shear testing results of three triple layered porous samples at a rate of 0.001 s^{-1}.

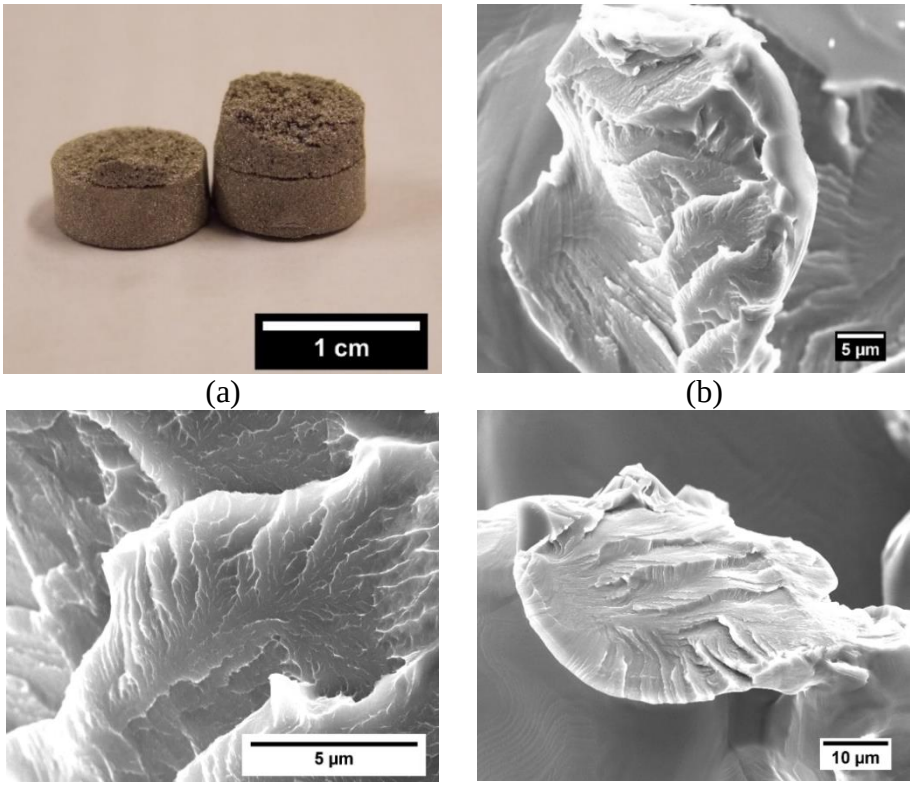

(a) (b)

(c) (d)

Figure 86. (a) triple layered porous sample after shear testing, (b) Secondary electron SEM image of a broken Ti particle in the triple layered porous sample (c) Secondary electron SEM of the Ti particle at high magnification, (d) Secondary electron SEM image of a Ti particle with striations after failure.

In order to investigate the suitability of the MIM-SH process to produce relatively small and complex part, a biomedical implant was selected, and an attempt was made to process porous surgical staples. These staples are knotless fixation implants that were developed to replace conventional suturing for repairing incisions during surgical operations [265]. Furthermore, the body of these surgical staples are sometimes barbed in order to anchor the staple to the surrounding tissue and provide improved fixation. A feedstock with 60%vol KCl was prepared using the procedure outlined in **section 3.1.2** and injection moulded into a surgical staple mould with five barbs. The KCl used was cubic with a mean particle size of 348 μm. For comparison, some surgical staples were also injection moulded using a feedstock with similar solid loading, but without space holder. Green surgical staples of both feedstocks with their sintered counterparts are depicted in **Figure 87 (a)-(d)**. It was noted that the macroporous barbed staples, which were made using the feedstock with space holder, have retained their shape to some degree even though they shrank significantly compared to those processed without space holder (the microporous ones). However, the interconnected macropores formed crack-like paths at the edges of the staples, and thus it is expected to have much inferior mechanical properties compared to the microporous ones made without space holder. In terms of dimensional shrinkage, the macroporous staples shrank in length more than three times that of the microporous ones after sintering (see **Figure 88**). Such a significant shrinkage could be an issue which might require modifications to the design of the part in order to be overcome.

Another attempt was made to process a potential biomedical part and join a thin porous layer onto the surface of a femoral stem for a hip implant. Hip implants are used to replace severely damaged hips or hips with severe osteoarthritis (a term or condition used for representing a heterogeneous group of joint disorders that cause pain and stiffness and result in significant morbidity, particularly in elderly people) [266, 267]. From 2003 to 2015 796,636 hip replacement surgeries were successfully carried out in just England and Wales, and 92% of those who required the surgery were diagnosed with osteoarthritis [268].

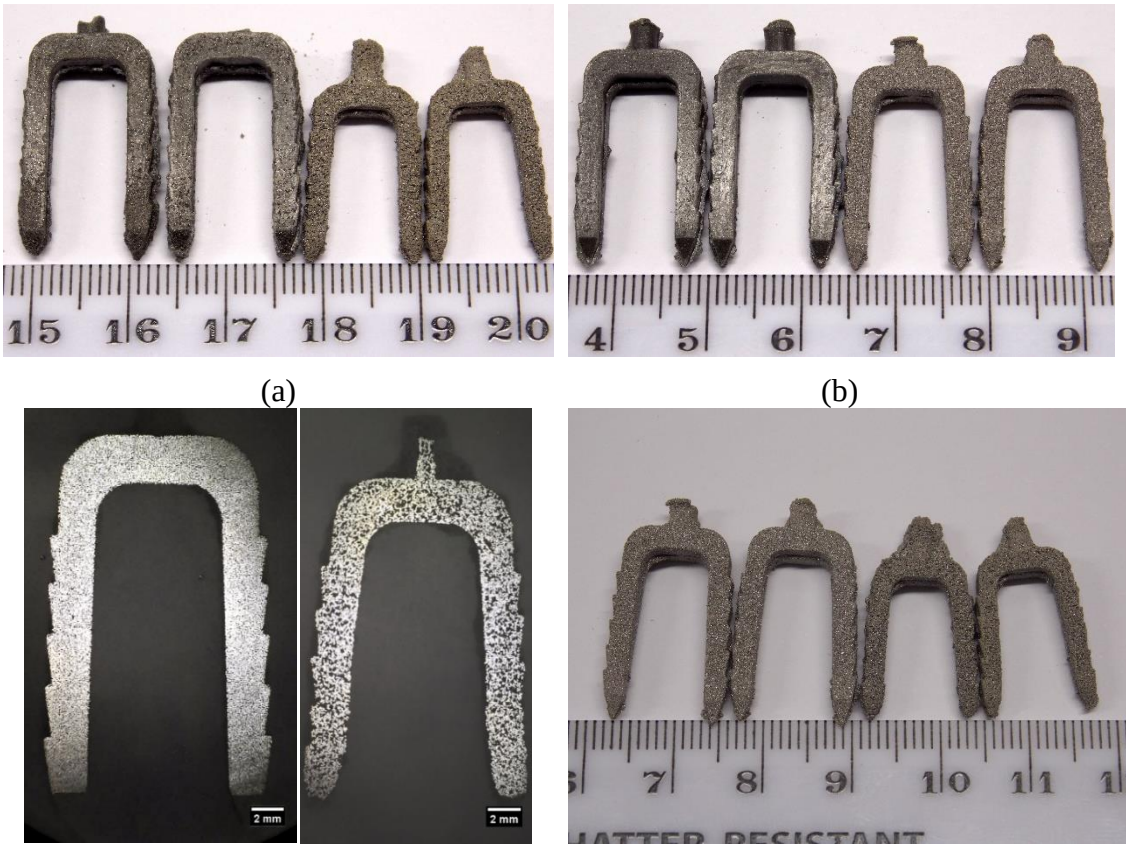

Figure 87. (a) green state and sintered macroporous staples, (b) two green state and sintered microporous staples, (c) and (d) sintered micro and macroporous surgical staples.

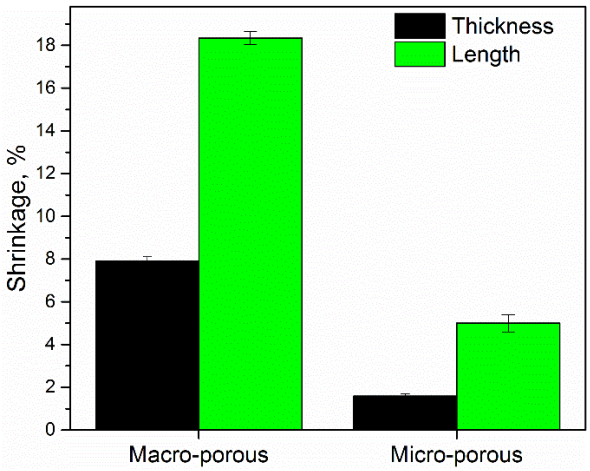

Figure 88. Dimensional shrinkage of medical staples after sintering

However, the number one cause for implant failure and urgency for revision operation is aseptic loosening, according to the National Joint Registry, where the fixation between the implant and the surrounding bone gets loose and fails [268, 269]. One solution for this

problem is to deposit a layer of macroporous Ti onto the surface of the implant, to potentially help improve the integrity and bonding between the implant and the bone itself, via providing porous channels or space for the bone to grow in. Thus, a trial was made to investigate the use of MIM-SH process to deposit a porous layer onto a modified femoral stem. The stem was a JRI Orthopaedics Furlong Evolution®, presented in **Figure 89 (a)**. The forged and machined stem was approximately 8 cm in length (the length was estimated from the bottom to the neck of the stem) and made of Ti-6Al-4V with a 2 mm deep groove or cavity machined in the middle for deposition of the porous layer.

The stem was placed inside a mould (**Figure 89 (b-d))** comprised of two pieces joined together via screws with a cavity similar in shape to that of the stem so that the only area or space to be filled with feedstock during injection is the machined groove in the implant. The mould cavity was designed to be 2% larger than the stem for ease of placing it inside the cavity and removing it before and after injecting the feedstock. Some tolerances were set in order to account for shrinkage during sintering and match the final thickness for the porous part to that of the stem (approximately 30%). The inlets for the feedstock were located at the upper part of the injection area and on both sides of the mould in order to ensure equal filling for the two sides. The inlets are equally fed with feedstock through a gate or a hole made in a plate that sits over the two halves of the mould. A feedstock with 60 %vol KCl was prepared using the procedure outlined in **section 3.1.2** and injection moulded at a temperature of 150 °C to produce green parts as illustrated in **Figure 90 (a)**.

The moulded parts were then water debound before drying and sintering at 1320 °C for 2h. One sintered part is shown in **Figure 90 (b).** It was found that the shrinkage of the porous layer on the longitudinal direction resulted in a gap between the porous layer and the edge of the stem, as demonstrated in **Figure 90 (d)**. The gap was about 2.94±0.18 mm in width. This is expected as the shrinkage in the longitudinal direction has not been accounted for due to design and shape restrictions. The thickness of the stem in the area of the deposited porous layer was about 10.25±0.10 mm, while the thickness of the bottom dense neighbouring region to the machined groove region was about 10.48±0.12 mm. In addition, recrystallization and significant grain growth occurred in the stem body surrounding the porous layer, which could result in deterioration of the mechanical strength of the forged stem. The sintered part was

sectioned into five segments as shown in **Figure 91** and analysed via SEM in order to verify the bonding between the stem surface and the deposited porous layer. SEM images of the analysed cross-sections are shown in **Figure 92**.

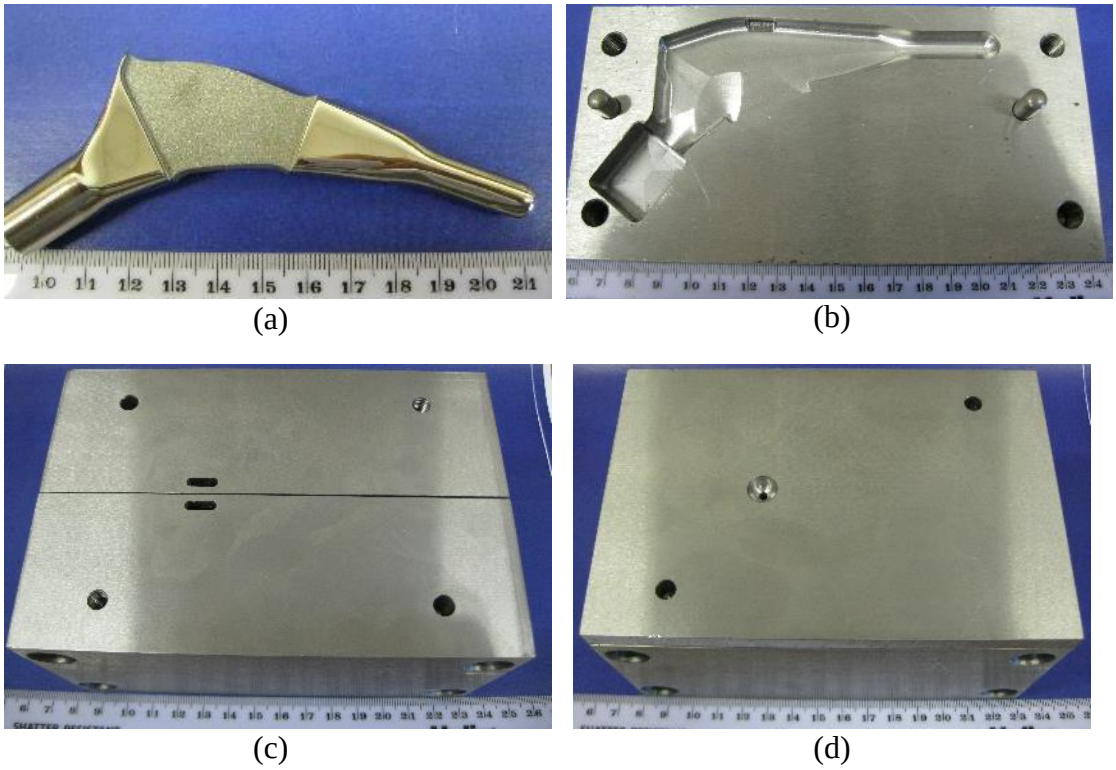

(a) (b)

(c) (d)

Figure 89. (a) femoral stem, (b) half-mould showing the cavity of the femoral stem, (c) the mould with the two halves assembled, (d) the mould after complete assembly of its parts showing the gate for injecting the feedstock in.

SEM images of the analysed sections indicated the presence of areas of intimate bonding between the edge of the stem and the deposited porous layer. Nevertheless, some separation was noted, particularly for the bottom part of section 1, where it was much more noticeable compared to the other sections. This might be due to the inability of the edges of the porous structure to stay bonded with the surface of the stem while significantly shrinking during sintering, unlike the middle part, where less movement is expected. In addition, it was generally noted that the porous structure was smeared, the shape of the pores was deformed and some micropores were sealed or closed. This could be ascribed to the action of sectioning with the SiC cutting disk.

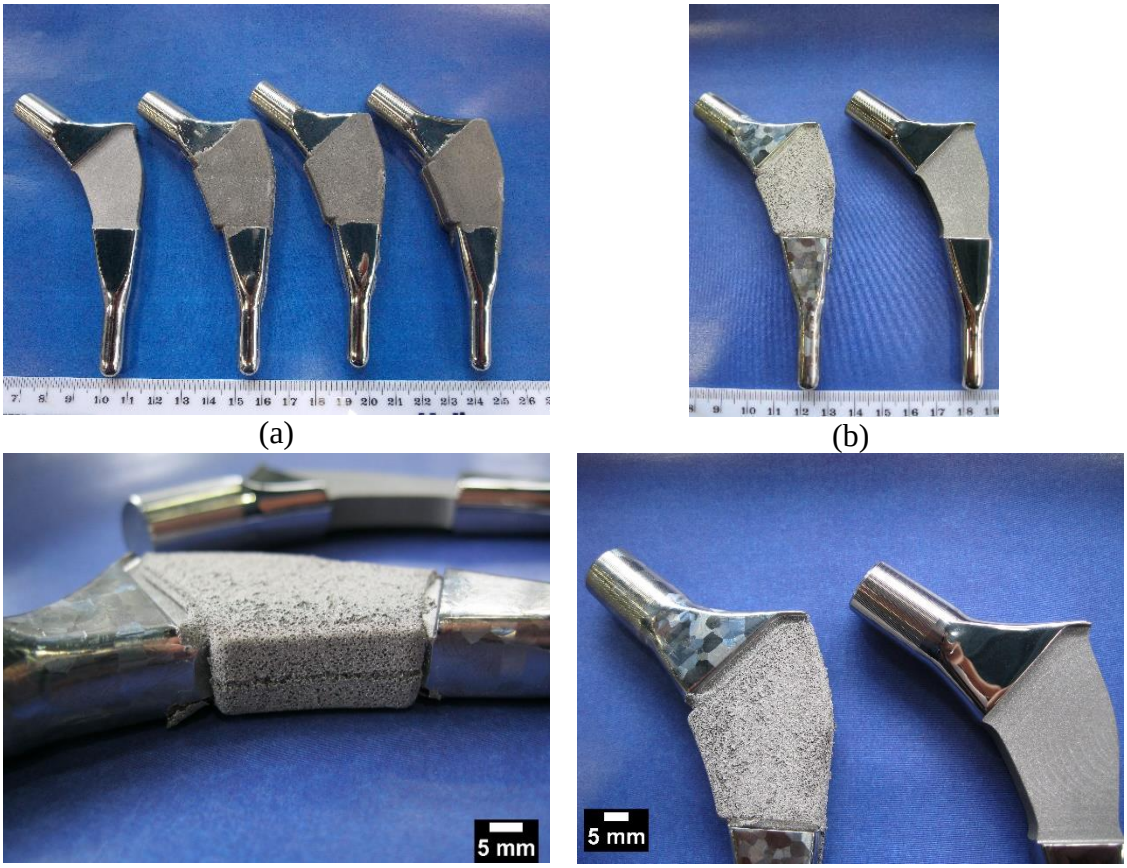

Figure 90. (a) femoral stem before and after injecting the porous layer, (b)-(d) top, side and cross-sectional view of femoral stem with a deposited porous layer after sintering.

EDS analysis was carried out on the as-sectioned part (**Figure 93**) and the results indicated that the structure is highly contaminated with Si and C from the cutting disk. Similar results were reported in the literature [6]. It is worth noting that avoiding the closure of the pores, smearing of the structure and increased contamination associated with machining are the main rationales behind developing a near net shape manufacturing technique for foams such as MIM-SH.

Although partial bonding of the porous layer onto the modified femoral stem was successfully achieved here, it would not be effective for the final application of the processed part, where complete bonding is required in order to avoid any layer separation and no gap should be present between the deposited layer and the femoral stem. Thus, to be of any use for such applications, the part would need to be processed completely using MIM-SH,

including the forged stem; this is impractical given the fact that the part size is relatively large compared to the size of parts typically produced by MIM-technology. Therefore, MIM-SH process would not be the optimum technique to deposit the porous layer onto the femoral stem and would be more suitable for processing of other biomedical implants, particularly smaller ones such as dental implants. Other foaming techniques such as press and sinter (space holder technique) might be more applicable in this case as less shrinkage is typically encountered.

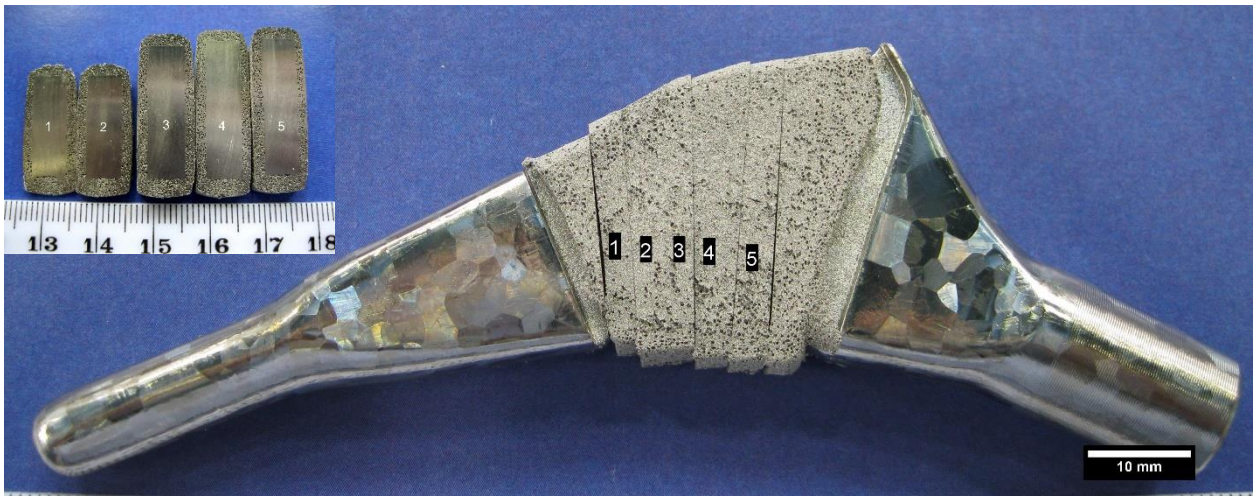

Figure 91. Femoral stem with a deposited porous layer made by a Ti feedstock with 60%vol KCl after sectioning

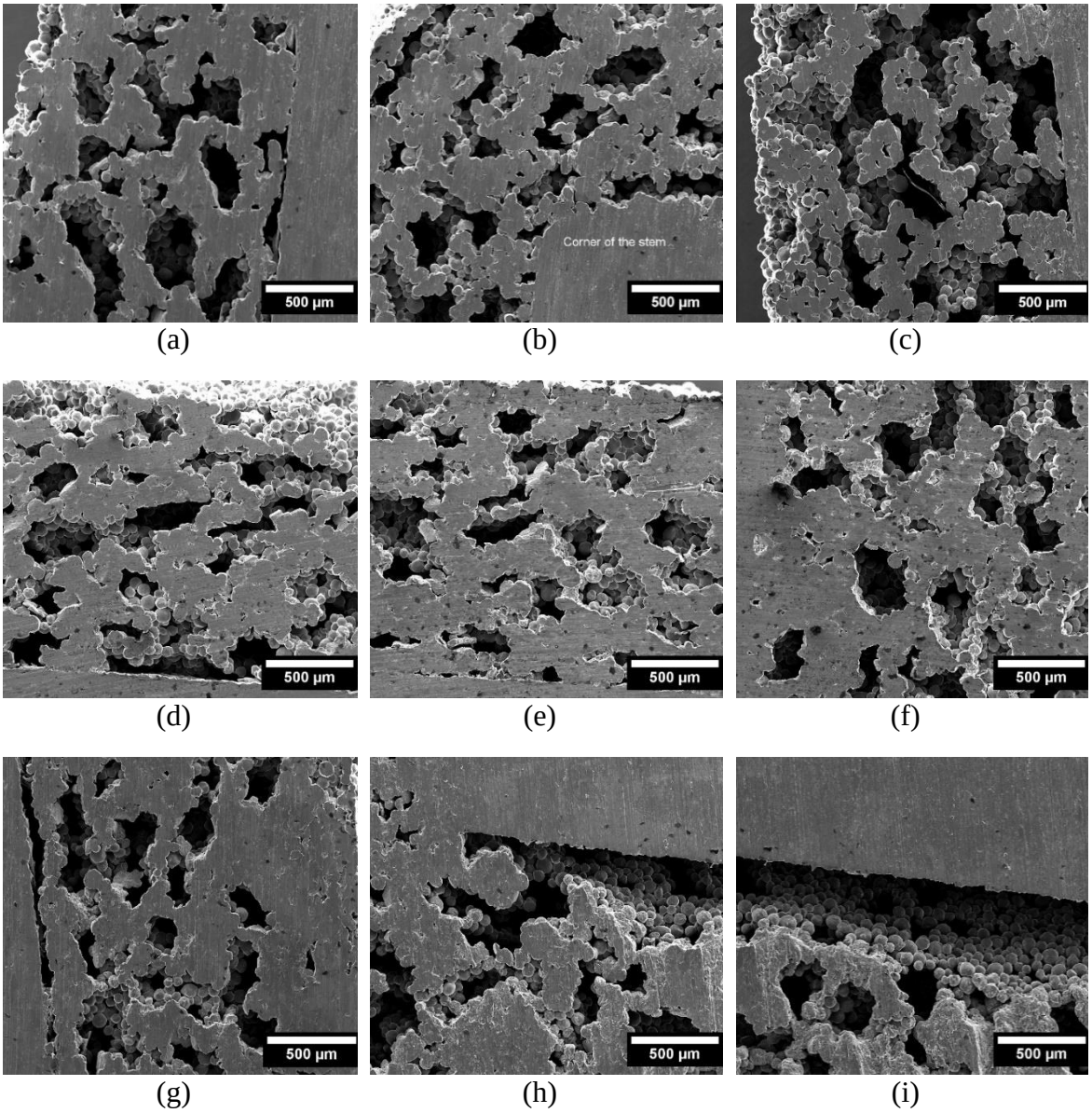

Figure 92. (a)-(c) Secondary electron microscopy images of section 5, (d)-(f) Secondary electron microscopy images of section 3, (g)-(i) Secondary electron microscopy images of section 1.

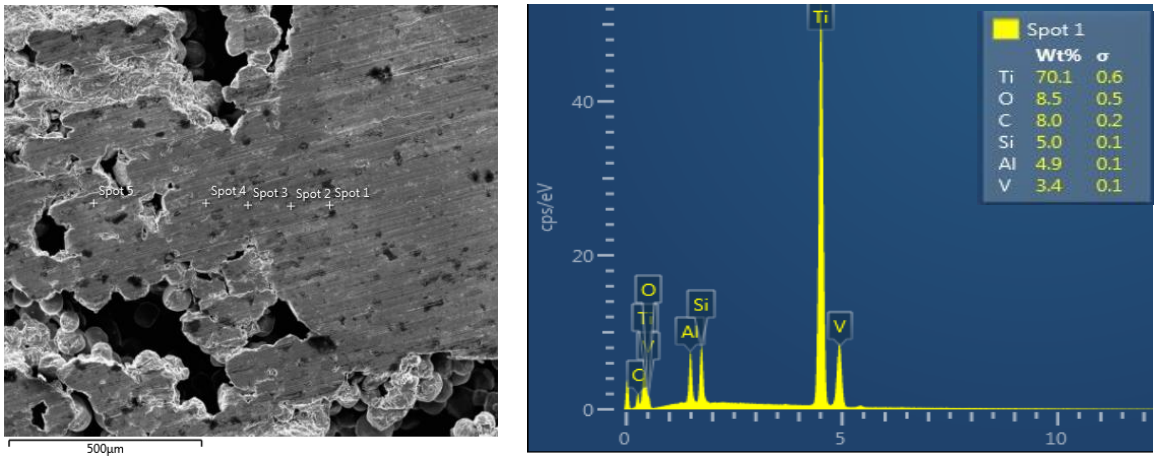

(a) (b)

Figure 93. (a) Secondary electron microscopy image showing the EDS spots analysed, (b) EDS spectrum for spot 1.

Table 16. Results of the EDS analysis for the investigated spot scans.

Element\Spot no.	Spot 1	Spot 2	Spot 3	Spot 4	Spot 5
Ti (wt. %)	70.1	78.3	84.8	73.8	92.0
Al (wt. %)	4.9	4.1	3.2	0.7	0.1
V (wt. %)	3.4	3.4	3.2	-	-
Si (wt. %)	5.0	2.8	0.2	0.1	0.1
C (wt. %)	8.0	11.4	8.6	25.4	3.9
O (wt. %)	8.5	-	-	-	3.9

7 Improving the bioactivity of Ti foams via hydroxyapatite addition

7.1 Fabrication of Ti-HA composite foam

One potential barrier towards using Ti and Ti based foams for biomedical applications is that they are biologically inactive materials and form only a mechanical bond with the bone. This might not be enough to limit implant loosening during motion, depending on the implant. One approach to solve this and increase implant fixation is to incorporate into these foams a biologically active material such as Hydroxyapatite (HA), as this has a chemical composition similar to that of the mineral component of natural bone [270, 271]. This will help bonding the implant chemically and mechanically to the surrounding tissue, resulting in better fixation.

Adding HA can be achieved by several techniques such as coating these foams with a HA layer via plasma spraying [272-274]. However, these coatings can be delaminated due to the high residual stresses forming HA debris, which can subsequently cause abrasive wear [275, 276]. Another technique is to mix the Ti powder with HA during processing and sinter them together, thus producing bio-composites. Several studies have investigated the addition of HA to dense Ti with processing via press and sinter [277-281] as well as spark plasma sintering [282] and the subject has been recently reviewed [283]. However, a limited number of studies have been carried out combining HA with porous Ti. Hence, this chapter was dedicated to investigate the use of metal injection moulding in combination with space holder to produce Ti-HA biocomposite foams using two different HA powders with different particle sizes and followed by in vitro biological tests in order to assess cell viability. One of the HA powders used was micro-sized and the other one was nano-sized. The morphology of the powders used and the particle size distribution are shown in **Figure 94 and Figure 95.**

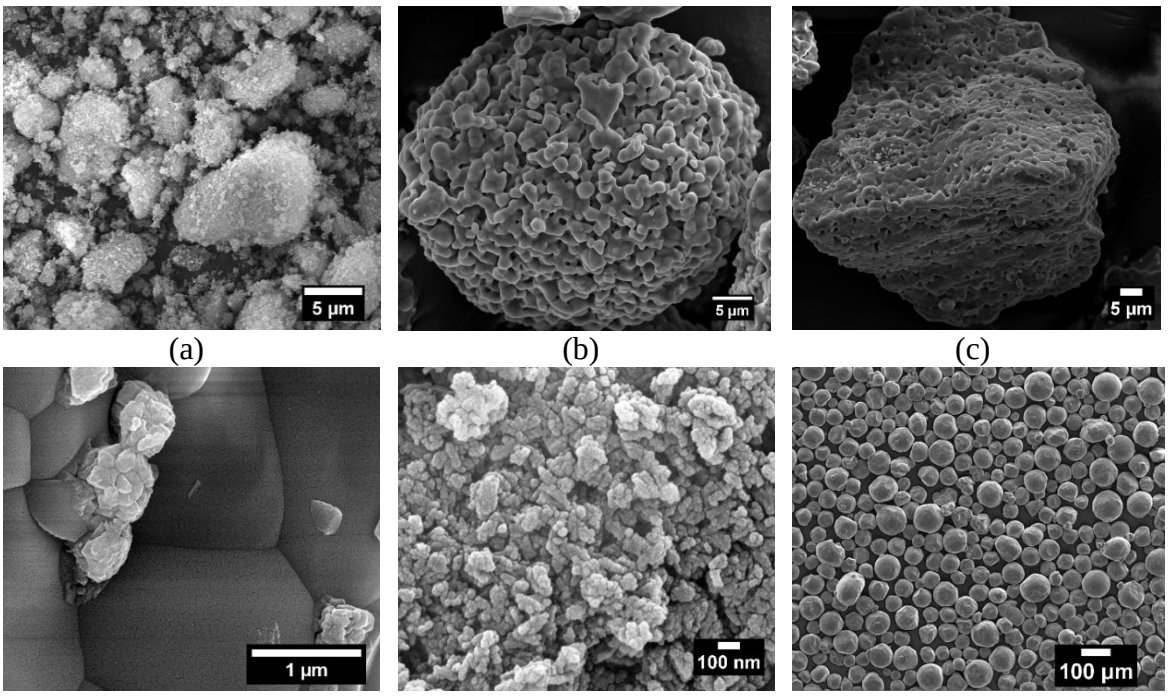

(a) (b) (c)

(d) (e) (f)

Figure 94. The morphology of: (a) nano-sized HA powder at low magnification, (b) micro-sized HA powder at low magnification (penny shaped), (c) micro-sized HA powder at low magnification (rock like shape), (d) micro-sized HA powder at high magnification, (e) nano-sized HA powder at high magnification, (f) Ti powder at low magnification.

It can be seen from **Figure 94** that the nano-hydroxyapatite is agglomerated into micron-sized agglomerates, each of which consists of thousands of nanoparticles joined together. For the micron sized hydroxyapatite, two particle shapes were noted in the powder, namely rock-like shape with irregular geometry and penny-shaped particles. The latter seems to have more porosity than the former, as can be noticed from the SEM image in **Figure 94**. High magnification images of the rock like shape particles (**Figure 94.(d)**) suggest that each particle consists of micron-sized grains well sintered together. XRD analysis of both HA powders were carried out and the results are shown in **Figure 95. (b)**. It can be noted that the HA peaks for the micro powder have higher peak intensities and are much narrower than that of the nano powder, reflecting the nanoscale nature of the latter, as well as its lower crystallinity compared to the micro sized powder [284-287]. In terms of the particle size distribution **Figure 95.(a)**, the Ti powder and the micro HA powder are comparable, but the micro HA powder has a broader particle size distribution. In comparison, the nano HA powder has a smaller and narrower particle size distribution. However, the result is only an indication of the size of the agglomerates and not the particles themselves as it was difficult

for the particle size analyser to break these agglomerates during measurements, due to the high surface area and affinity of these powders to aggregate.

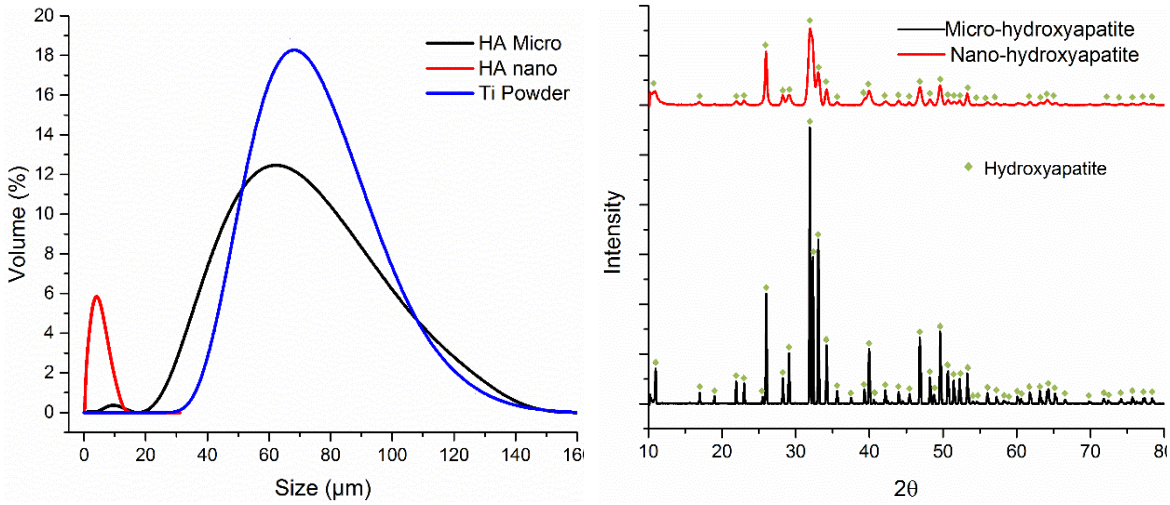

(a) (b)

Figure 95. (a) particle size distribution for Ti and HA powders, (b) XRD profiles for the HA powders used

However, these agglomerates were broken during mixing with the Ti powder, where the HA nanoparticles are seen to adhere to the outside surface of the Ti particles forming a weakly-bonded coat over these Ti particles as shown in **Figure 96**. In addition, some Ti particles were joined together underneath the HA coat to form one larger particle.

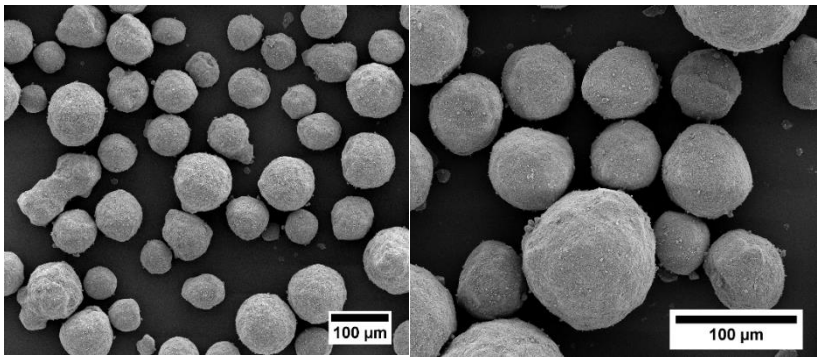

Figure 96. SEM images of Ti powder with nano HA powder after mixing

XRD spectra of the Ti-HA powders after mixing are shown in **Figure 97**. The XRD spectrum of Ti powder was added for comparison. The same observation as before mixing with the peaks for the nano powder being broader, and having less intensity and being less apparent.

The fact that the HA peaks were detected in both powder mixtures refers to the homogeneity of the powder mixtures and the effectiveness of the mixing procedure.

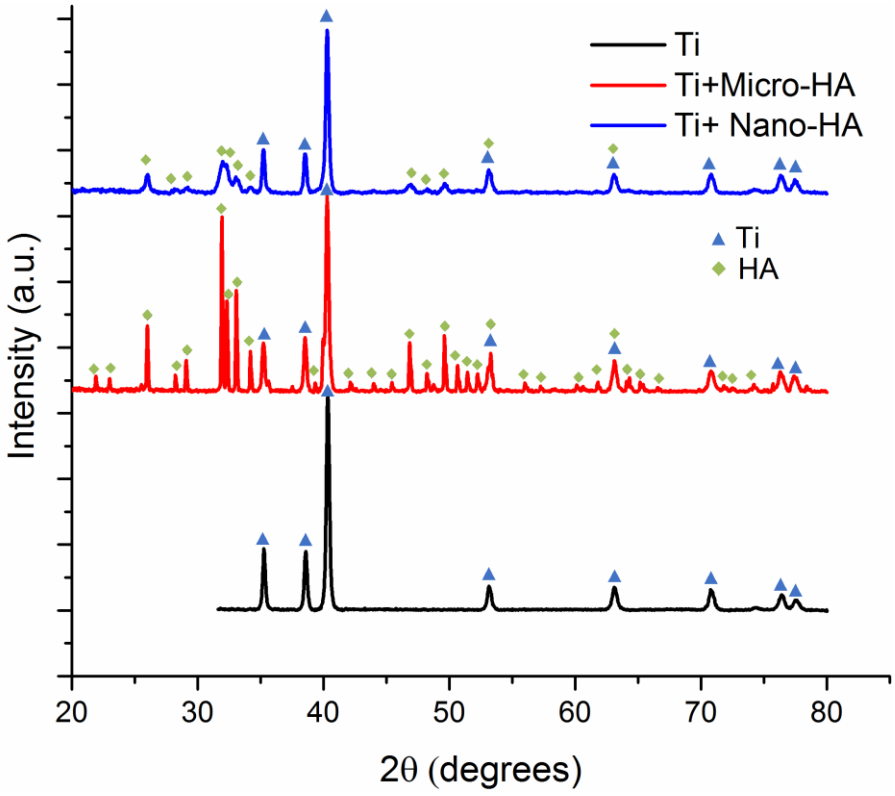

Figure 97. XRD spectrums of Ti and Ti-HA powders after mixing

The effect of adding 7% micro-HA powder to the Ti in terms of viscosity is shown in **Figure 98**. The results indicate that the addition of micro HA powder to the feedstock would result in a slight increase in viscosity, despite the fact that the density of the HA is lower than that of Ti. This can be attributed to the irregular shape of the HA particles. The Ti particles with approximately spherical shape can flow easily past each other upon shearing, unlike the rock-like and penny-shaped HA particles which would require higher shear rate in order to flow and hence its addition will result in an increase in the viscosity of the prepared feedstock. Similar findings were reported for feedstock made by irregular powders compared to spherical ones [234]. One would expect the addition of nano-HA powder would result in a further increase in the viscosity of the feedstock due to having smaller particle size, higher surface area and higher tendency to agglomerate during shearing than the micro-HA. However, this might not be the case as there are several studies in the literature which report that the addition of small amounts of nano-scale powders to micron-scale ones can have a

positive effect in reducing the viscosity of the feedstocks [288, 289]. Such findings are attributed to the roller bearing effect, where the nano particles act as a solid lubricant during shearing of the micro-particles and can occupy the spaces among the micro-particles resulting in a better packing density powder and reduced viscosity.

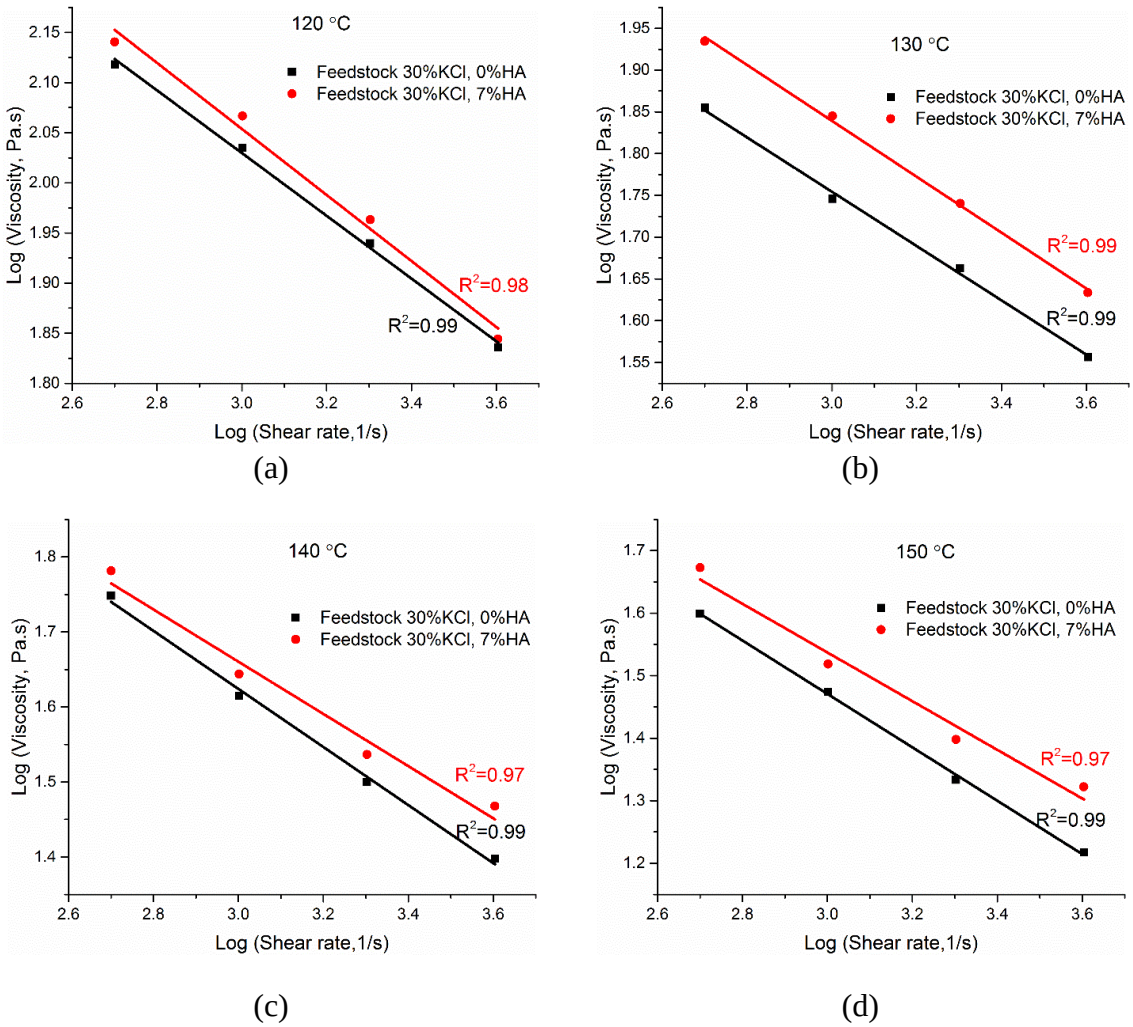

Figure 98. Viscosity rheograms of two feedstocks, namely one without HA addition and one with 7% micro-HA addition at: (a) 120 °C, (b) 130 °C, (c) 140 °C, (d) 150 °C.

It was also generally found that the viscosity of both feedstocks decreased with increasing shear rate, which is an indication of pseudoplastic behaviour or shear thinning, desirable behaviour in the MIM industry. The sensitivity of the viscosity of the feedstocks to shear rate, which is also known as the flow behaviour index *(n)*, with and without 7% HA is presented in **Table 17**.

Table 17. Flow behaviour index for feedstocks with and without HA addition

Variable	Temperature (°C)	Feedstock without HA	Feedstock with 7% micro-HA
Flow behaviour index (n)	120	0.687	0.671
	130	0.675	0.666
	140	0.613	0.652
	150	0.573	0.611

The lower the value of *(n)*, the faster the viscosity is reduced with shear rate and the more suitable the feedstock for processing of complex parts as it will inject and fill the moulds more readily [290, 291]. Feedstock without HA had a higher shear sensitivity at the injection temperature (150 ºC) than that with 7% micro-HA, and thus is considered to be better in terms of suitability for injection of complex parts. However, in terms of the effect of temperature on the viscosity, the feedstock with 7% micro-HA is more preferable, as its activation energy was about 55.54 kJ mol^{-1}, lower than that for feedstock without HA, which was about 64.27 kJ mol^{-1}. The activation energy values were estimated from an Arrhenius plot of Ln η against Ln (1/T) as shown in **Figure 99** and multiplying the values of the slope by the gas constant. It should be noted that the lower the activation energy for the feedstock, the less the sensitivity of the viscosity to temperature variations and the lower the probability of sudden viscosity drop during injection. This effect is useful in avoiding undue stress concentrations that might occur leading to cracking and distortion in the moulded parts [290].

A group of four samples after debinding is shown in **Figure 100**. It is evident that the samples are still perfectly intact with several macropores in their structure, which reflects the size of the KCl powder or space holder used. In comparison with pure Ti foams after debinding, porous Ti-HA composite samples have lighter colour.

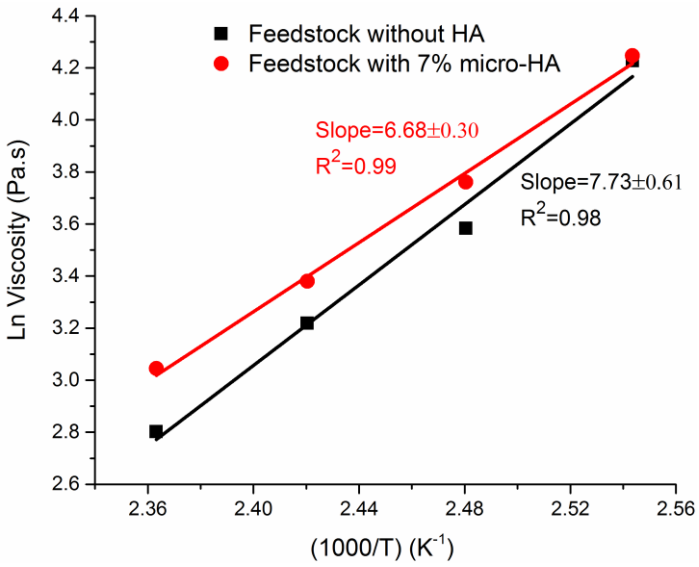

Figure 99. The change in the viscosity of the feedstock with temperature in the temperature range of 120-150 ºC at a shear rate of 4016 s^{-1}.

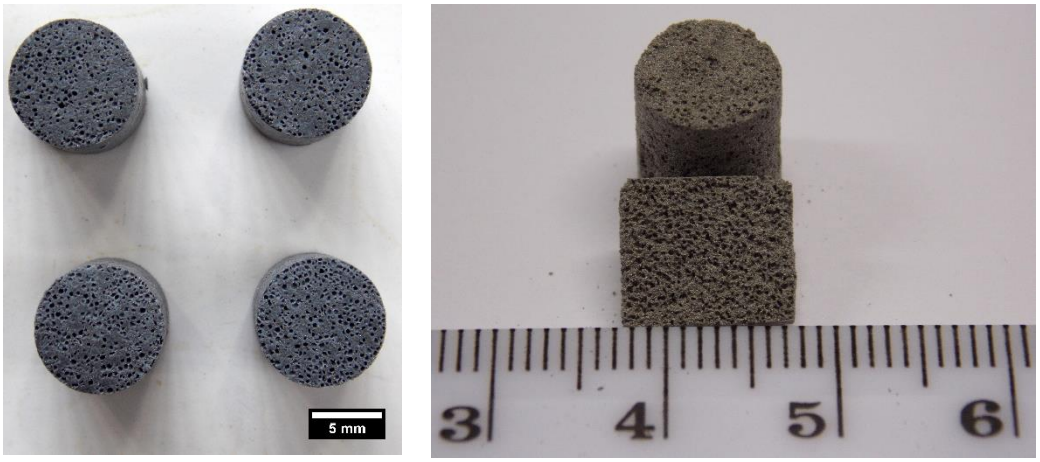

(a) (b)

Figure 100. (a) Ti-Ha composite samples after water debinding, (b) Sintered sample made of Ti with 7% nano-HA

Figure 100 (b) shows sintered Ti-HA composite foams made of feedstock with 7%vol. nano-HA powder. The composite foams produced have interconnected macropores that are apparent to the naked eye and which are of potential benefit for nutrient exchange and bone ingrowth in biomedical applications. The volume percentages of porosities in the Ti-HA composite foams made with 7% nano and micro-HA were found to be equal to 63.5±1.1 and 64.1±1.3 % respectively and indicate that the use of nano-HA powder would result in insignificantly different porosity to that of micro-HA powder. In a similar process higher

density was reported in the literature for a mixture of micro and nano powders compared to only micro-powder and attributed to faster densification due to higher surface area and driving force for sintering [292]. However, this is not seen here suggesting behaviour is dominated by the coarser powders.

The results of the compression tests for both composite foams are shown in **Figure 101**. The strength of the Ti-micro HA composite foams is more than three times higher than that made with the nano HA. In the case of the latter, Ti particles did not have the chance to be bonded properly due to the presence of the HA coating covering their surface, which comprised of individual nano HA particles that sinter at a much faster rate than the Ti particles. Hence, the mechanical strength of the structure is dependent on the weak bonding between the products of the sintering of the nano HA particles, which results in a shell-like ceramic structure surrounding the Ti particles, which can be easily broken. SEM images of the sintered Ti-nano HA composite foams after compression supports this view as shown in **Figure 102**, where it was found that there were few bonds between the Ti particles. It is also important to point out that the surfaces of the broken bonds were smooth without any micro-dimples, referring to the brittleness of the structure.

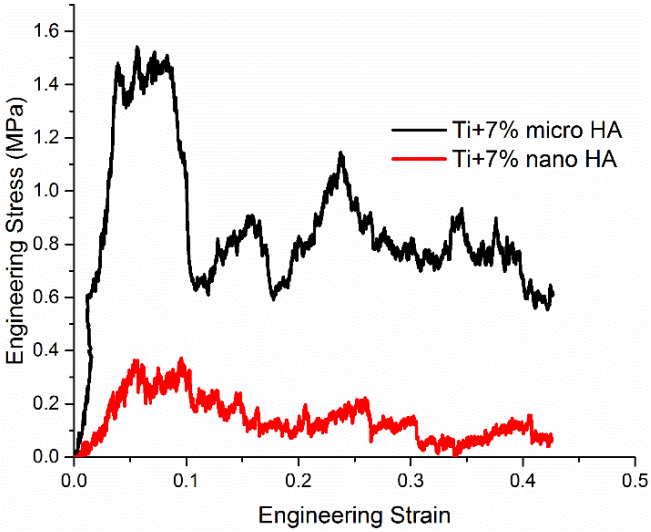

Figure 101. Compression testing results of Ti-Ha composite foams with 7% micro and nano HA.

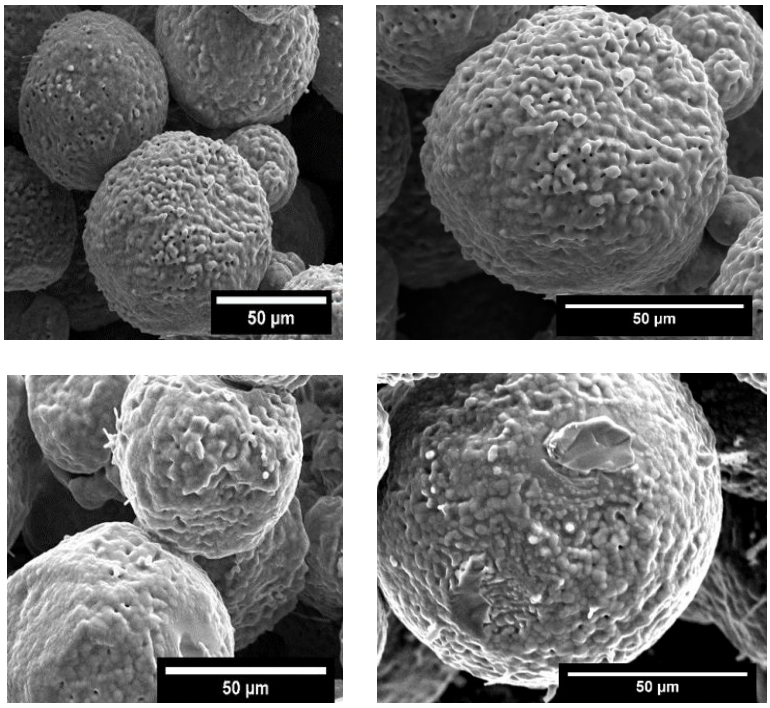

Figure 102. SEM images of sintered samples made of Ti with 7% nano-HA

Compared to Ti with nano HA composite foams, Ti with micro HA was much better sintered and many bonds between the Ti particles were noted, as can be seen from the SEM images in **Figure 103**. The presence of HA in larger particles, which do not cover the Ti particles, has given the chance for the Ti particles to bond properly during sintering, resulting in increased mechanical strength. Nevertheless, some small deposits can be still noticed on the surface of some of the Ti particles. Furthermore, it was also noted from the SEM images that wherever there is HA in the structure, the Ti particles nearby fail dramatically in a very brittle manner with smooth edges, indicating that there might be a connection between brittleness and HA presence. This observation is in good agreement with what has been reported in the literature in the case of dense Ti with HA, where adding more HA reduces global ductility and increases brittleness [277]. However, in the current study the behaviour was more localised with samples displaying some yield before failure. It is also worth noting that the shape of stress strain curves for the samples has a close resemblance to a ceramic material rather than a metallic foam; once the load reaches the yield strength, the material fails dramatically without having the ability to withstand any plastic deformation, unlike typical pure Ti foams which display a long plateau region after yielding.

For further explanation of the reason for such brittleness in the Ti particles, Energy-Dispersive X-ray Spectroscopy (EDS) was performed on the surface of Ti particles in both composite foams. For Ti-nano HA composite foams, no calcium was detected in the sintered samples and the dominant elements found by EDS were phosphorous and titanium (shown in **Figure 104**). Similar observations have been reported in the literature, attributed to the entrapment of the calcium in the Ti lattice, without the occurrence of any peak shifting [293, 294]. Other studies have reported the disappearance of calcium compounds and ascribed it to the occurrence of complete decomposition [295, 296].

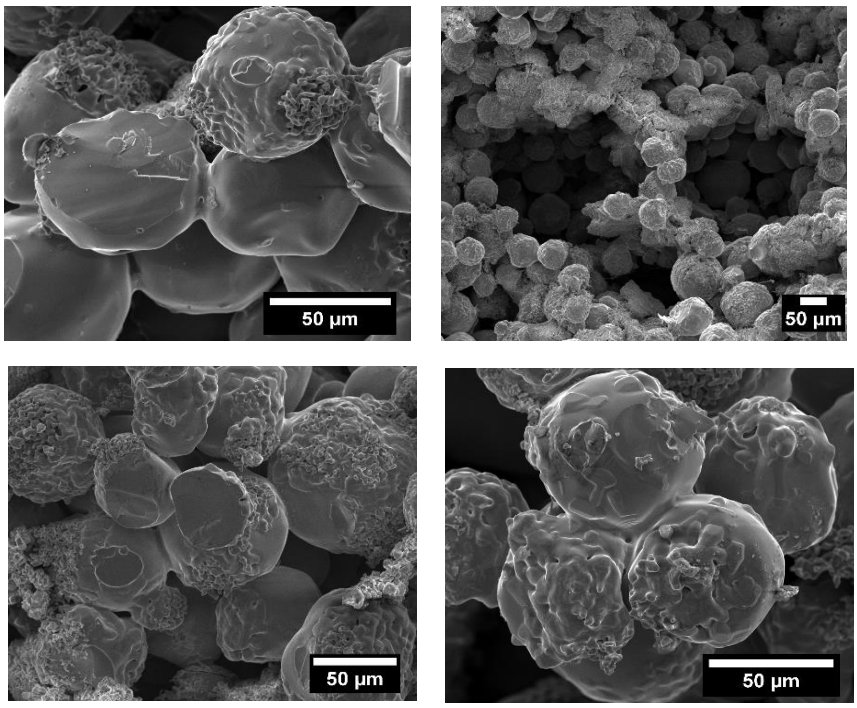

Figure 103. SEM images of porous Ti with 7% micro-HA after compression test.

In comparison with Ti-nano HA composite foams, Ca and P were detected in the Ti-micro HA composite foams (**Figure 105**) and can be taken as evidence for the significant influence of the HA particle size on the chemical composition and final properties of the composite foams produced. Further characterization of the Ca and P contents in both composite foams were carried out using XRF and are enumerated in **Table 18.** The samples made with micro-HA were mainly composed of Ti with double the amount of Ca than P. Considering the atomic weight of Ca is 40 and P 31 amu, then the Ca/P ratio is approximately equal to 1.5 and corresponds to Tri-Calcium-Phosphate (TCP), which means that the micro-HA is

decomposing to some extent under the sintering conditions (1320ºC for 2h). While for nano HA, the Ca/P ratio is approximately equal to 0.4, which is considerably lower than that of the micro HA, referring to the greater extent of decomposition in the nano HA. One approach to inhibit HA decomposition and improve mechanical strength is through reinforcing the composite with yttria, which has been shown recently to be effective in similar materials [297, 298].

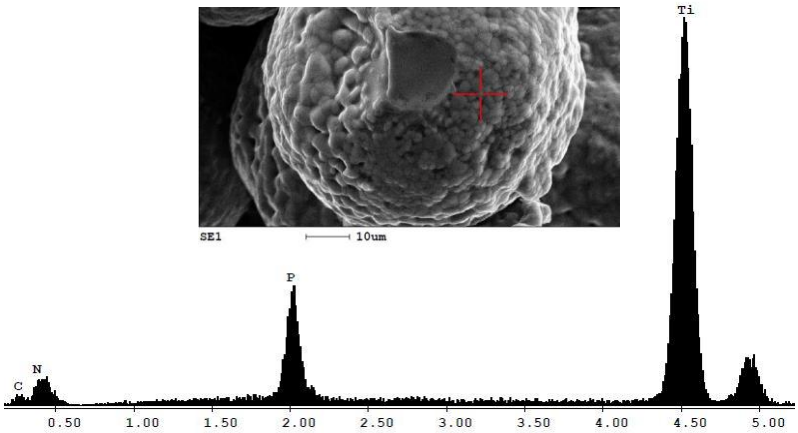

Figure 104. EDS elemental analysis result of a Ti particle in a porous Ti foam with 7% nano-HA.

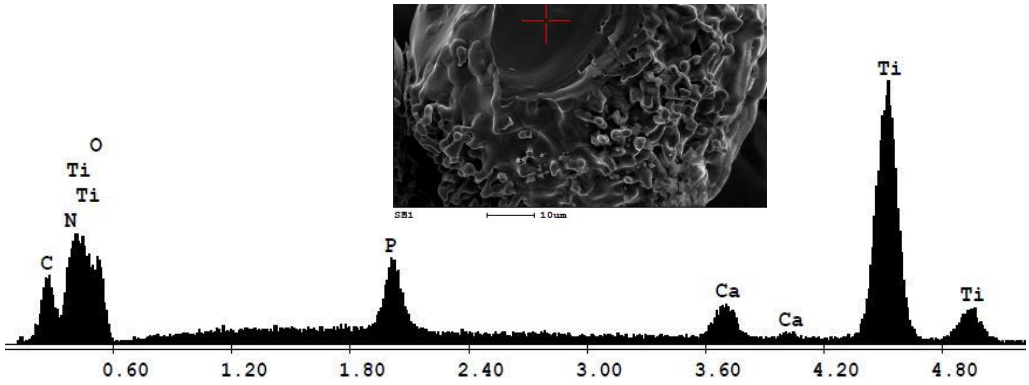

Figure 105. EDS analysis result of a Ti particle in a porous Ti foam with 7% macro-HA

It is also important to point out that the Ca percentage in the Ti-nano HA composite foams is much lower than that for the Ti-micro HA composite foams, and while the EDX analysis results did not show the presence of any Ca in the former, yet XRF results revealed its presence in small amounts. The finding gives an emphasis to the importance of the particle size of the HA in dictating the speed of the decomposition during sintering and consequently the resultant chemical composition of the foams produced. However, regardless of the

particle size of the HA powder used, the composite foams suffered brittle failure in the presence of HA. Such failure is not typically encountered in pure Ti foams, and therefore, one might argue that using less HA can result in better mechanical properties and reduced brittleness. Thus, a third experiment was carried out using Ti with 2%vol. micro-HA. The mixing of the powders and sample preparation procedures were the same as in previous experiments. The sintering process was carried out under two different temperatures, namely, 1250 and 1320°C for 2 h. The former sintering temperature was chosen based on a study in the literature, which states that the optimum sintering temperature for HA without decomposition is 1250ºC [299].

Table 18. XRF analysis results of Ti-HA porous composite

	Ti/HA Micro	**Error (%)**	**Ti/HA Nano**	**Error (%)**
Element	Concentration (%)		Concentration (%)	
Ti	86.71	0.20	90.24	0.10
Ca	8.77	0.50	3.24	0.05
P	4.52	0.20	6.27	0.07

The mechanical test was carried out at the same strain rate and the result is compared with a foam made using 52% KCl without HA and shown in **Figure 106.** It can be seen from **Figure 106** that the offset yield strength ($\sigma_{0.2}$) of the Ti-HA composite foams made with 2% micro-HA and sintered at 1320ºC for 2h is significantly higher than that for those made with 7% micro-HA, which are previously presented in **Figure 101.** Furthermore, it is even higher than that for foams made without HA, where the yield strength for Ti-HA composite foams sintered at 1320ºC for 2h was equal to 50.93 MPa, whereas for the Ti foams without HA it is about 31.6 MPa. Thus, it seems that adding smaller amounts of HA enhances strength of the Ti foams. Nevertheless, the samples made with HA still have generally less ability to absorb energy than the ones made without HA and the structure collapses after yielding without any plateau region similar to a ceramic material. The volume percentages of porosity for samples made with 2% micro-HA and those without HA were found to be approximately similar and equal to 62±1.2%, while the average pore size was equal to 348 µm with a roundness of about 0.73. It should be noted that reducing the amount of HA powder added to the mixture from 7 to 2% resulted in a reduction in the final porosity of the samples by approximately 2%.

This finding coincides with the results in the literature, where adding more HA can reportedly cause a small increment in the amount of porosity in the samples [282]. The percentage of porosity in the Ti-HA composite foams produced here is significantly higher than the maximum porosity so far achieved in the literature. For instance, Li et al have produced NiTi-HA composite foams with a maximum porosity of about 37% by adding 10% HA; and the foams produced had an ultimate compressive strength of about 57 MPa, which soared to about 222 MPa on reducing the amount of HA to about 3%, while the porosity in the sample decreased to about 29% [282].

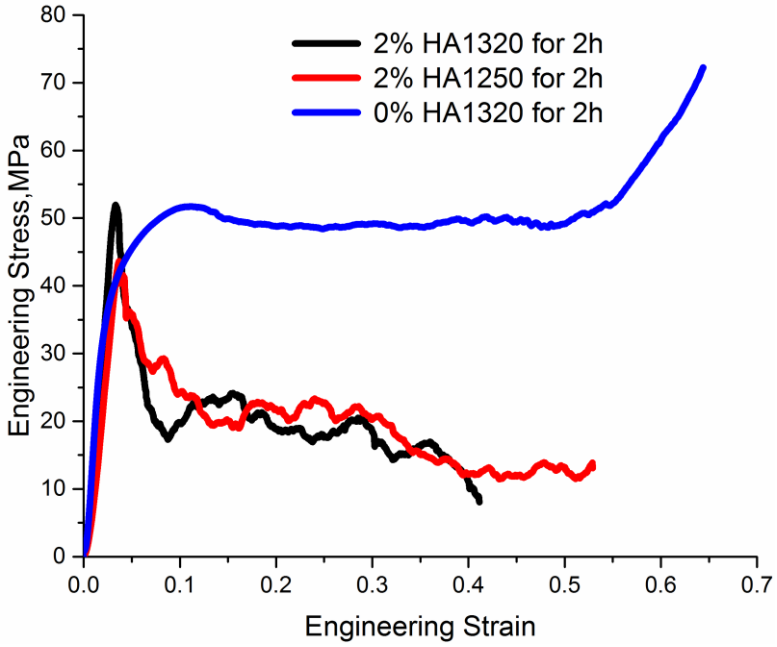

Figure 106. Compression test results of Ti-HA composite foam with 2% micro-HA.

The yield strength for the Ti-HA composite foams sintered at 1320ºC for 2h was found to be also higher than that for those sintered at 1250ºC for 2h, as the latter had a lower yield strength of 43.4 MPa. Such a finding can be attributed to a better inter-particle bonding and densification with increased sintering temperature. Despite the fact that sintering HA at higher temperatures might result in the formation of more TCP, which can be detrimental for the mechanical properties according to some studies, the amount of HA added is not significant (2%) and thus, the resultant TCP would not have a significant impact. Georgiou and Knowles sintered HA-glass composite samples at 1350ºC for 1h and found that only 5% TCP was present in samples with no harmful effect on the strength [300]. In addition, some

studies in the literature report that dense TCP has a higher compressive strength and fracture toughness than HA [301].

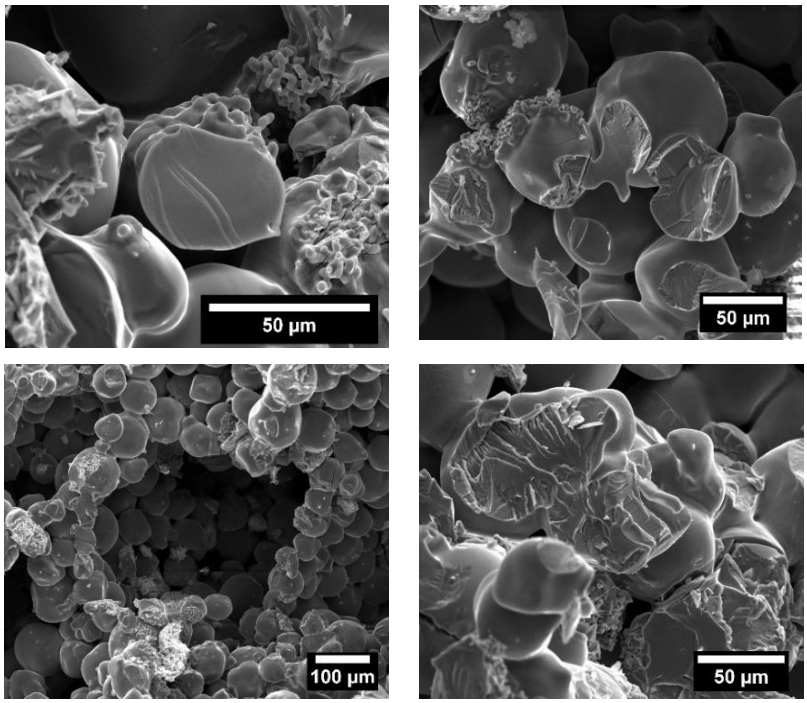

Figure 107. SEM images of Ti foam with 2% micro-HA after compression testing.

SEM images of Ti-HA composite foams after mechanical tests are shown in **Figure 107**. Ti particles which are not in close proximity with HA particles showed some signs of mechanical deformation with some striations, which are typically observed in Ti foams. Yet others which are neighbouring to HA particles are still seen to fracture catastrophically with very smooth failure surfaces. Further analysis for the reason behind such brittle behaviour was performed by evaluating the phases formed in the Ti-HA composite foams through XRD with the results illustrated in **Figure 108**. The crystal phases detected in the sample with the 2% micro-HA were Ti, $CaTiO_3$, Ti_2O, TCP and Ti_3P which are similar to the crystal phases found in Ti-HA dense composites as reported in the literature [277, 293]. The decomposition of the HA and the formation of these crystal phases could be the reason for weakening the structure and the cause of brittle failure in the foams, where the ceramic phases among these bond weakly to the Ti particles. Balbinotti et al [277] reported that phases containing Ca are partially removed during polishing of the Ti-HA composites, indicating the weakness of such phases to support load. It should be noted that calcium titanate is a biocompatible material

with the ability to promote apatite formation and improve the HA electrical conductivity and polarizability to match that of the natural bone (HA itself has a poor electrical conductivity) [302, 303]. The presence of $CaTiO_3$ can thus have a positive impact on the bioactivity of the composite foams prepared. However, increased amount of calcium titanate promoted by an increase in the amount of HA added to the mixture and its reaction with Ti can have a detrimental influence on the mechanical properties and might be a contributing factor to the reduction of mechanical properties with the increase of HA [304]. In addition, Ti_2O has been shown to promote and induce the nucleation and formation of apatite in Ti-HA dense composites after 2h immersion in simulated body fluid [278].

Several important events and reactions take place during sintering of Ti-HA composite foams. One is related to the thermal decomposition of the second part of the binder (PMMA) and occurs in the temperature range 200-450ºC. This is followed or accompanied by the dehydroxylation of the HA or gradual loss of the hydroxyl group upon heating in the temperature range 295-1200ºC, resulting in hydroxyl ion-deficient or oxy-hydroxyapatite ($Ca_{10}(PO_4)_6(OH)_{2-2x}O_x\square_x$ where $\square$ is non-charged vacancy, x < 1) and water vapour [305-307]. Studies in the literature reported that the dehydroxylation of the HA starts to occur at a temperature of 600ºC and continues until as high as 1000 ºC [308], whereas others have stated that the dehydroxylation takes place at a temperature as low as 700ºC [309]. The water vapour reacts with the Ti to form titanium oxide which is a very important reaction as it might be another contributing factor in increasing the brittleness of the Ti particles in the Ti-HA composite foams. The more the HA added to the mixture the more the abundant the oxygen, which results from the loss of the hydroxyl group upon heating, and the higher the chance of exposure of Ti to significant levels of oxygen in the porous structure, thus forming Ti oxide. The oxide is then dissolved in the Ti during sintering forming a solid solution and a newly formed oxide layer is then made upon exposure of Ti to lower temperatures during cooling [310]. There has been evidence in the literature associating increased strength and brittle failure in Ti foams with increased oxygen content [310] which might explain the higher strength and the brittle failure for the Ti-HA composite foams sintered at 1320ºC for 2 h compared to those without HA. In the case of remaining HA, it decomposes and transforms into a mixture of HA and β-TCP during sintering from 700-1100°C; the latter can then be transformed into α-TCP at about 1200°C [311]. Next, TCP reacts with some of the titanium

resulting in $CaTiO_3$ and phosphorous, which in turn reacts with Ti to form Ti_3P. These reactions have been reported in the literature on Ti-HA dense composites [293]. It is worth noting that the lattice mismatch between the various formed phases (hcp in the case of Ti and HA and orthorhombic structure for $CaTiO_3$) can also play a role in inducing large quantities of defects upon cooling, which consequently could affect the ability of Ti-HA composite foams to absorb energy through plastic deformation [312].

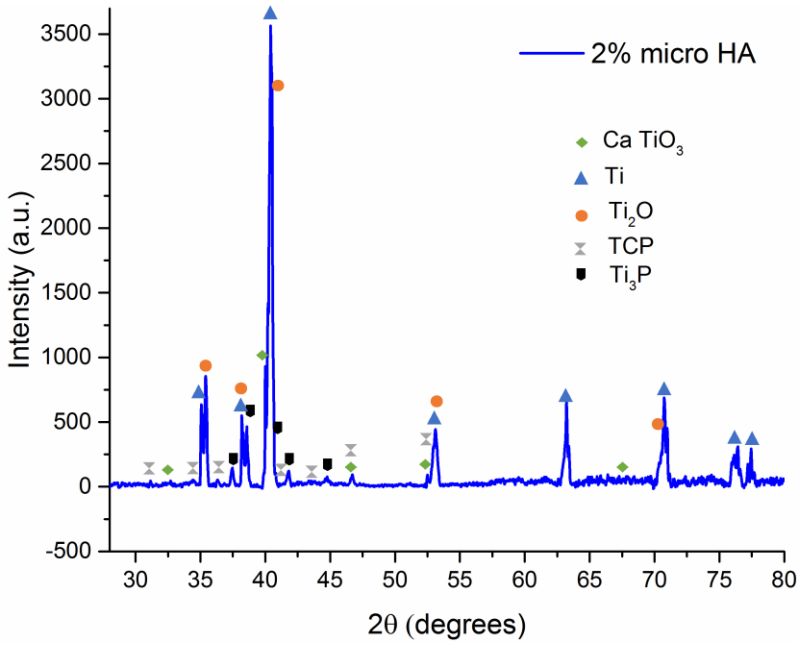

Figure 108. XRD spectrum of Ti foam with 2% micro-HA sintered at 1320 °C for 2h

7.2 Biological Test Results

Cell culture trials were carried out as explained in **section 3.5**, at the University of Sheffield by Ms Z. Wally. Overall, MLOA5 cells were found to be viable (i.e. increased in concentration) on both scaffolds during the 28 days of cell culture. Cells followed a similar pattern of viability on both scaffolds with time (**Figure 109 (A)**). The viability increased significantly from day 4 to day 7 with similar values found on scaffolds with and without HA, indicating that the porous titanium scaffolds with 2% micro-HA do not improve (and also do not hinder) bone cells attachment and ingrowth into the scaffolds.

Both porous titanium scaffolds supported calcium and collagen production after 28 days of cell culture. The highest calcium deposition was on 2% HA scaffolds seeded with cells

(**Figure 109 (B)**), while scaffolds without HA supported the best collagen formation (**Figure 109 (C)**). Nevertheless, differences between the scaffolds were not statistically significant. It is reported that the presence of HA with Ti can promote better bone formation, increased alkaline phosphatase activity and collagen production [313, 314]. However, it is believed that the small amount of HA added here (2%vol) was not sufficient to cause significant differences.

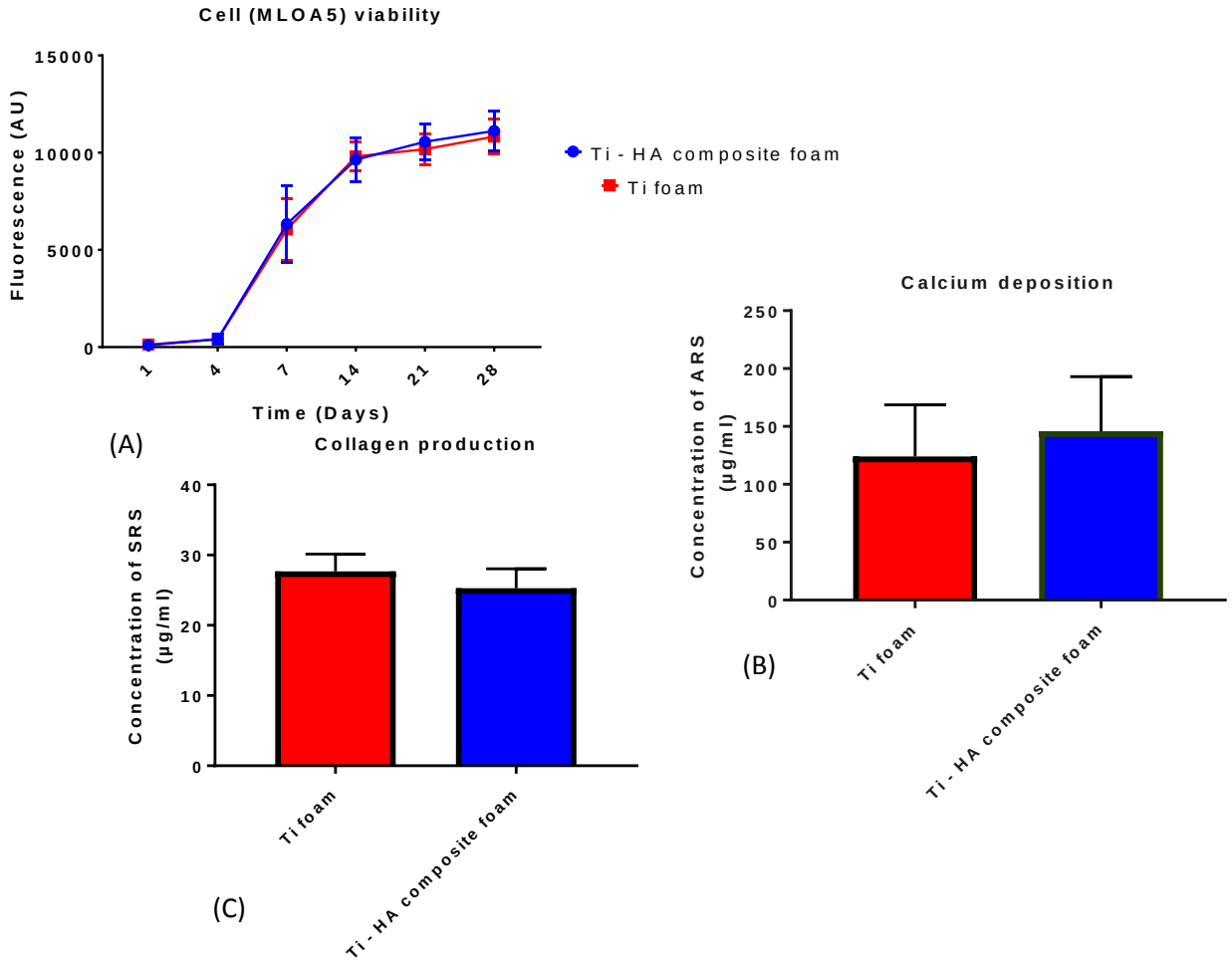

Figure 109. Mean ± SD for (A) cell viability of MLO-A5s on Ti foam and Ti-HA composite foams over 28 days (B) calcium staining and (C) collagen staining on day 28 of cell culture, (n=6).

8 Improving the bioactivity of Ti foams through surface modification

8.1 PEO treatment of porous Ti and resulting coatings

The possibility of developing biologically active ceramic coating on porous Ti samples was investigated by treating three groups of samples with different amounts of porosity in an electrolyte of anhydrous disodium phosphate (Na_2HPO_4). The treatment was performed in DC mode by sweeping the potential up to a maximum value of 500 V at scan rates of 2.12 and 4.22 V s^{-1}. The first group of samples had an average porosity of about 7 vol% with a mean pore size of 17 µm (**Figure 110. a**), whereas the second group had a porosity of about 20 vol% with a mean pore size of 57 µm (**Figure 110. b)**. The third group of samples had a total porosity of 62 % and a mean pore size of 348 µm. For ease of distinguishing among different groups, these samples will be referred to as a relatively dense, microporous and macroporous samples respectively.

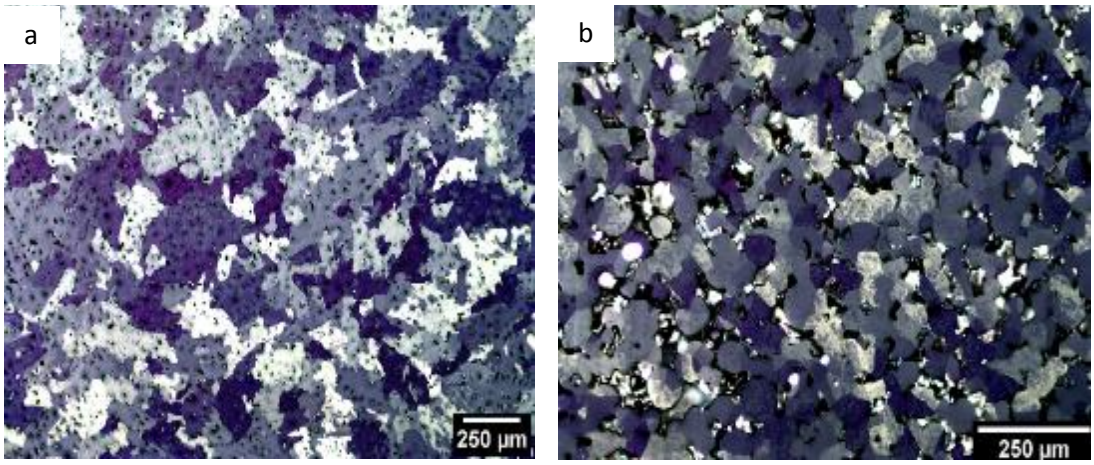

Figure 110. Optical micrographs of the polished samples using colloidal silica mixed with 30% hydrogen peroxide to reveal the microstructure for: (a) Sample sintered using commercial Ti feedstock; (b) Sample sintered using relatively coarse Ti powder reproduced from Shbeh, M., et al. Appl Surf Sci. 2018; 439 801-814.

The cyclic voltammograms for the porous Ti samples treated at scan rates of 4.22 V s^{-1} in the region 0-500 V are shown in **Figure 111**. All voltammograms showed a similar general trend. In the forward scan, an increase in the charging current occurred in response to the potential applied (region a-c) and continued until the current peaked at region (c), before dropping significantly in the post peak region (c-d) until the maximum voltage of 500 V was reached.

The reverse scan is characterised by a period of local instabilities and disturbances accompanied by a slight increase in current, where the curves behave erratically due to the evolution of gaseous products, with abundant bubbles partially shielding the anode from the electrolyte and consequently depleting the shielded regions of the electroactive species (d-e). The instability period proceeds until the current peaks again at region (e), before decaying dramatically back to its initial value, thereafter a capacitive discharging of the double layer at the anode-electrolyte interface occurs. Aside from the aforementioned general trend, the cyclic voltammograms for the samples with different porosity have some unique and distinguishing characteristics from each other. It can be noted that for relatively dense samples, the initial current increase in the forward scan is very slow and the first peak (a) is barely noticeable. However, once the voltage applied reaches a value of 250 V (b), the current starts increasing dramatically, reaching a peak value of 1573 mA cm^{-2} (c) before dropping rapidly to 1067 mA cm^{-2} and then increasing slightly and subsequently decreasing in the region (d) to a minimum value of 651 mA cm^{-2} at the highest voltage of 500 V. In the reverse scan, as the applied voltage decreases, the current increases almost linearly up to the maximum current value of 1054 mA cm^{-2} corresponding to 493 V and then it decreases and increases intermittently during a period of local instabilities before peaking to 1533 mA cm^{-2} at region (e). Next, the current drops dramatically and discharging of the interfacial double layer occurs. Compared to the relatively dense samples, the current in the microporous samples rises significantly quicker with the potential applied in the initial stage of the forward scan (a) reaching a maximum current value of 267 mA cm^{-2} (more than nine times the value reached for the relatively dense sample, where the current density reached a maximum value of only 28 mA cm^{-2} at region (a)). Furthermore, the voltage at which the current peaked in region (a) has been dramatically shifted from 16 V for the relatively dense samples to about 66 V for the microporous samples. The current then drops slightly before monotonically increasing again at the inflection point (b) corresponding to 160 V. Unlike the relatively dense samples, where one prominent peak is detected, several conjoined wide peaks appear in region (c) for the microporous samples and the voltage at which the current peaked has been lowered from 396 V for the relatively dense sample to about 328 V for the microporous sample. In addition, the current density in the microporous sample dropped to a minimum value of 571 mA cm^{-2} in region (d), which is lower than that for the relatively dense samples.

It was also noted in the reverse scan that the maximum peak current reached in the microporous samples was significantly higher and corresponds to a lower voltage compared to the relatively dense sample, where the current density peaked in region (e) at 1955 mA cm^{-2} at 274 V in the case of the microporous sample, while for the relatively dense sample the current density peaked at 1533 mA cm^{-2} at 284 V.

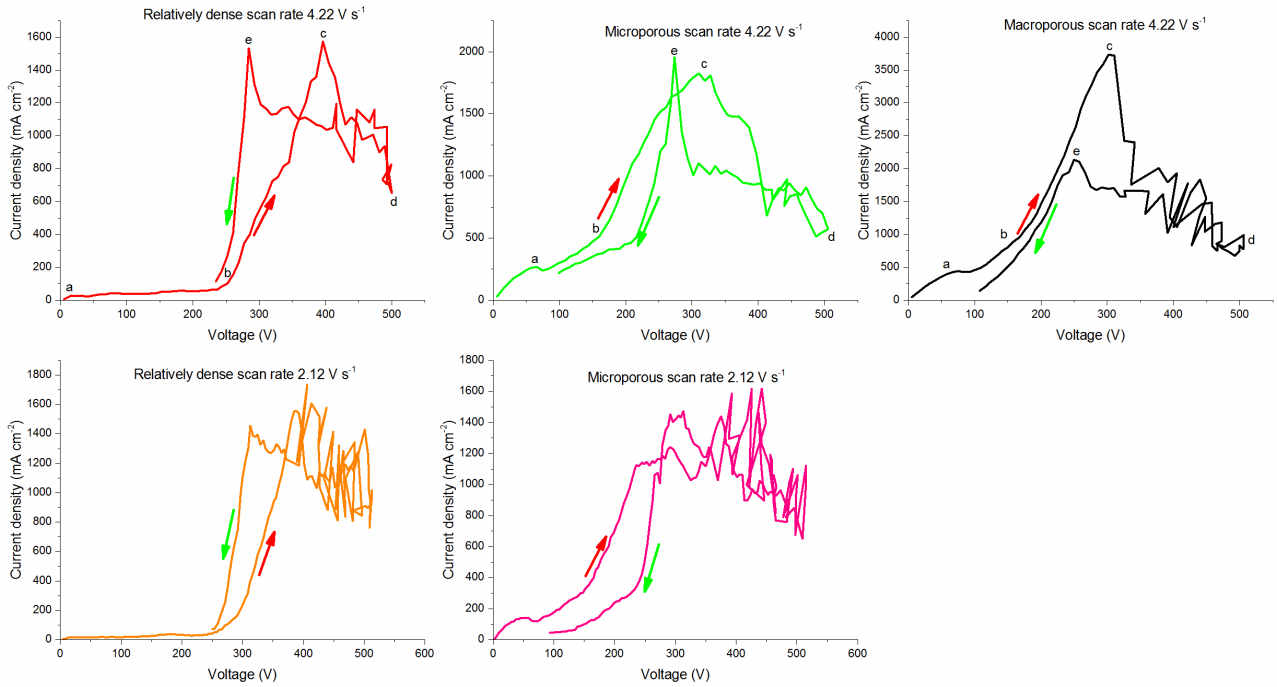

Figure 111. Cyclic voltammograms for different porous Ti samples in 14 g L^{-1} disodium phosphate electrolyte at scan rates of 4.22 V s^{-1} and 2.12 V s^{-1} reproduced from Shbeh, M., et al. Appl Surf Sci. 2018; 439 801-814.

Macroporous samples showed a similar, significant increase in the charging current with voltage in the initial stage of the forward scan region (a) compared to that observed for the microporous samples, but the incremental growth in current with the applied voltage persists up to a higher value of current (446 mA cm^{-2}) and approximately double the value reached in the microporous samples and the voltage at which the current peaked at region (a) shifted further from 66 V for microporous to 75 V for the macroporous sample. The slopes of the linear regions between (a) and (b) were found to be 0.2, 3.3 and 7.1 mA V^{-1} cm^{-2} for the relatively dense, microporous and macroporous samples respectively. It was also noticed in the macroporous samples that the current density peaked in region (c) at a value of 3739 mA cm^{-2}, which is more than double the value reached in region (c) for both microporous and

relatively dense samples, but at a lower corresponding voltage (302 V). The current density for the macroporous sample in the reverse scan peaked at region (e) with a value of 2137 mA cm^{-2} at voltage of 250 V before the double layer discharging occurs and the current diminished.

In addition, the highest electrolyte temperature of 32 °C was recorded during experiments with the macroporous samples, in contrast to only about 20 °C and 27 °C for the relatively dense and microporous samples respectively. This might be due to a combination of a higher Joule heating by a higher current passing through the electrolyte and the increased resistivity of the electrolyte solution inside the porous channels of the metal electrode.

Compared to cyclic polarisation curves at the fast scan rate (4.22 V s^{-1}), those at the slow rate (2.12 V s^{-1}) showed a similar general trend and a more erratic behaviour in the post peak region (c). In addition, it was noted that the change in the scan rate did not significantly impact the cyclic polarisation curve for the relatively dense samples, where the peak height at region (a) was still barely noticeable and approximately similar to that at fast scan rate (about 21 mA cm^{-2} corresponding to 16 V), while the slope of the linear region (a-b) was about 0.1 mA/V.cm^2. In terms of the peak in region (c), the height slightly decreased from 1573 to 1555 mA cm^{-2} and the corresponding voltage was lowered from 396 to 385 V.

However, for the microporous samples, there were some distinguishing characteristics among the voltammograms with different scan rates. The potential at which the current peaks in region (a) decreased from 66 to 46 V with slowing the scan rate, while the peak height declined by as much as 47%, reaching a value of 142 mA cm^{-2}. In addition, the slope of linear region between (a) and (b) reduced from 3.3 to 2.9 mA/V.cm^2. Furthermore, the peak height in region (c) reduced from 1810 to 1440 mA cm^{-2}.

It was generally noted that during anodic polarisation, a large amount of gas bubbles evolved around the specimen, shielding it from the electrolyte until the voltage reaches about 250 V, where electrical discharges normally start occurring. These discharges are initially formed intermittently via least resistive regions of the shielded surface and hit the weakest points of the previously formed oxide. As the discharge occurs, a mixture of vapour and gases heats up rapidly without having enough time to expand and thus it is pressurised and explodes on the Ti surface, with strong acoustic emission, enabling further reaction of electrolyte anions with Ti substrate.

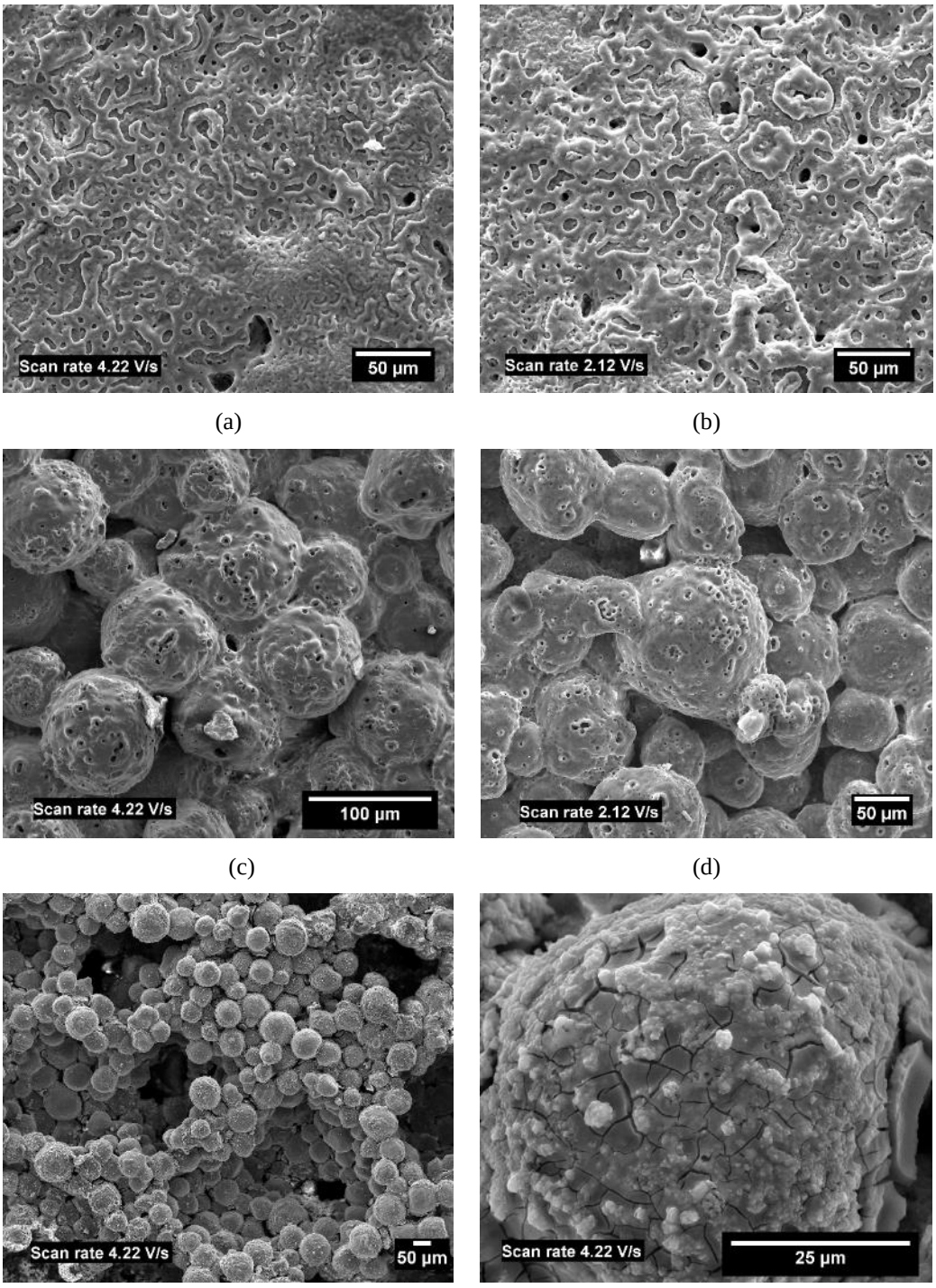

Figure 112. SEM micrographs of: (a) and (b) relatively dense samples, (c) and (d) microporous samples, (e) and (f) macroporous sample at low and high magnification reproduced from Shbeh, M., et al. Appl Surf Sci. 2018; 439 801-814.

The heat released by these discharges causes local melting of the affected region of the previously formed oxide, with the melt being then expelled, leaving behind a microporous channel with a crater-like opening. As the oxide weakens significantly, the electrical discharges form concurrently, covering a large area of the sample surface by progressive breakage of the existing oxide film and continuous bombardment of the surface with secondary electrons and electrolyte anions, forming new rapidly solidified oxide layers with low electrical conductivity and the process is repeated again. It should be noted that the acoustic emission was much stronger for the porous samples, especially for the macroporous ones, with a significantly higher optical emission intensity. In addition, the population density of sparks at the low scan rate was generally observed to be less, but the intensity and size were significantly larger than those at the high scan rate were. The observation is in a good agreement with the findings of others [203]. During the reverse scan, the frequency of these sparks was reduced once the voltage dropped below 200 V.

The resultant surface morphology for the samples processed at the scan rates of 4.22 and 2.12 V s^{-1} is shown in **Figure 112.** Relatively dense samples polarised at the scan rate of 4.22 V s^{-1} are covered with a very fine cellular-like oxide network with some micropores, but much fewer craters were observed compared to the microporous samples. Following the scan performed at the lower speed 2.12 V s^{-1} the features of the oxide network on the sample surface become coarser, due to a longer residence time at higher voltages where more intense discharges were generated.

The microporous samples were covered with a rough surface oxide layer displaying some microporous craters that result from electrical discharges developed in the high-voltage region. The average diameter for the craters was found to be about 4.2±0.4 and 5.5±0.5 μm for the samples polarised at scan rates of 4.22 and 2.12 V s^{-1} respectively. In addition, the micropores that result from the incomplete sintering of the Ti powder were partially encrusted with oxide layer as shown in **Figure 112** leading to a smaller pore size.

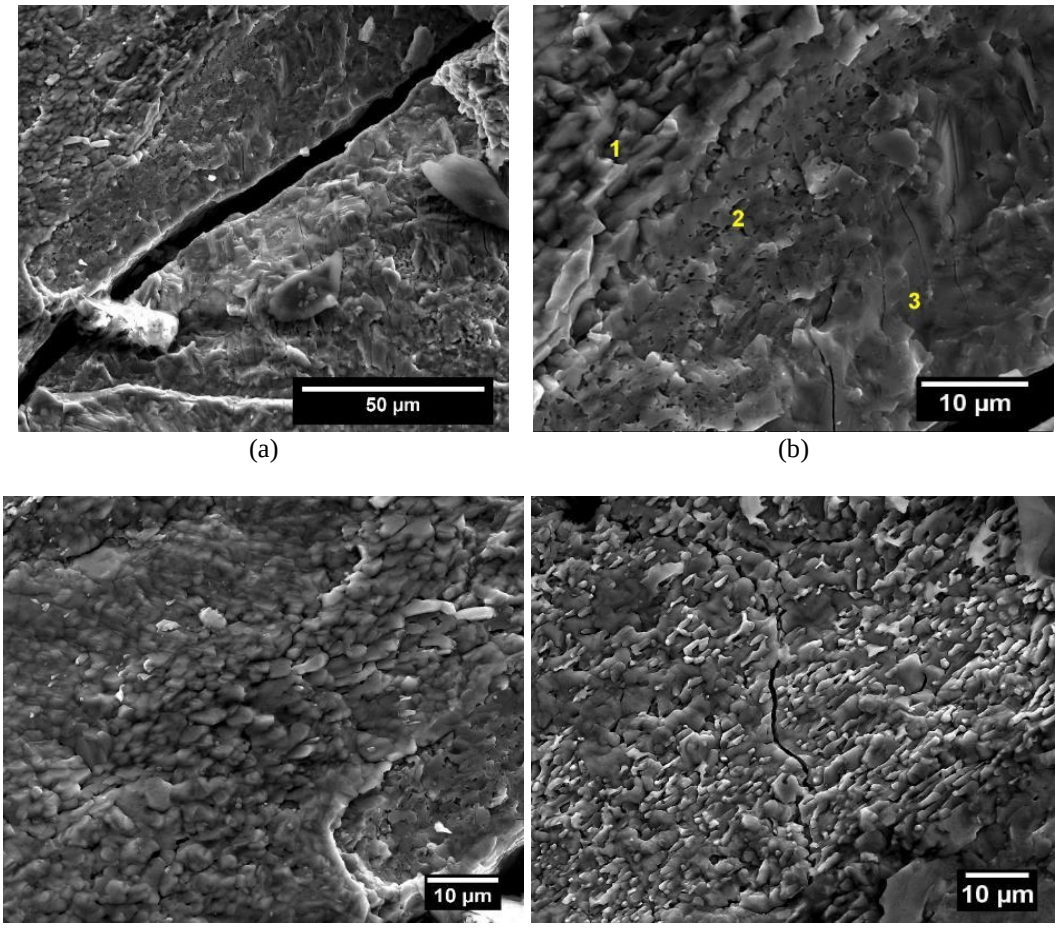

(a) (b)

(c) (d)

Figure 113. Secondary electron microscopy images of different regions of the globular sediment reproduced from Shbeh, M., et al. Appl Surf Sci. 2018; 439 801-814.

The macroporous samples polarised at the scan rate of 4.22 V s^{-1} did not show any of the features which are typically encountered during oxidation treatment of Ti and showed instead some layers deposited on the surface of Ti particles composed of small individual particles joined together and in some cases agglomerated as shown in **Figure 112**. Some of these individual deposited particles appear light in colour (**Figure 112.f**), which seems similar to that reported for sodium titanium phosphate [315]. The average size of individual nodular deposits was analysed on six Ti particles using image J software and found to be in the region of 3 µm. It is important to point out that the macroporous samples treated at the scan rate of 2.12 V s^{-1} were disintegrated into globular sediments in the electrolyte and only parts of the samples still remained attached to the Ti bar. In order to further analyse the reason behind

this failure, the globular sediment was characterised using SEM and the images taken are demonstrated in **Figure 113**. Several large cracks with smooth edges were noticed throughout the globular sediment indicating the occurrence of brittle failure in the surface layer. In addition, three different regions were observed in the area adjacent to the crack, as shown in **Figure 113.b.** The first region is characterised by a dense structure comprising facets of TiO_2 crystals with different morphologies deposited onto the surface of the sample, beneath which resides a second layer with high porosity and average pore size of 2 μm. The third layer lies underneath the second and possesses a smooth and dense morphology featuring small cracks. A series of spot EDS analyses was carried out in those three surface regions, with the mean average concentrations of the main elements provided in **Table 19**.

The EDS results in **Table 19** indicate that the cracked region 3 is significantly richer in phosphorus compared to other regions in the coating. In comparison, the porous region 2 has over-stoichiometric O content in respect to TiO_2, where for every Ti atom there is approximately 2.1± 0.2 oxygen atoms.

Cross-sectional SEM images and corresponding EDS maps showing the distribution of chemical elements in the surface layer of samples polarised at the scan rate of 4.22 V s^{-1} are provided in **Figure 114-Figure 118.**

Table 19. Results of EDS analysis for different regions in the coating area adjacent to the crack

Element at.%	Region		
	1	**2**	**3**
O	67.9± 0.1	73.5± 0.2	65.2± 3.8
Ti	31.8± 0.2	26.4± 0.1	30.5± 1.2
P	0.1± 0.1	0.1± 0.1	4.1± 2.7
Na	0.2± 0.1	0± 0.1	0.2± 0.2

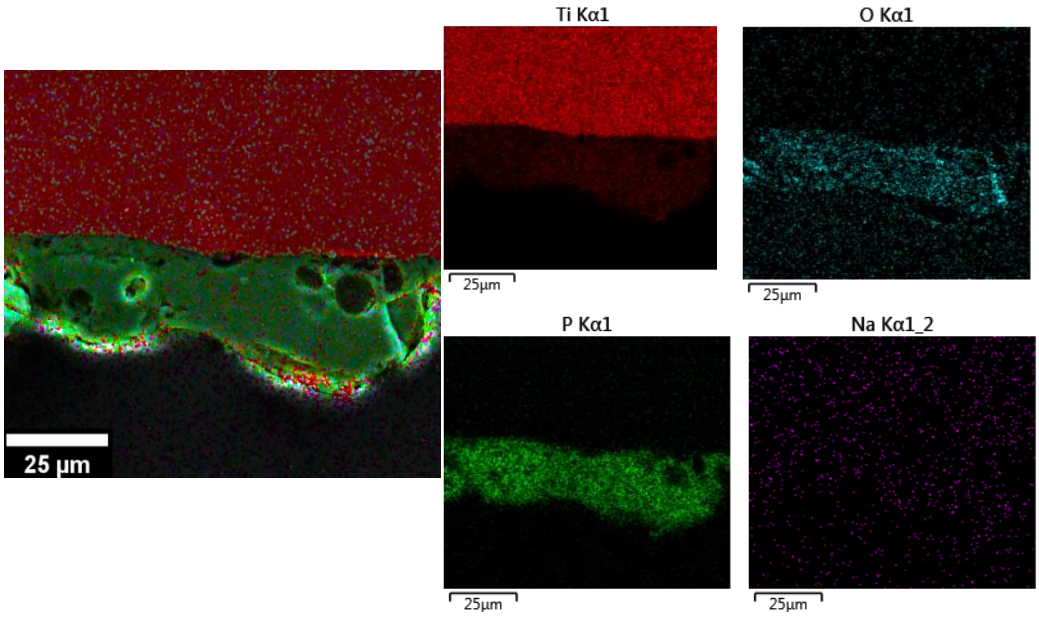

Figure 114. Cross-sectional SEM image combined with EDS element mapping of the surface region of the relatively dense sample subjected to cyclic anodic polarisation at a scan rate of 4.22 V s^{-1}. The colours in the composite image match those used for the individual element maps reproduced from Shbeh, M., et al. Appl Surf Sci. 2018; 439 801-814.

The relatively dense samples showed rough, non-uniform morphology of the oxide layer with good adhesion to the Ti substrate. The lack of open pores in the relatively dense samples led to oxide formation on the surface of the sample only. The average thickness of oxide layers developed in the relatively dense samples at scan rates of 4.22 and 2.12 V s^{-1} was 13±3 and 16±6 µm.

From the cross-sectional image of the microporous sample, it can be observed that it is covered with a thick non-uniform surface oxide layer that extends to the inner structure of the sample through the micropores which are connected to the surface, forming a network of interconnected surface and subsurface oxides.

Compared to the relatively dense samples, the coatings developed in the microporous samples were thicker and seemed rougher and more interconnected. It is important to point out that the relatively dense samples did also have some pores (**Figure 110 (a)**), but the pores were likely to be closed and isolated with no access to the surface, as shown later. The oxide layers developed on the microporous samples had average thickness of about 47±6 and 55 ±5 µm for the scan rates of 4.22 and 2.12 V s^{-1} respectively.

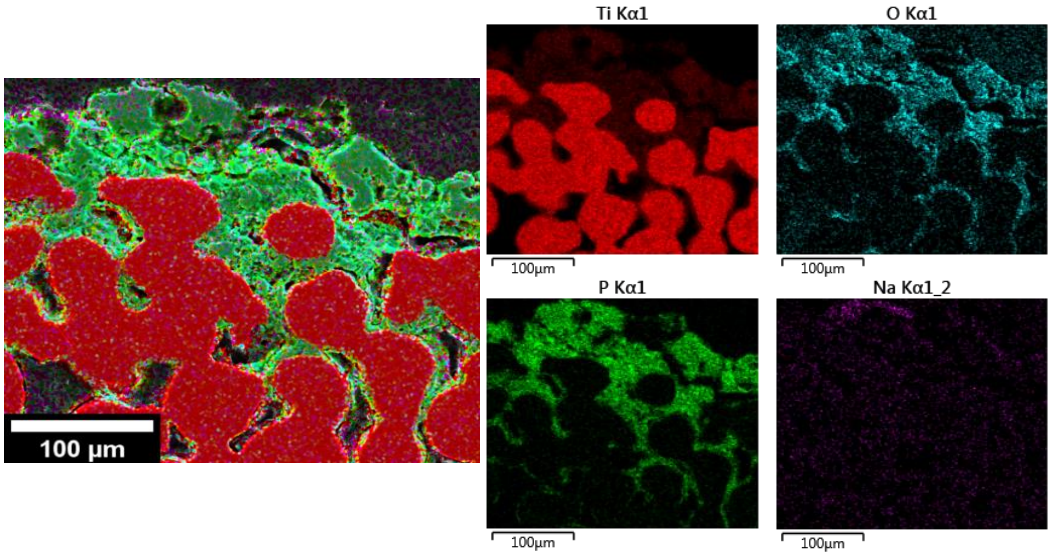

Figure 115. Cross-sectional SEM image combined with EDS element mapping of the surface region of the microporous sample subjected to cyclic anodic polarisation at a scan rate of 4.22 V s^{-1}. The colours in the composite image match those used for the individual element maps. Red for Ti, green for P, cyan for O and purple for Na reproduced from Shbeh, M., et al. Appl Surf Sci. 2018; 439 801-814.

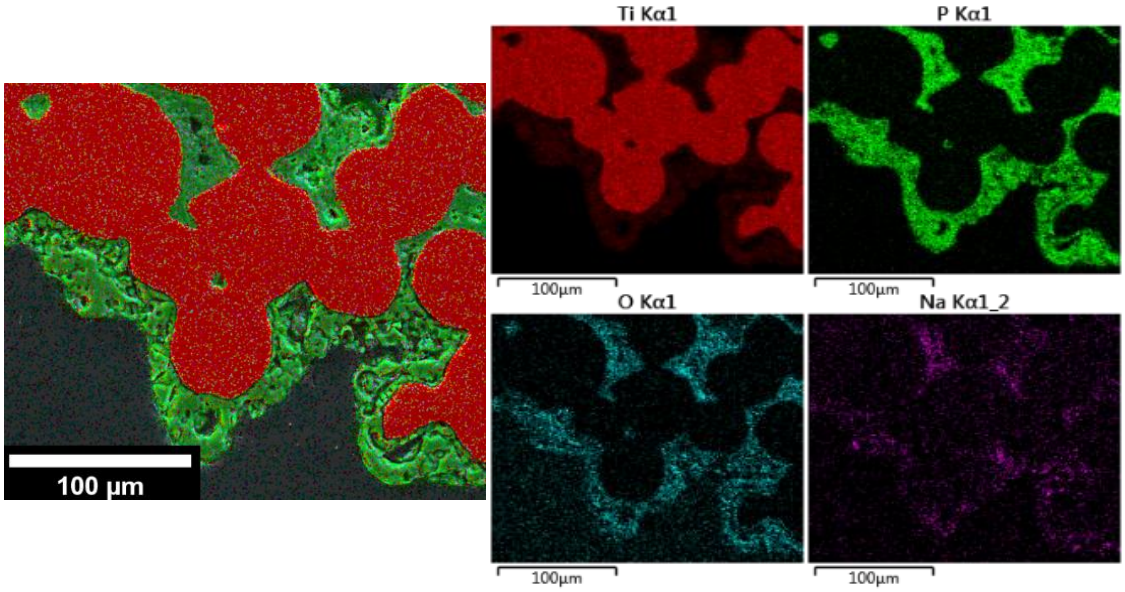

Figure 116. Cross-sectional SEM image combined with EDS element mapping of the surface region of the macroporous sample subjected to cyclic anodic polarisation at a scan rate of 4.22 V s^{-1} reproduced from Shbeh, M., et al. Appl Surf Sci. 2018; 439 801-814.

Similarly to the microporous substrates, the oxide layers formed on the macroporous samples extended into the inner substrate structure through interconnected porous networks, although these coatings were slightly thinner (41±14 µm for the scan rate of 4.22 V s^{-1}), showing no

signs of cracks and appearing to be better adhered to the metal substrate. In addition, the oxide layer thickness was noticed to decrease to about 10±4 µm at a depth of 4.3 mm from the sample surface.

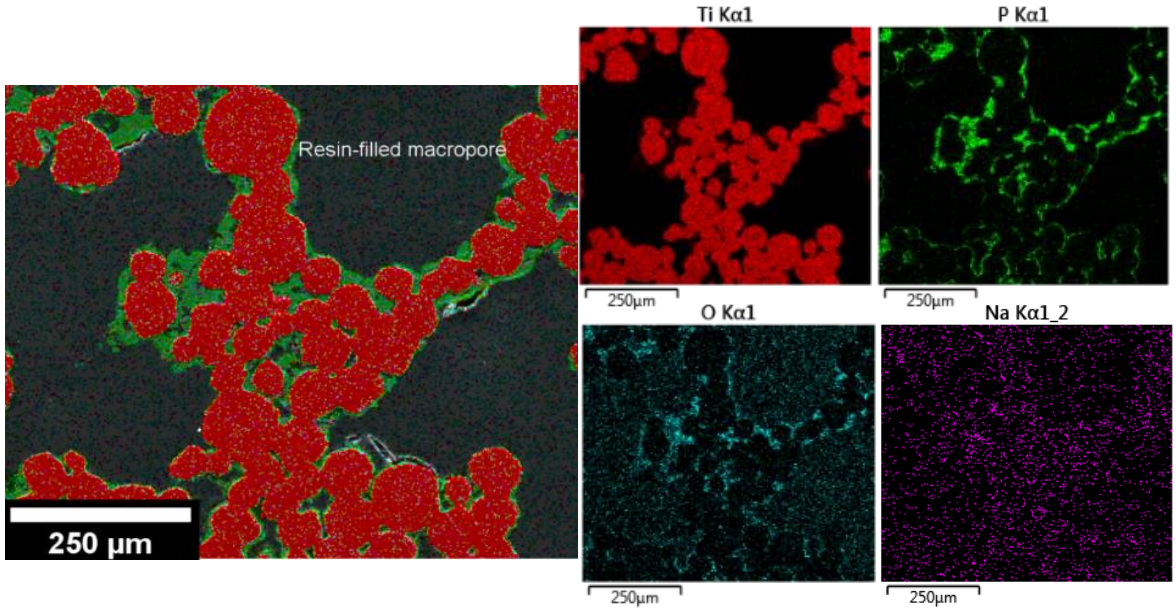

Figure 117. Cross-sectional SEM image combined with EDS element mapping at a depth of 1.62 mm from the surface of the macroporous sample subjected to cyclic anodic polarisation at a scan rate of 4.22 V s^{-1} reproduced from Shbeh, M., et al. Appl Surf Sci. 2018; 439 801-814.

Results of the XRF analysis of oxide chemical composition are shown in **Figure 119.** Elements, such as Al and Si, detected in very small amounts are not shown, as they might be due to contamination during sample and electrolyte preparation.

The general trend seen from **Figure 119** is that the atomic percentage of Ti decreases with decreasing scan rate, while the converse is true for oxygen. It seems that it is harder for the Ti ions to diffuse through the thicker coating layers formed at the slow scanning rate and migrate to the surface to form new oxide layers, leading to a deficiency or depletion of Ti in the upper layers of the coating. It should be noticed that XRF is not an effective technique in estimating the content of light elements and hence the results can be taken as a rough approximation for the atomic percentages in the coatings. However, such results can help understanding the change in atomic concentrations of the elements with the change in the scanning rate.

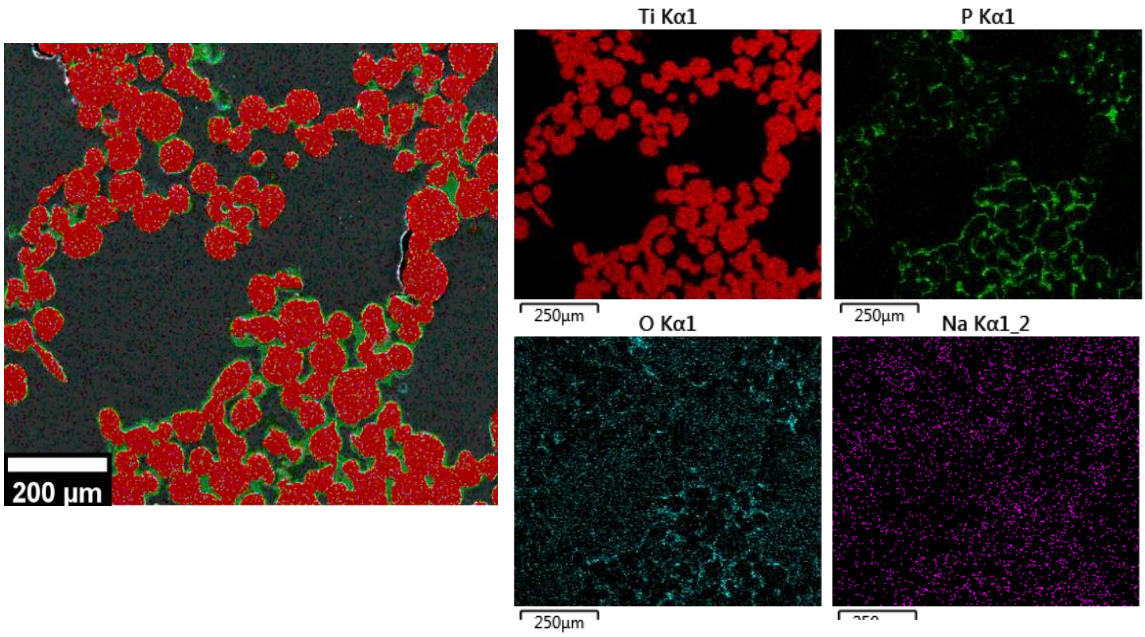

Figure 118. Cross-sectional SEM image combined with EDS element mapping at a depth of 3.11 mm from the surface of the macroporous sample subjected to cyclic anodic polarisation at a scan rate of 4.22 V s^{-1} reproduced from Shbeh, M., et al. Appl Surf Sci. 2018; 439 801-814.

The EDS results for a relatively dense sample scanned at 4.22 V s^{-1} shown in **Figure 120** suggest that the oxide is composed of approximately equal amounts of P and Ti and did not penetrate into the pores in the structure. As in the case of microporous samples, the pores present here did not have access to the electrolyte via the surface, leading to the formation of a surface coating without having subsurface layers.

The results of the EDS analysis for the coating cross-section on the microporous sample scanned at 4.22 V s^{-1} are shown in **Figure 121.** It can be seen that the atomic percentage of Ti increases when moving away from the surface towards the bulk of the sample with the lowest value being at the coating area, while the contents of O, P and Na decrease towards internal structure of the sample, with the highest concentrations being in the surface region. Unlike microporous samples, coatings developed on the macroporous substrates did not show any significant differences in the chemical composition with depth as illustrated by the EDS results presented in **Figure 122**.

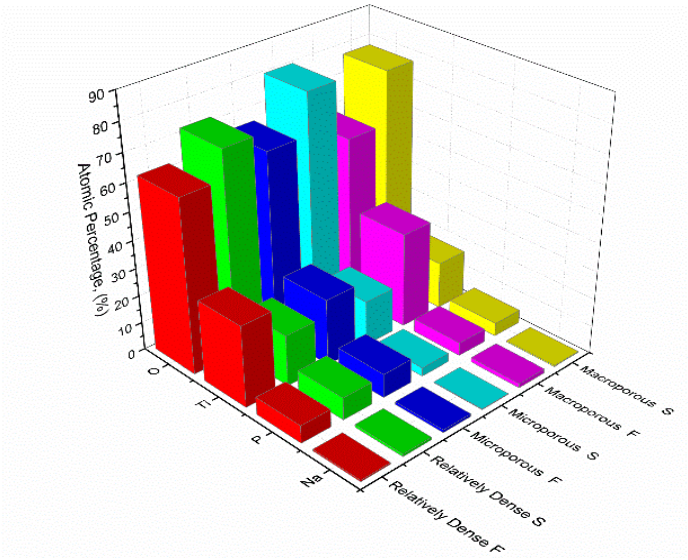

Figure 119. Surface XRF analysis of oxide films produced on the studied Ti samples, where F and S stand for fast and slow scan rates (4.22 and 2.12 V s^{-1}). For the macroporous sample with the slow scan rate (2.12 V s^{-1}), the globular sediment was used in its XRF characterisation reproduced from Shbeh, M., et al. Appl Surf Sci. 2018; 439 801-814.

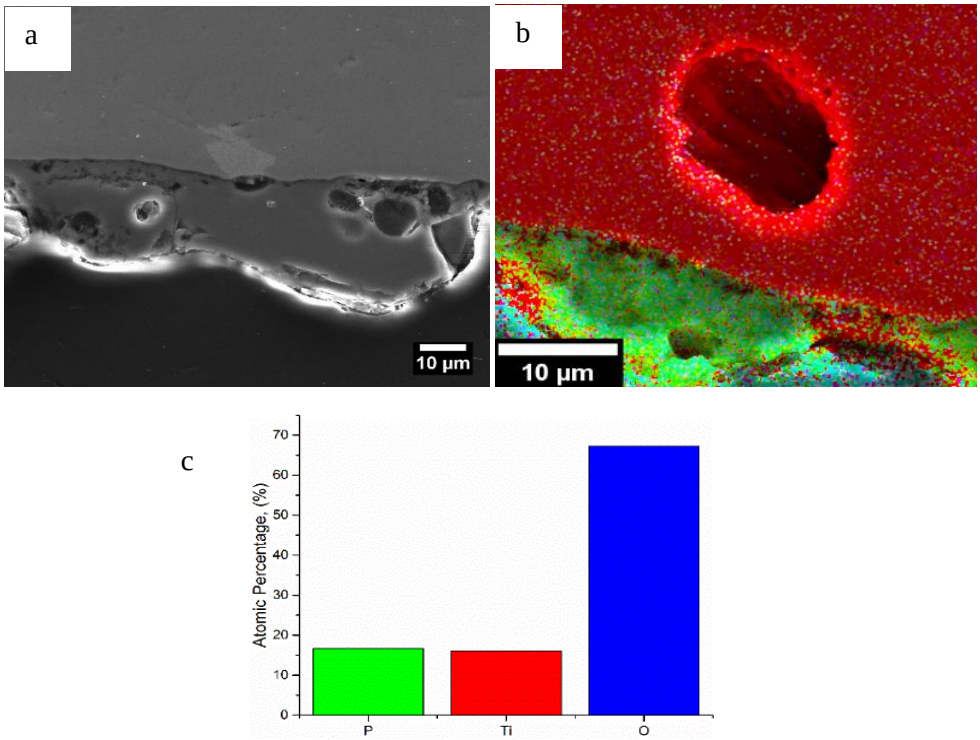

Figure 120. (a) Secondary electron microscopy image of the coating developed in the relatively dense sample subjected to cyclic anodic polarisation at a scan rate of 4.22 V s^{-1}, (b) and (c) EDS element mapping and quantification results reproduced from Shbeh, M., et al. Appl Surf Sci. 2018; 439 801-814.

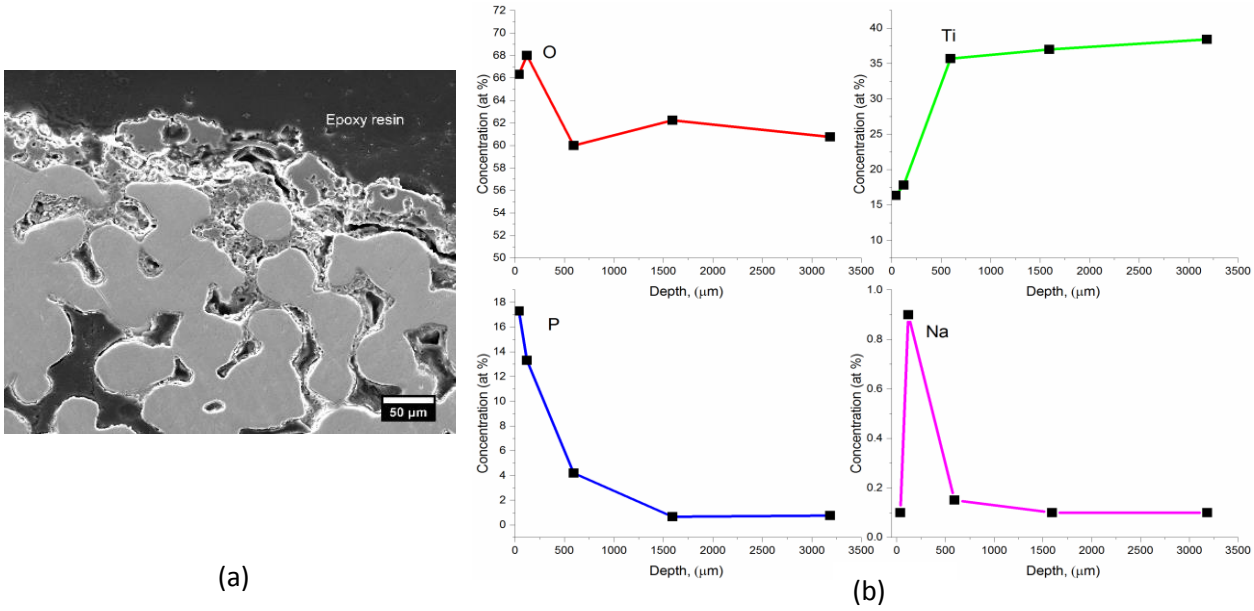

Figure 121. (a) Cross-sectional SEM image the studied surface region in the microporous sample subjected to the cyclic anodic polarisation at a rate of 4.22 V s^{-1}; (b) Depth profiles of the main elements based on the data of EDS point analysis reproduced from Shbeh, M., et al. Appl Surf Sci. 2018; 439 801-814.

Figure 123 presents the results of XRD phase composition analysis for the samples scanned at 4.22 V s^{-1}. The coatings developed in all samples were composed of a mixture of rutile (PDF #04-004-4337) and anatase (PDF #01-073-1764) as well as sodium titanium phosphate $NaTi_2(PO_4)_3$ (PDF #04-002-2744) and titanium phosphate $Ti P_2O_7$ (PDF #04-012-4504). The peak intensities for the microporous and relatively dense samples were higher and much narrower compared to the macroporous samples. Such observation is normally encountered in nanostructured materials, reflecting the lower crystallinity of the coating phases for macroporous samples compared to the microporous and relatively dense samples. It might also be due to scattering by the rougher surface of the macroporous samples provided by coarser porosity. It is also worth noting that the intensity of the peak at $2\theta = 24.6°$ corresponding to the sodium titanium phosphate phase increases when moving from the relatively dense to the macroporous samples in respect to the peak of titanium phosphate at $2\theta = 23°$. This can be taken as evidence for a strong relationship between the accessibility of the pores to the electrolyte, the porosity in the sample and the amount of sodium incorporated in the developed oxide layers. Furthermore, XRD analysis of the internal surface of the

microporous sample was also carried out (**Figure 124**) and only anatase with some rutile were detected, which is in a good agreement with the EDS results.

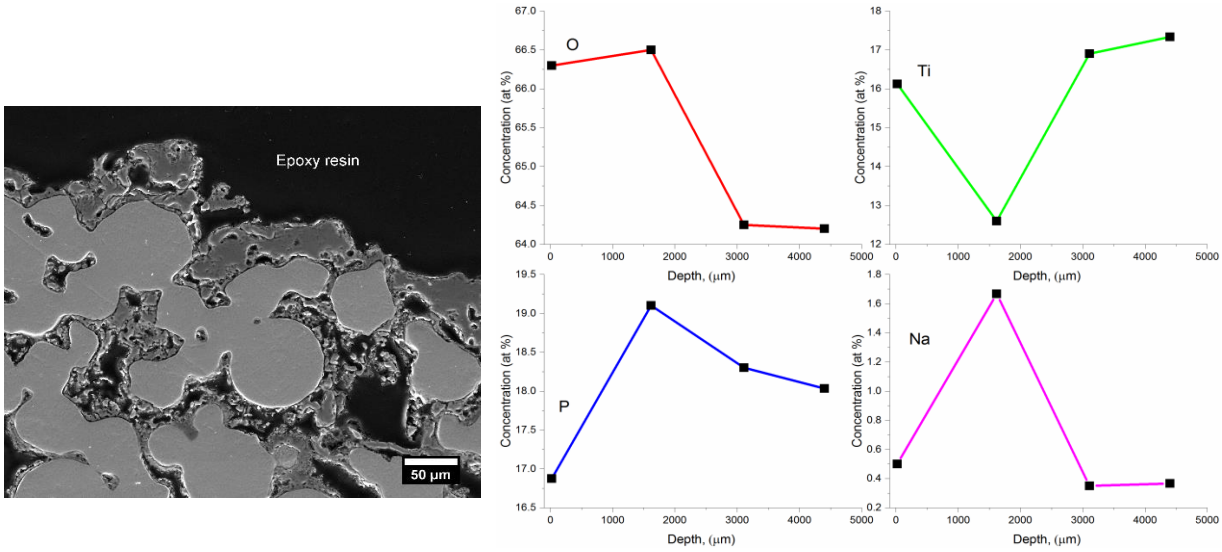

(a) (b)

Figure 122. (a) Cross-sectional SEM image the studied surface region in the macroporous sample subjected to the cyclic anodic polarisation at a rate of 4.22 V s^{-1}; (b) Depth profiles of the main elements based on the data of EDS point analysis reproduced from Shbeh, M., et al. Appl Surf Sci. 2018; 439 801-814.

8.2 Discussion

The anodic behaviour of Ti substrates with different porosity in an aqueous solution of disodium hydrogen phosphate has been evaluated at two different scan rates, namely 4.22 V s^{-1} and 2.12 V s^{-1}. Three main topics will be discussed in this section; the first is concerned with the phenomena and electrochemical reactions that take place during the high-voltage anodic polarisation of the samples, the second is the effect of the scan rate on the thickness of the developed oxide films and the third is the rationale behind disintegration of the macroporous samples at the slow scan rate.

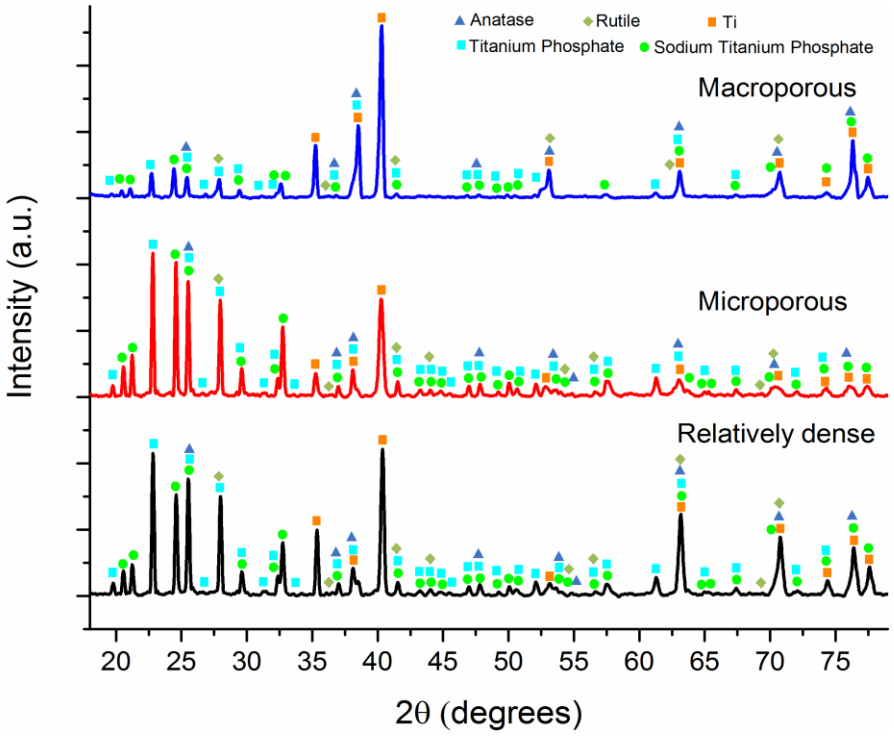

Figure 123. Results of XRD analysis for the studied Ti substrates subjected to cyclic anodic polarisation at the scan rate of 4.22 V s^{-1}. Rutile (PDF #04-004-4337), anatase (PDF #01-073-1764), sodium titanium phosphate (PDF #04-002-2744) and titanium phosphate (PDF #04-012-4504) reproduced from Shbeh, M., et al. Appl Surf Sci. 2018; 439 801-814.

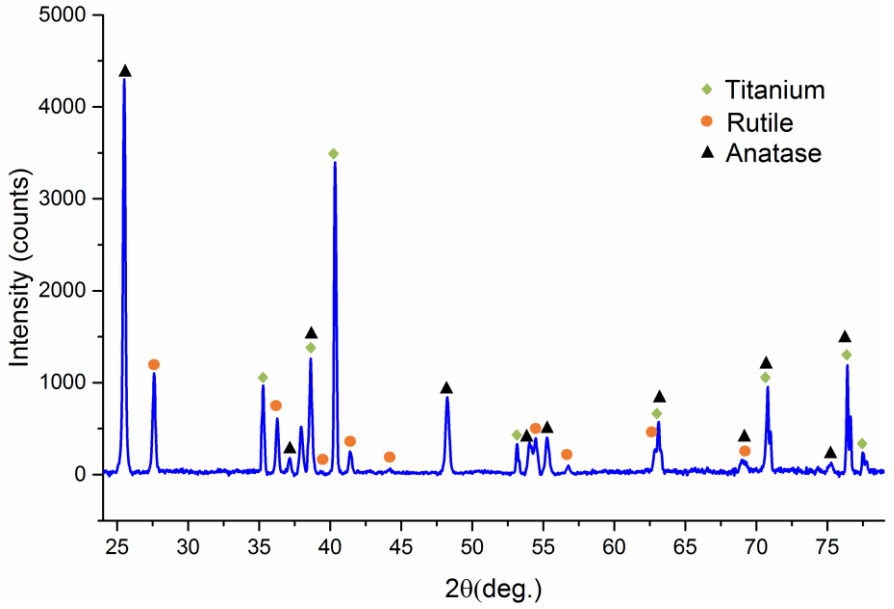

Figure 124. XRD analysis of the internal surface of the microporous sample reproduced from Shbeh, M., et al. Appl Surf Sci. 2018; 439 801-814.

8.2.1 Phenomena and anodic reactions

In the initial stage of polarisation, the current rises with the increase in voltage and a series of processes take place. One is related to the formation of the double layer capacitance between the Ti anode and the electrolyte through the charging current (a-b). The slopes of the linear regions between (a) and (b) were found to be 0.2, 3.3 and 7.1 mAV^{-1} cm^2 for the relatively dense, microporous and macroporous samples respectively. Judging by the values of the slopes of the linear regions, porous Ti samples exhibit higher charging current of the double layer capacitance than relatively dense ones during the primary stage of anodic polarisation due to having a larger surface area. Shi [316] studied the double layer capacitance in nano porous activated carbon and reported that the total capacitance is the sum of the capacitance of both the external surface and the nano pores. He also found that the contribution of the nanopores is smaller than that of the outer surface and some reports attributed his finding to difficulty in adsorbing the electrolyte ions into the pores due their small size [316, 317]. However, in our case the pores are open and significantly larger with extensive access to the internal structure, thus offering the possibility for the ions to be adsorbed easily into the internal structure and hence the contribution of pores to the double layer capacitance should be significant and not negligible. However, for relatively dense samples the contribution of pores should be lower:

$$C_{total} = C_p \times S_p + C_s \times S_s \quad (16)$$

where C_s and S_s are the capacitance and surface area of the outer surface, C_p and S_p are the capacitance and surface area of the pores respectively. The fact that macroporous samples had a charging current double that reached in the microporous samples at the scan rate of 4.22 V s^{-1} indicates the importance of the pore size and accessibility in dictating the amount of the double layer capacitance, and also shows the greater ability of the macroporous samples to store electrical energy, where the higher the surface area the higher the double layer capacitance and the more the current passed for charging the surface. However, accurate estimations of the capacitance could not be performed due to the contribution of the Faradaic current and insufficient number of scan rates. More reliable techniques, such as in-situ impedance spectroscopy [318], should be used for this purpose.

The Ti atoms are initially oxidised into quadruple charged cations according to **reaction 1**:

$$Ti \rightarrow Ti^{4+} + 4e^{-} \quad (1)$$

Generally, two adsorbates compete between each other for adsorption sites onto the outer surface and the inner surface of the Ti substrates, namely the hydroxide and the hydrophosphate anions which form after partial dissociation of the prepared electrolyte (Na_2HPO_4) (**reaction 2**). Based on the pH of the electrolyte the predominant species is HPO_4^{2-}, as this species is stable in the pH range of 7 to 12, within which the pH of the electrolyte falls [319]. In the hydroxide occupied adsorption sites, the hydroxide anions react with the Ti cations forming Ti hydroxide, $Ti(OH)_4$ according to **reaction 3**, which are dehydrated during subsequent polarisation to form anatase TiO_2 according to r**eaction 4** [320]. While in the phosphate occupied adsorption sites, the hydrophosphate anions react with Ti to form titanium phosphate according to **reaction 5**,

$$Na_2HPO_4 \rightarrow 2Na^+ + HPO_4^{2-} \quad (2)$$

$$Ti^{4+} + 4OH^- \rightarrow 4e^- + Ti(OH)_4 \quad (3)$$

$$Ti(OH)_4 \rightarrow TiO_2 + 2H_2O \quad (4)$$

$$Ti^{4+} + 2HPO_4^{2-} \rightarrow TiP_2O_7 + H_2O \quad (5)$$

Anodic polarisation is accompanied by the evolution of gaseous oxygen according to **reaction 6**.

$$4OH^- \rightarrow O_2 \uparrow + 2H_2O + 4e^- \quad (6)$$

The growth of the oxide layers upon the porous substrates proceeds until the oxide layer formed is thick enough to slow down the swift increment in current as well as the oxygen and vapour which could be evolved due to localised boiling of the electrolyte at the anode/electrolyte interface, partially shield the anode resulting in increased electrical resistivity of the system and further decrease in the current growth with potential.

Generally, it has been found that the peak potential in region (c) decreased with increasing sample porosity from 396 V to 302 V, while the peak current density (peak height) increased from 1573 to 3739 mA cm^{-2} with increased porosity. This is consistent with what has been reported in the literature, in particular that the current peak height is directly proportional to the surface coverage of the sample by the adsorbates and consequently the surface area as well as the potential scan rate [321].

In the case of porous samples, the presence of pores will provide additional reaction sites or contact areas among the electrode, electrolyte and the evolved gas products and thus increased species migration occurs not only on the outer surface of the sample, but also inside the pores under the effect of the higher current, leading to higher total amounts of Joule heat generated. This explains the increased temperature of the electrolyte in the case of porous samples compared to the relatively dense ones. Eventually, electrical discharges are formed in the gaseous regions and significant heat released in the vicinity of the discharges as a result, with a temperature reportedly reaching up to 3000 K [322]. The heat causes localised thermally-induced phase changes in the newly developed oxide according to **reaction 7**, where anatase transforms irreversibly into rutile at about 600 °C [323]. Due to the short-lived nature of these electrical discharges, fast localised quenching of the molten material takes place via the electrolyte surrounding the discharging areas. This subsequent quenching can result in significant thermal residual stresses which might lead to the generation of cracks in the surface layer. The formation of sodium titanium phosphate might also be connected with the heat generated by electrical discharges. It is reported that sodium titanium phosphate can be synthesised by heating sodium metaphosphate with titanium hydroxide at a temperature of 1100 °C [324], although the reaction is very slow. Generally, one would expect sodium cations to move towards the cathode after dissociating from the Na_2HPO_4. However, this might indicate the presence of some un-dissociated disodium phosphate in the electrolyte that participates in subsequent reactions during the anodic polarisation. For example, Trout and Glenn [325] studied the dissociation of disodium phosphate at a pH value of 6 and found that only 91.6% is dissociated. Another study reported a degree of dissociation of about 95.4% [326]. It is also worth noting that the degree of dissociation is strongly reliant on the pH value of the solution, where the higher the pH value of solution the higher the chance of complete dissociation [327] and the less the amount of un-dissociated disodium phosphate. Hence, having regions with low pH value and lower concentration of electrolyte, such as pores in the sample, will result in less degree of dissociation and more un-dissociated disodium phosphate in the porous samples than in relatively dense samples. This might explain the increased amount of sodium phosphate involved in the reaction with increased porosity, being higher for macroporous samples than for microporous and relatively dense samples according to the XRD results. It should be noted that there are numerous reports in the

literature about the incorporation of sodium in small percentages in the developed oxide coating during the oxidation treatment [328, 329]. However, these references have not reported the reactions which take place, nor the phases formed. One possible route for the formation of the sodium titanium phosphate in our case is the reaction of TiP_2O_7 with TiO_2 to form $(TiO)_2P_2O_7$ according to **reaction 8**, which reportedly occurs at about 1000 °C [330]. The titanyl pyrophosphate subsequently reacts with the un-dissociated Na_2HPO_4 yielding Na $Ti_2(PO_4)_3$ according to **reaction 9** [331]. The reaction is reported to take place at a temperature between 900-1000 °C, which leaves no doubt that the formation of sodium titanium phosphate is strongly reliant on the heat generated during the electrical discharges and might indicate that Na_2HPO_4 is not fully dissociated during the oxidation treatment.

$$TiO_2(\text{anatase}) \xrightarrow{>600\,℃} TiO_2\ (\text{rutile}) \tag{7}$$

$$TiO_2 + TiP_2O_7 \xrightarrow{1000\,℃} (TiO)_2P_2O_7 \tag{8}$$

$$(TiO)_2P_2O_7 + Na_2HPO_4 \xrightarrow{900-1000\,℃} Na\ Ti_2(PO_4)_3 + H_2O \tag{9}$$

It is also worth mentioning that in the reverse scan of the cyclic polarisation curve for the relatively dense sample only one main prominent narrow peak was detected in region (e) beyond which the current diminished dramatically, unlike those for the microporous and macroporous samples, where multiple distinctive peaks were noted with much higher peak currents at lower voltage values. This indicates the occurrence of complex multi-electron transfer processes in the reverse scan of the porous samples before discharging the surface and gradual desorption of the electroactive species. In the case of porous samples, pores act as pressure release sites and the trapped gaseous products penetrate into the internal structure of the sample through the pores, pushing with them the electrolyte species. The gases escape and the anion species penetrate the sample to much higher depth through the 3D network of interconnected porous channels, particularly in the case of macroporous samples, where larger open macropores are present. In addition to the electric field, the differences in concentration of the electrolyte species between the external surface and the regions inside the pores provide a driving force for the electrolyte species to penetrate through the porosity. Thus, a deposited layer with approximately consistent chemical composition with depth was

formed on the surface and subsurface region of the porous Ti substrate. This is consistent with the results of EDS analysis of the macroporous sample (**Figure 122**) showing insignificant variations in concentrations of the main elements in the deposited layer with depth. The fact that the layer thickness was reduced by a quarter when moving from the surface towards the centre of the sample, even though the inner regions had a good access to the electrolyte, could be ascribed to the distribution of primary electric field within the macroporous structure of the metal substrate. Unlike dense electrodes, where the electric field over the surface is distributed relatively uniformly (according to the inter-electrode distance), the field at the porous electrodes is mainly concentrated on the outer surface, while its intensity is reduced significantly inside the porous channels due to the shielding effect **[332]**.

The narrow porous channels and relatively low total porosity (20%) of the microporous samples reduced the active adsorption sites, limited species migration and resulted in the formation of a layer with elemental composition varying with depth, as backed up by corresponding EDS results in **Figure 121**. These observations emphasise the importance of the accessibility of the inner structure to the electrolyte, reliant on the openness and the size of the pores to allow electrolyte penetration throughout the whole structure, where macroporous samples had a pore size six times larger and porosity more than three times higher than that for the microporous samples. The relatively dense samples differ significantly in not having open pores, making the process relatively straight forward without any complex reactions taking place in the inner structure of the samples, and hence the oxide layer with equal amounts of P and Ti is formed only on the outer sample surfaces.

It should be noted that we have previously analysed in **section 6.5** a 4 mm section of a foam with a porosity of about 61.5% (approximately similar to that for the macroporous samples in this study), made by the same technique, using micro-computed tomography and found that 99.7% of pores are open pores and the surface area of the solid making up the foam was 22 times higher than that of a solid shape of the same volume. This gives a rough estimate of the difference between the surface area of the relatively dense and macroporous samples.

8.2.2 Coating thickness and scan rate

In terms of the thickness of the coatings developed, the microporous samples had the thickest coating (more than three times thicker than that for the relatively dense samples). This fact

indicates the importance of the rate of the electrical discharge flowing through the samples, or the value of current density and its significant influence on the final coating thickness. The value was significantly higher for microporous samples than relatively dense ones at the scan rate of 4.22 V s^{-1} and this is in a good agreement with PEO studies in the literature, where it has been reported that increased current density leads to the development of thicker PEO coatings [333]. However, it was also reported by the same study that higher current density leads to a lower number of pores in the coatings developed, which was not noted here. In addition, a higher current was passed through macroporous samples than microporous samples, yet the coating thickness was in fact slightly lower. This might be due to increased non-uniformity in the distribution of current throughout the sample with increased porosity and pore size due to the edge or shielding effect. The coating developed in the microporous samples seemed less adhered to the substrate than the others, though it is believed that this separation occurred during the micro-preparation stage due to the use of diamond-based composite fine grinding and polishing disks.

The formation of a network of interconnected surface and subsurface oxide layers in the porous materials is quite promising in the fact that these materials do not only offer a solution for the stress shielding problem by accounting for the differences between the elastic moduli of the Ti and the surrounding bone, but might also promote chemical integration both internally and externally throughout their structure. It should be noted that the presence of phosphate as well as anatase in the coatings has been shown to improve the bioactivity of the implant by improving cell attachment and inducing apatite formation and deposition [334, 335].

Interestingly, slowing the scan rate during polarisation from 4.22 to 2.12 V s^{-1} did not have a dramatic impact on the electrochemical activity of the relatively dense samples, unlike microporous samples, where significant changes took place, including notable reductions in the peak potential, peak current in region (a) and the slope of linear region between (a) and (b) and this might refer to the fact that porous samples are more sensitive to scan rate than relatively dense ones. The slope of the linear region is a function of surface area and scan rate only. Hence, one can have a rough idea whether increased or reduced electrochemical activity and adsorption of the electrolyte ions is taking place in the microporous samples with slowing the scan rate through estimating the ratio of adsorption peak intensities in region (a)

and comparing it with the ratio of the slopes of linear region between (a) and (b) for the different scan rates. By doing so, one finds that the ratio of the slopes (2.9/3.3 = 0.88) is bigger than the ratio of the peak intensities (142/267 = 0.53), which indicates that slowing the scan rate would result in reduced adsorption of electroactive species in the porous structure and reduced electrochemical activity. However, it was found generally the coatings developed in porous samples are significantly thicker than those in relatively dense ones, regardless of the speed of the scan rate.

8.2.3 Disintegration of macroporous samples at slow scan rate

Although the reason behind the disintegration of the macroporous samples into globular sediments treated at slower scan rate (2.12 V s^{-1}) is not clear, the following two hypotheses can be considered. One is mechanical failure by breaking up the bonding areas between the Ti particles within the pores due to the high pressure created by the bursting bubbles, where the current has to pass the convoluted surface of the bonding regions between the Ti particles, where the electric field is concentrated causing local vaporisation of the electrolyte within the pores and the creation of vapour phase. The gaseous products generated put a significant pressure on the bonding regions leading to their disintegration. It should be noted that this local instantaneous pressure is experienced by not only macroporous but also microporous samples. However, this does not have as dramatic impact on the latter substrates because of their lower porosity. In addition, the average yield strength of the microporous samples was previously determined under compression loading (**section 4.1.4)** and found to be 191 MPa, while for the macroporous samples it is about 31.6 MPa, which is 83% lower than that of the microporous samples. Thus, the extent of damage would be expected to be significantly higher for the macroporous samples. It is also worth pointing out that the local pressure inside the discharge channels can reach up to 100 MPa [206, 336], which would be sufficient to cause damage to the macroporous samples.

The second (and perhaps more plausible) hypothesis consists in weakening of the bonding areas due to preferential adsorption of phosphate anions and their reaction with Ti to form brittle products with high ionic conductivity. The adsorption of phosphate is widely reported to take place by ligand exchange with the surface hydroxyl groups [337]. Titanium is initially oxidised forming hydrated oxides, whereas the Na_2HPO_4 dissociates leaving the

hydrophosphate group and two sodium cations [338]. The mechanism of phosphate adsorption on to these hydroxides in the bonding areas relies mainly on the concentration of the phosphate anions in the surrounding area. When the concentration is low, they act by replacing the water molecules on the surface of the Ti hydroxide, resulting in a reduction of the positive surface charge [339]. An increase in phosphate concentration would result in a larger proportion of hydroxyl groups being replaced and eventually the bonds that bridge the hydroxyl groups (OH-Ti-OH) would start breaking, forming new active sites for phosphate adsorption. Thus, the electrical resistance of bonding regions is reduced and accelerated anodic dissolution of Ti takes place to form titanium phosphate causing cracks (as shown in **Figure 112.f)** by aggressively attacking the oxide layers. This would weaken the bonds between the poorly bonded Ti particles in the macroporous structure and result in part disintegration.

The phosphate adsorption efficiency of metal hydroxides is reportedly dependent on the specific surface area and porosity of the samples as well as on temperature and the pH of the environment [340]. Thus, one would expect that the macroporous samples would have the highest tendency to adsorb the phosphate strongly, which is promoted by the larger pores, greater amount of porosity and the higher temperature of the electrolyte during polarisation. This could be supported by the fact that the macroporous samples had the largest adsorption peaks in region (a).

The results of the SEM and EDS analyses of the globular sediment in the areas adjacent to the fracture showed the presence of three regions with different morphologies and chemical compositions. Region 3 is rich in phosphorous with high lateral micro-cracks density. In comparison, the porous region 2 has over-stoichiometric O content in respect to TiO_2 with a Ti/O ratio of (1/ (2.1 ±0.2)) and this can be mainly attributed to the presence of OH species on the surface. Borghols et al [341] made similar observation, but their Ti/O ratio was relatively higher than the value reported here (1/(3.5±0.5)), and they ascribed this to the adsorption of H_2O/OH species on to the surface. Another study reported a similar Ti/O ratio of (1/2.11) [342]. Our EDS results suggested the occurrence of selective adsorption of different anions in different regions through competing for active adsorption sites. Hence, cracks initiate in the brittle areas comprising Ti phosphate and propagate easily through the porous region 2 comprising Ti oxides with pre-formed stress concentration sites before

reaching the upper denser region 1. This indicates that preferential adsorption of phosphate and its interaction with Ti inside the pores plays a significant role in the occurrence of failure and thus, the findings can be taken as a supporting evidence for the second hypothesis previously proposed. However, this does not necessarily mean that the gaseous phase generated by electrolysis does not have a role in the failure of the samples, as it can act as a contributing factor in putting a significant load on these brittle areas, particularly at the sintering necks between the Ti particles (which are around 30.5 μm in diameter) and further weaken them, leading to sample disintegration. This can be confirmed by the fracture surface shown in **Figure 113**.**b** where some rough areas can be seen in region 3, indicating the material underwent plastic deformation and showed some mechanical resistance to the pressure applied by the bursting bubbles.

9 Conclusions

The main aim of the present work was to examine the use of Metal Injection Moulding in combination with a Space Holder (MIM+SH) for producing near net shape, open-celled Ti foams, with different volume percentages of porosity and pore shapes, with the potential for biomedical applications.

The first step towards achieving that was the development of a homogenised feedstock (without space holder) that can be easily injection moulded into the desired shapes. This was then compared in terms of performance (rheological, melting and sintering behaviours, as well as dimensional shrinkages) against a benchmark commercial feedstock in order to assess its suitability for the production of Ti foams. The commercial feedstock which was chosen for comparison purposes was PolyMIM® Grade 2. The feedstock developed had a 58 vol % solid content comprised of relatively coarse Ti powder with a mean particle size of 75 μm.

It was found that samples made with the developed feedstock shrank 35% less than samples processed by the commercial feedstock and had a relative density 14% lower than that of the samples processed using commercial feedstock. The average pore diameter for samples processed by the developed feedstock was approximately three-times larger than that of the commercial feedstock, and the pores were less round with a sphericity of about 0.49. Based on the results, it was concluded that the use of coarse Ti powder could be beneficial in increasing the competitiveness of MIM among other processes for the production of biomedical parts, as it saves cost, reduces shrinkage and also results in more of the intentionally-induced micropores that are desired for cell attachment and bone ingrowth.

After confirming the suitability of the developed feedstock for MIM, it was decided to move into the next step of introducing a space holder material into the feedstock and the developing Ti foams. Potassium chloride was used as a space holder and added into the mixture in different particle sizes and shapes. However, one significant barrier towards producing Ti foams was the long debinding and dissolution time required to remove the space holder and the soluble part of the binder (PEG), which can take up to 72 h. Thus, different water debinding and space holder dissolution techniques was explored in order to quicken the process and shorten the amount of time required for the debinding stage.

Ultrasonic water dissolution at the peak melting temperature of PEG was found to be the fastest technique of water debinding and dissolution where the space holder and PEG were completely removed from a specimen of 10 mm in diameter and 6 mm in height within four hours. Hot plate stirring was second fastest method with a total removal time of 8 hours. It was also found that the dissolution temperature can play an important role in increasing the removal rate of PEG and space holder. The activation energy for the dissolution process was found to be 21.4 kJ/mol, consistent with the dissolution of PEG. Then, a selection diagram for the different debinding processes was created, showing the trade-off between dissolution temperature and time and the optimum conditions for an equal weighting of low time and temperature was estimated to be ultrasonic conditions at 50°C. Hence, these conditions were used for debinding samples in all further experiments.

After addressing the debinding problem and validating that the materials processed were suitable for the production of titanium foams, the relationship between the space holder percentage and the amount of final porosity and strength was investigated by varying the amount of space holder in the feedstock from 17-60 vol%. It was found that the relationship between the space holder amount added to the mixture and the final amount of porosity in the foams is not linear and follows a more complex one-phase exponential decay function in increasing form, where the percentage of porosity in the samples increased very rapidly at first, and then the increase slowed down to become asymptotic to an upper limit. Such behaviour was ascribed to increased volume shrinkage in the samples with increasing amount of space holder. This claim was supported by the amount of shrinkage in the sintered samples with the amount of space holder added, where it was found that the amount of volume shrinkage in the samples increases exponentially with increasing the amount of space holder added. The relationship between the relative density and the yield strength of the foams produced was observed to give an adequate fit to both linear and power law regressions, and therefore it was difficult to draw a firm conclusion concerning the trend of relative yield strength with relative density outside the density range tested.

The effect of the shape and size of the space holder on the final amount of porosity and strength of the foams produced was also investigated by preparing four different feedstocks using fine and coarse spherical and cubic KCl powders. The results were found to suggest that the shape of the space holder does not have a remarkable impact on the percentage of final porosity in foams produced, unlike what has been reported in the

literature for other systems. However, Ti foams made by spherical space holder had a higher yield stress than those made with the cubic space holder. Such difference was ascribed to the shape of pores present in the samples, where cracks can initiate more easily in the samples with irregular and angular pores compared to regular spherical pores, as such angular pore shapes act as stress concentration sites with pre-formed crack tips.

Making foams with a hierarchically organised structure and gradient porosity was also attempted by sequential injection moulding of feedstocks with different compositions (with and without space holder) at different intervals. The results showed that it is possible to produce double and triple layered porous titanium with macro and micro porous layers, nonetheless layer separation occurred during the debinding stage, arising from the differences in dimensional shrinkage and resulting in failure of samples at an early stage.

Several trials were also carried out in order to investigate the suitability of the MIM-SH in processing of complex biomedical parts such as surgical staples and a modified femoral stem with a deposited porous layer. In the case of the staples, they retained their shape to some degree after sintering, while partial bonding of the porous layer onto the modified femoral step was achieved. The findings suggest that shrinkage could be an issue, which can be overcome by modifying the design of the part to account for it.

Since they were produced with the potential for biomedical applications, Ti foams should not be only porous to remedy the stress shielding problem, but also bioactive in order to promote better bone ingrowth, mechanical fixation and induce chemical integration. Thus, two approaches were investigated in order to address the bioinertness of Ti.

The first technique used involved adding a bioactive material (hydroxyapatite) into the powder mixture in very small volume percentages. The result suggested that the addition of HA to Ti can induce brittleness in the structure and reduces the load bearing ability of the titanium foams significantly by resulting in weak ceramic phases. The extent of this brittleness depends on the amount of HA added to the structure and thus, special care must be taken by balancing between the amount of HA added and the strength obtained in order to achieve a good strength in the structure as well as potentially better biocompatibility. It was also found that adding 2% of coarse HA powder into the powder mixture can yield Ti foams with a yield strength higher than that without HA. Nevertheless, the foams made with HA had reduced ductility and so less ability to absorb energy than those made without HA; the structure collapses after yielding without any

plateau region similar to a ceramic material. The effect of adding 2% HA on the biological activity of the Ti foams was also investigated in vitro and the results showed that the addition of HA did not significantly improve bone cell attachment and ingrowth into the porous foams.

The second technique investigated to potentially remedy the bioinertness of Ti was to treat the samples in an aqueous solution of disodium hydrogen phosphate using cyclic voltammetry at two different scan rates. Three group of samples with different percentages of porosity and pore sizes were treated, namely relatively dense (7% porosity), microporous (20% porosity) and macroporous (62% porosity). The shapes of the cyclic voltammograms for the relatively dense samples were less erratic and sensitive to the change in the scan rate with more distinctive peaks particularly for the scan rate of 4.22 V s^{-1}, unlike that for porous samples were they had a hump-shaped start and less distinctive peaks, indicating occurrence of complex multi-electron transfer processes. The results also showed that relatively dense samples or samples scanned at 4.22 V s^{-1} with very low porosity (7%) and closed pores exhibited less charging current. This was due to them having less surface area promoted by the lack of open pores and the limited availability of active adsorption sites, which resulted in reduced capacitance and electroactivity compared to more highly porous materials. This situation has led to the development of relatively thin surface oxide layers with a thickness which increased slightly with decreasing scan rate. In comparison, samples with higher porosity and open pores required much higher charging current, due to increased capacitance, and developed much thicker surface layers that can reach more than three times the thickness developed in relatively dense samples. The layers penetrate through the pore surfaces in the samples, forming a network of surface and subsurface coatings. The uniformity of the layer chemical composition with depth in the porous samples was found to be greatly dependent on the porosity and pore size, which dictate how well the structure is accessible to the electrolyte and the number of active sites for the specific adsorption of different electrolyte anions. The samples with the highest porosity (61.5%) and coarsest pores (average pore size 348 μm) had consistent chemical composition with depth, unlike samples with smaller pores (57 μm) and lower porosity (20%), where concentration difference in phosphate with depth was observed. In addition, it was also noted that the oxide thickness developed in porous samples is reduced with depth due to preferential concentration of the electrical field on the external surface of the sample. The oxides

formed were mainly composed of anatase, rutile and Ti phosphate. The results demonstrate significant potential of surface engineered porous samples for biomedical applications in not only addressing the stress shielding problem, but also improving the chemical integration as they have accessible large internal surface area covered with rough and porous oxide layers, which would theoretically be beneficial for improved cell attachment.

10 Future Work

Increasing the solid content of the feedstock via further optimization of the processing parameters can be conducted in order to produce foams with a higher volume percentage of porosity (i.e. lower relative density) by adding a higher percentage of space holder and/or lower shrinkage after sintering by increasing the percentage of the Ti powder. This would be useful in increasing the potential use of such foams as a substitute material for bones with high porosity percentage (≥70% vol) such as trabecular bone, and reducing the problems associated with the shape change on sintering.

In addition, although double and triple layered porous titanium foams were successfully produced through MIM-SH process, this type of process could be developed further. Some layer separation occurred at the interface during debinding in this work and this led to sample failure at low levels of shear stress during shear testing at the interface. This problem could be overcome through the use of a low pressure injection moulding system with a multi barrel system or two component injection moulding, where two injection units (vertical and horizontal) can inject feedstocks with different compositions simultaneously.

While the impact of adding HA to the Ti was evaluated and found to have a detrimental effect on the amount of energy absorbed by the foams, yet using a finer Ti powder and sintering at a lower temperature can be investigated to prevent or lessen the extent of decomposition of the HA and the formation of the weak ceramic phases. In addition, further characterization of the coatings developed through PEO such as surface roughness and hardness can be carried out. Furthermore, assessing the bioactivity of the PEO coating developed is recommended for future work.

References

1. Lütjering, G. and J.C. Williams, *Titanium*. Vol. 2. 2003: Springer.
2. Donachie, M.J., *Titanium: a technical guide*. 2000: ASM international.
3. Xu, Q., B. Gabbitas, S. Matthews, and D. Zhang, *The development of porous titanium products using slip casting.* Journal of Materials Processing Technology, 2013. **213**(8): p. 1440-1446.
4. Li, Y., Z.M. Guo, J.J. Hao, and S.B. Ren, *Gelcasting of porous titanium implants.* Powder Metallurgy, 2008. **51**(3): p. 231-236.
5. Manonukul, A., M. Tange, P. Srikudvien, N. Denmud, and P. Wattanapornphan, *Rheological properties of commercially pure titanium slurry for metallic foam production using replica impregnation method.* Powder Technology, 2014. **266**: p. 129-134.
6. Bram, M., C. Kempmann, A. Laptev, D. Stöver, and K. Weinert, *Investigations on the machining of sintered titanium foams utilizing face milling and peripheral grinding.* Advanced Engineering Materials, 2003. **5**(6): p. 441-447.
7. Merhar, J., *Overview of metal injection moulding.* Metal Powder Report, 1990. **45**(5): p. 339-342.
8. Barbosa, A.P.C., M. Bram, D. Stover, and H.P. Buchkremer, *Realization of a Titanium Spinal Implant with a Gradient in Porosity by 2-Component-Metal Injection Moulding.* Advanced Engineering Materials, 2013. **15**(6): p. 510-521.
9. Tuncer, N., M. Bram, A. Laptev, T. Beck, A. Moser, and H.P. Buchkremer, *Study of metal injection molding of highly porous titanium by physical modeling and direct experiments.* Journal of Materials Processing Technology, 2014. **214**(7): p. 1352-1360.
10. Daudt, N., M. Bram, A.C. Barbosa, and C. Alves, *Surface modification of highly porous titanium by plasma treatment.* Materials letters, 2015. **141**: p. 194-197.
11. Carreño-Morelli, E., M. Rodríguez-Arbaizar, A. Amherd, and J.E. Bidaux, *Porous titanium processed by powder injection moulding of titanium hydride and space holders.* Powder Metallurgy, 2014. **57**(2): p. 93-96.
12. Banhart, J., *Foam metal: the recipe.* Europhysics news, 1999. **30**(1): p. 17-20.
13. Banhart, J., *Manufacture, characterisation and application of cellular metals and metal foams.* Progress in Materials Science, 2001. **46**(6): p. 559-632.
14. Aly, M.S., *Effect of pore size on the tensile behavior of open-cell Ti foams: Experimental results.* Materials letters, 2010. **64**(8): p. 935-937.
15. Baril, E., L.-P. Lefebvre, Y. Thomas, and F. Ilinca, *Foam-coated MIM gives new edge to titanium implants.* Metal Powder Report, 2008. **63**(8): p. 46-55.
16. Bi, Z., M.P. Paranthaman, P.A. Menchhofer, R.R. Dehoff, C.A. Bridges, M. Chi, B. Guo, X.-G. Sun, and S. Dai, *Self-organized amorphous TiO 2 nanotube arrays on porous Ti foam for rechargeable lithium and sodium ion batteries.* Journal of Power Sources, 2013. **222**: p. 461-466.
17. Jakubowicz, J., G. Adamek, and M. Dewidar, *Titanium foam made with saccharose as a space holder.* Journal of Porous Materials, 2013. **20**(5): p. 1137-1141.
18. Jha, N., D. Mondal, J.D. Majumdar, A. Badkul, A. Jha, and A. Khare, *Highly porous open cell Ti-foam using NaCl as temporary space holder through powder metallurgy route.* Materials & Design, 2013. **47**: p. 810-819.
19. Kashef, S., J. Lin, P.D. Hodgson, and W. Yan, *Mechanical Properties of Titanium Foam for Biomedical Applications.* International Journal of Modern Physics B, 2008. **22**(31n32): p. 6155-6160.

20. Queheillalt, D.T., D.D. Hass, D.J. Sypeck, and H.N. Wadley, *Synthesis of open-cell metal foams by templated directed vapor deposition.* Journal of Materials Research, 2001. **16**(04): p. 1028-1036.
21. Sharma, M., G. Gupta, O. Modi, and B. Prasad, *PM processed titanium foam: influence of morphology and content of space holder on microstructure and mechanical properties.* Powder Metallurgy, 2013. **56**(1): p. 55-60.
22. Sharma, M., G. Gupta, O. Modi, B. Prasad, and A.K. Gupta, *Titanium foam through powder metallurgy route using acicular urea particles as space holder.* Materials letters, 2011. **65**(21): p. 3199-3201.
23. Smorygo, O., A. Marukovich, V. Mikutski, A. Gokhale, G.J. Reddy, and J.V. Kumar, *High-porosity titanium foams by powder coated space holder compaction method.* Materials Letters, 2012. **83**: p. 17-19.
24. Esen, Z. and S. Bor, *Processing of titanium foams using magnesium spacer particles.* Scripta Materialia, 2007. **56**(5): p. 341-344.
25. Ye, B. and D.C. Dunand, *Titanium foams produced by solid-state replication of NaCl powders.* Materials Science and Engineering a-Structural Materials Properties Microstructure and Processing, 2010. **528**(2): p. 691-697.
26. Chen, L.J., T. Li, Y.M. Li, H. He, and Y.H. Hu, *Porous titanium implants fabricated by metal injection molding.* Transactions of Nonferrous Metals Society of China, 2009. **19**(5): p. 1174-1179.
27. Niu, W.J., C.G. Bai, G.B. Qiu, and Q. Wang, *Processing and properties of porous titanium using space holder technique.* Materials Science and Engineering a-Structural Materials Properties Microstructure and Processing, 2009. **506**(1-2): p. 148-151.
28. Oh, I.-H., N. Nomura, N. Masahashi, and S. Hanada, *Mechanical properties of porous titanium compacts prepared by powder sintering.* Scripta Materialia, 2003. **49**(12): p. 1197-1202.
29. Queheillalt, D.T., H.N. Wadley, B.W. Choi, and D.S. Schwartz, *Creep expansion of porous Ti-6Al-4V sandwich structures.* Metallurgical and Materials transactions A, 2000. **31**(1): p. 261-273.
30. Wen, C., M. Mabuchi, Y. Yamada, K. Shimojima, Y. Chino, and T. Asahina, *Processing of biocompatible porous Ti and Mg.* Scripta Materialia, 2001. **45**(10): p. 1147-1153.
31. Yook, S.-W., H.-E. Kim, and Y.-H. Koh, *Fabrication of porous titanium scaffolds with high compressive strength using camphene-based freeze casting.* Materials Letters, 2009. **63**(17): p. 1502-1504.
32. Goodall, R.M., A., *Porous Metals*, in *Physical Metallurgy*, L.K. David, H., Editor. 2014. p. 2399-2595.
33. Salvo, L., G. Martin, M. Suard, A. Marmottant, R. Dendievel, and J.J. Blandin, *Processing and structures of solids foams.* Comptes Rendus Physique, 2014. **15**(8-9): p. 662-673.
34. Dunand, D.C., *Processing of titanium foams.* Advanced engineering materials, 2004. **6**(6): p. 369-376.
35. Standard, A., *F2792. 2012. Standard Terminology for Additive Manufacturing Technologies.* West Conshohocken, PA: ASTM International. See www. astm. org.(doi: 10.1520/F2792-12), 2012.
36. Prakasam, M., J. Locs, K. Salma-Ancane, D. Loca, A. Largeteau, and L. Berzina-Cimdina, *Fabrication, properties and applications of dense hydroxyapatite: A review.* Journal of functional biomaterials, 2015. **6**(4): p. 1099-1140.
37. German, R.M., *Sintering Trajectories: Description on How Density, Surface Area, and Grain Size Change.* JOM, 2016. **68**(3): p. 878-884.
38. Kuczynski, G., *The mechanism of densification during sintering of metallic particles.* Acta Metallurgica, 1956. **4**(1): p. 58-61.
39. German, R.M. *Sintering Simplified: Surface Area, Density, and Grain Size Relations*. in *Materials Science Forum*. 2016. Trans Tech Publications Ltd.

40. Tanaka, H., A. Yamamoto, J.-i. Shimoyama, H. Ogino, and K. Kishio, *Strongly connected ex situ MgB2 polycrystalline bulks fabricated by solid-state self-sintering.* Superconductor Science and Technology, 2012. **25**(11): p. 115022.
41. Thieme, M., K.P. Wieters, F. Bergner, D. Scharnweber, H. Worch, J. Ndop, T.J. Kim, and W. Grill, *Titanium powder sintering for preparation of a porous functionally graded material destined for orthopaedic implants.* Journal of Materials Science-Materials in Medicine, 2001. **12**(3): p. 225-231.
42. Sypeck, D.J., P.A. Parrish, and H.N. Wadley. *Novel hollow powder porous structures*. in *MRS Proceedings*. 1998. Cambridge Univ Press.
43. Hurysz, K., J. Clark, A. Nagel, C. Hardwicke, K. Lee, J. Cochran, and T. Sanders. *Steel and titanium hollow sphere foams*. in *MATERIALS RESEARCH SOCIETY SYMPOSIUM PROCEEDINGS*. 1998. DTIC Document.
44. Yu, P., G. Stephani, S. Luo, H. Goehler, and M. Qian, *Microwave-assisted fabrication of titanium hollow spheres with tailored shell structures for various potential applications.* Materials Letters, 2012. **86**: p. 84-87.
45. Öchsner, A. and T. Fiedler, *Geometrical Properties of Hollow Sphere Structures*, in *Multifunctional Metallic Hollow Sphere Structures*. 2009, Springer. p. 31-46.
46. Kearns, M.W., *Formation of porous bodies*. 1987: U.S. .
47. Davis, N., J. Teisen, C. Schuh, and D. Dunand, *Solid-state foaming of titanium by superplastic expansion of argon-filled pores.* Journal of Materials Research, 2001. **16**(05): p. 1508-1519.
48. Kearns, M.W., P. Blenkinsop, A. Barber, and T. Farthing, *Manufacture of a novel porous metal.* International journal of powder metallurgy (1986), 1988. **24**(1): p. 59-64.
49. Queheillalt, D.T., K.A. Gable, and H.N. Wadley, *Temperature dependent creep expansion of Ti-6Al-4V low density core sandwich structures.* Scripta materialia, 2001. **44**(3): p. 409-414.
50. Oppenheimer, S. and D.C. Dunand, *Solid-state foaming of Ti–6Al–4V by creep or superplastic expansion of argon-filled pores.* Acta Materialia, 2010. **58**(13): p. 4387-4397.
51. Machado, A. and J. Wallbank, *Machining of titanium and its alloys—a review.* Proceedings of the Institution of Mechanical Engineers, Part B: Journal of Engineering Manufacture, 1990. **204**(1): p. 53-60.
52. Murray, N. and D. Dunand, *Microstructure evolution during solid-state foaming of titanium.* Composites Science and Technology, 2003. **63**(16): p. 2311-2316.
53. Murray, N. and D. Dunand, *Effect of thermal history on the superplastic expansion of argon-filled pores in titanium: Part I kinetics and microstructure.* Acta materialia, 2004. **52**(8): p. 2269-2278.
54. Neirinck, B., T. Mattheys, A. Braem, J. Fransaer, O. Van der Biest, and J. Vleugels, *Preparation of Titanium Foams by Slip Casting of Particle Stabilized Emulsions.* Advanced Engineering Materials, 2009. **11**(8): p. 633-636.
55. Bauer, W., H.J. Ritzhaupt-Kleissl, and J.H. Hausselt, *Slip casting of ceramic microcomponents.* Microsystem Technologies, 1998. **4**(3): p. 125-127.
56. Rak, Z.S. and J. Walter, *Porous titanium foil by tape casting technique.* Journal of Materials Processing Technology, 2006. **175**(1-3): p. 358-363.
57. Singh, R., P.D. Lee, J.R. Jones, G. Poologasundarampillai, T. Post, T.C. Lindley, and R.J. Dashwood, *Hierarchically structured titanium foams for tissue scaffold applications.* Acta Biomaterialia, 2010. **6**(12): p. 4596-4604.
58. Erk, K.A., D.C. Dunand, and K.R. Shull, *Titanium with controllable pore fractions by thermoreversible gelcasting of TiH 2.* Acta materialia, 2008. **56**(18): p. 5147-5157.
59. Ho, M.H., P.Y. Kuo, H.J. Hsieh, T.Y. Hsien, L.T. Hou, J.Y. Lai, and D.M. Wang, *Preparation of porous scaffolds by using freeze-extraction and freeze-gelation methods.* Biomaterials, 2004. **25**(1): p. 129-138.

60. Deville, S., *Freeze-Casting of Porous Biomaterials: Structure, Properties and Opportunities.* Materials, 2010. **3**(3): p. 1913-1927.
61. Chino, Y. and D.C. Dunand, *Directionally freeze-cast titanium foam with aligned, elongated pores.* Acta Materialia, 2008. **56**(1): p. 105-113.
62. Yook, S.W., B.H. Yoon, H.E. Kim, Y.H. Koh, and Y.S. Kim, *Porous titanium (Ti) scaffolds by freezing TiH2/camphene slurries.* Materials Letters, 2008. **62**(30): p. 4506-4508.
63. Deville, S., *Freeze-casting of porous ceramics: a review of current achievements and issues.* Advanced Engineering Materials, 2008. **10**(3): p. 155-169.
64. Deville, S., E. Saiz, and A.P. Tomsia, *Ice-templated porous alumina structures.* Acta Materialia, 2007. **55**(6): p. 1965-1974.
65. Wegst, U.G., M. Schecter, A.E. Donius, and P.M. Hunger, *Biomaterials by freeze casting.* Philosophical Transactions of the Royal Society of London A: Mathematical, Physical and Engineering Sciences, 2010. **368**(1917): p. 2099-2121.
66. Jung, H.-D., S.-W. Yook, H.-E. Kim, and Y.-H. Koh, *Fabrication of titanium scaffolds with porosity and pore size gradients by sequential freeze casting.* Materials letters, 2009. **63**(17): p. 1545-1547.
67. Yook, S.W., H.D. Jung, C.H. Park, K.H. Shin, Y.H. Koh, Y. Estrin, and H.E. Kim, *Reverse freeze casting: A new method for fabricating highly porous titanium scaffolds, with aligned large pores.* Acta Biomaterialia, 2012. **8**(6): p. 2401-2410.
68. Ahmad, S., N. Muhamad, A. Muchtar, J. Sahari, M. Ibrahim, K. Jamaludin, and N.M. Nor, *Development and characterization of titanium alloy foams.* International Journal of Mechanical and Materials Engineering (IJMME), 2010. **5**(2): p. 244-250.
69. Wang, C., H. Chen, X. Zhu, Z. Xiao, K. Zhang, and X. Zhang, *An improved polymeric sponge replication method for biomedical porous titanium scaffolds.* Materials Science and Engineering: C, 2016.
70. Manonukul, A., P. Srikudvien, M. Tange, and C. Puncreobutr, *Geometry anisotropy and mechanical property isotropy in titanium foam fabricated by replica impregnation method.* Materials Science and Engineering: A, 2016. **655**: p. 388-395.
71. Mondal, D.P., J. Datta Majumder, N. Jha, A. Badkul, S. Das, A. Patel, and G. Gupta, *Titanium-cenosphere syntactic foam made through powder metallurgy route.* Materials & Design, 2012. **34**: p. 82-89.
72. de Vasconcellos, L.M.R., F.N. Oliveira, D. de Oliveira Leite, L.G.O. de Vasconcellos, R.F. do Prado, C.J. Ramos, M.L. de Alencastro Graça, C.A.A. Cairo, and Y.R. Carvalho, *Novel production method of porous surface Ti samples for biomedical application.* Journal of Materials Science: Materials in Medicine, 2012. **23**(2): p. 357-364.
73. Bekoz, N. and E. Oktay, *Effects of carbamide shape and content on processing and properties of steel foams.* Journal of Materials Processing Technology, 2012. **212**(10): p. 2109-2116.
74. Xiang, C., Y. Zhang, Z. Li, H. Zhang, Y. Huang, and H. Tang, *Preparation and compressive behavior of porous titanium prepared by space holder sintering process.* Procedia Engineering, 2012. **27**: p. 768-774.
75. Imwinkelried, T., *Mechanical properties of open-pore titanium foam.* Journal of Biomedical Materials Research Part A, 2007. **81A**(4): p. 964-970.
76. Torres, Y., J.J. Pavon, and J.A. Rodriguez, *Processing and characterization of porous titanium for implants by using NaCl as space holder.* Journal of Materials Processing Technology, 2012. **212**(5): p. 1061-1069.
77. Mansourighasri, A., N. Muhamad, and A.B. Sulong, *Processing titanium foams using tapioca starch as a space holder.* Journal of Materials Processing Technology, 2012. **212**(1): p. 83-89.
78. Köhl, M., T. Habijan, M. Bram, H.P. Buchkremer, D. Stöver, and M. Köller, *Powder Metallurgical Near-Net-Shape Fabrication of Porous NiTi Shape Memory Alloys for Use*

as Long-Term Implants by the Combination of the Metal Injection Molding Process with the Space-Holder Technique. Advanced Engineering Materials, 2009: p. NA-NA.
79. Rivard, J., V. Brailovski, S. Dubinskiy, and S. Prokoshkin, *Fabrication, morphology and mechanical properties of Ti and metastable Ti-based alloy foams for biomedical applications.* Mater Sci Eng C Mater Biol Appl, 2014. **45**: p. 421-33.
80. Dabrowski, B., W. Swieszkowski, D. Godlinski, and K.J. Kurzydlowski, *Highly porous titanium scaffolds for orthopaedic applications.* Journal of Biomedical Materials Research Part B-Applied Biomaterials, 2010. **95B**(1): p. 53-61.
81. Hong, T.F., Z.X. Guo, and R. Yang, *Fabrication of porous titanium scaffold materials by a fugitive filler method.* Journal of Materials Science-Materials in Medicine, 2008. **19**(12): p. 3489-3495.
82. Mondal, D., M. Patel, H. Jain, A. Jha, S. Das, and R. Dasgupta, *The effect of the particle shape and strain rate on microstructure and compressive deformation response of pure Ti-foam made using acrowax as space holder.* Materials Science and Engineering: A, 2015. **625**: p. 331-342.
83. Wen, C.E., Y. Yamada, K. Shimojima, Y. Chino, H. Hosokawa, and M. Mabuchi, *Novel titanium foam for bone tissue engineering.* Journal of Materials Research, 2002. **17**(10): p. 2633-2639.
84. Aydoğmuş, T. and Ş. Bor, *Processing of porous TiNi alloys using magnesium as space holder.* Journal of Alloys and Compounds, 2009. **478**(1-2): p. 705-710.
85. Kwok, P.J., S.M. Oppenheimer, and D.C. Dunand, *Porous Titanium by Electro-chemical Dissolution of Steel Space-holders.* Advanced Engineering Materials, 2008. **10**(9): p. 820-825.
86. Pinho, S.P. and E.A. Macedo, *Solubility of NaCl, NaBr, and KCl in water, methanol, ethanol, and their mixed solvents.* Journal of Chemical & Engineering Data, 2005. **50**(1): p. 29-32.
87. Engin, G., B. Aydemir, and H.Ö. Gülsoy, *Injection molding of micro-porous titanium alloy with space holder technique.* Rare Metals, 2011. **30**(6): p. 565-571.
88. Ghasemi, A., S.R. Hosseini, and S.K. Sadrnezhaad, *Pore control in SMA NiTi scaffolds via space holder usage.* Materials Science and Engineering: C, 2012. **32**(5): p. 1266-1270.
89. Li, D.S., Y.P. Zhang, X. Ma, and X.P. Zhang, *Space-holder engineered porous NiTi shape memory alloys with improved pore characteristics and mechanical properties.* Journal of Alloys and Compounds, 2009. **474**(1-2): p. L1-L5.
90. Wang, X.J., Y.C. Li, J.Y. Xiong, P.D. Hodgson, and C.E. Wen, *Porous TiNbZr alloy scaffolds for biomedical applications.* Acta Biomaterialia, 2009. **5**(9): p. 3616-3624.
91. Smorygo, O., A. Marukovich, V. Mikutski, A.A. Gokhale, G.J. Reddy, and J.V. Kumar, *High-porosity titanium foams by powder coated space holder compaction method.* Materials Letters, 2012. **83**: p. 17-19.
92. Bram, M., C. Stiller, H.P. Buchkremer, D. Stover, and H. Baur, *High-porosity titanium, stainless steel, and superalloy parts.* Advanced Engineering Materials, 2000. **2**(4): p. 196-199.
93. Hong, T.F., Z.X. Guo, and R. Yang, *Fabrication of porous titanium scaffold materials by a fugitive filler method.* Journal of Materials Science: Materials in Medicine, 2008. **19**(12): p. 3489-3495.
94. Esen, Z. and S. Bor, *Characterization of Ti-6Al-4V alloy foams synthesized by space holder technique.* Materials Science and Engineering a-Structural Materials Properties Microstructure and Processing, 2011. **528**(7-8): p. 3200-3209.
95. Barbosa, A.P.C., M. Bram, D. Stöver, and H.P. Buchkremer, *Realization of a Titanium Spinal Implant with a Gradient in Porosity by 2-Component-Metal Injection Moulding.* Advanced Engineering Materials, 2013. **15**(6): p. 510-521.
96. Aydogmus, T. and S. Bor, *Processing of porous TiNi alloys using magnesium as space holder.* Journal of Alloys and Compounds, 2009. **478**(1-2): p. 705-710.

97. Ibrahim, A., F.M. Zhang, E. Otterstein, and E. Burkel, *Processing of porous Ti and Ti5Mn foams by spark plasma sintering.* Materials & Design, 2011. **32**(1): p. 146-153.
98. Zhang, F., E. Otterstein, and E. Burkel, *Spark plasma sintering, microstructures, and mechanical properties of macroporous titanium foams.* Advanced Engineering Materials, 2010. **12**(9): p. 863-872.
99. Kim, S.W., H.-D. Jung, M.-H. Kang, H.-E. Kim, Y.-H. Koh, and Y. Estrin, *Fabrication of porous titanium scaffold with controlled porous structure and net-shape using magnesium as spacer.* Materials Science and Engineering: C, 2013. **33**(5): p. 2808-2815.
100. Khramtsov, V., *The packing density of the particles in powder mixtures of different dispersities.* Russian Journal of Non-Ferrous Metals, 2009. **50**(3): p. 294-297.
101. Kotan, G. and A.Ş. Bor, *Production and characterization of high porosity Ti-6Al-4V foam by space holder technique in powder metallurgy.* Turkish Journal of Engineering and Environmental Sciences, 2007. **31**(3): p. 149-156.
102. Hartwig, T., G. Veltl, F. Petzoldt, H. Kunze, R. Scholl, and B. Kieback, *Powders for metal injection molding.* Journal of the European Ceramic Society, 1998. **18**(9): p. 1211-1216.
103. Guden, M., E. Celik, A. Hizal, M. Altindis, and S. Cetiner, *Effects of compaction pressure and particle shape on the porosity and compression mechanical properties of sintered Ti6Al4V powder compacts for hard tissue implantation.* J Biomed Mater Res B Appl Biomater, 2008. **85**(2): p. 547-55.
104. Gulsoy, H.O., N. Gulsoy, and R. Calisici, *Particle morphology influence on mechanical and biocompatibility properties of injection molded Ti alloy powder.* Biomed Mater Eng, 2014. **24**(5): p. 1861-73.
105. Mutsuddy, B.C. and R.e.G. Ford, *Ceramic injection moulding*. 1995, London: Chapman & Hall.
106. Bram, M., C. Stiller, H.P. Buchkremer, D. Stöver, and H. Baur, *High-Porosity Titanium, Stainless Steel, and Superalloy Parts.* Advanced Engineering Materials, 2000. **2**(4): p. 196-199.
107. Eagleson, M., H.-D. Jakubke, and H. Jeschkeit, *Concise encyclopedia chemistry*. 1994, Berlin: W. de Gruyter.
108. Ismail, M.H., R. Goodall, H.A. Davies, and I. Todd, *Porous NiTi alloy by metal injection moulding/sintering of elemental powders: Effect of sintering temperature.* Materials Letters, 2012. **70**: p. 142-145.
109. Sidambe, A.T., F. Derguti, and I. Todd, *Metal Injection Moulding of Low Interstitial Titanium.* Powder Metallurgy of Titanium: Powder Processing, Consolidation and Metallurgy of Titanium, 2012. **520**: p. 145-152.
110. Sidambe, A.T., I.A. Figueroa, H.G.C. Hamilton, and I. Todd, *Metal injection moulding of CP-Ti components for biomedical applications.* Journal of Materials Processing Technology, 2012. **212**(7): p. 1591-1597.
111. Guoxin, H., Z. Lixiang, F. Yunliang, and L. Yanhong, *Fabrication of high porous NiTi shape memory alloy by metal injection molding.* Journal of materials processing technology, 2008. **206**(1): p. 395-399.
112. Deing, A., B. Luthringer, D. Laipple, T. Ebel, and R. Willumeit, *A Porous TiAl6V4 Implant Material for Medical Application.* Int J Biomater, 2014. **2014**: p. 904230.
113. Chan, T.Y. and S.T. Lin, *Effects of stearic acid on the injection molding of alumina.* Journal of the American Ceramic Society, 1995. **78**(10): p. 2746-2752.
114. German, R.M., *Powder injection molding*. 1990: Metal Powder Industries Federation.
115. Nor, N.H.M., N. Muhamad, K.R. Jamaludin, S. Ahmad, and M.H.I. Ibrahim, *Characterisation of Titanium Alloy feedstock for Metal Injection Moulding Using Palm Stearin Binder System.* Advances in Materials and Processing Technologies Ii, Pts 1 and 2, 2011. **264-265**: p. 586-591.

116. Ahn, S., S.J. Park, S. Lee, S.V. Atre, and R.M. German, *Effect of powders and binders on material properties and molding parameters in iron and stainless steel powder injection molding process.* Powder Technology, 2009. **193**(2): p. 162-169.
117. Jamaludin, K.R., N. Muhamad, H. Abolhasani, Murtadhahadi, and M.N. Ab Rahman, *An Influence of a Binder System to the Rheological Behavior of the Ss316l Metal Injection Molding (Mim) Feedstock.* Advances in Materials and Processing Technologies Ii, Pts 1 and 2, 2011. **264-265**: p. 554-558.
118. German, R.M. and A. Bose, *Injection molding of metals and ceramics*. 1997: Metal Powder Industries Federation.
119. Thian, E.S., N.H. Loh, K.A. Khor, and S.B. Tor, *Effects of debinding parameters on powder injection molded Ti-6Al-4V/HA composite parts.* Advanced Powder Technology, 2001. **12**(3): p. 361-370.
120. Shibo, G., Q. Xuanhui, H. Xinbo, Z. Ting, and D. Bohua, *Powder injection molding of Ti–6Al–4V alloy.* Journal of Materials Processing Technology, 2006. **173**(3): p. 310-314.
121. Thian, E.S., N.H. Loh, K.A. Khor, and S.B. Tor, *Microstructures and mechanical properties of powder injection molded Ti-6Al-4V/HA powder.* Biomaterials, 2002. **23**(14): p. 2927-2938.
122. Nor, N.H.M., N. Muhamad, A.K.A.M. Ihsan, and K.R. Jamaludin, *Sintering Parameter Optimization of Ti-6Al-4V Metal Injection Molding for Highest Strength Using Palm Stearin Binder.* International Tribology Conference Malaysia 2013, 2013. **68**: p. 359-364.
123. Wei, S., Y. Bangchao, Z. Xuanhong, M. Jianhua, P. Qifeng, and W. Xingwei, *Effect of Sintering Time on the Microstructure of Porous Tantalum.* Rare Metal Materials and Engineering, 2015. **44**(2): p. 319-322.
124. Gerling, R., E. Aust, W. Limberg, M. Pfuff, and F.P. Schimansky, *Metal injection moulding of gamma titanium aluminide alloy powder.* Materials Science and Engineering: A, 2006. **423**(1-2): p. 262-268.
125. Ishizaki, K., S. Komarneni, and M. Nanko, *Sintering mechanisms and advanced sintering methods for porous materials*, in *Porous Materials*. 1998, Springer. p. 38-66.
126. Rice, R., *Evaluation and extension of physical property-porosity models based on minimum solid area.* Journal of materials science, 1996. **31**(1): p. 102-118.
127. Ramakrishnan, N. and V. Arunachalam, *Effective elastic moduli of porous ceramic materials.* Journal of the American Ceramic Society, 1993. **76**(11): p. 2745-2752.
128. Te Wu, T., *The effect of inclusion shape on the elastic moduli of a two-phase material.* International Journal of Solids and Structures, 1966. **2**(1): p. 1-8.
129. Ramakrishnan, N. and V. Arunachalam, *Effective elastic moduli of porous solids.* Journal of materials science, 1990. **25**(9): p. 3930-3937.
130. Rice, R.W. *The porosity dependence of physical properties of materials: a summary review*. in *Key Engineering Materials*. 1996. Trans Tech Publ.
131. Rice, R., *Use of normalized porosity in models for the porosity dependence of mechanical properties.* Journal of materials science, 2005. **40**(4): p. 983-989.
132. Gibson, L.J. and M.F. Ashby, *Cellular solids: structure and properties*. 1999: Cambridge university press.
133. Wang, X.-h., J.-s. Li, H. Rui, H.-c. Kou, and Z. Lian, *Mechanical properties of porous titanium with different distributions of pore size.* Transactions of Nonferrous Metals Society of China, 2013. **23**(8): p. 2317-2322.
134. Gibson, L., *Mechanical behavior of metallic foams.* Annual review of materials science, 2000. **30**(1): p. 191-227.
135. Bram, M., A. Laptev, H. Buchkremer, and D. Stöver. *Application of powder metallurgy for the production of highly porous functional parts with open porosity*. in *Mater. Forum*. 2005.

136. Cachinho, S.C. and R.N. Correia, *Titanium porous scaffolds from precursor powders: rheological optimization of TiH 2 slurries.* Powder Technology, 2007. **178**(2): p. 109-113.
137. Jenei, P., H. Choi, A. Tóth, H. Choe, and J. Gubicza, *Mechanical behavior and microstructure of compressed Ti foams synthesized via freeze casting.* Journal of the Mechanical Behavior of Biomedical Materials, 2016. **63**: p. 407-416.
138. Khodaei, M., M. Meratian, and O. Savabi, *Effect of spacer type and cold compaction pressure on structural and mechanical properties of porous titanium scaffold.* Powder Metallurgy, 2015. **58**(2): p. 152-160.
139. Laptev, A.M., N.F. Daudt, O. Guillon, and M. Bram, *Increased Shape Stability and Porosity of Highly Porous Injection-Molded Titanium Parts.* Advanced engineering materials, 2015. **17**(11): p. 1579-1587.
140. Muñoz, S., J. Pavón, J. Rodríguez-Ortiz, A. Civantos, J. Allain, and Y. Torres, *On the influence of space holder in the development of porous titanium implants: Mechanical, computational and biological evaluation.* Materials Characterization, 2015. **108**: p. 68-78.
141. Rivard, J., V. Brailovski, S. Dubinskiy, and S. Prokoshkin, *Fabrication, morphology and mechanical properties of Ti and metastable Ti-based alloy foams for biomedical applications.* Materials Science and Engineering: C, 2014. **45**: p. 421-433.
142. Singh, R., P. Lee, J. Jones, G. Poologasundarampillai, T. Post, T. Lindley, and R. Dashwood, *Hierarchically structured titanium foams for tissue scaffold applications.* Acta biomaterialia, 2010. **6**(12): p. 4596-4604.
143. Wang, X.-h., J.-s. Li, H. Rui, and H.-c. Kou, *Mechanical properties and pore structure deformation behaviour of biomedical porous titanium.* Transactions of Nonferrous Metals Society of China, 2015. **25**(5): p. 1543-1550.
144. Amsterdam, E., R. Goodall, A. Mortensen, P. Onck, and J.T.M. De Hosson, *Fracture behavior of low-density replicated aluminum alloy foams.* Materials Science and Engineering: A, 2008. **496**(1): p. 376-382.
145. Kashef, S., A. Asgari, T.B. Hilditch, W.Y. Yan, V.K. Goel, and P.D. Hodgson, *Fracture toughness of titanium foams for medical applications.* Materials Science and Engineering a-Structural Materials Properties Microstructure and Processing, 2010. **527**(29-30): p. 7689-7693.
146. Combaz, E. and A. Mortensen, *Fracture toughness of Al replicated foam.* Acta Materialia, 2010. **58**(14): p. 4590-4603.
147. Diologent, F., Y. Conde, R. Goodall, and A. Mortensen, *Microstructure, strength and creep of aluminium-nickel open cell foam.* Philosophical Magazine, 2009. **89**(13): p. 1121-1139.
148. Diologent, F., R. Goodall, and A. Mortensen, *Creep of aluminium-magnesium open cell foam.* Acta Materialia, 2009. **57**(3): p. 830-837.
149. Burteau, A., J.D. Bartout, Y. Bienvenu, and S. Forest, *On the creep deformation of nickel foams under compression.* Comptes Rendus Physique, 2014. **15**(8-9): p. 705-718.
150. Choe, H. and D.C. Dunand, *Synthesis, structure, and mechanical properties of Ni-Al and Ni-Cr-Al superalloy foams.* Acta Materialia, 2004. **52**(5): p. 1283-1295.
151. Boonyongmaneerat, Y. and D.C. Dunand, *Effects of strut geometry and pore fraction on creep properties of cellular materials.* Acta Materialia, 2009. **57**(5): p. 1373-1384.
152. Mueller, R., S. Soubielle, R. Goodall, F. Diologent, and A. Mortensen, *On the steady-state creep of microcellular metals.* Scripta Materialia, 2007. **57**(1): p. 33-36.
153. Kashef, S., A. Asgari, T.B. Hilditch, W. Yan, V.K. Goel, and P.D. Hodgson, *Fatigue crack growth behavior of titanium foams for medical applications.* Materials Science and Engineering: A, 2011. **528**(3): p. 1602-1607.

154. Asik, E.E. and S. Bor, *Fatigue behavior of Ti-6Al-4V foams processed by magnesium space holder technique.* Materials Science and Engineering a-Structural Materials Properties Microstructure and Processing, 2015. **621**: p. 157-165.
155. Wally, Z.J., W. van Grunsven, F. Claeyssens, R. Goodall, and G.C. Reilly, *Porous Titanium for Dental Implant Applications.* Metals, 2015. **5**(4): p. 1902-1920.
156. Murr, L.E., S.M. Gaytan, E. Martinez, F. Medina, and R.B. Wicker, *Next generation orthopaedic implants by additive manufacturing using electron beam melting.* International journal of biomaterials, 2012. **2012**.
157. Pavón, J., P. Trueba, J. Rodríguez-Ortiz, and Y. Torres, *Development of new titanium implants with longitudinal gradient porosity by space-holder technique.* Journal of Materials Science, 2015. **50**(18): p. 6103-6112.
158. Gunther, S., G.T. Dambaev, T. Chekalkin, J. Kang, J. Kim, and V. Gunther, *Porous TiNi-based material and infrared radiation in needle-free treatment of diabetic patients.*
159. Nouri, A., *Titanium foam scaffolds for dental applications.* Metallic Foam Bone: Processing, Modification and Characterization and Properties, 2016: p. 131.
160. United Orthopedic. *U2 Matrix Porous Stem*. 2017 [cited 2017 17/02/2017]; Available from: http://www.uoc.com.tw/en/product.asp?cnum=8&pnum=45.
161. Parker, M.E., P. Cieplak, and B. Gorecka, *Turbo titanium coating technology for broad application* 2015: U.S. .
162. 3C-Crista Chemical Company. *Titanium Foam for Next-generation Car Batteries*. 2016 [cited 2017 18/02/2017]; Available from: http://cristachemical.com/foams.php.
163. Joslin, R.D., *Aircraft Laminar Flow Control 1.* Annual review of fluid mechanics, 1998. **30**(1): p. 1-29.
164. NASA. *F-16XL Supersonic Laminar Flow*. 2004 [cited 2015 10 July]; Available from: http://www.nasa.gov/centers/dryden/about/Organizations/Technology/Facts/TF-2004-12-DFRC.html.
165. Qian, M. and F.H. Froes, *Titanium Powder Metallurgy: Science, Technology and Applications*. 2015: Butterworth-Heinemann.
166. Komeya, K. and H. Inoue, *Sintering of aluminium nitride: particle size dependence of sintering kinetics.* Journal of Materials Science, 1969. **4**(12): p. 1045-1050.
167. Thelen, S., F. Barthelat, and L.C. Brinson, *Mechanics considerations for microporous titanium as an orthopedic implant material.* Journal of Biomedical Materials Research Part A, 2004. **69**(4): p. 601-610.
168. Contreras, J.M., A. Jiménez-Morales, and J.M. Torralba, *Fabrication of bronze components by metal injection moulding using powders with different particle characteristics.* Journal of Materials Processing Technology, 2009. **209**(15–16): p. 5618-5625.
169. Lampman, S., *Characterization and failure analysis of plastics*. 2003: ASM International.
170. Edirisinghe, M.J., *The effect of processing additives on the properties of a ceramic-polymer formulation.* Ceramics International, 1991. **17**(2): p. 89-96.
171. Rajabi, J., N. Muhamad, A.B. Sulong, A. Fayyaz, and M.R. Raza, *The effect of nano-sized stainless steel powder addition on mechanical and physical properties of micropowder injection molded part.* Materials & Design, 2014. **63**: p. 223-232.
172. Hixson, A.W. and J.H. Crowell, *Dependence of reaction velocity upon surface and agitation II - Experimental procedure in study of surface.* Industrial and Engineering Chemistry, 1931. **23**: p. 1002-1009.
173. Bhattarai, S.R., K.A.R. Khalil, M. Dewidar, P.H. Hwang, H.K. Yi, and H.Y. Kim, *Novel production method and in-vitro cell compatibility of porous Ti-6Al-4V alloy disk for hard tissue engineering.* Journal of Biomedical Materials Research Part A, 2008. **86A**(2): p. 289-299.

174. Ibrahim, M., N. Muhamad, A. Sulong, I. Murtadhahadi, K. Jamaludin, S. Ahmad, and N. Nor, *Rheological Characteristic of Water Atomised Stainless Steel Powder for Micro Metal Injection Molding.* 2008.
175. Schramm, G., *A practical approach to rheology and rheometry*. 1994: Haake Karlsruhe.
176. Huang, B.Y., S.Q. Liang, and X.H. Qu, *The rheology of metal injection molding.* Journal of Materials Processing Technology, 2003. **137**(1-3): p. 132-137.
177. Chhabra, R.P. and J.F. Richardson, *Non-Newtonian flow and applied rheology: engineering applications*. 2011: Butterworth-Heinemann.
178. Gaisford, S., V. Kett, and P. Haines, *Principles of thermal analysis and calorimetry*. 2016: Royal society of chemistry.
179. Prime, R.B., H.E. Bair, S. Vyazovkin, P.K. Gallagher, and A. Riga, *Thermogravimetric analysis (TGA).* Thermal analysis of polymers: Fundamentals and applications, 2009: p. 241-317.
180. Stuart, B., *Infrared spectroscopy*. 2005: Wiley Online Library.
181. Boerckel, J.D., D.E. Mason, A.M. McDermott, and E. Alsberg, *Microcomputed tomography: approaches and applications in bioengineering.* Stem cell research & therapy, 2014. **5**(6): p. 144.
182. Stauber, M. and R. Müller, *Micro-computed tomography: a method for the non-destructive evaluation of the three-dimensional structure of biological specimens.* Osteoporosis: Methods and Protocols, 2008: p. 273-292.
183. Debelle, A. and A. Declémy, *XRD investigation of the strain/stress state of ion-irradiated crystals.* Nuclear Instruments and Methods in Physics Research Section B: Beam Interactions with Materials and Atoms, 2010. **268**(9): p. 1460-1465.
184. Drenth, J., *X-ray Diffraction: Principles.* eLS.
185. Brouwer, P., *Theory of XRF.* Almelo, Netherlands: PANalytical BV, 2006.
186. Potts, P., *X-ray fluorescence analysis: principles and practice of wavelength dispersive spectrometry*, in *A Handbook of Silicate Rock Analysis*. 1987, Springer. p. 226-285.
187. Bounakhla, M. and M. Tahri, *X-ray fluorescence analytical techniques.* National Center for Energy Sciences and Nuclear Techniques (CNESTEN), Rabat, Morocco.
188. Uo, M., T. Wada, and T. Sugiyama, *Applications of X-ray fluorescence analysis (XRF) to dental and medical specimens.* Japanese Dental Science Review, 2015. **51**(1): p. 2-9.
189. Kalidindi, S., A. Abusafieh, and E. El-Danaf, *Accurate characterization of machine compliance for simple compression testing.* Experimental mechanics, 1997. **37**(2): p. 210-215.
190. McCormick, N. and J. Lord, *Digital Image Correlation.* Materials Today, 2010. **13**(12): p. 52-54.
191. Palanca, M., G. Tozzi, and L. Cristofolini, *The use of digital image correlation in the biomechanical area: a review.* International biomechanics, 2016. **3**(1): p. 1-21.
192. Solutions, C., *VIC-3D 2010: Testing Guide.* Correlated Solutions. Irmo, SC, USA, 2010.
193. PI, L.Y., L. Smith, M.A. Gothekar, and M.X. Chen, *Measure Strain Distribution Using Digital Image Correlation (DIC) for Tensile Tests.* 2010.
194. Shettlemore, M.G. and K.J. Bundy, *Toxicity measurement of orthopedic implant alloy degradation products using a bioluminescent bacterial assay.* Journal of Biomedical Materials Research Part A, 1999. **45**(4): p. 395-403.
195. Lucas, L., J. Lemons, and R. Buchanan. *Biocompatibility evaluations of Fe, Co and Ti base alloys [J]*. in *Transactions of the Annual Meeting of the Society for Biomaterials in Conjunction with the Interna*. 1983.
196. Hench, L.L., *Bioceramics: from concept to clinic.* Journal of the american ceramic society, 1991. **74**(7): p. 1487-1510.
197. Kim, H.-M., T. Himeno, T. Kokubo, and T. Nakamura, *Process and kinetics of bonelike apatite formation on sintered hydroxyapatite in a simulated body fluid.* Biomaterials, 2005. **26**(21): p. 4366-4373.

198. Krishna, B.V., S. Bose, and A. Bandyopadhyay, *Low stiffness porous Ti structures for load-bearing implants.* Acta biomaterialia, 2007. **3**(6): p. 997-1006.
199. Taniguchi, N., S. Fujibayashi, M. Takemoto, K. Sasaki, B. Otsuki, T. Nakamura, T. Matsushita, T. Kokubo, and S. Matsuda, *Effect of pore size on bone ingrowth into porous titanium implants fabricated by additive manufacturing: an in vivo experiment.* Materials Science and Engineering: C, 2016. **59**: p. 690-701.
200. Thull, R. and D. Grant, *Physical and chemical vapor deposition and plasma-assisted techniques for coating titanium*, in *Titanium in medicine*. 2001, Springer. p. 283-341.
201. Zhao, Z.-w., G. Zhang, and H.-g. Li, *Preparation of calcium phosphate coating on pure titanium substrate by electrodeposition method.* Journal of Central South University of Technology, 2004. **11**(2): p. 147-151.
202. Narayanan, R. and S. Seshadri, *Phosphoric acid anodization of Ti–6Al–4V–Structural and corrosion aspects.* Corrosion Science, 2007. **49**(2): p. 542-558.
203. Shokouhfar, M., C. Dehghanian, M. Montazeri, and A. Baradaran, *Preparation of ceramic coating on Ti substrate by plasma electrolytic oxidation in different electrolytes and evaluation of its corrosion resistance: Part II.* Applied Surface Science, 2012. **258**(7): p. 2416-2423.
204. Ceschini, L., E. Lanzoni, C. Martini, D. Prandstraller, and G. Sambogna, *Comparison of dry sliding friction and wear of Ti6Al4V alloy treated by plasma electrolytic oxidation and PVD coating.* Wear, 2008. **264**(1): p. 86-95.
205. Wang, Y., B. Jiang, T. Lei, and L. Guo, *Dependence of growth features of microarc oxidation coatings of titanium alloy on control modes of alternate pulse.* Materials letters, 2004. **58**(12): p. 1907-1911.
206. Yerokhin, A., X. Nie, A. Leyland, and A. Matthews, *Characterisation of oxide films produced by plasma electrolytic oxidation of a Ti–6Al–4V alloy.* Surface and Coatings Technology, 2000. **130**(2): p. 195-206.
207. Cheng, Y.-l., X.-Q. Wu, Z.-g. Xue, E. Matykina, P. Skeldon, and G. Thompson, *Microstructure, corrosion and wear performance of plasma electrolytic oxidation coatings formed on Ti–6Al–4V alloy in silicate-hexametaphosphate electrolyte.* Surface and Coatings Technology, 2013. **217**: p. 129-139.
208. Martini, C., L. Ceschini, F. Tarterini, J. Paillard, and J. Curran, *PEO layers obtained from mixed aluminate–phosphate baths on Ti–6Al–4V: Dry sliding behaviour and influence of a PTFE topcoat.* Wear, 2010. **269**(11): p. 747-756.
209. Rudnev, V., K. Kilin, I. Malyshev, T. Yarovaya, P. Nedozorov, and A. Popovich, *Plasma-electrolytic oxidation of titanium in Zr (SO4) 2-containing electrolyte.* Protection of Metals and Physical Chemistry of Surfaces, 2010. **46**(6): p. 704-709.
210. Arrabal, R., E. Matykina, T. Hashimoto, P. Skeldon, and G. Thompson, *Characterization of AC PEO coatings on magnesium alloys.* Surface and Coatings Technology, 2009. **203**(16): p. 2207-2220.
211. Khan, R., A. Yerokhin, X. Li, H. Dong, and A. Matthews, *Influence of current density and electrolyte concentration on DC PEO titania coatings.* Surface Engineering, 2014. **30**(2): p. 102-108.
212. Supati, R., N. Loh, K. Khor, and S. Tor, *Mixing and characterization of feedstock for powder injection molding.* Materials Letters, 2000. **46**(2): p. 109-114.
213. Roberjot, S., D. Auzene, L. Iordache, and U. Baraldi, *Water solvent debinding for PIM parts.* PIM International, 2011. **5**: p. 51.
214. Peacock, A.J., *THE CHEMISTRY OF POLYETHYLENE*.* Journal of Macromolecular Science, Part C: Polymer Reviews, 2001. **41**(4): p. 285-323.
215. Kumar, S. and R. Singh, *Recovery of hydrocarbon liquid from waste high density polyethylene by thermal pyrolysis.* Brazilian Journal of Chemical Engineering, 2011. **28**(4): p. 659-667.

216. Klar, E. and P.K. Samal, *Powder metallurgy stainless steels: processing, microstructures, and properties*. 2007: ASM international.
217. Zeng, W., S. Li, and W. Chow, *Preliminary studies on burning behavior of polymethylmethacrylate (PMMA).* Journal of fire sciences, 2002. **20**(4): p. 297-317.
218. Petunina, Y.V., *Effect of high oxygen and nitrogen contents on the mechanical properties of titanium.* Metal Science and Heat Treatment, 1961. **3**(5): p. 276-279.
219. Saito, T., M. Takemoto, S. Fujibayashi, M. Neo, T. Murakami, F. Miyaji, and T. Nakamura, *Quantitative Comparison of Osteoconduction between PorousApatite and Wollastonite-Containing Glass-Ceramics with5 Different Pore Sizes.* Bioceramics Development and Applications, 2011. **1**.
220. Butev, E., Z. Esen, and S. Bor, *In vitro bioactivity investigation of alkali treated Ti6Al7Nb alloy foams.* Applied Surface Science, 2015. **327**: p. 437-443.
221. Loukili, A., *Self compacting concrete*. 2013: John Wiley & Sons.
222. Li, Y.-m., B.-y. Huang, and X.-h. Qu, *Viscosity and melt rheology of metal injection moulding feedstocks.* Powder Metallurgy, 2013.
223. Krauss, V.A., E.N. Pires, A.N. Klein, and M.C. Fredel, *Rheological properties of alumina injection feedstocks.* Materials Research, 2005. **8**(2): p. 187-189.
224. Smith, Y., *High Speed Mixing of MIM Feedstock.* Metal Powder Report(UK), 1991. **46**(11): p. 34-37.
225. Srikanth, V. and G. Upadhyaya, *Effect of tungsten particle size on sintered properties of heavy alloys.* Powder Technology, 1984. **39**(1): p. 61-67.
226. Seetharaman, S., *Fundamentals of metallurgy*. 2005: Elsevier.
227. Tandon, R., *Net-shaping of Co-Cr-Mo (F-75) via metal injection molding*, in *Cobalt-Base Alloys for Biomedical Applications*. 1999, ASTM International.
228. Demangel, C., D. Auzène, M. Vayssade, J.-L. Duval, P. Vigneron, M.-D. Nagel, and J.-C. Puippe, *Cytocompatibility of titanium metal injection molding with various anodic oxidation post-treatments.* Materials Science and Engineering: C, 2012. **32**(7): p. 1919-1925.
229. Zhang, J., M. Gungor, and E. Lavernia, *The effect of porosity on the microstructural damping response of 6061 aluminium alloy.* Journal of materials science, 1993. **28**(6): p. 1515-1524.
230. Hayat, M.D., G. Wen, M.F. Zulkifli, and P. Cao, *Effect of PEG molecular weight on rheological properties of Ti-MIM feedstocks and water debinding behaviour.* Powder Technology, 2015. **270**: p. 296-301.
231. Li, Y., L. Li, and K. Khalil, *Effect of powder loading on metal injection molding stainless steels.* Journal of Materials Processing Technology, 2007. **183**(2): p. 432-439.
232. Allaire, F., B.R. Marple, and J. Boulanger, *Injection molding of submicrometer zirconia: blend formulation and rheology.* Ceramics international, 1994. **20**(5): p. 319-325.
233. Park, S.J., D. Kim, D. Lin, S.J. Park, and S. Ahn, *Rheological Characterization of Powder Mixture Including a Space Holder and Its Application to Metal Injection Molding.* Metals, 2017. **7**(4): p. 120.
234. Park, S.-J., Y. Wu, D.F. Heaney, X. Zou, G. Gai, and R.M. German, *Rheological and Thermal Debinding Behaviors in Titanium Powder Injection Molding.* Metallurgical and Materials Transactions A, 2009. **40**(1): p. 215-222.
235. Sri Yulis, M.A., J. Khairur Rijal, and M. Norhamidi, *Rheological properties of SS316L MIM feedstock prepared with different particle sizes and powder loadings.* 2009.
236. Mewis, J. and N.J. Wagner, *Colloidal suspension rheology*. 2012: Cambridge University Press.
237. González-Gutiérrez, J., G.B. Stringari, and I. Emri, *Powder injection molding of metal and ceramic parts*. 2012: INTECH Open Access Publisher.

238. Hausnerova, B., B.N. Mukund, and D. Sanetrnik, *Rheological properties of gas and water atomized 17-4PH stainless steel MIM feedstocks: Effect of powder shape and size.* Powder Technology, 2017. **312**: p. 152-158.
239. Chhabra, R.P., *Non-Newtonian fluids: an introduction*, in *Rheology of complex fluids*. 2010, Springer. p. 3-34.
240. Shangguan, J. and L. Guoqin, *Morphology and Thermal Behaviour of Poly(Methyl Methacrylate)/Poly(Ethylene Glycol) Semi-Interpenetrating Polymer Networks.* Journal of the Chilean Chemical Society, 2011. **56**(4): p. 918-921.
241. Deing, A., B. Luthringer, D. Laipple, T. Ebel, and R. Willumeit, *A porous TiAl6V4 implant material for medical application.* International journal of biomaterials, 2014. **2014**.
242. Arifvianto, B. and J. Zhou, *Fabrication of Metallic Biomedical Scaffolds with the Space Holder Method: A Review.* Materials, 2014. **7**(5): p. 3588-3622.
243. Chen, G., P. Cao, G. Wen, and N. Edmonds, *Debinding behaviour of a water soluble PEG/PMMA binder for Ti metal injection moulding.* Materials Chemistry and Physics, 2013. **139**(2-3): p. 557-565.
244. Omar, M.A., R. Ibrahim, M.I. Sidik, M. Mustapha, and M. Mohamad, *Rapid debinding of 316L stainless steel injection moulded component.* Journal of Materials Processing Technology, 2003. **140**(1-3): p. 397-400.
245. Lynden-Bell, R.M.e., *Water and life : the unique properties of H2O*. 2010, Boca Raton, Fla.: CRC ; London : Taylor & Francis [distributor].
246. Ashby, M.F. and D. Cebon, *Materials selection in mechanical design.* Le Journal de Physique IV, 1993. **3**(C7): p. C7-1-C7-9.
247. Bhattarai, S.R., K.A.R. Khalil, M. Dewidar, P.H. Hwang, H.K. Yi, and H.Y. Kim, *Novel production method and in-vitro cell compatibility of porous Ti-6Al-4V alloy disk for hard tissue engineering.* Journal of Biomedical Materials Research Part A, 2008. **86**(2): p. 289-299.
248. Hayat, M.D., T. Li, G. Wen, and P. Cao, *Suitability of PEG/PMMA-based metal injection moulding feedstock: an experimental study.* The International Journal of Advanced Manufacturing Technology, 2015: p. 1-7.
249. Jha, N., D.P. Mondal, M.D. Goel, J.D. Majumdar, S. Das, and O.P. Modi, *Titanium cenosphere syntactic foam with coarser cenosphere fabricated by powder metallurgy at lower compaction load.* Transactions of Nonferrous Metals Society of China, 2014. **24**(1): p. 89-99.
250. Sidambe, A.T., I.A. Figueroa, H.G.C. Hamilton, and I. Todd, *Taguchi Optimization of Mim Titanium Sintering.* International Journal of Powder Metallurgy, 2011. **47**(6): p. 21-28.
251. Kato, K., *Effect of Sintering Temperature on Density and Tensile Properties of Titanium Compacts by Metal Injection Molding.* 粉体および粉末冶金, 1999. **46**(8): p. 865-869.
252. Fu, S.-Y., X.-Q. Feng, B. Lauke, and Y.-W. Mai, *Effects of particle size, particle/matrix interface adhesion and particle loading on mechanical properties of particulate–polymer composites.* Composites Part B: Engineering, 2008. **39**(6): p. 933-961.
253. Ashby, M.F. and R.M. Medalist, *The mechanical properties of cellular solids.* Metallurgical Transactions A, 1983. **14**(9): p. 1755-1769.
254. Venkatesh, V., A.L. Pilchak, J.E. Allison, S. Ankem, R.R. Boyer, J. Christodoulou, H.L. Fraser, M.A. Imam, Y. Kosaka, and H.J. Rack, *Proceedings of the 13th World Conference on Titanium*. 2016: John Wiley & Sons.
255. Weiner, B.B., *What is a continuous particle size distribution.* Brookhaven Instruments Corporation White Paper, Holtsville, 2011.
256. Ghasemi, A., S. Hosseini, and S. Sadrnezhaad, *Pore control in SMA NiTi scaffolds via space holder usage.* Materials Science and Engineering: C, 2012. **32**(5): p. 1266-1270.

257. Li, D., Y. Zhang, X. Ma, and X. Zhang, *Space-holder engineered porous NiTi shape memory alloys with improved pore characteristics and mechanical properties.* Journal of alloys and compounds, 2009. **474**(1): p. L1-L5.
258. Li, H., S.M. Oppenheimer, S.I. Stupp, D.C. Dunand, and L.C. Brinson, *Effects of pore morphology and bone ingrowth on mechanical properties of microporous titanium as an orthopaedic implant material.* Materials Transactions, 2004. **45**(4): p. 1124-1131.
259. Hannink, G. and J.C. Arts, *Bioresorbability, porosity and mechanical strength of bone substitutes: what is optimal for bone regeneration?* Injury, 2011. **42**: p. S22-S25.
260. Wang, X. and Q. Ni, *Determination of cortical bone porosity and pore size distribution using a low field pulsed NMR approach.* Journal of Orthopaedic Research, 2003. **21**(2): p. 312-319.
261. Kohl, M., M. Bram, H.P. Buchkremer, D. Stover, T. Habijan, and M. Koller, *Powder Metallurgical Production, Mechanical and Biomedical Properties of Porous NiTi Shape Memory Alloys.* Medical Device Materials Iv, 2008: p. 14-19.
262. Gibson, L.J., *The mechanical behaviour of cancellous bone.* Journal of biomechanics, 1985. **18**(5): p. 317-328.
263. Rho, J.-Y., L. Kuhn-Spearing, and P. Zioupos, *Mechanical properties and the hierarchical structure of bone.* Medical engineering & physics, 1998. **20**(2): p. 92-102.
264. Chappard, C., S. Bensalah, C. Olivier, P. Gouttenoire, A. Marchadier, C. Benhamou, and F. Peyrin, *3D characterization of pores in the cortical bone of human femur in the elderly at different locations as determined by synchrotron micro-computed tomography images.* Osteoporosis International, 2013. **24**(3): p. 1023-1033.
265. Javid, F., D. Pasini, and J. Angeles, *A New Surgical Barbed Staple for Minimally Invasive Surgery.* Journal of Medical Devices, 2014. **8**(3): p. 030951.
266. Felson, D.T., *Epidemiology of hip and knee osteoarthritis.* Epidemiologic reviews, 1988. **10**: p. 1-28.
267. Lane, N.E., *Osteoarthritis of the hip.* New England Journal of Medicine, 2007. **357**(14): p. 1413-1421.
268. Porter, M., M. Borroff, and P. Gregg, *National Joint Registry for England, Wales, Northern Irland and the Isle of Man.* 13th annual report . http://www-new. njrcentre. org. uk/njrcentre/Reports, (date last accesesed 18 August 2017), 2016.
269. DeOrio, J.K. and S.G. Parekh, *Total Ankle Replacement: An Operative Manual*. 2014: Lippincott Williams & Wilkins.
270. Zhou, H. and J. Lee, *Nanoscale hydroxyapatite particles for bone tissue engineering.* Acta biomaterialia, 2011. **7**(7): p. 2769-2781.
271. Fathi, M.H., A. Hanifi, and V. Mortazavi, *Preparation and bioactivity evaluation of bone-like hydroxyapatite nanopowder.* Journal of Materials Processing Technology, 2008. **202**(1–3): p. 536-542.
272. Mohseni, E., E. Zalnezhad, and A. Bushroa, *Comparative investigation on the adhesion of hydroxyapatite coating on Ti–6Al–4V implant: A review paper.* International Journal of Adhesion and Adhesives, 2014. **48**: p. 238-257.
273. Tsui, Y.C., C. Doyle, and T.W. Clyne, *Plasma sprayed hydroxyapatite coatings on titanium substrates Part 1: Mechanical properties and residual stress levels.* Biomaterials, 1998. **19**(22): p. 2015-2029.
274. Klein, C.P., P. Patka, H. Van der Lubbe, J. Wolke, and K. De Groot, *Plasma-sprayed coatings of tetracalciumphosphate, hydroxyl-apatite, and α-TCP on titanium alloy: An interface study.* Journal of biomedical materials research, 1991. **25**(1): p. 53-65.
275. David, A., J. Eitenmüller, G. Muhr, A. Pommer, H. Bär, P. Ostermann, and T. Schildhauer, *Mechanical and histological evaluation of hydroxyapatite-coated, titanium-coated and grit-blasted surfaces under weight-bearing conditions.* Archives of orthopaedic and trauma surgery, 1995. **114**(2): p. 112-118.

276. Morscher, E., A. Hefti, and U. Aebi, *Severe osteolysis after third-body wear due to hydroxyapatite particles from acetabular cup coating.* Bone & Joint Journal, 1998. **80**(2): p. 267-272.
277. Balbinotti, P., E. Gemelli, G. Buerger, S.A.d. Lima, J.d. Jesus, N.H.A. Camargo, V.A.R. Henriques, and G.D.d.A. Soares, *Microstructure development on sintered Ti/HA biocomposites produced by powder metallurgy.* Materials Research, 2011. **14**(3): p. 384-393.
278. Ning, C.Q. and Y. Zhou, *In vitro bioactivity of a biocomposite fabricated from HA and Ti powders by powder metallurgy method.* Biomaterials, 2002. **23**(14): p. 2909-2915.
279. Salman, S., O. Gunduz, S. Yilmaz, M.L. Öveçoğlu, R.L. Snyder, S. Agathopoulos, and F.N. Oktar, *Sintering effect on mechanical properties of composites of natural hydroxyapatites and titanium.* Ceramics International, 2009. **35**(7): p. 2965-2971.
280. Chenglin, C., Z. Jingchuan, Y. Zhongda, and W. Shidong, *Hydroxyapatite–Ti functionally graded biomaterial fabricated by powder metallurgy.* Materials Science and Engineering: A, 1999. **271**(1–2): p. 95-100.
281. Göller, G., F.N. Oktar, D. Toykan, and E. Kayali. *The improvement of titanium reinforced hydroxyapatite for biomedical applications*. in *Key Engineering Materials*. 2003. Trans Tech Publ.
282. Zhang, L., Z. He, Y. Zhang, Y. Jiang, and R. Zhou, *Enhanced in vitro bioactivity of porous NiTi–HA composites with interconnected pore characteristics prepared by spark plasma sintering.* Materials & Design, 2016. **101**: p. 170-180.
283. Arifin, A., A.B. Sulong, N. Muhamad, J. Syarif, and M.I. Ramli, *Material processing of hydroxyapatite and titanium alloy (HA/Ti) composite as implant materials using powder metallurgy: a review.* Materials & Design, 2014. **55**: p. 165-175.
284. Han, Y., X. Wang, H. Dai, and S. Li, *Nanosize and surface charge effects of hydroxyapatite nanoparticles on red blood cell suspensions.* ACS applied materials & interfaces, 2012. **4**(9): p. 4616-4622.
285. Li, C., X. Ge, S. Liu, G. Li, A. Zhang, J. Bai, C. Su, and R. Ding, *Redispersible dried hydroxyapatite particles with grafted pH-sensitivity polymer brushes of poly (styrene-co-4-vinylpyridine).* Powder technology, 2011. **210**(2): p. 167-174.
286. Manoj, M., R. Subbiah, D. Mangalaraj, N. Ponpandian, C. Viswanathan, and K. Park, *Influence of growth parameters on the formation of hydroxyapatite (HAp) nanostructures and their cell viability studies.* Nanobiomedicine, 2015. **2**: p. 2.
287. Shan, Y., Y. Qin, Y. Chuan, H. Li, and M. Yuan, *The synthesis and characterization of hydroxyapatite-β-alanine modified by grafting polymerization of γ-benzyl-L-glutamate-N-carboxyanhydride.* Molecules, 2013. **18**(11): p. 13979-13991.
288. Müller, M., W. Bauer, and H. Kleissl, *Low-pressure injection molding of ceramic micro devices using sub-micron and nano scaled powders.* Multi-material Micro Manufacture, 2005: p. 1-4.
289. You, W.-K., J.-P. Choi, S.-M. Yoon, and J.-S. Lee, *Low temperature powder injection molding of iron micro-nano powder mixture.* Powder technology, 2012. **228**: p. 199-205.
290. Li, Y.-m., B.-y. Huang, and X.-h. Qu, *Viscosity and melt rheology of metal injection moulding feedstocks.* Powder Metallurgy, 1999. **42**(1): p. 86-90.
291. Ismail, M.H., *Porous NiTi alloy by metal injection moulding (MIM) using partly water soluble binder system*. 2012, University of Sheffield.
292. Choi, J.-P., H.-G. Lyu, W.-S. Lee, and J.-S. Lee, *Densification and microstructural development during sintering of powder injection molded Fe micro–nanopowder.* Powder Technology, 2014. **253**: p. 596-601.
293. Bovand, D., M. Yousefpour, S. Rasouli, S. Bagherifard, N. Bovand, and A. Tamayol, *Characterization of Ti-HA composite fabricated by mechanical alloying.* Materials & Design, 2015. **65**: p. 447-453.

294. Raza, M.R., A.B. Sulong, N. Muhamad, M.N. Akhtar, and J. Rajabi, *Effects of binder system and processing parameters on formability of porous Ti/HA composite through powder injection molding.* Materials & Design, 2015. **87**: p. 386-392.
295. Barinov, S., J. Rau, S.N. Cesaro, J. Ďurišin, I. Fadeeva, D. Ferro, L. Medvecky, and G. Trionfetti, *Carbonate release from carbonated hydroxyapatite in the wide temperature rage.* Journal of Materials Science: Materials in Medicine, 2006. **17**(7): p. 597-604.
296. Lidin, R., L. Andreeva, and V. Molochko, *Spravochnik po neorganicheskoi khimii (Handbook of Inorganic Chemistry), Moscow: Khimiya, 1987.* p. 319.
297. Auger, M., B. Savoini, A. Muñoz, T. Leguey, M. Monge, R. Pareja, and J. Victoria, *Mechanical characteristics of porous hydroxyapatite/oxide composites produced by post-sintering hot isostatic pressing.* Ceramics International, 2009. **35**(6): p. 2373-2380.
298. Elbadawi, M. and M. Shbeh, *High Strength Yttria-reinforced HA scaffolds fabricated via Honeycomb Ceramic Extrusion.* Journal of the Mechanical Behavior of Biomedical Materials, 2017.
299. Muralithran, G. and S. Ramesh, *The effects of sintering temperature on the properties of hydroxyapatite.* Ceramics International, 2000. **26**(2): p. 221-230.
300. Georgiou, G. and J. Knowles, *Glass reinforced hydroxyapatite for hard tissue surgery—part 1: mechanical properties.* Biomaterials, 2001. **22**(20): p. 2811-2815.
301. Metsger, D., M. Rieger, and D. Foreman, *Mechanical properties of.* Journal of Materials Science: Materials in Medicine, 1999. **10**(1): p. 9-17.
302. Coreno, J. and O. Coreno, *Evaluation of calcium titanate as apatite growth promoter.* Journal of Biomedical Materials Research Part A, 2005. **75**(2): p. 478-484.
303. Lahiri, D., V. Singh, A.K. Keshri, S. Seal, and A. Agarwal, *Carbon nanotube toughened hydroxyapatite by spark plasma sintering: microstructural evolution and multiscale tribological properties.* Carbon, 2010. **48**(11): p. 3103-3120.
304. Linh, N.T.B., D. Mondal, and B.T. Lee, *In vitro study of CaTiO3–hydroxyapatite composites for bone tissue engineering.* ASAIO Journal, 2014. **60**(6): p. 722-729.
305. Mobasherpour, I., M.S. Heshajin, A. Kazemzadeh, and M. Zakeri, *Synthesis of nanocrystalline hydroxyapatite by using precipitation method.* Journal of Alloys and Compounds, 2007. **430**(1): p. 330-333.
306. Wang, P.E. and T. Chaki, *Sintering behaviour and mechanical properties of hydroxyapatite and dicalcium phosphate.* Journal of Materials Science: Materials in Medicine, 1993. **4**(2): p. 150-158.
307. Liu, H.-S., T.S. Chin, L. Lai, S. Chiu, K. Chung, C. Chang, and M. Lui, *Hydroxyapatite synthesized by a simplified hydrothermal method.* Ceramics International, 1997. **23**(1): p. 19-25.
308. Ooi, C., M. Hamdi, and S. Ramesh, *Properties of hydroxyapatite produced by annealing of bovine bone.* Ceramics international, 2007. **33**(7): p. 1171-1177.
309. Park, E., R.A. Condrate, D. Lee, K. Kociba, and P.K. Gallagher, *Characterization of hydroxyapatite: Before and after plasma spraying.* Journal of Materials Science: Materials in Medicine, 2002. **13**(2): p. 211-218.
310. Lefebvre, L.P. and E. Baril, *Effect of oxygen concentration and distribution on the compression properties on titanium foams.* Advanced Engineering Materials, 2008. **10**(9): p. 868-876.
311. Hak, C.R.C., I. Besar, R. Mustaffa, M.R. Yusof, and N.A. Bakar, *Effects of sintering time on the physical and compositional properties of porous biphasic calcium phosphate foam.* Journal of Nuclear and Related Technologies, 2009. **6**(1): p. 203-212.
312. Ning, C. and Y. Zhou, *On the microstructure of biocomposites sintered from Ti, HA and bioactive glass.* Biomaterials, 2004. **25**(17): p. 3379-3387.
313. Arinzeh, T.L., T. Tran, J. Mcalary, and G. Daculsi, *A comparative study of biphasic calcium phosphate ceramics for human mesenchymal stem-cell-induced bone formation.* Biomaterials, 2005. **26**(17): p. 3631-3638.

314. Ramires, P., A. Romito, F. Cosentino, and E. Milella, *The influence of titania/hydroxyapatite composite coatings on in vitro osteoblasts behaviour.* Biomaterials, 2001. **22**(12): p. 1467-1474.
315. Sun, F., R. Wang, H. Jiang, and W. Zhou, *Synthesis of sodium titanium phosphate at ultra-low temperature.* Research on Chemical Intermediates, 2013. **39**(4): p. 1857-1864.
316. Shi, H., *Activated carbons and double layer capacitance.* Electrochimica Acta, 1996. **41**(10): p. 1633-1639.
317. Wang, L., M. Fujita, and M. Inagaki, *Relationship between pore surface areas and electric double layer capacitance in non-aqueous electrolytes for air-oxidized carbon spheres.* Electrochimica acta, 2006. **51**(19): p. 4096-4102.
318. Yerokhin, A., E. Parfenov, and A. Matthews, *In situ impedance spectroscopy of the plasma electrolytic oxidation process for deposition of Ca-and P-containing coatings on Ti.* Surface and Coatings Technology, 2016. **301**: p. 54-62.
319. Huang, H.-H., *The Eh-pH Diagram and Its Advances.* Metals, 2016. **6**(1): p. 23.
320. Sugimoto, T. and X. Zhou, *Synthesis of uniform anatase TiO2 nanoparticles by the Gel–Sol method: 2. adsorption of OH− ions to Ti (OH) 4 gel and TiO2 particles.* Journal of Colloid and Interface Science, 2002. **252**(2): p. 347-353.
321. Wang, J., *Analytical electrochemistry*. 2006: John Wiley & Sons.
322. Van, T.B., S.D. Brown, and G.P. Wirtz, *Mechanism of anodic spark deposition.* Am. Ceram. Soc. Bull.;(United States), 1977. **56**(6).
323. Hanaor, D.A. and C.C. Sorrell, *Review of the anatase to rutile phase transformation.* Journal of Materials science, 2011. **46**(4): p. 855-874.
324. Hagman, L.-O. and P. Kierkegaard, *The crystal structure of NaMe2 IV (PO4) 3; MeIV= Ge, Ti, Zr.* Acta Chem. Scand, 1968. **22**(6): p. 1822-32.
325. Trout, G.R. and G.R. Schmidt, *Effect of chain length and concentration on the degree of dissociation of phosphates used in food products.* Journal of Agricultural and Food Chemistry, 1986. **34**(1): p. 41-45.
326. Wall, F.T. and R.H. Doremus, *Electrolytic transference properties of polyphosphates.* Journal of the American Chemical Society, 1954. **76**(3): p. 868-870.
327. Wazer, V., *Phosphorus and its compounds. Volume 1: Chemistry*. 1958, Interscience NewYork.
328. Gowtham, S., T. Arunnellaiappan, and N. Rameshbabu, *An investigation on pulsed DC plasma electrolytic oxidation of cp-Ti and its corrosion behaviour in simulated body fluid.* Surface and Coatings Technology, 2016. **301**: p. 63-73.
329. Matykina, E., A. Berkani, P. Skeldon, and G. Thompson, *Real-time imaging of coating growth during plasma electrolytic oxidation of titanium.* Electrochimica Acta, 2007. **53**(4): p. 1987-1994.
330. Bamberger, C.E. and G.M. Begun, *Synthesis and characterization of titanium phosphates, TiP2O7 and (TiO) 2P2O7.* Journal of the Less Common Metals, 1987. **134**(2): p. 201-206.
331. Bamberger, C.E., G.M. Begun, and O. Cavin, *Synthesis and characterization of sodium-titanium phosphates, Na4 (TiO)(PO4) 2, Na (TiO) PO4, and NaTi2 (PO4) 3.* Journal of Solid State Chemistry, 1988. **73**(2): p. 317-324.
332. Parfenov, E., A. Yerokhin, R. Nevyantseva, M. Gorbatkov, C.-J. Liang, and A. Matthews, *Towards smart electrolytic plasma technologies: an overview of methodological approaches to process modelling.* Surface and Coatings Technology, 2015. **269**: p. 2-22.
333. Pezzato, L., K. Brunelli, S. Gross, M. Magrini, and M. Dabala, *Effect of process parameters of plasma electrolytic oxidation on microstructure and corrosion properties of magnesium alloys.* Journal of Applied Electrochemistry, 2014. **44**(7): p. 867-879.

334. Cimenoglu, H., M. Gunyuz, G.T. Kose, M. Baydogan, F. Uğurlu, and C. Sener, *Micro-arc oxidation of Ti6Al4V and Ti6Al7Nb alloys for biomedical applications.* Materials Characterization, 2011. **62**(3): p. 304-311.
335. Rohanizadeh, R., M. Al-Sadeq, and R. LeGeros, *Preparation of different forms of titanium oxide on titanium surface: effects on apatite deposition.* Journal of Biomedical Materials Research Part A, 2004. **71**(2): p. 343-352.
336. Yerokhin, A., X. Nie, A. Leyland, A. Matthews, and S. Dowey, *Plasma electrolysis for surface engineering.* Surface and Coatings Technology, 1999. **122**(2): p. 73-93.
337. Georgantas, D. and H. Grigoropoulou, *Orthophosphate and metaphosphate ion removal from aqueous solution using alum and aluminum hydroxide.* Journal of Colloid and Interface Science, 2007. **315**(1): p. 70-79.
338. Hinchcliff, K.W., A.J. Kaneps, and R.J. Geor, *Equine exercise physiology: The science of exercise in the athletic horse*. 2008: Elsevier Health Sciences.
339. Yu, T., *Chemistry of variable charge soils*. 1997: Oxford University Press.
340. Li, M., J. Liu, Y. Xu, and G. Qian, *Phosphate adsorption on metal oxides and metal hydroxides: A comparative review.* Environmental Reviews, 2016. **24**(3): p. 319-332.
341. Borghols, W.J., D. Lützenkirchen-Hecht, U. Haake, W. Chan, U. Lafont, E.M. Kelder, E.R. van Eck, A.P. Kentgens, F.M. Mulder, and M. Wagemaker, *Lithium storage in amorphous TiO2 nanoparticles.* Journal of The Electrochemical Society, 2010. **157**(5): p. A582-A588.
342. Pavanello, M.A., C. Claeys, and J.A. Martino, *Microelectronics technology and devices-SBMicro 2010*. 2011, vol.